



HAL
open science

Modelling Concrete Behaviour At Early-Age : Multiscale Analysis And Simulation Of A Massive Disposal Structure

Tulio Honorio de Faria

► **To cite this version:**

Tulio Honorio de Faria. Modelling Concrete Behaviour At Early-Age : Multiscale Analysis And Simulation Of A Massive Disposal Structure. Other. École normale supérieure de Cachan - ENS Cachan, 2015. English. NNT : 2015DENS0045 . tel-01241585

HAL Id: tel-01241585

<https://theses.hal.science/tel-01241585>

Submitted on 10 Dec 2015

HAL is a multi-disciplinary open access archive for the deposit and dissemination of scientific research documents, whether they are published or not. The documents may come from teaching and research institutions in France or abroad, or from public or private research centers.

L'archive ouverte pluridisciplinaire **HAL**, est destinée au dépôt et à la diffusion de documents scientifiques de niveau recherche, publiés ou non, émanant des établissements d'enseignement et de recherche français ou étrangers, des laboratoires publics ou privés.

**THESE DE DOCTORAT
DE L'ECOLE NORMALE SUPERIEURE DE CACHAN**

Présentée par

Monsieur **Túlio HONORIO DE FARIA**

pour obtenir le grade de
DOCTEUR DE L'ECOLE NORMALE SUPERIEURE DE CACHAN

Domaine :
MECANIQUE- GENIE MECANIQUE – GENIE CIVIL

Sujet de la thèse :
**MODELLING CONCRETE BEHAVIOUR AT EARLY-AGE: MULTISCALE
ANALYSIS AND SIMULATION OF A MASSIVE DISPOSAL STRUCTURE**

Thèse présentée et soutenue à Cachan le 28 septembre 2015 devant le jury composé de

Alain SELLIER	Professeur, Université Paul Sabatier	Examineur
Jean-Michel TORRENTI	Professeur, ENPC	Rapporteur
Qi-Chang HE	Professeur, Université de Marne-La-Vallée	Rapporteur
Miguel AZENHA	Professeur assistant, Université de Minho	Examineur
Julien SANAHUJA	Ingénieur chercheur, EDF	Examineur
Wim BASTIAENS	Ingénieur, ONDRRAF/NIRAS	Examineur
Benoît BARY	Ingénieur chercheur, CEA	Directeur de thèse
Farid BENBOUDJEMA	Professeur, ENS Cachan	Co-Encadrant

LMT- Cachan
ENS-Cachan/CNRS/Université Paris
Saclay
61, avenue du Président Wilson, 94235
CACHAN CEDEX (France)

**Laboratoire d'Etude du Comportement
des Bétons et des Argiles (LECBA)**
CEA/DEN/DPC/SECR/LECBA
CEA SACLAY
91191 Gif-sur-Yvette Cedex, France

ABSTRACT

The accurate prediction of the long and short-term behaviour of concrete structures in the nuclear domain is essential to ensure optimal performances (integrity, containment properties) during their service life. In the particular case of massive concrete structures, at early age the heat produced by hydration reactions cannot be evacuated fast enough so that high temperatures may be reached and the resulting gradients of temperature might lead to cracking according to the external and internal restraints to which the structures are subjected.

The goals of this study are (1) to perform numerical simulations in order to describe and predict the thermo-chemo-mechanical behaviour at early-age of a massive concrete structure devoted to nuclear waste disposal on surface, and (2) to develop and apply upscaling tools to estimate rigorously the key properties of concrete needed in an early-age analysis from the composition of the material.

Firstly, a chemo-thermal analysis aims at determining the influence of convection, solar radiation, reradiation and hydration heat on the thermal response of the structure. Practical recommendations regarding concreting temperatures are provided in order to limit the maximum temperature reached within the structure. Then, by means of a mechanical analysis, simplified and more complex (i.e. accounting for coupled creep and damage) modelling strategies are used to assess scenarios involving different boundary conditions defined from the previous chemo-thermal analysis.

Secondly, a study accounting for the multiscale character of concrete is performed. A simplified model of cement hydration kinetics is proposed. The evolution of the different phases at the cement paste level can be estimated. Then, analytical and numerical tools to upscale the ageing properties are presented and applied to estimate the mechanical and thermal properties of cement-based materials. Finally, the input data used in the structural analysis are compared with the estimations obtained in the multiscale analysis.

To conclude, the entire strategy proposed in this thesis aims at predicting the behaviour of massive concrete structures from the composition of the concrete by means of a sequenced approach: concrete behaviour is estimated using the upscaling tools, providing then the input data to the phenomenological analysis at the structure level.

Keywords: concrete; early age; thermo-chemo-mechanical analysis; ageing viscoelasticity; homogenization

RESUME

La prédiction précise du comportement à long et court terme des structures en béton dans le domaine nucléaire est essentielle pour assurer des performances optimales (intégrité, capacité de confinement) pendant leur durée de vie. Dans le cas particulier des structures massives en béton, la chaleur produite au jeune âge par les processus d'hydratation ne peut pas s'évacuer rapidement, si bien que des températures élevées peuvent être atteintes et les gradients de température qui en résultent peuvent conduire à la fissuration, en fonction des conditions aux limites et contraintes internes auxquelles ces structures sont soumises.

Les objectifs de cette étude sont (1) d'effectuer des simulations numériques afin de décrire et prédire le comportement thermo-chimio-mécanique au jeune âge d'une structure massive en béton dédiée au stockage de déchets en surface, et (2) de développer et appliquer des outils de changement d'échelle pour estimer rigoureusement, à partir de la composition du matériau, les propriétés physiques du béton nécessaires à une analyse au jeune âge.

Une étude chimio-thermique visant à déterminer l'influence de la convection, du rayonnement solaire, du re-rayonnement et de la chaleur d'hydratation sur la réponse thermique de la structure est tout d'abord menée. Des recommandations pratiques concernant les températures de bétonnage sont fournies afin de limiter la température maximale atteinte au sein de la structure. Ensuite, au moyen d'une analyse mécanique, des stratégies de modélisation simplifiées et plus complexes (prenant en compte l'endommagement couplé au fluage) sont mises en œuvre pour évaluer des scénarios intégrant différentes conditions aux limites issues de l'analyse chimio-thermique précédente.

Dans un second temps, une étude prenant en compte le caractère multi-échelle du béton est réalisée. Un modèle simplifié de cinétique d'hydratation du ciment est proposé. Les évolutions des fractions volumiques des différentes phases au niveau de la pâte de ciment peuvent être alors estimées. Par la suite des outils d'homogénéisation analytiques et numériques développés dans un cadre vieillissant sont présentés et appliqués pour estimer les propriétés mécaniques et thermiques des matériaux cimentaires. Les données d'entrée utilisées dans l'analyse structurelle sont finalement comparées avec les estimations obtenues dans l'analyse multi-échelle.

Pour conclure, la stratégie proposée dans cette thèse vise à prédire le comportement des structures massives en béton à partir de la composition du béton au moyen d'une approche séquentielle: le comportement du béton est estimé via les outils de changement d'échelle, fournissant ainsi les données d'entrée pour l'analyse phénoménologique à l'échelle de la structure.

Mots-clés: béton; jeune âge; analyse thermo-chimio-mécanique; viscoélasticité vieillissante; homogénéisation.

RESUMO

A previsão do comportamento a longo e curto prazos de estruturas de concreto no domínio nuclear é essencial para assegurar um desempenho ótimo (integridade, a capacidade de contenção) dessas estruturas em sua vida útil. No caso particular de estruturas massivas de concreto, o calor gerado nas primeiras idades pelos processos de hidratação não pode ser evacuado de forma suficientemente rápida, de modo que temperaturas elevadas podem ser alcançadas e os gradientes de temperatura resultantes podem levar à fissuração em função das condições limites e das restrições internas às quais a estrutura é submetida.

Os objetivos deste estudo são: (1) realizar simulações numéricas para descrever e prever o comportamento termo-químico-mecânico de uma estrutura de concreto maciço nas primeiras idades e (2) desenvolver e aplicar ferramentas de homogeneização para determinar rigorosamente, a partir da composição do material, as propriedades do concreto necessárias para realizar uma análise nas primeiras idades.

Em primeiro lugar, um estudo químico-térmico visa determinar a influência de diferentes fenômenos (convecção, radiação solar, re-radiação e calor de hidratação) que afetam a resposta térmica da estrutura estudada. São fornecidas recomendações práticas sobre as temperaturas de concretagem com objetivo de limitar a temperatura máxima atingida no interior da estrutura. Em seguida, a partir de análise mecânica, são estudadas estratégias de modelagem simplificadas e outras mais complexas (tendo em conta o acoplamento entre o dano e a fluência) a fim de avaliar criticamente diferentes cenários da análise químico-térmica precedente.

Em segundo lugar, é feito um estudo que leva em conta o caráter multiescalar do concreto. É proposto um modelo simplificado da cinética de hidratação do cimento. A evolução das frações volumétricas das fases presentes na escala da pasta de cimento podem então ser estimadas. Em seguida, são desenvolvidas ferramentas de homogeneização em um contexto em que o envelhecimento do material é considerado. Essas ferramentas são, em seguida, aplicadas na estimação das propriedades mecânicas e térmicas dos materiais cimentícios. Os dados utilizados na análise estrutural são finalmente comparados com as estimativas obtidas na análise multi-escala.

Com a estratégia proposta nesta tese, a previsão do comportamento de estruturas maciças a partir da composição de concreto é possível por meio de uma abordagem sequencial: o comportamento do concreto é determinado usando a estratégia baseada em mecanismos que fornece, por sua vez, os dados de entrada para a análise fenomenológica na escala da estrutura.

Palavras-chave: concreto; primeiras idades; análise termo-químico-mecânica; viscoelasticidade com envelhecimento; homogeneização.

ACKNOWLEDGMENTS

This present work has been performed as part of the project on disposal of LILW-SL that is carried out by ONDRAF/NIRAS, the Belgian Agency for Radioactive Waste and enriched Fissile Materials.

I wish firstly to address my great gratitude to Benoit Bary for the supervision for the research project, the insightful and constructive discussions and permanent availability; without his supervision this work could not have been successfully carried out.

I acknowledge Farid Benboudjema for the co-supervision and for bringing another important critical perspective about the methodologies and results obtained in this thesis.

I am very grateful to Professors Jean-Michel Torrenti and Qi-Chang He, for having accepted to review my dissertation and also to Professors Alain Sellier and Miguel Azenha who accepted to examine my work.

I thank Julien Sanahuja for accepting to examine this work and for the perceptive discussions during the collaboration meetings, which were very important to the accomplishment of this thesis.

Thanks Wim Bastiens for following my work (especially for asking the right “practical” questions concerning the first part of this thesis) as well as examining this manuscript. I also acknowledge Robert Gens for following the project and for the kind and fast responses about the necessary information regarding cAt Project as well as the authorization for publishing the results of this work.

Thanks Valérie L’Hostis for presenting the challenge and for accepting my proposition of participation on Nanocem consortium and RILEM Technical Committee on Thermal cracking of massive concrete structures, as well as in different conferences, which allowed disseminate the results I obtained in this thesis.

In spite of all the distractions they provoked every day after 6pm and the permanent and contagious hunger, thanks for the friendliness, Rita and Sylvain, as well as the other guys of the 2nd floor (the ones that are still here and the many other one who left...).

This thesis was written mainly under the effect of “Tristan und Isolde”, Belle & Sebastian, Stravinsky, PJ Harvey, MC Carol and Villa-Lobos.

∞

Não por essa tese mas por muito mais
Mais que gratidão
E apesar de um afastamento que nao tinha razão,
a distância nunca vai superar o amor que tenho por vocês
Divina, Luana e Walter.

TABLE OF CONTENTS

Abstract	2
Résumé.....	3
Resumo.....	4
Acknowledgments	5
Table of Contents	6
List of Tables	10
List of Figures	11
1.Introduction.....	16
1.1 Industrial context	16
1.2 Objectives, Scope and Outline of the thesis	17
1.2.1 Concrete and massive structures at early age	17
1.2.2 Cement-based materials: multiscale character and ageing behaviour	19
1.2.3 Goals	20
1.2.4 Limitations and further definition of the scope.....	21
1.2.5 Chapter outline.....	22
PART I. Structure and its environment: Phenomenological modelling at the structure scale	24
2.Chemo-thermalmodelling	24
2.1 Definition of the thermo-chemical problem	25
2.1.1 Heat of hydration	26
2.1.2 Characteristic length of heat diffusion.....	27
2.2 Thermal boundary conditions.....	28
2.2.1 Convection and reradiation	28
2.2.2 Solar radiation.....	30
2.2.3 Conduction through the ground and old structural members.....	33
2.3 Preliminary analysis of the contribution of the boundary conditions on the thermal response	33
2.3.1 Solution for the inhomogeneous problem with inhomogeneous boundary conditions.....	34
2.3.2 Results of the analytical study	37
2.4 FEM Numerical simulations of the chemo-thermal problem.....	39
2.4.1 Chemo-thermal properties	40
2.4.2 Definition of the initial conditions.....	42
2.4.3 Description of the ambient temperature, convection and reradiation	42
2.4.4 Solar radiation.....	43
2.4.5 Ground temperature	44
2.4.6 Definition of the scenarios for FEM simulations.....	45

2.5	Results and discussion	46
2.5.1	Validation of the chemo-thermal model	47
2.5.2	Influence of the solar flux	48
2.5.3	Influence of the wind on convection conditions	49
2.5.4	Competing mechanisms	51
2.5.5	Influence of concreting temperatures.....	52
2.5.6	Influence of the formwork material	57
2.5.7	Placing frequency.....	58
2.6	Conclusions and perspectives	59
3	Mechanical modelling.....	61
3.1	Thermo-chemo-mechanical problem.....	63
3.1.1	Autogenous strains.....	63
3.1.2	Thermal strains.....	64
3.1.3	Ageing elasticity	64
3.1.4	Basic creep.....	65
3.1.5	Damage	66
3.1.6	Cracking index	67
3.1.7	Crack opening	68
3.2	Description of FEM simulations.....	68
3.2.1	Restraint conditions	69
3.2.2	Mechanical input data	70
3.2.3	Structural assembly.....	71
3.2.4	Mechanical properties of the ground	71
3.3	Results and discussion	71
3.3.1	Influence of restraint and thermal boundary conditions: evaluation by the cracking index	71
3.3.2	Influence of the thermal conditions	75
3.3.3	Placing frequency.....	77
3.3.4	Simulations accounting for damage.....	78
3.3.5	Crack opening	82
3.4	Conclusions and perspectives	83
	PART II. Estimation of ageing properties from the paste composition	85
4	Modelling Hydration	85
4.1	Objectives	88
4.2	Mechanisms driving the kinetics	88
4.2.1	Boundary nucleation and growth (BNG).....	89
4.2.2	Space-filling.....	91
4.2.3	Interaction with neighbouring particles and reacting zone hypothesis	91
4.2.4	Diffusion-controlled growth (DF) and slow reaction period	93
4.2.5	Influence of the Particle Size Distribution.....	95
4.2.6	Degree and rate of hydration.....	96

4.2.7	Effects of the temperature.....	97
4.3	Application to alite early hydration.....	97
4.3.1	Influence of the PSD.....	97
4.3.2	Influence of the w/c ratio.....	99
4.4	Application to cement early and late hydration.....	100
4.4.1	Hydration reactions balance.....	101
4.4.2	Experimental data.....	102
4.4.3	Early hydration and influence of the temperature.....	103
4.4.4	Late hydration.....	104
4.4.5	Evolution of the volume fractions.....	105
4.5	Conclusion and perspectives.....	107
5	Homogenization in an ageing linear viscoelastic framework.....	108
5.1	Ageing linear viscoelasticity.....	109
5.1.1	Creep and relaxation tests.....	109
5.1.2	Definition of a division ring.....	111
5.1.3	Correspondence with elasticity.....	112
5.2	Analytical homogenization.....	112
5.2.1	Estimation of the effective behaviour.....	112
5.2.2	Mori-Tanaka estimations.....	113
5.2.3	Generalized self-consistent (GSC) scheme: n-coated spherical inclusion estimations.....	113
5.2.4	Numerical evaluation of the Volterra integral.....	121
5.3	Numerical homogenization.....	121
5.3.1	Mesostructure generations.....	122
5.3.2	Influence of the boundary conditions.....	123
5.3.3	Determination of effective properties.....	124
5.4	Application to ageing materials.....	124
5.4.1	Two-phase material.....	126
5.4.2	Three-phase material.....	128
5.4.3	Influence of the discretization.....	131
5.5	Conclusions.....	133
6	Estimation of the ageing linear viscoelastic properties of cement-based materials.....	134
6.1	Origins of the viscoelastic behaviour in cement-based materials.....	135
6.2	Multiscale strategy.....	137
6.3	Cement paste scale.....	138
6.3.1	Dissolution/Precipitation and solidification mechanisms.....	138
6.3.2	C-S-H behaviour.....	140
6.3.3	Effective properties at the cement paste scale.....	143
6.4	Mortar scale.....	145
6.4.1	Definitions of ITZ volume and composition.....	145
6.4.2	Effective properties at the mortar scale.....	147
6.5	Concrete scale.....	148

6.5.1	Mesostructures	149
6.5.2	Effective properties at the concrete level.....	150
6.5.3	Local information and influence of the aggregate shape	151
6.6	Conclusions and perspectives	156
7	Contribution of the mutliscale analysis to the structural analysis	157
7.1	Elastic properties	157
7.2	Ageing Viscoelastic behaviour	159
7.3	Thermal properties.....	159
7.3.1	Heat capacity.....	161
7.3.2	Thermal conductivity.....	162
7.3.3	Coefficient of thermal expansion.....	164
7.4	Conclusions an perspectives	165
8	General conclusions and perspectives	167
8.1	Structure and its environment: Phenomenological modelling at the structure scale	168
8.2	Estimation of ageing properties from the concrete composition	169
	References.....	172

LIST OF TABLES

Table 2.1 Chemo-thermal properties.....	41
Table 2.2 Formulation of concrete	41
Table 2.3 Sets of temperature.....	43
Table 2.4 Ground thermal properties	45
Table 2.5 Simulation campaign: thermo-chemical model	46
Table 2.6 Fitting parameters for Eq. 1.39	56
Table 3.1 Mechanical properties and parameters for concrete	70
Table 3.2 Elastic and thermal properties of the ground layers.....	71
Table 4.1 Parameters used in the simulations based on values in the literature, for $w/c = 0.4$	98
Table 4.2 Properties of phases (Tennis and Jennings, 2000)	101
Table 4.3 Normative cement composition computed from the oxide composition as provided by Holcim...	102
Table 4.4 Fitting parameters for each clinker phase	103
Table 5.1 Elastic properties and parameters for the generalized Maxwell model	125
Table 6.1 Elastic properties of the different phases	139
Table 7.1 Thermal properties: results for different temperatures (ranging from 10 to 30 °C): the bold values are used in the simulations.....	160

LIST OF FIGURES

Figure 1.1 Surface disposal solution for low emissivity nuclear waste: cAt project in Dessel, Belgium (ONDRAF/NIRAS, 2010)	16
Figure 1.2 Multiscale character of cement-based materials and structures	19
Figure 2.1 Schematic representation of the phenomena involved in the chemo-thermal analysis of a concrete structure (radiation from the ground and other neighbouring elements is not considered in the following).....	26
Figure 2.2 Schematic representation of an inclined surface with an indication of the parameters involved in the model (from (Van Breugel and Koenders, 2001)).....	31
Figure 2.3 Influence of the surface inclination θ for 1st August	32
Figure 2.4 Variation of solar flux according to the day in the year	32
Figure 2.5 Linear approximation of the thermo-activation factor for $T_0 = 20\text{ }^\circ\text{C}$	35
Figure 2.6 Evolution of the temperatures at different distances from the surface: full lines for scenarios with convection and reradiation; dashed lines for scenarios with convection, reradiation and constant solar flux; in all cases T_a is kept constant.....	37
Figure 2.7 Profiles of temperatures at different times: scenarios with (dashed lines) and without (full lines) solar flux; in all cases T_a is kept constant.....	37
Figure 2.8 Gradient of temperature: scenarios with (dashed lines) and without (full lines) solar flux. In both cases convection with $V_{wind} = 4.6\text{ m/s}$	38
Figure 2.9 Profile of temperature at different times (1 day and 1.5 days) for different wind velocities. Dashed lines correspond to $t = 1.0\text{ day}$ and full lines to $t = 1.5\text{ days}$	39
Figure 2.10 Sensibility of the solar flux ($q_s = 134\text{ W/m}^2$). Dashed lines correspond to $t = 1.0\text{ day}$ and full lines to $t = 1.5\text{ days}$	39
Figure 2.11 Structure orientation and discretization: concrete structure and ground (Honorio et al., 2014a).....	40
Figure 2.12 Affinity and Heat released (as also studied by (Craeye et al., 2010, 2009))	41
Figure 2.13 Hydration heat diffusion length l_h , after Eq. (1.5)	41
Figure 2.14 Sets of temperature	43
Figure 2.15 Solar flux: modelling and comparison with experimental data	43
Figure 2.16 Solar radiation used as input for the simulations for an inclination of 90° (laterals of the walls) and for an inclination of 0° (top of the wall and top of the base slab)	44
Figure 2.17 Profile of temperature in a hot month (August) and in a cold month (November) computed from a transient analysis considering the three previous months	45
Figure 2.18 Evolution of the temperature: comparison of model and experimental results for core temperatures (A) and Surface temperatures (B). Full lines correspond to model results and points correspond to experimental results.....	47

Figure 2.19 Evolution of the temperatures according to the solar flux: feedback on core (70 cm wall) and surface temperatures. Note that the curves corresponding to the core mean flux and core with flux are superposed.....	49
Figure 2.20 Evolution of the maximum temperatures according to the wind velocity.....	50
Figure 2.21 Evolution of temperatures according to the wind velocity. Core temperature (A), surface temperatures (B) in a current zone (at 2 m from corner in the outer part of the East wall).....	50
Figure 2.22 Temperature profiles at the peaks of temperature: scenario with solar flux and mean V_{wind}	51
Figure 2.23 Influence of placing temperature on the maximum temperatures (zoom in the zones within the rectangles) in the walls (top) and in the base slab (bottom).....	52
Figure 2.24 Influence of placing temperature on surface temperatures (in a current zone at 2 m from corner in the outer part of the East wall).....	53
Figure 2.25 Evolution of the maximum temperatures according to the different temperature scenarios in the walls (top) and in the base slab (bottom).....	54
Figure 2.26 Influence of ambient temperature on minimal temperature reached in the structure.....	54
Figure 2.27 Sensibility analysis for Set 3.....	55
Figure 2.28 Maximum temperatures from simulations.....	56
Figure 2.29 Fitted surface.....	56
Figure 2.30 Maximum, mean and minimal temperatures.....	58
Figure 2.31 Surface and core temperatures.....	58
Figure 2.32 Maximum temperatures reached for different placing days.....	58
Figure 3.1 Rheological model for ageing creep.....	65
Figure 3.2 Meshed reinforcement of walls and base slab.....	69
Figure 3.3 Determination of strength evolution: comparison against experimental data.....	70
Figure 3.4 Autogenous (a) and basic creep (b) strains: fitted curves and experimental results.....	70
Figure 3.5 Highest eigenstress for RC1 and RC4 (other cases not shown for conciseness), $t=15.31$ days.....	72
Figure 3.6 CI at $t = 15.31$ days.....	73
Figure 3.7 CI for the walls (a) and slab (b) according to the thermal boundary conditions.....	73
Figure 3.8 First eigenstress within the walls: scenario with (right) and without (left) reinforcement (no damage considered).....	75
Figure 3.9 Highest eigenstress at $t = 15.08$ days according to the thermal boundary conditions, RC4.....	76
Figure 3.10 Cracking index for the walls (a) and slab (b) according to the thermal boundary conditions.....	77
Figure 3.11 Highest eigenstress after the assembly (to be compared with the assembly at 14 days as shown in Figure 2.14 -Set 3), RC4.....	77
Figure 3.12 Uniaxial stress-strain response in tension as a function of β and ξ (τ indicates the ξ of the time at which the loading is applied), rate of strain loading = 7.50×10^{-9} s ⁻¹	79
Figure 3.13 Highest eigenstress (left) and damage (right) at $t=15.08$ days, RC4.....	80
Figure 3.14 Highest eigenstress (left) and damage (right) at $t=15.08$ days for November temperatures (Set 5), RC4.....	81
Figure 3.15 Cracking opening at 31.33 days (RC4, $\beta = 0.2$). EPXX [m] is the maximum value of the crack opening tensor in its principal basis.....	82
Figure 4.1 Confined reaction zone.....	92

Figure 4.2 ffree for different particles sizes and reaction zones thickness: elim= 0.5 μm (dashed lines), elim= 1 μm (full lines) and elim= 10 μm (dotted lines).....	92
Figure 4.3 Schematic representation of (a) Jander and (b) Ginstiling-Brounstein diffusion-controlled kinetics	94
Figure 4.4 Algorithm for the determination of the degree of hydration	96
Figure 4.5 Rate and degree of hydration for monodisperse cases. Particle sizes: (a) 2 μm, (b) 5 μm, (c) 10 μm and (d) 20 μm. w/c = 0.4; elim= 0.5 μm; g2= = 0.3 μm/h; t1/2=7 h, kDEN= 0.01 g/cm3/h; ρmax = 2.2 g/cm3; ρmin=0.2 g/cm3.....	98
Figure 4.6 Particle size distribution of alite from Costoya (2008) experimental data (dots) and fitted curves (full lines).....	98
Figure 4.7 Fitted calorimetric data (dots are experiments (Costoya, 2008), lines are the model results) for C3S hydration according to different PSD: (a) 18 μm, (b) 38 μm and (c) 83 μm. w/c = 0.4; The parameters used here are presented in 0.....	99
Figure 4.8 Rates of hydration according to the particle size and w/c ratio. Same parameters as in the sensibility study in	100
Figure 4.9 Heat flux and degree of hydration according to different w/c ratios for the PSD 18 μm . Parameters from Table 4.1. Note that the curves for w/c = 0.4 and 0.5 are superposed.....	100
Figure 4.10 Passing particle size distribution of cement. The dots are experimental measures (provided by Holcim) and the full line the fitted distribution	102
Figure 4.11 Experimental and modelled heat flux of cement. w/c=0.5; elim= 0.475 μm.....	103
Figure 4.12 Cement heat flux for different temperatures; comparison with isothermal calorimetric data from (Craeye et al., 2010). w/c=0.5; elim= 0.475 μm.	104
Figure 4.13 Degree of hydration according to different w/c ratios for cement. elim= 0.475 μm; g2= 0.42 μm/h; t1/2= 11 h, kDEN= 0.005 g/cm3/h; ρmax = 2.2 g/cm3; ρmin=0.2 g/cm3; Di = 15x10-15 cm2/h.....	105
Figure 4.14 Evolution of the volume fractions according to the w/c ratio	106
Figure 5.1 Creep test (uniaxial).....	110
Figure 5.2 Relaxation test	110
Figure 5.3 Microstructure representation.....	114
Figure 5.4 Example of verification of the isotropy (left) for a meshed mesostructure (right): Evaluation of the ratio strain/stress in the direction ii of the loading. The curves are superposed.	123
Figure 5.5 Ageing function. The degree of reaction (DoR) is given by Eq. (5.59)	125
Figure 5.6 Bulk and shear relaxation behaviour of phases: Phase 0 (Dashed) and Phase 2 (Dotted).....	126
Figure 5.7 Biphasic mesostructures: matrix (bottom) and inclusions (top).....	126
Figure 5.8 Bulk and shear relaxation function for uniaxial loading at different loading ages: comparison with numerical homogenization (SUBC).....	127
Figure 5.9 Creep functions for uniaxial loading at different loading ages: comparison with numerical homogenization (KUBC and SUBC).....	127
Figure 5.10 Effect of the volume fraction: GSC (dashed lines) compared to Mori-Tanaka (dotted lines) and numerical SUBC (full lines) estimations.....	128

Figure 5.11 Three-phase mesostructure: matrix (right) and biphasic inclusions (left). 40% of inclusions: core (25%) and coat (15%)	129
Figure 5.12 Bulk and shear relaxation functions: analytical (dashed lines) compared to numerical SUBC (full lines) estimations.....	129
Figure 5.13 Creep functions: analytical (dashed lines) compared to numerical SUBC (full lines) estimations.	130
Figure 5.14 Average strains per phase: analytical estimations (lines) compared to numerical estimations (points)	131
Figure 5.15 Average stresses per phase: analytical estimations (lines) compared to numerical estimations (points)	131
Figure 5.15 Discretization: 0.98 (left), 1.81(centre) and 3.67 (right) millions tetrahedral finite elements	132
Figure 5.16 Influence of the mesh refinement: bulk and shear relaxation (up) and creep function (down)...	132
Figure 6.1 Structure of C-S-H according to Jennings Colloid model (adapted from (Jennings, 2008)) : (a) globule scale with the IGP, (b) local arrangement of globules and (c) globule flocs overlapping.....	136
Figure 6.2 Multiscale strategy with combined analytical and numerical homogenization.....	137
Figure 6.3 Schematic representation of the solidification process adopted	139
Figure 6.4 Repartition of the products: Inner and Outer products. The ITZ is shown in Figure 6.14.....	140
Figure 6.5 C-S-H HD and LD deviatoric and volumetric components of compliance tensor: non-ageing behaviour, no space filling accounted for.	142
Figure 6.6 C-S-H packing density evolution according to Eq. (6.8).....	143
Figure 6.7 C-S-H deviatoric and volumetric components of compliance tensor for different loading ages: intrinsically ageing behaviour accounting for space filling process.....	143
Figure 6.8 Inner and outer layers: estimated bulk (full lines) and shear (dashed lines) relaxation functions for different loading ages	144
Figure 6.9 Effect of the discretization of the ageing function on the bulk relaxation function of the HD product layer.....	144
Figure 6.10 Effective behaviour of the cement paste: bulk (full brown lines) and shear (green dashed lines) relaxation function.....	145
Figure 6.11 Effective behaviour of the cement paste: creep function.....	145
Figure 6.12 Passing volume fraction of sand used in the simulation (sand 0/4).....	146
Figure 6.13 ITZ volume fraction according to the thickness of the ITZ (eITZ).....	146
Figure 6.14 Composition of the ITZ according to the thickness of the ITZ (same legend as in Figure 6.4)..	147
Figure 6.15 ITZ: estimated bulk (full lines) and shear (dashed lines) relaxation functions (see Figure 6.8 to be compared with LD layer)	148
Figure 6.16 Effective behaviour of the mortar: bulk and shear relaxation function.....	148
Figure 6.17 Effective behaviour of the mortar: creep function.....	148
Figure 6.18 Mesostructures with matrix and spherical inclusions (up) and Voronoi inclusions (down) used in FEM simulations.....	149
Figure 6.19 Particle size of the inclusions in both meshes (a) Spherical and (b) Voronoi inclusions.....	149
Figure 6.20 Estimated bulk and shear relaxation functions of concrete: comparison between the mesostructures with spherical (full lines) and Voronoi (dotted lines) inclusions.....	150

Figure 6.21 Overall uniaxial creep function of concrete obtained by combined numerical and analytical homogenization: comparison between the mesostructures with spherical (full lines) and Voronoi (dotted lines) inclusions.....	151
Figure 6.22 Dispersion of the uniaxial strain averaged within matrix subvolumes and the aggregates, $t_0 = 2$ days	152
Figure 6.23 Distribution of the uniaxial strain for the matrix and the aggregates, $t_0 = 2$ days	152
Figure 6.24 Dispersion of the uniaxial strain averaged within matrix subvolumes and the aggregates, $t_0 = 14$ days	153
Figure 6.25 Distribution of the uniaxial strain for the matrix and the aggregates, $t_0 = 14$ days	153
Figure 6.26 Distribution of the uniaxial strain for the matrix: comparison between microstructures with spherical and Voronoi inclusions	154
Figure 6.27 Coefficient of variation according to the shape of the inclusions and loading time.....	154
Figure 6.28 Strains (in the direction of the loading) within aggregates and mortar matrix at different ages for $t_0 = 2$ and 14 days	155
Figure 7.1 Young modulus: evolution as a function of (a) time and (b) degree of hydration	158
Figure 7.2 Elastic Poisson ratio (no viscous effects considered): as a function of (a) time and (b) degree of hydration	158
Figure 7.3 Basic creep tests at concrete level: experimental (dots) and numerical estimations (full and dashed lines).....	159
Figure 7.4 Evolution of the heat capacity of the cement paste, mortar and concrete, $w/c = 0.5$: as a function of time (a) and of the degree of hydration (b).....	162
Figure 7.5 Evolution of the thermal conductivity of the cement paste, ITZ, mortar and concrete, $w/c = 0.5$: as a function of time (a) and of the degree of hydration (b)	163
Figure 7.6 Evolution of the CTE of the cement paste, mortar and concrete, $w/c = 0.5$: as a function of time.....	165

1. INTRODUCTION

This project lies within the framework of the study of the feasibility of nuclear waste disposal structures built in reinforced concrete. In this context, the prediction of the long and short-term behaviour of concrete structures is essential to ensure an adequate performance through their service life. In the particular case of nuclear structures, these predictions help the design processes in which the integrity and confinement properties must be ensured.

1.1 INDUSTRIAL CONTEXT

The project is inscribed in the domain of radioactive waste management, which consists in an integrated action involving: accumulation, processing, handling, packaging, transporting, storage, disposal and decontamination and decommissioning (Saling, 2001). The project focuses on a disposal solution proposed by ONDRAF/NIRAS, the *Belgium National Agency for Radioactive Waste and Enriched Fissile Material*, which is the body responsible for radioactive waste management in Belgium. The study is a part of the *cAt project* in Dessel, which is the integrated project for surface disposal of Belgian category A waste (ONDRAF/NIRAS, 2010). To answer the requirements of radioactive waste management, this solution aims at immobilising and separating radioactive material, in order to prevent any contact with human beings and prevent their entry into the environment during the time it needs to lose most of its radioactivity through decay of short-lived elements (300 years) (ONDRAF/NIRAS, 2010). Belgian category A waste comprises low emissivity waste, i.e. waste that has been processed and conditioned. This kind of waste contains a limited amount of radioactive substances, a reduced portion of which is long-lived (ONDRAF/NIRAS, 2010). Due to these properties, category A waste is safe for surface disposal (ONDRAF/NIRAS, 2010).



Figure 1.1 Surface disposal solution for low emissivity nuclear waste: cAt project in Dessel, Belgium (ONDRAF/NIRAS, 2010)

The procedures of this disposal solution are summarised (Figure 1.1) as follows (ONDRAF/NIRAS, 2010):

-
- The waste is placed in concrete caissons and then encapsulated with mortar to form a monolith, which blocks radioactive radiation and immobilises radioactive substances constituting a first key safety element.
 - The monoliths are placed in **concrete modules**, which are structures with thick reinforced concrete walls – 34 modules are currently planned. After backfilling, the modules are closed off with a concrete cover. A permanent roof covering all modules will offer protection against weather conditions before, during and after backfilling.
 - In time, the fixed roof will be replaced by a permanent waterproof final cover. Two tumuli will remain after that. The repository currently provides for disposal of 1,000 monoliths per annum.

The present research project concerns exclusively the concrete modules (shown at the centre in Figure 1.1). Previous studies were performed to ensure the safety of the concrete modules. Long term studies concerning the integrity of the structure and dynamics loading were also conducted previously (BBRI, 2007). Regarding the concrete used in the modules and monoliths, a PhD project carried out by Craeye (2010), studied the mix proportioning and some aspects related to the mechanical behaviour of the concrete at early-age (Craeye et al., 2011, 2010, 2009).

A demonstration test comprising the reconstruction of different building blocks of the disposal modules was conducted in Dessel region. The demonstration test aimed at testing the construction techniques and phasing, testing and monitoring different construction parameters (bearing power, concrete curing and shrinkage, formation of cracks...), and substantiating the more detailed design (ONDRAF/NIRAS, 2010).

A parallel experimental campaign concerning ONDRAF/NIRAS concrete is being carried out by C. Imbert and S. Poyet at LECBA. The available results of this campaign are used in the validation of the modelling and simulations performed in this thesis. However, some tests are still in progress at the time of writing of this manuscript and could not have been integrated in the study. In the wake of this thesis, future studies are to be performed to revalidate and/or apply the modelling tools developed in this thesis to the ensemble of the experimental data still to be acquired.

1.2 OBJECTIVES, SCOPE AND OUTLINE OF THE THESIS

1.2.1 Concrete and massive structures at early age

Because of the dimensions of the concrete modules and the characteristics of the concrete used, the structure can be considered as a massive one (ACI, 1996; Ulm and Coussy, 2001). We define a concrete massive structure as *a structure whose dimensions and materials properties (notably the affinity of hydration reactions and thermal properties) determine the existence of zones in which the heat produced by hydration reactions cannot be evacuated fast enough so that a quasi-isothermal state is observed within the structure at early age*. The resulting gradient of temperature

in a non-isothermal state might lead to cracking according to the external and internal restraints to which the structure is subjected. Note that with this definition, the evolution of the temperature in the core does not need to be strictly adiabatic (this aspect is discussed in more details in Chapter 2).

The existence of cross-effects between hydration reactions, temperature evolution and deformation demands a coupled analysis in a multiphysical framework. The chemo-thermal response at early ages is a key issue in the design of massive concrete structures. Especially in the core of these structures, because of the heat released by hydration, the temperature may reach values that may potentially induce Delayed Ettringite Formation (DEF) problems (Diamond, 1996; LCPC, 2009). In addition, the structure is generally subjected to an environment exposure that may lead to a complex thermal response in which an unsteady thermal state is always present. According to the thermal boundary conditions, gradients of temperature may arise. The resulting thermal stresses have the same order of magnitude of those induced by live load (Potgieter and Gamble, 1983). These stresses allied to the volume variation undergone by the material, may induce damage and cracking within the structure (Potgieter and Gamble, 1983).

Besides the heat released by hydration, on the boundaries conduction, convection and radiation phenomena take place. The solar radiation and the wind conditions (which affect the convection conditions) are reported to be important in determining the thermal response of concrete structures (Briffaut et al., 2011; Buffo-Lacarrière et al., 2007; Cope et al., 2002; Gaspar et al., 2014; Hilaire et al., 2014; Honorio et al., 2014a; JCI, 2008; Loukili et al., 2000; Potgieter and Gamble, 1983; Tailhan and D'Aloia, 2010; Torrenti and Buffo-Lacarrière, 2009; Toutlemonde and Torrenti, 2012; Ulm and Coussy, 2001, 1998; Van Breugel and Koenders, 2001).

The mechanical response are also affected by internal restraint (due to the volume of concrete itself or the reinforcement) and external restraint (due to the fixing conditions or linked structural members) (Cope et al., 2002). In the case of structures with many lifts or assembled structural members, the chemo-thermal behaviour of both new and old material is affected since the heat released by the new structural member can be evacuated through the older members (Fairbairn et al., 2004). Also, the old members function as a restraint condition to the new placed members.

Different modelling strategies may be used to assess the mechanical response at early-age. Simplified strategies based on Cracking Indexes (CI) are often used (Fairbairn et al., 2004; JCI, 2008). More detailed descriptions accounting for a chemo-thermo-visco-damage behaviour (smeared crack), in which a coupling between creep and damage is introduced (Mazzotti and Savoia, 2003), are proposed by other authors (Benboudjema and Torrenti, 2008; Hilaire et al., 2014). The choices of modelling strategies have an impact on the adequacy of the analysis results, and for this reason this choice has to be investigated.

For a relevant early-age analysis, these aspects need to be carefully considered so that the prediction of the structure performance and the identification of the critical issues related to the

thermo-chemo-mechanical problem can be properly performed, helping either in the decision making of the construction processes or in the definition of aspects to be accounted for in predictive modelling of the structural behaviour.

To solve the multiphysics problem at the structure level, phenomenological approaches are nowadays of current use (Azenha, 2009; Briffaut et al., 2012, 2011; de Borst and van den Boogaard, 1994; De Schutter, 2002a; Gawin et al., 2006; Hattel and Thorborg, 2003; Ishida et al., 2011; Potgieter and Gamble, 1983; Toutlemonde and Torrenti, 2012), constituting an important tool in civil engineering practice. Good agreement is generally observed with experimental and field data. However, their results *a priori* cannot be extrapolated out of the domain in which the model was validated. Moreover, some aspects of the formulation present in such kind of approach may be not very well understood. For example, an aspect often present in early-age analysis is the coupling between creep and damage (Briffaut et al., 2011; De Larrard, 2010; Mazzotti and Savoia, 2003), which still deserves further investigation to be better understood. Additionally, in such approaches the multiscale character of the material is not generally taken into account.

1.2.2 Cement-based materials: multiscale character and ageing behaviour

A relevant description of the behaviour of cement-based materials needs to account for the multiscale character of the material (Yip and Short, 2013). In general, industrial applications demand a good description of macroscopic properties at the relevant scale of application. However, the mechanisms modifying the properties of interest cannot generally be understood at that macroscopic scale. In the case of cement-based materials, these mechanisms occur at different time and space scales (Figure 1.2).

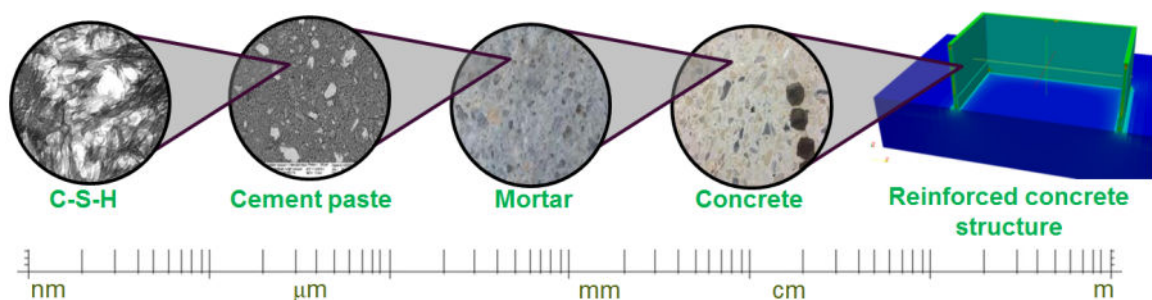


Figure 1.2 Multiscale character of cement-based materials and structures

The challenge in such kind of approach is to identify the relevant mechanisms affecting the properties of interest and then link these mechanisms through time and space scales in order to predict the properties at the scale of application. Upscaling methods based on continuum mechanics have been applied for the estimation of transport (Bary and Béjaoui, 2006) and mechanical properties (Bernard et al., 2003; Hashin and Monteiro, 2002), capturing important features of such materials. However, for some phenomena, such as creep for instance, a full multiscale analysis would require going down to scales which are nowadays not experimentally accessible and whose description

demands a change of theoretical framework (often “atomistic” simulations instead of continuum mechanics). In the present work, the smaller scale accessible is deemed to be fully described by continuum mechanics. Or, in other words, the microscale defined here is described phenomenologically.

Other limitations exist regarding mechanistic-based approaches. Homogenization methods require knowledge about the properties of interest of the phases at the microscale. For cement-based materials some of these basic properties of hydration products such as the elastic properties are still object of research, and generally can only be accessed by advanced techniques (Chae et al., 2013). Additionally, a mechanistic approach owns a more complex formulation which makes difficult their full implementation in numerical analysis codes (Finite Elements codes, for example).

To date, only few propositions to upscale the mechanical properties of cement-based materials in an ageing viscoelastic framework have been reported (Sanahuja, 2013a; Scheiner and Hellmich, 2009). Even if the pioneering works on ageing viscoelastic behaviours were actually applications to concrete (Lublinter and Sackman, 1966; Maslov, 1940), the level of maturity of the techniques used to assess such behaviour, especially concerning upscaling methods, demonstrate that there is still room for further developments. For example, a full prediction of the mechanical properties from the composition of cement and concrete in an ageing viscoelastic framework; and the elucidation of the ageing behaviour of calcium hydrated silicates and its impacts on the paste and mortar viscoelastic behaviour are still important subjects of research.

1.2.3 Goals

The two main goals of the PhD work are:

1. In a more practical way, to perform numerical simulations in order to describe and predict the thermo-chemo-mechanical behaviour of a concrete massive structure at early-age
2. In a more scientific context, to develop and apply upscaling tools to determine the key properties of concrete needed in an early-age analysis from the composition of the material.

The modelling and simulations aim at:

- Predicting the behaviour of the concrete itself and the concrete structure, providing supporting information regarding the construction of the studied structure.
- Understanding some phenomena and their relative contribution to the material and structural behaviour as well.

Phenomenological and mechanistic theoretical frameworks are combined to investigate these aspects.

Phenomenological analysis allows providing practical responses about the thermo-chemo-mechanical behaviour at the scale of the structure. Such responses will serve as support to the

construction process of the concrete modules in the ONDRAF/NIRAS solution for surface waste disposal described previously. For instance, phenomenological approaches are used to study the influence of the mechanical and thermal boundary conditions on the overall behaviour of the structure. The effect of these boundary conditions can be, *a priori*, investigated without the need of a detailed multiscale prediction. Useful information obtained includes the temperatures and environmental conditions to cast concrete avoiding DEF and limiting thermal cracking; the optimal phasing frequency; the adequacy of the reinforcement with respect to the early-age loadings; and the need of a detailed description of solar flux and its impacts on the thermo-chemo-mechanical response of the structure. These aspects were required by ONDRAF/NIRAS as support information for the construction of the concrete modules.

Regarding mechanistic based approaches, a study concerning the multiscale character of cement-based materials is carried out in order to understand more precisely some of the key phenomena affecting the evolution of mechanical properties at early-age. At first, a mechanism-based simplified model of cement hydration kinetics is proposed. Then, an investigation combining numerical and analytical tools to estimate the ageing viscoelastic properties of cementitious materials within a multiscale framework is carried out. With this proposition, the mechanical properties can be estimated from the composition of concrete. Thus, the estimation of properties of different mix proportioning of concrete (provided a necessary study for experimental revalidation) can be done. This part of the study also aims at contributing towards the better understanding and description of some aspects leading to the ageing behaviour of cement-based materials. Combined with the phenomenological analysis, this mechanistic investigation permits to assess critically the current engineering models employed, increasing its confidence and reducing its empiricism.

1.2.4 Limitations and further definition of the scope

Other aspects are reported to affect the performance of massive concrete structures at early-age. Depending on the type of the structure and the goals of the analysis some of these aspects can be neglected. In this study, the following aspects are not considered:

1. **Moisture transfer and resulting phenomena.** Drying phenomena in concrete induce (drying) shrinkage and creep and for low w/c concrete may affect the development of hydration reactions. Different authors proposed analysis accounting for the hydric transfer in a fully coupled problem (Bary et al., 2008; Buffo-Lacarrière et al., 2014; Gawin et al., 2006; Ulm and Coussy, 1998). However, the kinetics of drying is 10^3 to 10^5 times slower than the thermal transfer phenomena (Acker, P., 2001). Additionally, the presence of formworks combined with methods to prevent hydric exchanges (porous wet formwork protections) limits further the impact of moisture transfer at early-age; this is the case of the structure studied here. Because of these aspects, the hydric exchanges are neglected in this work. Moreover, evaporation itself is reported to decrease the temperature on concrete

surfaces (Hasanain et al., 1989; McCarter and Ben-Saleh, 2001). However, this effect is reported to be weak and temporary; also, due to the non-availability of free water on the surface, a decrease in the rate of evaporation is observed in the following of the processes limiting their impact (Hasanain et al., 1989). Again, this effect is not taken into account in this thesis.

2. **Detailed description of restraints and interface phenomena.** A variation of the restraint with the degree of hydration is reported (RILEM, Draft). The reinforcement provides additional restraint to the structure. A study accounting for these aspects requires a detailed description of the interfaces which would include thinner meshes, special finite elements (interface, contact) which would deserve a specific study. For the purposes defined in Section 1.2.3 such a detailed description is beyond the scope of the present analysis.
3. **Self-healing.** For some concrete, the microcracks formed at early-age may be cicatrized due to the development of hydration reactions (RILEM, Draft). This phenomenon depends on moisture transfer. Specific studies about the mechanisms and potential of self-healing for some mix proportioning are necessary to account properly for this effect. Again, regarding purposes defined in Section 1.2.3 such kind of study is beyond the scope of the thesis.

Other more specific simplifying hypotheses are adopted in the second part of this work and are presented in the corresponding chapters. In a general perspective, these limitations involve the description of hydration reactions and kinetics; the description of the microstructure at the cement paste and mortar level; the determination of the viscoelastic behaviour of the fundamental phases at the micro level.

1.2.5 Chapter outline

The thesis is divided in two parts. In the first part, a phenomenological modelling at the structure scale is performed based on the thermo-chemo-mechanical response of the structure. The problem is decoupled in a chemo-thermal analysis (Chapter 2) and a mechanical analysis (Chapter 3) based on the thermal response.

More specifically, in Chapter 2, the relative contributions of the factors affecting the chemo-thermal response of a massive concrete structure including: the boundary conditions of the thermal problem, the coupling with hydration and the initial conditions with respect to concreting temperatures are studied. This analysis highlights the determination of the maximum temperature reached within the structure.

The mechanical response to different scenarios from the chemo-thermal analysis is studied in Chapter 3. The model proposed by Benboudjema and Torrenti (2008) based on a chemo-thermo-

elastic-damage approach (smeared crack) is used. In that chapter, simplified and more realistic modelling strategies of coupled early-age analysis are critically investigated.

In the second part, tools to upscale the mechanical properties of cement-based materials are developed, so that the mechanical properties may be estimated from the composition of the cement paste up to the concrete scale. To do so, a relevant description of hydration kinetics is needed. In that spirit, a simplified mechanism-based hydration model is presented in Chapter 4.

Analytical and numerical upscaling methods are then subsequently combined to estimate the mechanical properties. Regarding analytical homogenization, some classical schemes are used here in the representation of the cement-based materials. These schemes need to be rederived in an ageing viscoelastic framework. A specific formalism based on a division ring (or skew field) with Volterra integral operator as the inner product is defined. In this ring, a correspondence principle with respect to elasticity is obtained (Sanahuja, 2013a). This task is performed in Chapter 5.

In Chapter 6, the combined numerical and analytical approach is applied to estimate the mechanical behaviour of cement-based materials. The properties of the cement paste and mortar are estimated by means of analytical homogenization. Numerical homogenization is used at the concrete level, defined here as the mesoscale. Numerical homogenization allows studying more complex microstructures and assessing local information. The dispersion of the values of stresses and strains within the inclusions and some subvolumes of the matrix can be evaluated, providing a promising tool to identify the zones the most likely to exceed the strength of the material at the mesoscale.

In Chapter 7, the properties estimated with the multiscale approach are confronted with the phenomenological description used in the Part I. The multiscale analysis permits, then, to critically assess the input data and evolution of the properties used in the phenomenological analysis, contributing to increase the confidence in the analysis performed in Part I and to reduce its empiricism.

Finally, Chapter 8 recapitulates the main conclusions drawn in this study and provides some perspectives for further investigations in the topic.

PART I. STRUCTURE AND ITS ENVIRONMENT: PHENOMENOLOGICAL MODELLING AT THE STRUCTURE SCALE

In this part, the Thermo-Chemo-Mechanical analysis of the concrete modules is performed. The problem was decoupled in two: a chemo-thermal and a mechanical part. We assume that there is no feedback of the mechanical problem (due for example to cracking) on the chemo-thermal problem. Note that this is not true if the hygral problem is also considered. The details about the formulation regarding each part of the problem are presented in the following two chapters.

2. CHEMO-THERMAL MODELLING

This chapter is based on the paper Honorio et al. (2014).

The chemo-thermal response of concrete structures has been extensively studied, being the object of norms and recommendations (ACI, 1996; JCI, 2008; LCPC, 2009). This kind of analysis is important not only for massive structures in concrete but also structures in shotcrete such as tunnels shells or other engineering problems in geomechanics (Hellmich et al., 1999). Because of the complexity of the problem, numerical solutions, by the Finite Elements Method (FEM) for instance, are the most appropriate solutions for most of practical cases and are current practice in civil engineering nowadays (Tailhan and Aloia, 2010). However, there is still room for further developments. Generally numerical simulation results may not be extrapolated to other scenarios of interest and may be computationally expensive. In the decision making process of the construction of massive structures different scenarios may be of interest (such as scenarios corresponding to hot or cold months, different wind conditions or different formwork materials). An analytical solution may be an interesting tool for a preliminary analysis in the design or construction process, and help in the determination of which aspects contribute more significantly for the thermal response, and then should be controlled or monitored during the construction phase. Finally, a simplified solution would help in the definitions of simulation scenarios for more sophisticated approaches such as THM analysis.

On the other hand, some aspects which are difficult to be treated analytically such as more complex geometries and boundary conditions generally require a 3D numerical solution. Even here some aspects can be investigated further. The variation of ambient temperature and solar radiation fluxes during a day affects the surface temperature, but it might not affect the core temperature for specific climatic conditions and geometries (Potgieter and Gamble, 1983); the effects of these complex thermal conditions and their impacts on hydration and the mechanical response are to be defined. Further investigations can be helpful in the definitions of modeling strategies in a phase of structural design regarding the choice of constant or varying boundary conditions.

In this chapter, we study the relative contributions of the factors affecting the chemo-thermal response of a massive concrete structure including: the boundary conditions of the thermal problem, the coupling with hydration and the initial conditions with respect to concreting temperatures. This study highlights the determination of the maximum temperature reached within the structure. The influence of model definitions such as the use of average or daily varying temperature and daily varying solar fluxes are also examined. The model is validated according to experiments performed in a real massive structure for nuclear waste disposal.

The analysis of the mechanical response is in the next chapter. As discussed in the introduction, it is known that mass transfer phenomena, in particular due to drying, are coupled with the chemo-thermal behavior. In this study this aspect is not accounted for. This simplification can be adopted for structures in which the formwork is present, preventing hydric exchanges.

2.1 DEFINITION OF THE THERMO-CHEMICAL PROBLEM

For a concrete structure at early age the thermal balance equation combined with the Fourier's law reads (DeGroot and Mazur, 1984; Ulm and Coussy, 1998):

$$\dot{T}(\mathbf{x}, t) = D \nabla^2 T(\mathbf{x}, t) + Q \quad (2.1)$$

$$\begin{cases} T(\mathbf{x}, 0) = T_0 & \forall \mathbf{x} \in \Omega_c \\ \lambda \nabla T(\mathbf{x}, t) \cdot \mathbf{n} - k [T(\mathbf{x}, t) - T_a] = q_i(t) & \forall \mathbf{x} \in \partial\Omega_i \end{cases} \quad (2.2)$$

where T_0 is the initial temperature of concrete [$^{\circ}\text{C}$]; T_a is the ambient temperature [$^{\circ}\text{C}$]; D is the thermal diffusivity [$\text{m}^2 \cdot \text{s}^{-1}$], k is an exchange coefficient [$\text{J m}^{-2} \text{s}^{-1} \text{K}^{-1}$] and the source term Q [$^{\circ}\text{C s}^{-1}$] accounts for the heat released by hydration. The initial conditions are defined for all point \mathbf{x} in the volume of concrete Ω_c . Robin (or Fourier) boundary conditions are imposed on the different concrete surfaces $\partial\Omega_i$ (with normal \mathbf{n}) according to the mechanisms involved. The mechanisms include convection, radiation and conduction phenomena and are represented by the different fluxes q_i accounting for convection q_c , reradiation q_r , solar radiation q_s and conduction q_n phenomena (Figure 2.1). Also, in Section 2.1, we show that in order to account for the variation of the temperature within a day, a flux-like term appears in the boundary conditions (Eq. 2.2).

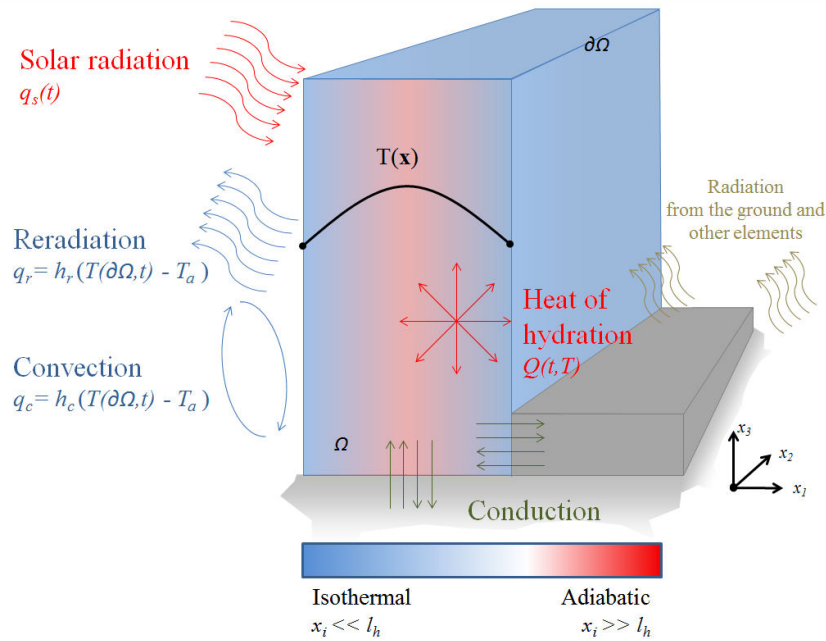


Figure 2.1 Schematic representation of the phenomena involved in the chemo-thermal analysis of a concrete structure (radiation from the ground and other neighbouring elements is not considered in the following)

Some simplifications are made in Eqs. (2.1) and (2.2). From the entropy balance equation applied to a closed porous medium, Ulm and Coussy (2001), derived the Eq. (2.1). In their derivation, a term with the latent heat per unit of (elastic) deformation, the terms accounting for the dissipation associated with hydration and the irreversible skeleton evolution as well as the latent heat of deformation are deemed to be negligible with respect to the exothermic latent hydration heat. Such simplifications are quite common in Thermo-Hygro-Mechanical (THM) modeling (Bary et al., 2008). Additionally, in the definition of the thermal diffusivity $D = \lambda/C$ we admit that the thermal properties, namely the heat capacity C [$\text{J m}^{-3} \text{K}^{-1}$] and the thermal conductivity of concrete λ [$\text{J m}^{-1} \text{s}^{-1} \text{K}^{-1}$] are isotropic and constant. Actually, the heat capacity C and the thermal conductivity λ of concrete at early ages are function of the temperature and the evolution of the microstructure of the material. Experimental results (Lura and Van Breugel, 2001; Morabito, 2001) show that variations of the thermal and mechanical response of the structure can rise from the variations of these properties due to hydration evolution as well as temperature variations. Briffaut et al. (2012) show, though, that accounting for the variations of these properties does not lead to very significant variations in the mechanical response of the structure at early-age. In the following, we then assume that these properties are constant with respect to the temperature and degree of hydration.

2.1.1 Heat of hydration

The hydration reactions are exothermic. In massive structures, the corresponding generation of heat requires measures to be taken in order to deal with the effects of the differential temperature rise within the structure (ACI, 1996). At first, for the considered chemo-thermal problem, the elementary

system may be assumed to be closed with respect to the reactants and products of the chemical reaction, and undeformable (Hellmich et al., 1999). The rate of hydration can be described by the general form of solid-state reaction (Khawam and Flanagan, 2006):

$$\dot{\xi} = A(\xi) \exp\left[-\frac{E_a}{R T}\right] \quad (2.3)$$

where $A(\xi)$ is the reaction model (or affinity) [s^{-1}] depending on the degree of hydration ξ ; R is the gas constant [$J \cdot mol^{-1} K^{-1}$]; E_a is the energy of activation [$J \cdot mol^{-1}$] and T is given in Kelvin. The affinity can be estimated by analytical kinetic models like Johnson-Mehl-Avrami-Kolmogorov model or obtained from adiabatic experiments (Khawam and Flanagan, 2006; Ulm and Coussy, 1998).

The kinetics of hydration determines the rate at which the heat is produced:

$$Q = \frac{L}{C} \dot{\xi} = \Delta T_{ad} \dot{\xi} \quad (2.4)$$

where L is the latent heat of hydration [$J \cdot m^{-3}$] and ΔT_{ad} is the adiabatic rise.

Variations in the characteristics of cements, such as the content of cement minerals or the particle size distribution, may lead to variations in hydration kinetics (Taylor, 1997). The composition of concrete may as well affect hydration kinetics either by the presence of admixtures and supplementary cementitious materials or even by a variation in the w/c ratio (Taylor, 1997). According to the boundary conditions, structure dimensions and geometry, slow reactions might lead to a less pronounced temperature rise since the heat produced by hydration has time to be transferred by conduction. On the other hand, fast reactions might lead to higher temperatures rises. Regarding the heat of hydration *per se*, the cement content, cement type and the w/c ratio are reported to affect the heat released (Torrenti and Buffo-Lacarrière, 2009). A variation in the order of 25 J/g (corresponding to a standard deviation) in the heat released by hydration has been reported in (Torrenti and Buffo-Lacarrière, 2009) for ordinary Portland cements.

2.1.2 Characteristic length of heat diffusion

After Ulm and Coussy (Ulm and Coussy, 2001), a characteristic length of hydration heat diffusion l_h can be defined and used to determine the dimensions from which, for a given material, a structure should be considered as a massive structure, i.e. a structure in which the heat of hydration affects significantly the overall thermo-chemo-mechanical behavior. For dimensions superior to l_h main parts of the structure are governed by adiabatic conditions. For dimensions inferior to l_h main parts of the structure are governed by isothermal conditions since heat diffusion is able to evacuate quickly the heat released by hydration. In the former case, non-negligible thermal stresses may arise which can lead to damage and cracking. The cited authors, using similarity solution for the problem Eq. (2.1) in one dimension, derived an expression to determine the hydration heat diffusion length l_h .

For Neumann boundary conditions for a semi-infinite domain in Eq. (2.1) we have (Ulm and Coussy, 2001):

$$l_h = \sqrt{\frac{D}{A(\xi)} \exp\left[-\frac{E_a}{RT}\right]} \quad (2.5)$$

Here, l_h is used as a criterion defining a massive structure.

2.2 THERMAL BOUNDARY CONDITIONS

Conduction, convection and radiation phenomena are present on concrete structures surfaces according to their exposure. The mathematical formulation corresponding to each phenomenon is developed in the following.

2.2.1 Convection and reradiation

In a surface $\partial\Omega_j$ exposed to convection and reradiation we have the Robin boundary conditions (Polianin, 2002):

$$\nabla T(\mathbf{x}, t) \cdot \mathbf{n} - \frac{k}{\lambda} [T(\mathbf{x}, t) - T_a] = 0 \quad \forall \mathbf{x} \in \partial\Omega_j \quad (2.6)$$

with $q_c + q_r = k [T(\mathbf{x}, t) - T_a]$, where $k = k_c + k_r$ is the coefficient accounting for both convection k_c and reradiation k_r phenomena. Simplifications, as shown in section 2.2.1.1, are made to linearize the reradiation. Note that these phenomena can be gathered together since they are both proportional to the difference of surface and ambient temperature $T(\mathbf{x}, t) - T_a$.

Regarding the reradiation, objects in which energy is stored emit long-wave radiation. Structures reradiate a part of the energy received which might come from solar radiation (or eventually from conduction) and from the heat produced by hydration reactions. This effect leads to a significant exchange of surface heat energy, especially at night (Potgieter and Gamble, 1983).

Regarding convection, heat losses take place on surfaces in contact with a fluid in which a temperature difference exists between the surface and the fluid. If the surrounding fluid is not stagnating, these losses are accentuated as a function of the fluid velocity with respect to the surface of interest.

2.2.1.1 Modelling reradiation

The **reradiation** emitted from a black body is given by the Stefan-Boltzmann law (DeGroot and Mazur, 1984):

$$q_r = \varepsilon_e \sigma_S (T(\mathbf{x}, t)^4 - T_a^4) \quad \forall \mathbf{x} \in \partial\Omega_r \quad (2.7)$$

where σ_S is the Stefan-Boltzmann constant taken as $5.67 \times 10^{-8} \text{ W} \cdot \text{m}^{-2} \cdot \text{K}^{-4}$; ε_e is the emissivity of the surface; $T(\mathbf{x}, t)$ is the temperature [K] of the concrete surface, the emissivity of the black body is 1.

Since the temperature variation remains low compared to the radiation heat transfer, Eq. (2.7) can be linearized:

$$q_r = k_r [T(\mathbf{x}, t) - T_a] \quad \forall \mathbf{x} \in \partial\Omega_r \quad (2.8)$$

with $k_r = 4 \varepsilon_e \sigma_s T_m^3$ and $T_m = \frac{[T(\mathbf{x}, t) - T_a]}{2}$.

2.2.1.2 Modelling convection

The heat loss by convection q_c on a surface $\partial\Omega_c$, according to Newton's law, is given by:

$$q_c = k_c [T(\mathbf{x}, t) - T_a] \quad \forall \mathbf{x} \in \partial\Omega_c \quad (2.9)$$

where the exchange coefficient k_c is estimated according to the type of convection and characteristic lengths of the structure (Briffaut et al., 2012):

$$k_c = \begin{cases} 0.13 \left(\frac{g \beta_f l_{c,Cr}}{\nu_f D_t} (T_s - T_{amb}) \right)^{1/3} \left(\frac{\lambda_{flu}}{l_{c,Cr}} \right) & \text{for natural convection} \\ 0.664 \left(\frac{V_{wind} l_{c,Re}}{\nu_f} \right)^{1/2} \left(\frac{\nu_f}{D_t} \right)^{1/3} \left(\frac{\lambda_{flu}}{l_{c,Re}} \right) & \text{for forced convection} \end{cases} \quad (2.10)$$

where g is the gravitational acceleration [m s^{-2}], β_f is the thermal dilatation coefficient of the fluid [K^{-1}], $l_{c,Cr}$ is the characteristic length of the natural convection [m], D_t is the thermal diffusivity [$\text{m}^2 \text{s}^{-1}$]; ν_f is the fluid kinematic viscosity [$\text{m}^2 \text{s}^{-1}$]; $l_{c,Re}$ is the characteristic length of the forced convective flux [m], V_{wind} is the wind velocity [m s^{-1}]; and, λ_{flu} is the thermal conductivity of the fluid [$\text{W m}^{-1} \text{K}^{-1}$]. Thereby, the determination of the wind conditions is important on the estimation of the convection losses. Note, however, that some hypothesis must be done regarding the wind velocity. To simplify the analysis, we assume that the intensity of V_{wind} remains constant during the simulation and its direction remains parallel to the surfaces of interest. Moreover, due to natural convection, even with stagnating air, convection losses occur. For the structure studied, h_c remains below $1 \text{ W K}^{-1} \text{ m}^{-2}$ for natural convection. For forced convection, we have $k_c = 0.8 \text{ J/m}^2/\text{s/K}$, $3.89 \text{ J/m}^2/\text{s/K}$ and $2.4 \text{ J/m}^2/\text{s/K}$, for the wind velocities $V_{min} = 0 \text{ m/s}$, $V_{max} = 11.8 \text{ m/s}$, $V_{mea} = 4.6 \text{ m/s}$, respectively (determined from the meteorological data provided by ONDRAF/NIRAS, see Section 2.4.3).

2.2.1.3 Description of the ambient temperature

The ambient temperature T_a is a key parameter in the present study since both reradiation and convection phenomena (as well as the initial conditions as will be discussed later) are directly affected by T_a . High T_a contribute to temperature rise in concrete; low T_a may induce higher temperature gradients (Torrenti and Buffo-Lacarière, 2009). Moreover, the oscillations of T_a during the day may affect the thermal response of the structure (even if it is reported to exert a smaller

influence than wind and solar radiation (Potgieter and Gamble, 1983)). In the case of varying ambient temperature, Eq. (2.6) can be rewritten as:

$$\nabla T(\mathbf{x}, t) \cdot \mathbf{n} - \frac{k}{\lambda} [T(\mathbf{x}, t) - T_a] = \frac{k}{\lambda} [\Delta T_a(t)] \quad \forall \mathbf{x} \in \partial \Omega_j \quad (2.11)$$

where the term $\Delta T_a(t)$ accounts for the variations with respect to the mean ambient temperature. This decomposition of the ambient temperature in a constant part T_a , which is the temperature that can be obtained from the meteorological data for instance, and a variable part $\Delta T_a(t)$, results in a time dependent flux term $\frac{k}{\lambda} [\Delta T_a(t)]$. Note that by definition, here $\Delta T_a(t)$ does not depend on \mathbf{x} . But T_a might depend on \mathbf{x} since the temperature may be different in sheltered zones under shadow or humid zones in contact with soil. In these particular cases, the corresponding T_a must be determined. For an outdoor structure, this term can be modeled by a sinusoidal function (Potgieter and Gamble, 1983).

2.2.1.4 Effect of the formwork

The presence of formwork also affects the convection and reradiation conditions. Solar radiation is not incident directly on concrete surface but in the formwork instead. Formworks made with materials with high thermal conductivity poorly affect the thermal exchanges on the structure surface. On the other hand, formworks with low thermal conductivities hamper the transfer of solar radiation in the direction of the structure, but also limit the transfer of the heat released by hydration through the environment. This effect can be considered by defining an equivalent exchange coefficient k_{eq} (Buffo-Lacarrière et al., 2007) for the surfaces $\partial \Omega_f$ with formwork:

$$\frac{1}{k_{eq}} = \frac{1}{k_c + k_r} + \frac{e_f}{\lambda_f} \quad (2.12)$$

where e_f is the formwork thickness [m] and λ_f is the thermal conductivity of the formwork [W/mK]. Because of its high thermal conductivity, steel formworks affect quite poorly the thermal response of the structure, being similar to a case with no formwork. By contrast, wooden formworks, because of its low thermal conductivity, can lead to insulation effects on the structure, lessening heat losses and enhancing higher temperature rises.

2.2.2 Solar radiation

The amount of energy that is daily radiated by the sun affects the thermal response of a structure exposed to the sun. At early-age this additional heat may modify non-negligibly the hydration kinetics since the reactions involved are thermo-activated. The flux of solar radiation on a given inclined plane surface $\partial \Omega_s$ exposed to the sun, as shown in Figure 2.2, is given by (Van Breugel and Koenders, 2001):

$$q_s(t) = q_m(t) \langle (\cos i)(t) \rangle_+ \quad (2.13)$$

where q_m [$W \cdot m^{-2}$] is the solar radiation near the earth surface, and $\cos i$ is a geometrical factor, both terms varying with respect to time. The operator positive part $\langle . \rangle_+ = \max(0, .)$ accounts for the presence of solar flux during daytime and the absence of solar flux during nighttime.

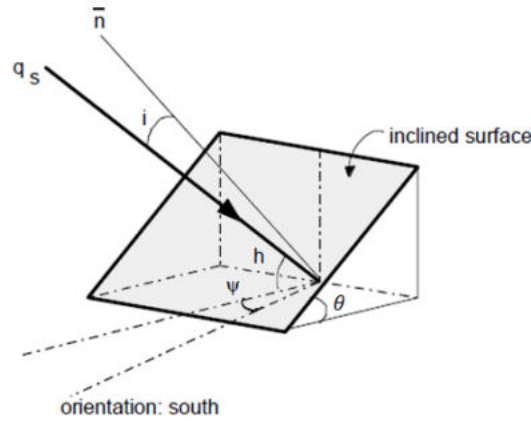


Figure 2.2 Schematic representation of an inclined surface with an indication of the parameters involved in the model (from (Van Breugel and Koenders, 2001))

During daytime, the solar radiation flux q_s [$W \cdot m^{-2}$] is the product of solar radiation near the earth surface q_m with a geometrical factor $\cos i$; during nighttime $q_s = 0$; so we can define the solar flux as in the Eq. (2.13). The angle i is the incidence of the solar radiation, i.e. the angle between q_s and the normal to the surface receiving the solar radiation. The amount of energy received by solar radiation will depend on the inclination of the surface of interest and its position and orientation with respect to the direction of solar radiation. The location of the structure on earth surface is important in the definition of the direction of solar radiation and its variations during a given day in a year. These aspects are briefly presented in the following. For more details see e.g. (Van Breugel and Koenders, 2001).

The estimation of solar radiation near the earth surface q_m used here was developed for The Netherlands region (Van Breugel and Koenders, 2001), which has conditions of solar flux close to the ones in region of interest of this research (Dessel, Belgium):

$$q_m = q_0 \exp \left[\frac{-\tau_L}{0.9 - 9.4 \sin(h)} \right] \quad (2.14)$$

where q_0 is the solar constant equals to $1367 W/m^2$. τ_L is the Linke turbidity, a dimensionless parameter accounting for dispersion, absorption and pollution effects in the atmosphere, this factor ranges from 2 (very clean cold air) to 7 (polluted air). We adopt here the Linke's turbidity value of 4 corresponding to moist, quite clean warm air or stagnating air. And, h is the solar elevation [$^\circ$] as observed from the earth surface. The solar elevation h (see Figure 2.2) is given by (Van Breugel and Koenders, 2001):

$$\sin h = \sin \varphi \sin \delta + \cos \varphi \cos \delta \cos (15^\circ t_h) \quad (2.15)$$

where φ is the earth's latitude ranging from 0 to 90°; t_h is the hour in the day and δ [°] is the solar declination. The geometrical factor $\cos i$, can be deduced from these parameters and the hour angle of the sun ($15^\circ t$) (Van Breugel and Koenders, 2001):

$$\cos i = (\cos \theta + \sin \theta \tan \varphi)(\sin \varphi \sin \delta + \cos \varphi \cos \delta \cos (15^\circ t)) - \sin \theta \frac{\sin \delta}{\cos \varphi} \quad (2.16)$$

with

$$\sin \delta = 0.39782 \sin \left(4.781 + \frac{2\pi}{360} d + 0.033 \sin \left(\frac{2\pi}{360} d \right) \right) \quad (2.17)$$

where (see Figure 2.2) θ is the angle of inclination of the surface relative to the horizontal plane [°], ψ is the azimuth of the projection of the normal to the surface of interest on a horizontal plane [°]; and, d is the day in a year.

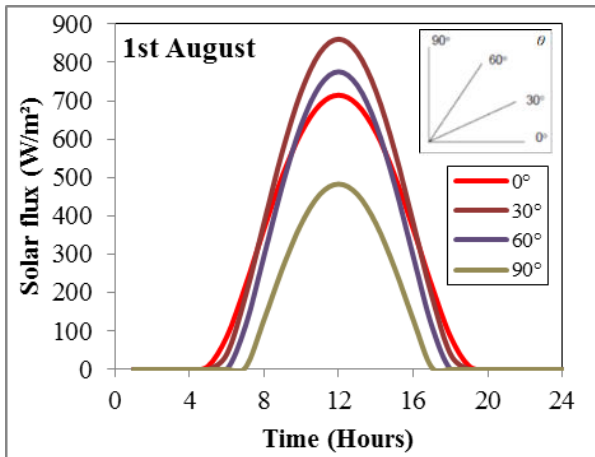


Figure 2.3 Influence of the surface inclination θ for 1st August

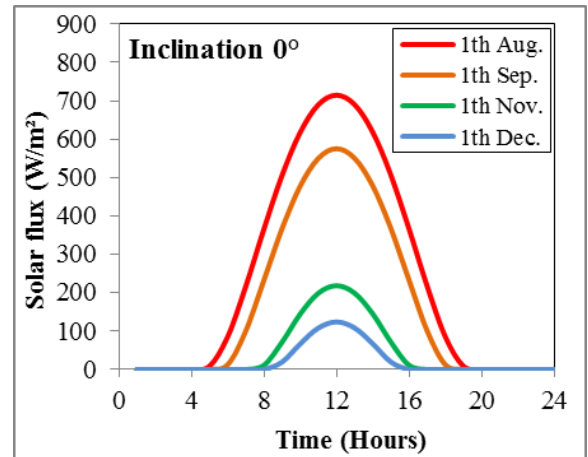


Figure 2.4 Variation of solar flux according to the day in the year

Thereby, surfaces with different inclinations are exposed to different intensities of solar radiation (Figure 2.3). Also, according to the day in a year, for a given surface inclination, high variations in the solar flux intensity are observed as well as different time for the sunrise, as presented in Figure 2.4.

Adding up the solar flux to Eq. (2.11) we have:

$$\nabla T(\mathbf{x}, t) \cdot \mathbf{n} - \frac{k}{\lambda} [T(\mathbf{x}, t) - T_a] = \frac{k}{\lambda} [\Delta T_a(t)] + \frac{1}{\lambda} q_s(t) \quad \forall \mathbf{x} \in \partial \Omega_i \quad (2.18)$$

which defines the boundary conditions for the problem with convection and solar radiation imposed on surface $\partial \Omega_j$.

2.2.3 Conduction through the ground and old structural members

Across the interface with the ground and/or old structural members, the condition of continuity of the temperature and heat flux holds (Potgieter and Gamble, 1983):

$$\begin{aligned} T_i &= T_j \\ \lambda_i \nabla T_i \cdot \mathbf{n} &= -\lambda_j \nabla T_j \cdot \mathbf{n} \end{aligned} \quad (2.19)$$

where i and j designate the materials in each side of the interface with normal n .

Regarding the ground temperature, the JCI (JCI, 2008) preconizes a transient analysis for the ground accounting for the three months before casting, for the determination of the starting temperature of the soil. Due to ground thermal inertia, a soil temperature higher than the ambient temperature can be found in the cold months. On the other hand, the soil temperature can be lower than the ambient temperature in hot months.

Ulm *et al.* (Ulm, F.-J. et al., 2004) proposed an equivalent exchange coefficient to model the conduction through the ground with a value ten times inferior to the air-concrete equivalent exchange coefficient (convection and re-radiation considered). This proposition may seem quite arbitrary, but avoids meshing the soil, which is costly computationally.

2.3 PRELIMINARY ANALYSIS OF THE CONTRIBUTION OF THE BOUNDARY CONDITIONS ON THE THERMAL RESPONSE

In this section we propose a simplified solution of a one-dimensional formulation of the problem in Eqs. (1.1) and (1.2) according to different combinations of boundary conditions. The goal is to identify preliminarily the relative contributions of convection and reradiation competing with the solar flux for a given set of initial and ambient temperatures. From this preliminary analysis, the critical scenarios to consider for numerical simulations regarding the solar flux and reradiation and convection with more complex geometries and boundary conditions are proposed. This will permit to considerably reduce the cases to investigate numerically and then the computation time.

The one-dimensional solution of a homogeneous form (i.e. without the source term Q) of the problem in Eq. (2.1) with non-homogeneous boundary conditions (1.2), for a semi-infinite domain is (Polianin, 2002):

$$T_{hom}(x, t) = T_1(x, t) + T_2(x, t) \quad (2.20)$$

where

$$T_1(x, t) = T_0 \left(1 - \operatorname{erfc} \left[\frac{x}{\sqrt{4 D t}} \right] + \exp \left[\frac{k}{D} (k t + x) \right] \operatorname{erfc} \left[\frac{2 k t + x}{\sqrt{4 D t}} \right] \right) \quad (2.21)$$

and, for constant ambient temperature T_a and constant solar flux \bar{q}_s :

$$T_2(x, t) = \left(T_a - \frac{\bar{q}_s}{k} \right) \left(\operatorname{erfc} \left[\frac{x}{\sqrt{4 D t}} \right] - \exp \left[\frac{k}{D} (k t + x) \right] \operatorname{erfc} \left[\frac{2 k t + x}{\sqrt{4 D t}} \right] \right) \quad (2.22)$$

The complementary error function $\operatorname{erfc}(z)$ is defined by $\operatorname{erfc}(z) = \frac{2}{\sqrt{\pi}} \int_z^\infty \exp[-t^2] dt$.

The solution $T_{hom}(x, t)$ corresponds, for instance, to the thermal behaviour of a concrete structure at late ages. At early age, the source term Q must be considered. Since hydration is thermo-activated, this source term depends non-linearly on $T(x, t)$ according to the Arrhenius term. This makes difficult the derivation of an analytical and explicit solution for the problem in Eqs. (2.1) and (2.2). Here, we are mostly interested in the contribution of phenomena taking place at the boundary surfaces. So some simplifying assumptions are made in order to make the problem more tractable regarding the source term Q . Using a first order expansion of the thermo-activation term of hydration with respect to a reference temperature, the final solution has the general form

$$T(x, t) \approx T_1(x, t) + T_2(x, t) + T_3(\xi, x, t) \quad (2.23)$$

where the term T_3 accounts for the heat of hydration as being activated by the temperature rise within the structure. The details of the derivation of Eq. (2.23) are presented in the following.

2.3.1 Solution for the inhomogeneous problem with inhomogeneous boundary conditions

In order to obtain the linearized solution in Eq. (2.23) some simplifications are made. One concerns the source term related to hydration heat. The thermal activation factor in the source term Eq. (2.24) is expanded using a Taylor expansion with respect to T in the neighborhood of \hat{T} resulting in the expression Eq. (2.25):

$$Q = L A(\xi) \exp \left[-\frac{E_a}{R} \left(\frac{1}{T} - \frac{1}{T_R} \right) \right] \quad (2.24)$$

$$\dot{Q} = Y(\xi) T(x, t) + Y_0(\xi) + O(T - \hat{T})^2 \quad (2.25)$$

with

$$Y(\xi) = \frac{E_a L A(\xi)}{R \hat{T}^2} \exp \left[-\frac{E_a}{R \hat{T}} \right] \exp \left[\frac{E_a}{R T_R} \right]; \quad Y_0(\xi) = Y(\xi) \left(\frac{R}{E_a} \hat{T}^2 - T \right) \quad (2.26)$$

In the following we will neglect the term $O(T - \hat{T})^2$ so that we have $\dot{Q}(t)$ as a linear function of $T(x, t)$. The thermo-activation is underestimated for higher values of \hat{T} (Figure 2.5) and overestimated for smaller values of T . In the cases considered in this study, it seems a good choice since it is in the middles of the range of temperature covered by the analysis (for T_0 close to 20°C and $\Delta T_{ad} = 46.6$ °C). This choice leads to an overestimation of the thermo-activation term for temperatures inferior to 60°C and underestimation of the thermo-activation term for higher temperatures. In the present analysis this underestimation remains reasonable for temperatures inferior to 70° C which are treated in this study.

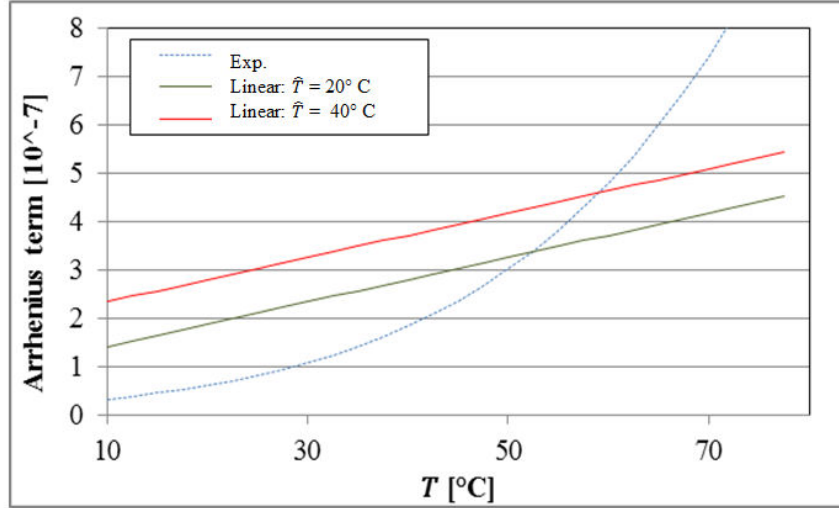


Figure 2.5 Linear approximation of the thermo-activation factor for $T_0 = 20^\circ\text{C}$

The linearization of the thermo-activation factor allows rewriting Eq. (2.1) in the form:

$$\dot{T}(x, t) = D \nabla^2 T(x, t) + Y(t)T(x, t) + Y_0(\xi) \quad (2.27)$$

Using the transformation $T(x, t) = U(x, t) \exp[\int Y(t) dt]$, we obtain a partial differential equation in terms of $U(x, t)$ with a source term function of the time $Y_0^*(\xi(t)) = Y_0(\xi) \exp[\int Y(\xi) dt]$ (Polianin, 2002):

$$\dot{U}(x, t) = D \nabla^2 U(x, t) + Y_0^*(\xi) \quad (2.28)$$

The solution of Eq. (2.28) for a semi-infinite domain ($0 \leq x < \infty$), with the Robin boundary conditions Eq. (2.18) has the general form (Polianin, 2002):

$$U(x, t) = \left[\int_0^\infty U(y, 0) G(x, y, t) dy - D \int_0^t q(\tau) G(x, 0, t - \tau) d\tau + \int_0^t \int_0^\infty Y_0^*(\xi) G(x, y, t - \tau) dy d\tau \right] \quad (2.29)$$

where the Green's function $G(x, y, t)$ is given by (Polianin, 2002):

$$G(x, y, t) = \frac{1}{\sqrt{4\pi D t}} \left\{ \exp\left[-\frac{(x-y)^2}{4 D t}\right] - \exp\left[-\frac{(x+y)^2}{4 D t}\right] - 2k \int_0^\infty \exp\left[-\frac{(x+y+\eta)^2}{4 D t} - k \eta\right] d\eta \right\} \quad (2.30)$$

The final solution has the form (Honorio et al., 2014a):

$$\dot{T}(x, t) = [T_1(x, t) + T_2(x, t) + T_3(x, t)] \theta(t) \quad (2.31)$$

where the term $T_1(x, t)$ refers to the initial conditions T_0 over the domain and the effect of Robin boundary conditions if $q_i(t) = 0$ in Eq. (1.18); $T_2(x, t)$ refers to the contribution of $q_i(t) (\neq 0)$

which may come from the solar radiation flux or from the ambient temperature and its eventual variations; and $T_3(x, t)$ as well as $\theta(t) = \exp[\int Y(\xi(t)) dt]$ refers to the contributions of hydration heat.

The term $T_1(x, t)$ is defined in Eq. (2.21). For constant ambient temperature ($q_i = k T_a$) or constant solar flux ($q_i = \langle q_s \rangle$), the term $T_2(x, t)$ is given by Eq. (2.22). Numerical solution for (2.33) can be obtained in the case of varying solar flux and varying ambient temperature.

In order to evaluate the terms related to hydration heat, the function $A(\xi)$ must be defined. The hydration evolution can be described by a sigmoid with respect to the hydration time t_h function of time t . Concerning the affinity, different functions can apply, here we chose the form $A(\xi(t_h)) = \frac{d}{dt} \left(1 + \exp \left[-\frac{(t_h - C_1)}{C_2} \right] \right)^{-1} \frac{dt}{dt_h}$, where C_1 and C_2 are constants. Considering that t varies homogeneously with t_h by a factor $p = O(1)$ we have $A(t) = \frac{p \exp \left[-\frac{(p t - C_1)}{C_2} \right]}{C_2 (1 + \exp \left[-\frac{(p t - C_1)}{C_2} \right])^2}$ and:

$$\theta(t) = \exp \left[-\frac{E_a L}{R \hat{T}^2} \exp \left[\frac{E_a}{R \hat{T}} - \frac{t}{C_2} \right] / \left(\exp \left[\frac{C_1}{C_2} \right] + \exp \left[\frac{t}{C_2} \right] \right) \right] p \quad (2.32)$$

The term $\theta(t) = 1.000 \pm 0.005$ for the values of E_a, R, C_1 and C_2 which can be used for cement based materials; so it can be neglected in Eq. (2.31). We have then:

$$Y_0^*(t_h) = 2L \frac{A(t) t}{C_2} \exp \left[\frac{C_1}{C_2} - \frac{E_a}{R \hat{T}} - \frac{t}{C_2} \right] / \left(1 + \exp \left[\frac{C_1 - t}{C_2} \right] \right)^2 \left(1 - \frac{E_a}{R \hat{T}} \right) \exp \left[\frac{E_a}{R T_R} \right] \quad (2.33)$$

Finally, the term $T_3(x, t)$ can be estimated by (Honorio et al., 2014a):

$$T_3(x, t) = -\frac{\exp \left[\frac{C_1 + t}{C_2} - \frac{E_a}{R \hat{T}} - \frac{E_a}{R T_R} \right] (E_a - R \hat{T})}{R \hat{T} C_2 \left(\exp \left[\frac{C_1}{C_2} \right] + \exp \left[\frac{t}{C_2} \right] \right)^2} \left(\left(\frac{a}{k^2} + t + \frac{x}{k} + \frac{x^2}{2a} \right) \operatorname{erfc} \left[\frac{x}{\sqrt{4 D t}} \right] - \frac{D}{k^2} \exp \left[\frac{k}{D} (k t + x) \right] \operatorname{erfc} \left[\frac{2 k t + x}{\sqrt{4 D t}} \right] - t - \frac{\exp \left[-\frac{x^2}{4 D t} \right]}{k \sqrt{D t} \sqrt{\pi}} (k t x - 2 D t) \right) \quad (2.34)$$

Note that, in spite of the simplifications adopted, the term T_3 is consistent with the physical aspects related to the adiabatic rise since $T_3 \rightarrow \Delta T_{ad}$ as $x \rightarrow \infty$.

2.3.2 Results of the analytical study

This simplified analytical analysis can be useful for a first estimation of the contributions of convection and radiation phenomena. Using the chemo-thermal properties described in Section 2.4.1, $V_{wind} = 4.6$ m/s (so $k_c = 3.89$ J/m²/s/K with Eq. (1.10)), a constant solar flux $\bar{q}_s = 134$ W/m², $T_0 = 23.25^\circ$ C and $T_a = 18.25^\circ$ C (corresponding to Set 2 as will be defined in section 2.4.2), we can compare scenarios with and without solar flux.

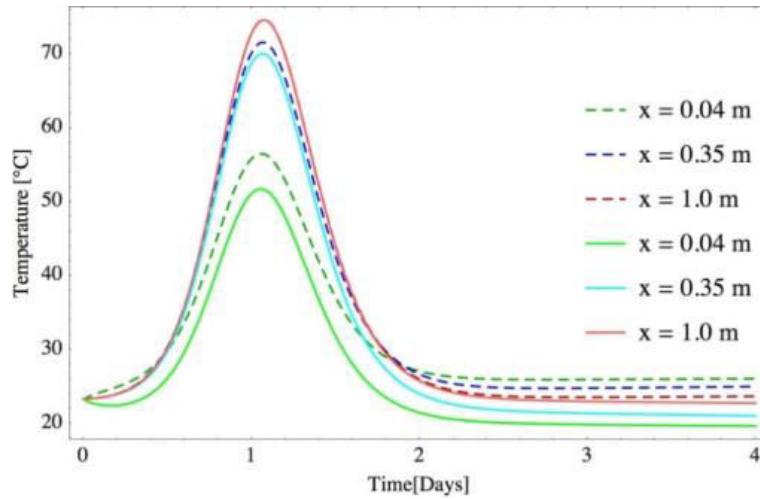


Figure 2.6 Evolution of the temperatures at different distances from the surface: full lines for scenarios with convection and reradiation; dashed lines for scenarios with convection, reradiation and constant solar flux; in all cases T_a is kept constant.

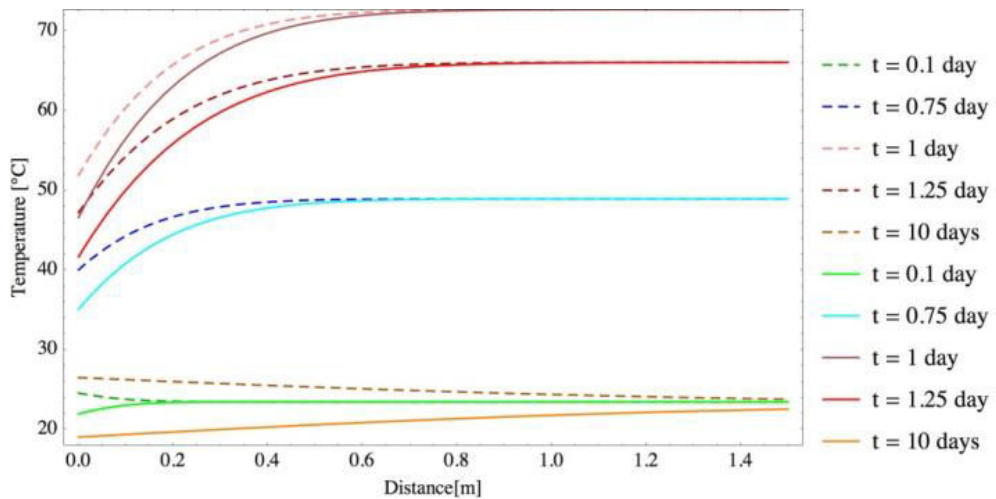


Figure 2.7 Profiles of temperatures at different times: scenarios with (dashed lines) and without (full lines) solar flux; in all cases T_a is kept constant.

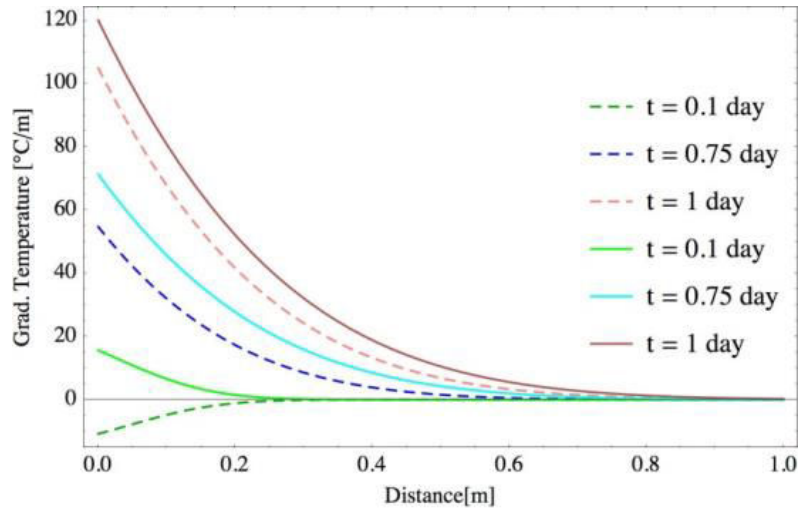


Figure 2.8 Gradient of temperature: scenarios with (dashed lines) and without (full lines) solar flux. In both cases convection with $V_{wind} = 4.6$ m/s

In Figure 2.6 and Figure 2.7 we observe, as expected, that higher temperatures on the surface (i.e. at $x = 0$) are found for the case with solar flux. Only a small feedback of the solar flux is observed in the core for structures with dimensions superior to 0.6 m. This is in agreement with the computed values of ℓ_h , as is shown in Section 2.4.1, corresponding to the concrete properties studied. In Figure 2.13, ℓ_h is about 0.6 m for degrees of hydration ranging from 0.1 to 0.8. A less pronounced difference between core and surface temperatures were found for the case with solar flux. This induces a less accentuated gradient of temperature for the scenarios with solar flux, as shown in Figure 2.8.

Regarding the influence of the wind velocity, in Figure 2.9, we observe that even for small changes in the convection coefficient, due to the different values of V_{wind} used to estimate k_c (as will be discussed further in Section 2.4.2), differences of temperature of about 4°C are found on the surface. As expected, for distances from the surface superior to 0.5 m almost no influence of these changes on convection conditions is perceived. In Figure 2.10, similar conclusions regarding the solar flux can be drawn. Note that in the sensibility study, a variation of 25% of the mean solar flux does not affect considerably the thermal response. This effect is however to be confirmed for scenarios with varying solar flux. Adopting 70°C as the maximum admissible temperature within concrete in order to prevent DEF problems (which corresponds to a current level of precaution in DEF prevention (LCPC, 2009)), this value is exceeded for $x \geq 1.0$ m.

The simplified solution given by Eq. (2.23) indicates that the temperature varies linearly with the ambient and initial temperatures. This is due to the simplification made with respect to the linearization of the thermo-activation of hydration and the integration to obtain T_3 . This linear form will be confronted to the 3D numerical simulation in the following sections.

The estimations given by Eq. (1.23) may not be accurate enough for more complex geometries. Also aspects as varying ambient temperature and solar flux model as developed in

section 1.2.2 are difficult to be accounted for analytically. These aspects are studied by means of FE numerical simulations and compared to in situ experimental results of the thermal response.

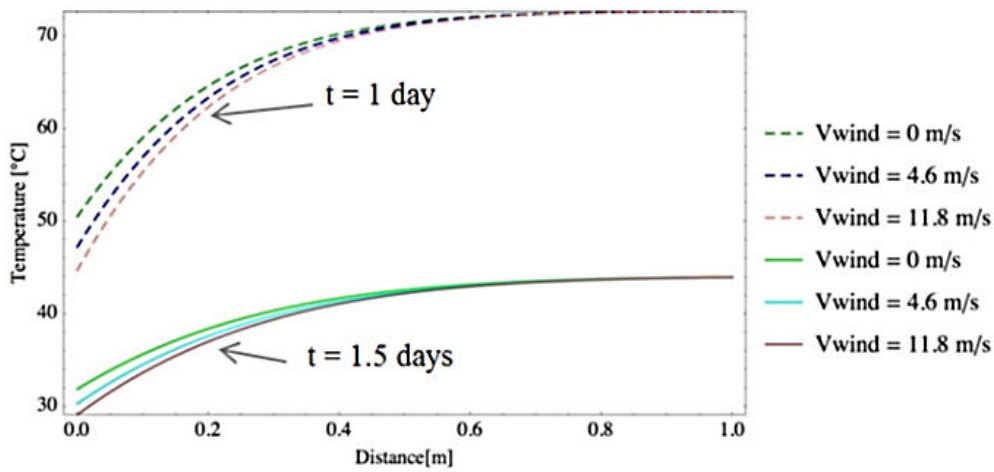


Figure 2.9 Profile of temperature at different times (1 day and 1.5 days) for different wind velocities. Dashed lines correspond to $t = 1.0$ day and full lines to $t = 1.5$ days.

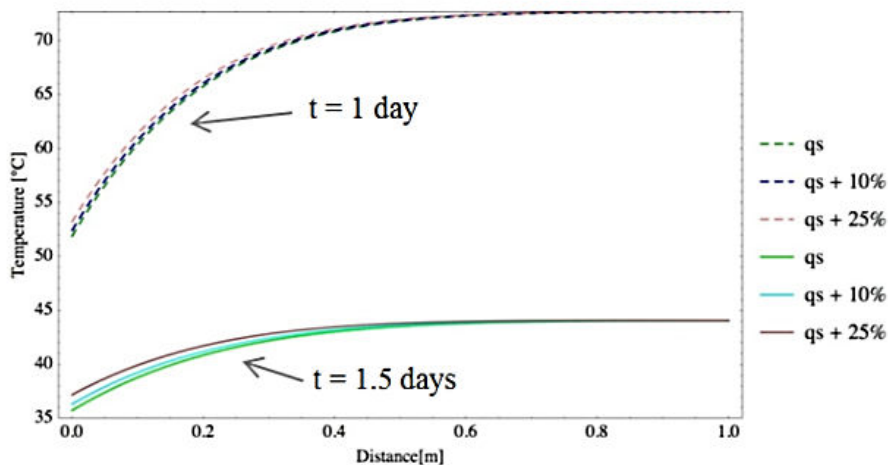


Figure 2.10 Sensibility of the solar flux ($\bar{q}_s = 134 \text{ W/m}^2$). Dashed lines correspond to $t = 1.0$ day and full lines to $t = 1.5$ days.

2.4 FEM NUMERICAL SIMULATIONS OF THE CHEMO-THERMAL PROBLEM

The massive structure for nuclear waste storage which is the object of the thesis project is considered for the numerical simulations. The structure is composed of walls and a base slab (green and blue, respectively, in Figure 2.11) of thickness varying from 70 cm to 85 cm. In the construction process, the base slab is placed after the wall.

The coupled chemo-thermal analysis is performed with the Finite Elements code CAST3M developed at CEA (www.cast3m.fr). The concrete structure was modelled using about 200 k cubic isoparametric finite elements; the ground was modelled by about 70 k prismatic elements (Figure

2.11). The solar flux incidences induce asymmetries regarding the temperature distribution within the structure. The asymmetry regarding the West-East axis is not considered here for concern of simplicity. As a first attempt this seems reasonable and allows reducing the cost of computation. Moreover, since variations inferior to 25% in the solar flux radiation (from the preliminary study in section 1.3) do not impact very strongly the temperature response, neglecting the one of the asymmetries derived from the solar flux seems adequate. A further mesh reduction with respect to the North-South axis would be possible; but the results obtained here will be used to evaluate the effect of this asymmetry on the mechanical response in a future contribution.

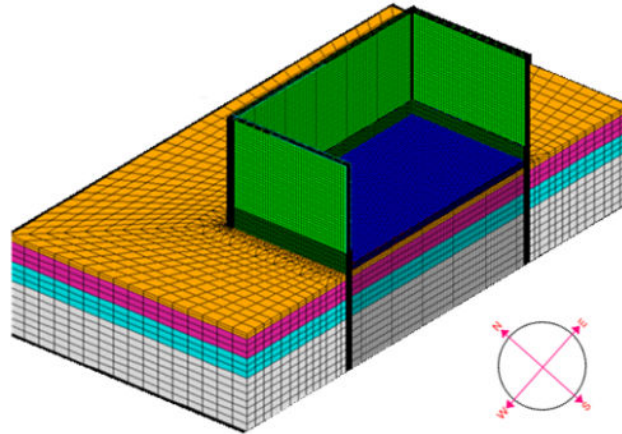


Figure 2.11 Structure orientation and discretization: concrete structure and ground (Honorio et al., 2014a)

In order to ensure a reasonable description of the temperature gradient across the wall and slab, 10 elements in the thickness of these members were imposed. The aspect ratio of the elements of the concrete structure was limited to 3, which is inferior to the maximum aspect ratio of 10 as recommended in the (JCI, 2008). With the purpose of well describing the acceleration and early post-peak periods of hydration as well as the solar flux and daily temperature variations, in the chemo-thermal analysis a timestep Δt of 1 hour is imposed for the days before the wall-slab assembly and the first 14 days after the assembly. A timestep of 2 hours is imposed for the rest of the simulation. The criterion proposed by (Ulm and Coussy, 2001) $t \leq \frac{\ell^2}{D} \leq \frac{\ell h^2}{D}$ with respect to the Δt and the finite element size ℓ is respected. The chemo-thermal computations take less than 3 days with a 12-cores, 2.8 GHz / 96Go machine, for all the assembly frequencies.

2.4.1 Chemo-thermal properties

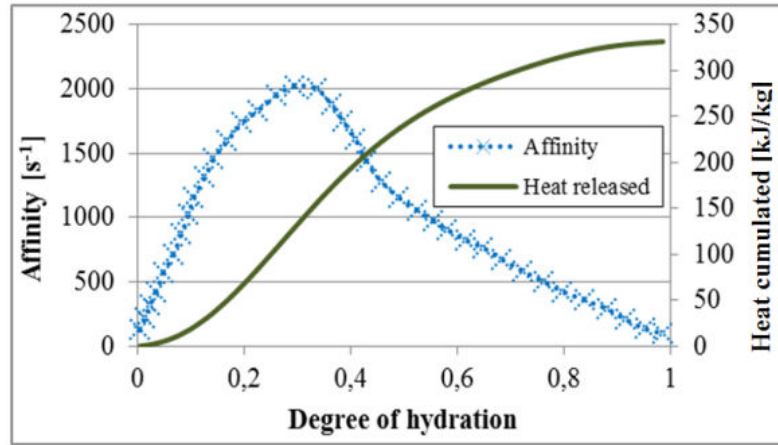
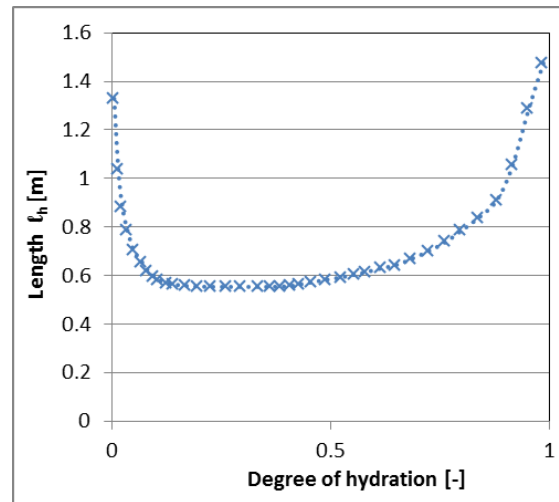
The affinity $A(\xi)$ and the latent heat of hydration L used in the simulations correspond to the experimental data provided by ONDRAF/NIRAS as shown in Figure 2.12 and Table 2.1 for the concrete formulation listed in Table 2.2. The same material was studied by Craeye et al. (Craeye, 2010; Craeye et al., 2010, 2009).

Table 2.1 Chemo-thermal properties

<i>Property</i>	<i>Value</i>
Energy of activation, E_a	39.3 KJ/mol
Heat of hydration, L	113.0×06 J/m ³
Thermal conductivity, λ	1.8 J/m.K
Heat capacity, C	2440 kJ/m ³ K
Emissivity, ϵ_e	0.92

Table 2.2 Formulation of concrete

<i>Component</i>	<i>kg/m³</i>
Cement CEM I 42.5 N HSR LA	350
Limestone filler	50
Limestone sand	708
Limestone coarse aggregate	1070
Water	175
Susperplasticizer	3.3

**Figure 2.12 Affinity and Heat released (as also studied by (Craeye et al., 2010, 2009))****Figure 2.13 Hydration heat diffusion length l_h , after Eq. (1.5)**

Using Eq. (2.5), the characteristic length l_h of hydration can be computed as a function of the affinity and the chemo-thermal properties, as shown in Figure 2.13. For the dimensions of the structure studied here, with walls with thickness of 70 and 85 cm (symmetry axis of 35 and 42.5 cm from the surface, respectively), according to the definition of l_h , no strictly adiabatic region would occur within the structure. Note, however, that this does not mean that the structure studied cannot be considered as a massive one. Actually since their dimensions are not very inferior to l_h at early ages the structure will be not completely in the isothermal regime. So, the heat of hydration will play an

important role in the thermal response, which characterizes a massive structure. Moreover, in the core of the structure some feedback of the boundary conditions is expected. Also, since the definition of l_h accounts only for Neumann boundary conditions, a more sophisticated analysis is needed in order to identify the effects of more complex boundary conditions on the temperature response.

2.4.2 Definition of the initial conditions

The initial or placement temperature T_0 of fresh concrete directly affects the maximum temperature reached in concrete. For example, in certain common situations, a 2 °C variation in the placing temperature is reported to induce a variation on temperature peak by approximately 1 °C (Cope et al., 2002). If no specific precooling measure is taken, T_0 exceeds the ambient temperature T_a . The JCI (JCI, 2008) recommends adopting:

$$T_0 = T_a(t = 0) + 5 \text{ (}^\circ\text{C)} \quad (2.35)$$

in order to account for the initial reactions, mixing and transportation of concrete. Other authors (Torrenti and Buffo-Lacarrière, 2009) adopted an empirical relation (based on studies in France) to estimate the placement temperature:

$$T_0 = 0.6 T_a(t = 0) + 11 \text{ (}^\circ\text{C)} \quad (2.36)$$

Both cases are considered in the study of the influence of the placement temperature on the thermal response in the following. Here, for the cases with temperatures oscillating during the day, $T_a(t = 0)$ corresponds to the mean ambient temperature at the time of placement at 6:00 a.m.

2.4.3 Description of the ambient temperature, convection and reradiation

Two reference months are chosen for the thermal analysis. August is the hot reference month and November the cold reference month. The values of mean, maximum and minimum average temperatures based on an analysis covering the period of 1985 to 1998 as well as the values for maximal yearly temperatures covering 1998 to 2009, both for region of interest, are considered. From these values, different scenarios of temperatures are proposed in Table 2.3 and Figure 2.14. These scenarios aim to cover the periods of interest for the construction process but remaining conservative. The scenarios with constant temperatures are compared to the scenarios with oscillating temperatures.

Regarding the wind conditions, the values of wind velocity for the region of interest are $V_{min} = 0$ m/s, $V_{max} = 11.8$ m/s, $V_{mea} = 4.6$ m/s. These values correspond to the convection coefficients k_c of 0.8 J/m²/s/K, 3.89 J/m²/s/K and 2.4 J/m²/s/K, respectively, calculated according to the definition of the convection exchange coefficient (see Section 1.2.1). The reradiation coefficient depends on the mean temperature T_m , which varies during the simulations. For instance, with $T_m = 20^\circ\text{C}$, the reradiation coefficient $k_r = 5.25$ J/m²/s/K.

Table 2.3 Sets of temperature

	T at 12	T at 0
Set 1	33.3°C : maximum temperature of the year, T_{xtr}	22.2°C: $T_{xtr} - \Delta_{max}$. Δ_{max} is the maximum difference of the maximum and minimum temperature within a month in a year. For the case studied here this corresponds to August temperatures: $\Delta_{max} = 23.8 - 12.7 = 11.1^\circ\text{C}$
Set 2	18.3°C: mean temperature of August	
Set 3	23.8°C: maximum average temperature in August	12.7°C : minimum average temperature in August
Set 4	23.8°C: maximum average temperature in August	
Set 5	9.6°C: maximum average temperature in November	3.1°C: minimum average temperature in November

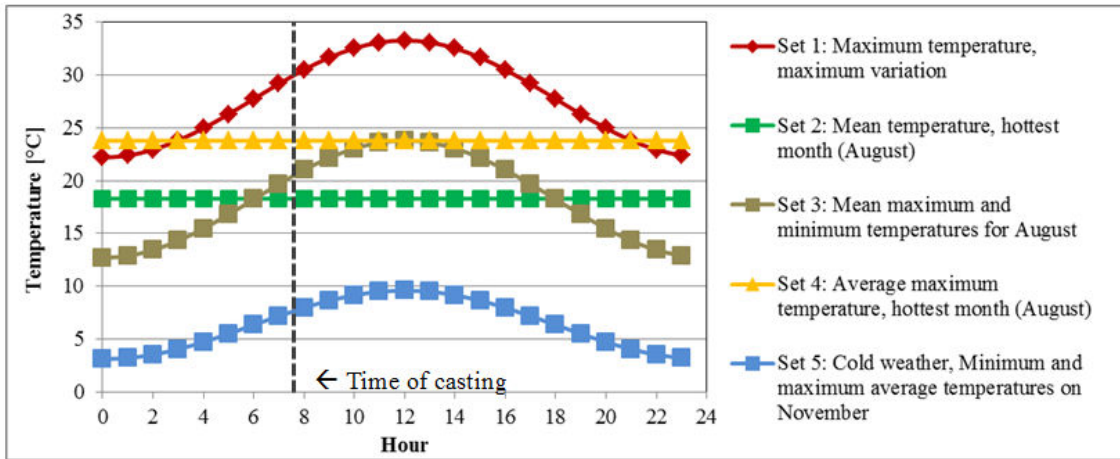


Figure 2.14 Sets of temperature

2.4.4 Solar radiation

Regarding the solar flux, different simplified exposition conditions were defined with respect to the structure orientation (Figure 2.11). The outer East wall surface and the inner West wall surface are exposed to the solar flux during the morning; the outer West wall surface and the inner East wall surface are exposed to the solar flux during the afternoon. The South wall surface and the wall top surface are exposed to the solar flux during the afternoon. The South wall surface and the wall top surface as well as the base slab top surface are exposed to solar flux all day long.

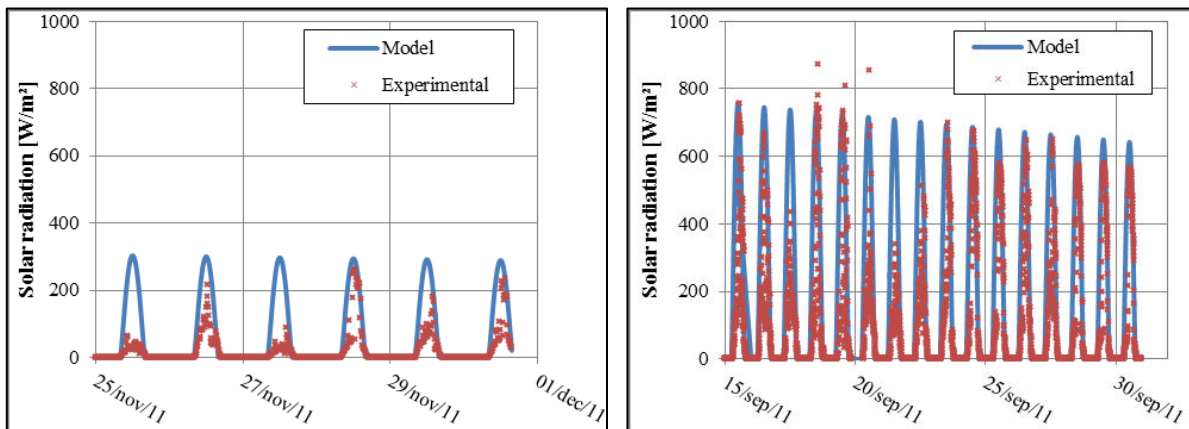


Figure 2.15 Solar flux: modelling and comparison with experimental data

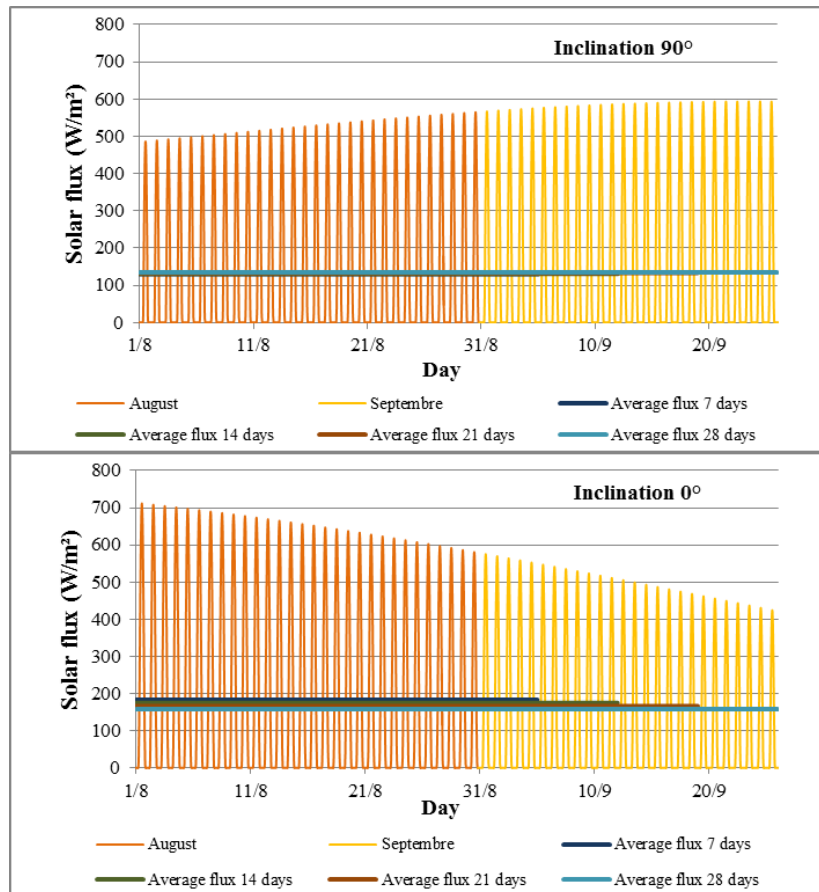


Figure 2.16 Solar radiation used as input for the simulations for an inclination of 90° (laterals of the walls) and for an inclination of 0° (top of the wall and top of the base slab)

The solar radiation model was validated against the experimental data from the region of interest. Good agreement was obtained with correlation coefficient (R^2) of 0.71 and 0.69 for the November and September (as seen in Figure 2.15) cases, respectively. The estimation of the solar radiation remains conservative since no dissipation (pollution, clouds) effects are considered.

The input values of solar radiation used in the simulation are presented in Figure 2.16. The inclination of 90° corresponds to the radiation received by the walls lateral surfaces and the inclination of 0° corresponds to the radiation received by the tops of the base slab and walls. The average solar fluxes were computed integrating the flux over the total time of the corresponding simulation; only slight variations were found among the average values.

2.4.5 Ground temperature

Following the JCI (JCI, 2008) recommendations the transient analysis accounting for the three months preceding the concreting was performed. The bottom surface of the layer of ground considered has the average mean temperature of the first month of this transient analysis as an imposed temperature. The thermal properties presented in Table 2.4 were used in this analysis. For August the ground was about 1 °C colder than the ambient temperature and for November the

ground was about 1 °C hotter than the ambient temperature (Figure 2.17). This difference will be neglected in the following. For the thermal analysis of the structure, the ground is meshed as showed in Figure 2.17.

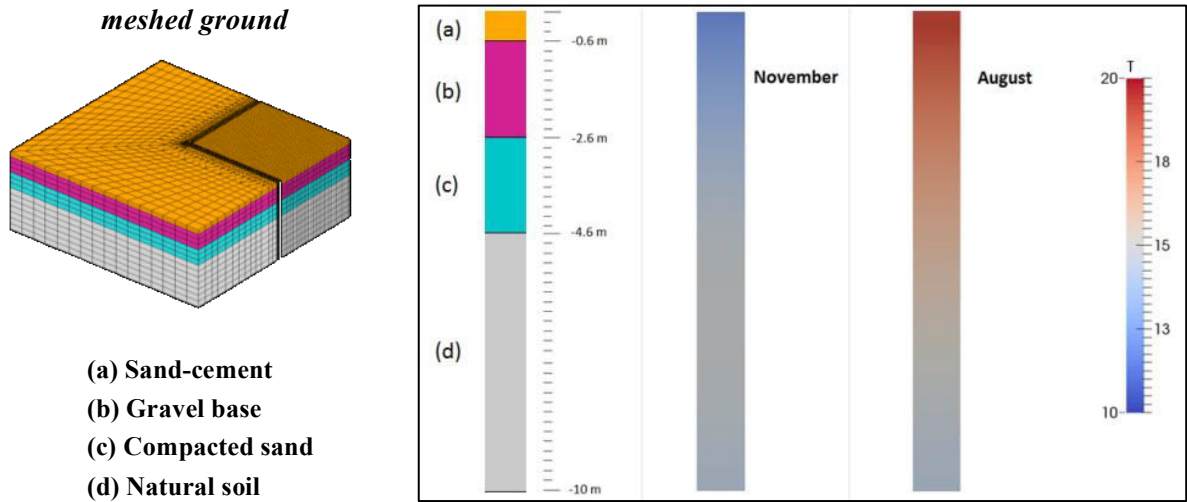


Figure 2.17 Profile of temperature in a hot month (August) and in a cold month (November) computed from a transient analysis considering the three previous months

Table 2.4 Ground thermal properties

	Specific mass [kg.m ⁻³]	Heat capacity [kg.m ⁻³]	Thermal conductivity [W/m K]	Emissivity
Sand-cement	2300	1100	1.7	0.76
Gravel base	2200	1100	1.5	0.76
Compacted sand	2100	900	2	0.76
Natural soil	2000	900	2	0.76

2.4.6 Definition of the scenarios for FEM simulations

From the 1D solution we observe that the solar flux and the convection conditions may affect the surface but also the temperature in the core of a structure with the dimensions and the material characteristics studied here (of course, for regions far from the junctions between perpendicular walls). The maximal temperatures reached within the structure and the core and surface temperatures are the variables of interest. Note that for the structure studied the maximum temperatures might be placed in the core of the region in the corner (i.e. not in the *current region* of the walls), and might not correspond to the same point for a given time. The results will be analysed keeping in mind this possible difference between the core temperatures (obtained in the current region of wall, and for which the conditions established for the 1D solution conditions are applicable *a priori*) and the maximum temperatures (not necessarily localized in a same point for all times).

The scenarios studied by means of FEM simulations are gathered in Table 2.5. At first, the 3D FE analysis focuses on the influence of the solar flux and wind, independently and combined, on the thermal response. The scenarios with constant solar flux are compared with the scenarios with

varying solar flux as described by the model in the section 1.2.2, for which analytical solution would not be feasible. The results of the sensibility study concerning the solar flux and the influence of the wind are confronted to the 3D numerical results. Scenarios with competition of convection and solar radiation are also studied in the following.

Table 2.5 Simulation campaign: thermo-chemical model

Aspect to be evaluated		Fixed conditions			Cases to be simulated
Preliminary sensibility study	Solar radiation	Hourly varying August temperatures (SET3)	$T_0 = T_a + 5 \text{ }^\circ\text{C}$	Placing frequency: 14 days	<ul style="list-style-type: none"> No flux Hourly varying flux Varying flux + 10% Varying flux + 25% Mean flux
	Wind				<ul style="list-style-type: none"> No wind Mean wind speed Maximum wind speed
	Combined scenarios				<ul style="list-style-type: none"> Mean wind AND Flux Mean wind AND Flux + 25% Mean wind + 10% AND Mean Flux Mean wind + 10% AND Mean Flux + 25%
Concreting temperature	Ambient temperature				<ul style="list-style-type: none"> 5 sets of temperature Sensibility on 1 Set of temperature ($\pm 5\%$ and $\pm 10\%$)
	Temperature of concrete at placement				<ul style="list-style-type: none"> $T_0 = T_a$ $T_0 = T_a + 5 \text{ }^\circ\text{C}$ $T_0 = T_a - 5 \text{ }^\circ\text{C}$ $T_0 = T_a + 2.59 \text{ }^\circ\text{C}$
Formwork material		Hourly varying August temperatures (SET3)	$T_0 = T_a + 5 \text{ }^\circ\text{C}$		<ul style="list-style-type: none"> Wooden Steel
Construction sequence	Placing frequency				

Then, the concreting temperatures, namely the initial temperature of concrete at placement and the ambient temperature are studied. From the analytical solution, the maximal temperature reached within the structure would depend linearly on both concreting temperatures, for a simplified geometry. Simulations are performed to verify if this is observed also for a more complex geometry in which the boundary conditions are not constant and with a more realistic description of the heat released by hydration. No simplifications regarding the Arrhenius thermo-activation term is made for the 3D FE simulations. In addition, the influence of the formwork material on convection and the influence of placing frequency on the overall structural thermal response, which were not discussed in the 1D solution but which have non-negligible importance regarding the thermal response, are studied in the following.

2.5 RESULTS AND DISCUSSION

The validation of the thermo-chemical model against experimental data is first presented, and then followed by the preliminary analysis in which the solar flux and the wind conditions are studied. Next, the effects of the concreting temperature and the formwork material are examined. Finally, the influence of the assembly of the structure at different times on the thermal response is studied.

2.5.1 Validation of the chemo-thermal model

The model was validated against the experimental data collected from a structure mock up built in the region of Dessel, Belgium. In the simulation the following conditions were respected: solar flux varying during the day; convection conditions with mean V_{wind} and steel formwork; ambient temperature oscillating from 16 °C (midnight) to 22 °C (midday), following a sinusoidal evolution; placing temperature as the first temperature measured experimentally within the concrete, $T_0 = 12.1$ °C; and finally, assembly of the base slab at 19 days.

Figure 2.18 shows the comparison between model and experimentally measured temperatures on different points within the structure. In this figure, the corresponding height (H), depth (D) and position with respect to the south-eastern corner of the structure were used to locate the points of reference in the model; this position corresponds to the placement of the sensors (Vantage Pro2 Console Manual weather station).

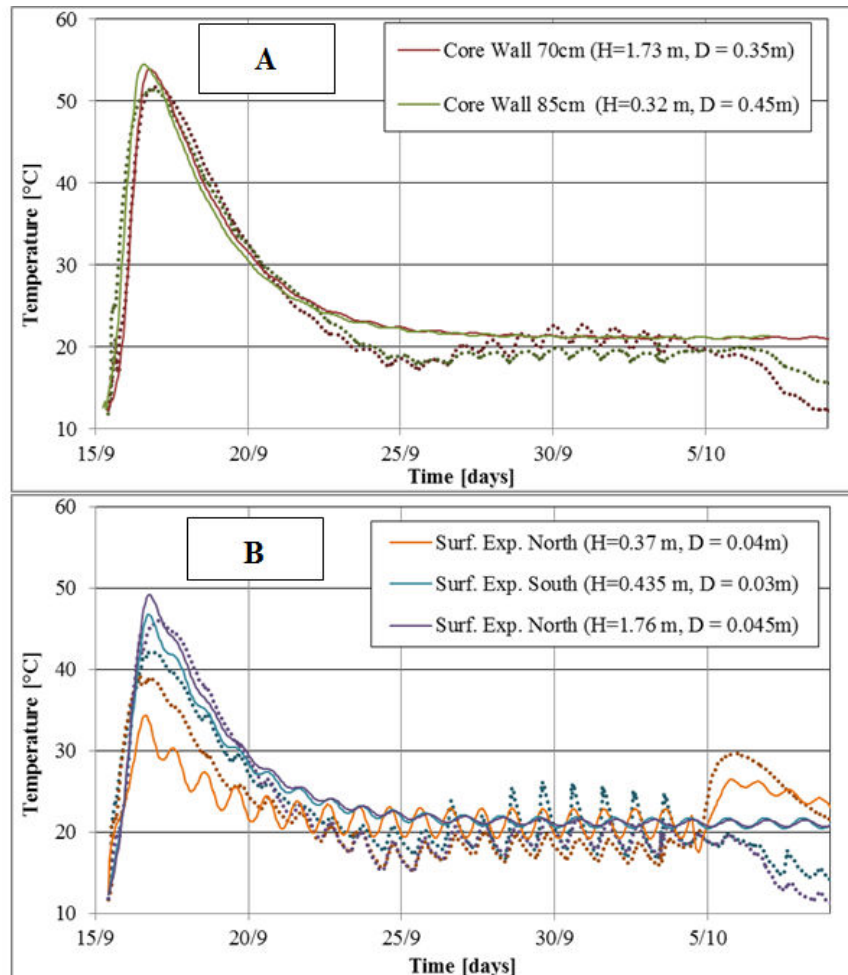


Figure 2.18 Evolution of the temperature: comparison of model and experimental results for core temperatures (A) and Surface temperatures (B). Full lines correspond to model results and points correspond to experimental results.

In order to reproduce the oscillations observed in the temperature, especially in the regions near the exposed surfaces, the choice of a cosinusoidal function to model the oscillations of the

ambient temperature during a day seems suitable. The solar radiation flux contributes to this oscillation in the temperatures near the surface as well.

The maximum temperature which takes place in the core is close to adiabatic conditions, either for the part of the wall with thickness 70 cm or the part of the wall with thickness 85 cm. The adiabatic rise for the concrete studied here is $\Delta T_{ad} = 46.6$ °C. Considering that the initial temperature of concrete is 12.1 °C, the temperature would reach in adiabatic conditions 58.7 °C, the numerical results returns 54.7 °C as the maximum temperature reached for the wall with thickness 85 cm and the maximum temperatures measured in situ were below 54 °C for the wall with thickness 85 cm .

The influence of the assembly of the slab on the wall temperatures was reproduced (orange curve on Figure 2.18 B). A part of the heat released by the hydration within the base slab is conducted through the wall leading to the temperature rise observed near the surface from 5th October. The 8°C amplitude of temperature adopted for the validation was not able to represent all the variations of temperature observed in the construction site during the 25 days of experimental measurements, especially for the dates between 25th September and 5th October. Note however that the mean tendencies of modelled and experimental temperatures are in agreement. A simulation accounting for the real temperatures measured in situ and its variations within the month is needed in order to obtain a better reproduction of these oscillations.

2.5.2 Influence of the solar flux

For the scenarios proposed here and in the next section the ambient temperature corresponds to the hottest month (Set 3) and the placing temperature of concrete is taken as the ambient temperature plus 5 °C. The assembly of the base slab takes place at the 14th day. This scenario is chosen as the reference scenario from which the others scenarios of interest are derived. In this section natural convection is considered for all cases. The influence of solar flux on the maximum temperatures reached and on the temperatures in specific points in the core and on the surface is discussed.

Regarding the maximum temperatures reached within the structure, the scenario with solar flux varying during the day presents, as expected, temperatures higher than the temperatures in the scenario with no flux. The maximum variation is 2.5 °C within the second day of simulation (see Figure 2.19).

When compared to the scenario with no solar flux, the scenario with mean solar flux presents a maximum variation of 1.03 °C. A similar result is obtained with the 1D solution presented in section 1.3. Figure 2.19 shows the evolution of the temperature in the core of the structure (the upper part of wall with thickness of 70 cm). Since the maximum temperatures are localized in the core of the structure, these results indicate that the contribution of the solar radiation is not limited to the surface proximities but also affects the temperature rise in the core of the structure considered here.

Regarding the surface temperatures, the scenario with solar flux varying during the day presents, again as expected, temperatures higher than the temperatures in the scenario with no flux. The maximum variation is 8.6 °C within the first day (Figure 2.19). When compared to the scenario with no solar flux, the scenario with mean solar flux presents a maximum variation of 4.3 °C. Again, this is coherent with the results of the 1D solution.

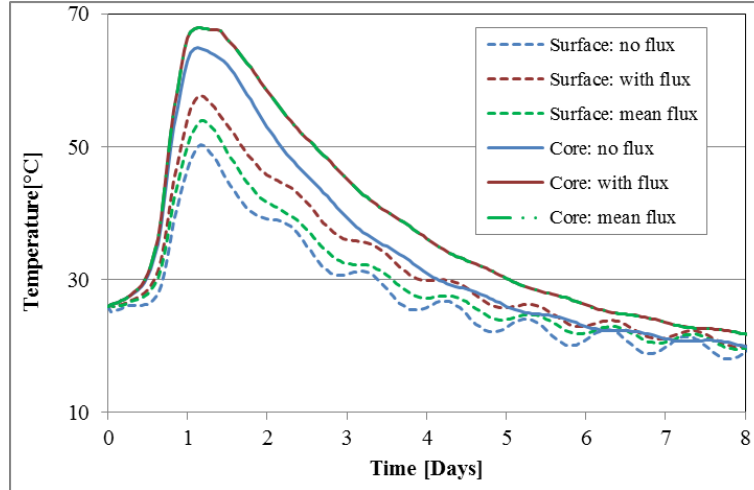


Figure 2.19 Evolution of the temperatures according to the solar flux: feedback on core (70 cm wall) and surface temperatures. Note that the curves corresponding to the core mean flux and core with flux are superposed.

Regarding the core temperatures, similar results were observed for the scenarios with varying solar flux and with mean solar flux. This justifies the use of mean values for solar radiation as a first attempt for modelling purposes, which allows reducing the timesteps necessary to the thermal analysis.

Regarding the sensibility of the solar flux contribution, scenarios with 10% and 25% more solar flux are considered. The latter implies a maximum variation of 0.50°C and the former 0.012°C within the first day. This indicates that an error in the estimation of the solar flux of the order of 10% does not lead to majors errors in the determination of the thermal response. These results are consistent with the 1D solution in which just small differences were found near the surface for increments of 10 and 25% in the solar flux.

2.5.3 Influence of the wind on convection conditions

Regarding the maximum temperatures reached in the wall, a maximum variation of 2.5 °C is found when the scenario with stagnating air is compared to the scenario with mean V_{wind} (Figure 2.20) A variation of 4.3 °C is observed when the scenario with stagnating air is compared to the scenario with maximum V_{wind} . For the base slab, the maximum variation is 1.1°C and 1.8°C for the mean V_{wind} and maximum V_{wind} , respectively. Note that the maximum variation does not take place at the peak of temperature but in the deceleration phase between day 3 and 4. At the peak, the temperature in the scenario with no wind reaches 70.8 °C. The maximum temperature reached for the

case with mean V_{wind} is 69.6 °C and for the case with maximum V_{wind} is 69.0 °C. Similar results were found for the core temperatures, which are illustrated in Figure 2.21 A. With these results, except in the presence of stagnating air, the constraint of 70°C as maximum admissible temperature is respected.

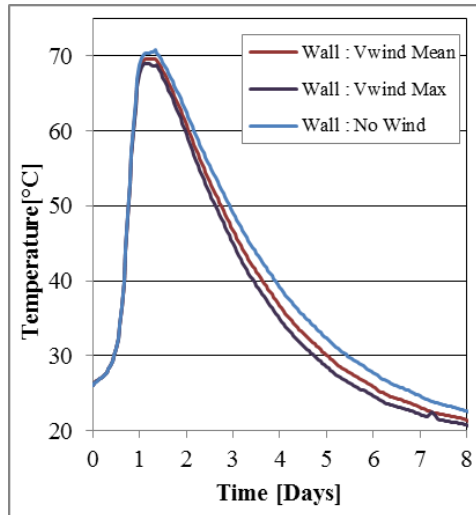


Figure 2.20 Evolution of the maximum temperatures according to the wind velocity

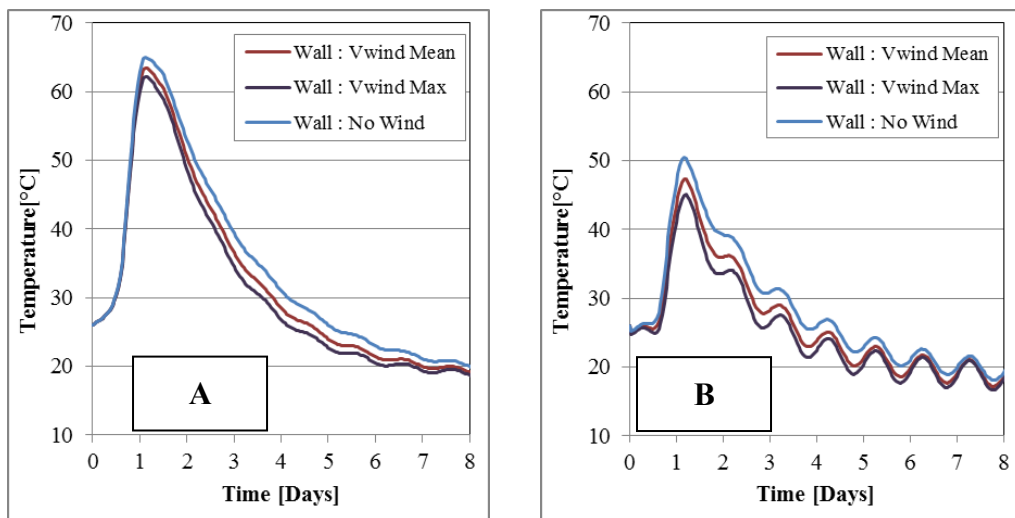


Figure 2.21 Evolution of temperatures according to the wind velocity. Core temperature (A), surface temperatures (B) in a current zone (at 2 m from corner in the outer part of the East wall).

Regarding the surface temperatures, the scenario with stagnating air when compared to the scenario with mean V_{wind} exhibits a maximum variation of 3.6 °C and when compared to the scenario with maximum V_{wind} the maximum variation is 6.4 °C. These maximum variations occur within the first 3 days, as shown in Figure 2.21 B. The 1D solution is consistent with these results (as shown in Figure 2.10).

Since the variations in the core temperatures are inferior to the variations on the surface, if we consider the difference between the core and the surface temperatures as an indicator of the gradient

across the thickness of the wall, then we can conclude that the presence of wind promotes an increase of the gradient of temperature in the thickness of the wall, and then tends to increase the thermal stresses. This should however be confirmed with a fully coupled THM analysis.

2.5.4 Competing mechanisms

The contributions of the solar radiation and combined convection and reradiation are opposed and have the same magnitude; these phenomena are then competing. An increase of 10% in the wind velocity leads to a maximum variation of 0.56°C in the core temperatures and 3.9°C on the surface temperatures. An increase of 25% in the solar flux leads to similar maximum variations (0.56°C in the core temperatures and 3.6°C on the surface temperatures). A combined scenario with an increase of 10% in the wind velocity and 25% in the solar flux leads to a temperature response very similar to the scenario with no increments (a difference of 0.20°C in core temperatures and 0.03°C on surface temperatures).

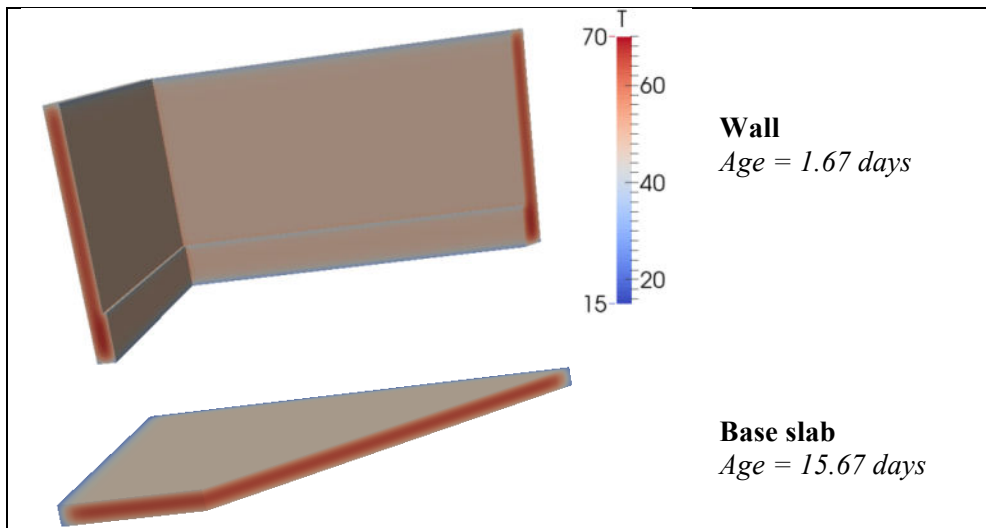


Figure 2.22 Temperature profiles at the peaks of temperature: scenario with solar flux and mean V_{wind}

This study shows that the influence of solar radiation and the impact of wind in convection conditions must be taken into account for a reliable thermal analysis. Figure 2.22 shows the temperatures within the structure near the age at which we observe the peak of temperature for the wall and for the base slab, respectively. The solar radiation induces temperature rises on the structure surface, but also affects the temperatures within the whole structure. Regarding the impact of wind on convection conditions, compared to a scenario with no wind (but in which natural convection is present), using the mean wind velocity, the temperatures on the surface and the core are reduced by less than 2 °C. For all scenarios here, the maximum temperatures reached within the structure do not exceed 70 °C.

2.5.5 Influence of concreting temperatures

During concreting, it is important to pay attention to the placing temperature of concrete as well as the ambient temperature. Both aspects are studied in this section, especially regarding the maximum temperature reached in the structure.

2.5.5.1 Influence of the placing temperature

The maximum temperature in the structure varies significantly with the placing temperature of fresh concrete. A difference of 4.9 °C is found between the scenario $T_0 = T_a$ and the scenario with $T_0 = T_a + 5$ (Figure 2.23, a zoom in the zones within the rectangles is shown). For the scenarios $T_0 = T_a + 2.59$ (corresponding to Eq. 1.38, for the temperatures of Set 3 and concreting at 8:00 am) and $T_0 = T_a - 5$, the variations are 2.34 °C and - 3.40 °C, respectively.

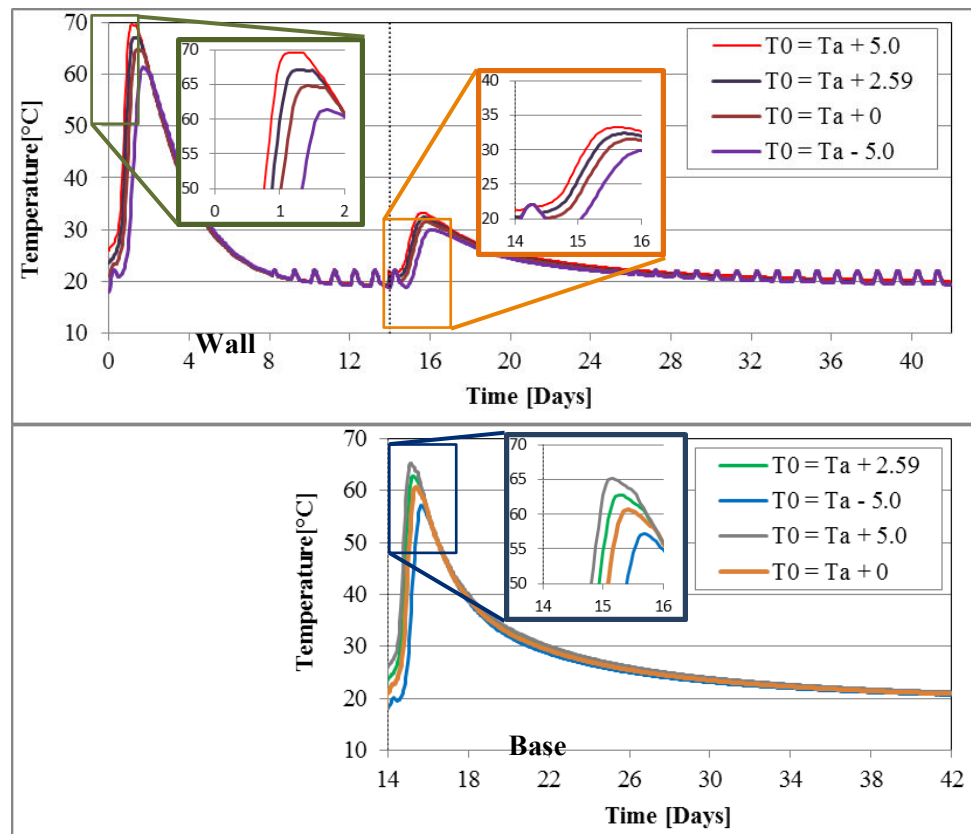


Figure 2.23 Influence of placing temperature on the maximum temperatures (zoom in the zones within the rectangles) in the walls (top) and in the base slab (bottom)

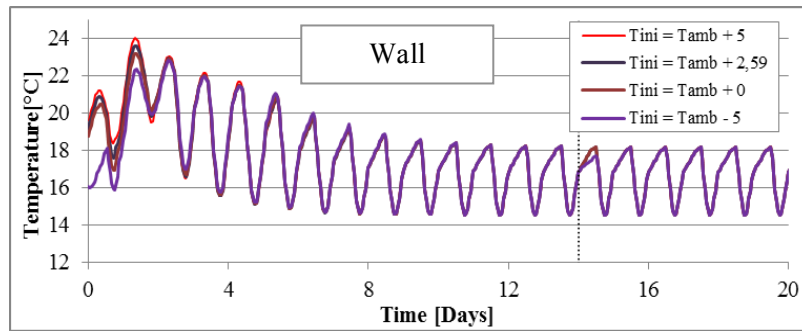


Figure 2.24 Influence of placing temperature on surface temperatures (in a current zone at 2 m from corner in the outer part of the East wall).

The placing temperature impacts the kinetics of hydration since the reactions are thermo-activated. With faster kinetics the heat released by hydration may not have enough time to be transferred to the environment, leading to conditions closer to adiabatic conditions in the zones far from exposed surfaces. On the other hand, with slower kinetics the heat transfer may be sufficient so that the heat evacuated allows considerably limiting the temperature increase, and the adiabatic conditions do not hold in the core of the structure, which is comparatively nearer to the isothermal regime. The thermal activation could explain why a higher T_0 leads to a higher temperature rise and why the peak in the scenario with $T_0 = T_a + 5$ was reached 20 hours before the peak of the scenario with $T_0 = T_a - 5$ (see Figure 2.23).

As expected, the influence on the surface temperatures is less pronounced (Figure 2.24 for wall temperatures). Comparing the scenarios with $T_0 = T_a + 5$ and $T_0 = T_a - 5$ the maximum variation observed is 6.43 °C for the base slab (not shown for conciseness) and 5.93 °C for the wall within the first day. Therefore, if we consider the difference between core and surface temperatures, higher temperatures gradients must take place in scenarios with higher placing temperatures for a given ambient temperature.

The peak of the maximum temperatures obtained for the scenario with $T_0 = T_a + 5$ slightly exceeds the maximum admissible temperature of 70° C. For the other scenarios all the temperatures are below 70° C.

2.5.5.2 Influence of the ambient temperature

The maximum temperatures reached in the structure according to the ambient temperature scenarios are shown in the Figure 2.25. With the Set 1 and 4 the maximum admissible temperatures are exceeded, which would potentially lead to DEF problems. As defined in Figure 2.14, the temperatures in Set 1 are 9.5 °C higher than the temperatures in Set 3. However, after the simulations, the maximum temperature reached within the structure found for Set 1 is 14.25 °C higher than for Set 3 (Figure 2.25). Similarly, the temperatures in the Set 5 are 11.9 °C lower than the temperatures in Set 3; the corresponding difference in the maximum temperature reached within the structure is 20.79 °C.

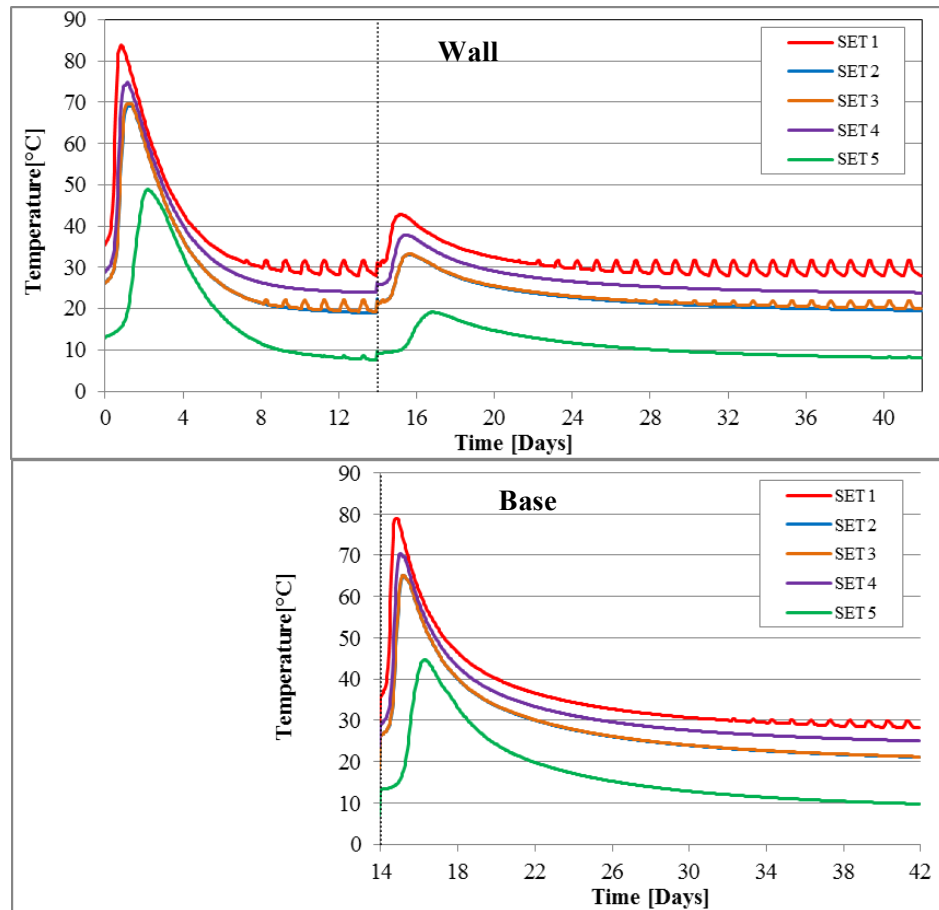


Figure 2.25 Evolution of the maximum temperatures according to the different temperature scenarios in the walls (top) and in the base slab (bottom)

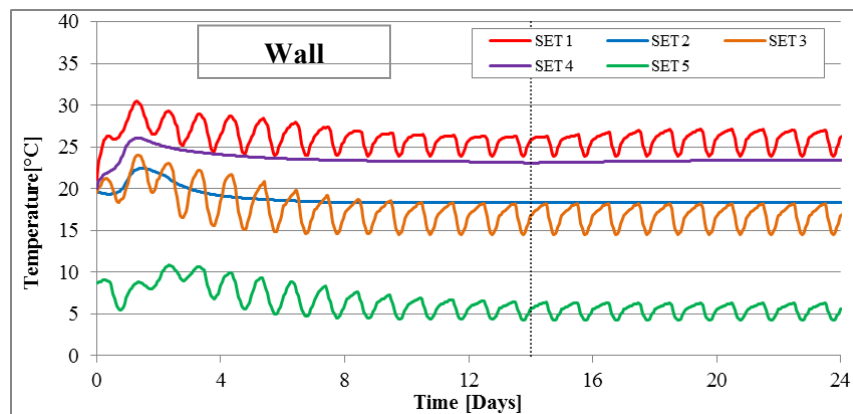


Figure 2.26 Influence of ambient temperature on minimal temperature reached in the structure

The result with the Set 2, which corresponds to Set 3 mean temperature, reproduces the same tendency as in the Set 3 but without the daily oscillation. The maximum temperature variation observed is 2.45 °C in the core and 5.5 °C (*i.e.* the amplitude of the Set 3) on the surface. A mechanical analysis must be performed to verify whether the stresses induced by the daily temperature oscillations can be neglected or lead to potential additional cracking (see Chapter 2).

The results for the minimal temperatures reached in the structure are presented in the Figure 2.26. Compared to the Set 3, a maximum difference of 13,9 °C was found for Set 1; 9.79 °C for Set 4, and 19.1°C for Set 5.

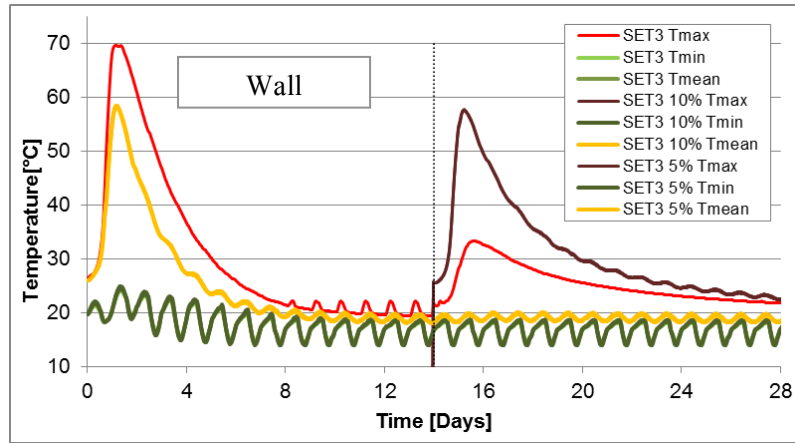


Figure 2.27 Sensibility analysis for Set 3

A sensibility study concerning the ambient temperature has been performed (Figure 2.27 with the case of Set 3). Regarding the maximum temperatures, in the wall the variation with respect to Set 3 is 0.935 °C for the case with 5% added up and 1.86 °C for the case with 10% added up. In the base slab, the variation with respect to Set 3 was 0.57 °C for the case with 5% added up and 1.17 °C for the case with 10% added up. Regarding the minimal temperatures, in the wall the variation with respect to Set 3 is 0.69 °C for the case with 5% added up and 1.13 °C for the case with 10% added up. In the base slab the variation with respect to Set 3 is 0.55 °C for the case with 5% added up and 1.18 °C for the case with 10% added up. So, for Set 3, and with the conditions retained for the simulations, each 1 °C added corresponds to an increase of about 1 °C on the maximum temperature. In other words, for ambient temperatures close to Set 3 the maximum temperature reached within the structure can be approximated as a linear function of the ambient temperature. Note that other effects such as the thermal activation of hydration reactions may intervene for temperature ranges that are not close to Set 3, such that the estimation of the maximal temperature becomes non-linear.

2.5.5.3 Determination of concreting temperatures

In order to assess the combined effects of the ambient and placing temperatures, in the following a simplified linearized model based on previous results is proposed to estimate the maximum temperature reached within the structure for any given set of ambient and placing temperatures:

$$T_{max} = c_1 T_0 + c_2 T_a + c_3 \quad (2.37)$$

where c_1 , c_2 and c_3 are fitting parameters. Comparing this equation with the analytical solution obtained in Section 3, we observe a term depending on the initial temperature, a term depending on the ambient temperature and a term related to hydration heat released.

The scenarios presented in the previous sections together with four additional scenarios are used here to determine the parameters introduced in Eq. 2.37. The additional scenarios are 1) Set 1 and $T_0 = T_a$; 2) Set 1 and $T_0 = T_a - 5$; 3) Set 5 and $T_0 = T_a - 5$; and 4) Set 5 and $T_0 = T_a$; which corresponds to scenarios with precooling of concrete, if we assume that a rise of temperature occurs due to transportation and mixing of fresh concrete. The maximum temperatures for all the scenarios studied are presented in Figure 2.28 and the fitted surface associated with Eq. 1.39 in Figure 2.29. The fitting is performed using a least squares method with *Mathematica*; the values obtained are shown in Table 2.6, with the correlation coefficient $R^2 = 0.81$.

Table 2.6 Fitting parameters for Eq. 1.39

c_1 [-]	1.28
c_2 [-]	0.359
c_3 [°C]	34.1

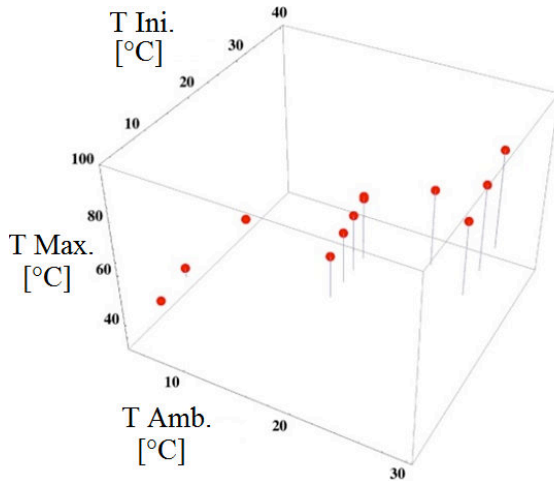


Figure 2.28 Maximum temperatures from simulations

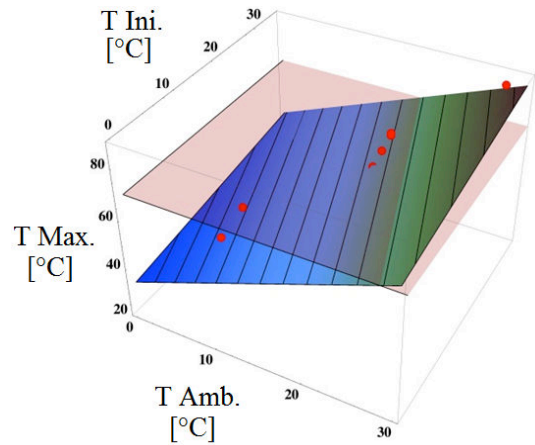


Figure 2.29 Fitted surface

Note that T_a , especially for the cases with temperatures oscillating during the day, corresponds to the mean ambient temperature at the time of placement, i.e. the temperature at 6:00 a.m. The coefficient c_3 has the same order of magnitude as the adiabatic rise of the material studied ($\Delta T_{ad} = 46.6$ °C). This result is expected since the maximum temperature occurs in the core of the structure and, since the structure is massive, the core presents conditions near to the adiabatic ones. Although Eq. 1.39 applies only for the material and environmental conditions described here, the previous discussion, supported by the combination of the analytical and numerical studies, may function as a more general strategy to determine the maximum temperature reached in mass concrete structures.

To conclude, in the cases studied here, Set 1 and 4 exceed the maximum admissible temperature of 70°C. Set 3, even with the unfavourable placing temperature $T_0 = T_a + 5$ does not

exceed 70 °C. The simulation with Set 5 presents gradients of temperature superior to the ones performed for the hot month. In the absence of solar flux the rise of temperature gradient near the exposed surface is increased. The definition of the maximum ambient temperature for concreting depends on the assumptions related to the amplitude of day temperature oscillations. Taking this amplitude as 10 °C and considering the unfavourable placing temperature $T_0 = T_a + 5$, concreting should be performed for temperatures below 24.2 °C considering the solar flux and the mean wind conditions. This temperature is slightly superior to the average maximal temperature for August which is 23.8 °C (i.e. the average of all maximum temperatures within the month calculated here for the period 1985 to 2009). This allows concluding that concreting can be performed if the average conditions regarding the maximum temperatures are respected for the hot months. Specific measures for cooling the concrete and the structure should be adopted in the case of extreme temperatures, as the ones of Set 1 and 4. Note that practical French guidance documents for DEF prevention in a performance-based approach (LCPC, 2009) refers to 5 °C margin beyond which special measures have to be taken. Adopting this margin, only the scenario with Set 1 would exceed the maximum admissible temperature.

2.5.6 Influence of the formwork material

The scenario with solar radiation varying during the day, mean V_{wind} , $T_0 = T_a + 5$ and with the Set 3 of ambient temperature was used to study the effect of the formwork material. The thermal conductivities of plywood is 0.13 W/(m.K) and steel is 16.3 W/(m.K). The thickness of plywood formwork is assumed to be $e_f = 2.1$ cm (Eq. 1.12).

The maximum and mean temperatures exhibited in the scenario with plywood formwork are higher than in scenario with steel formwork, as shown in Figure 2.30. A similar tendency is observed for the cores temperatures (Figure 2.31). A less pronounced variation was found with respect to surface temperatures. The maximum temperature variations with respect to the surface was 2.5°C (9.4%) and to the core 4.7°C (17.9%, core 70cm) or 6.5°C (24.9%, core 85 cm).

As expected, the plywood functions as an insulating material, i.e. harming the dissipation of the heat released by hydration. The evolution of the core temperatures in the scenario with plywood formwork is closer to the adiabatic elevation. Regarding the maximum admissible temperature of 70°C, plywood is more unfavourable than steel formwork.

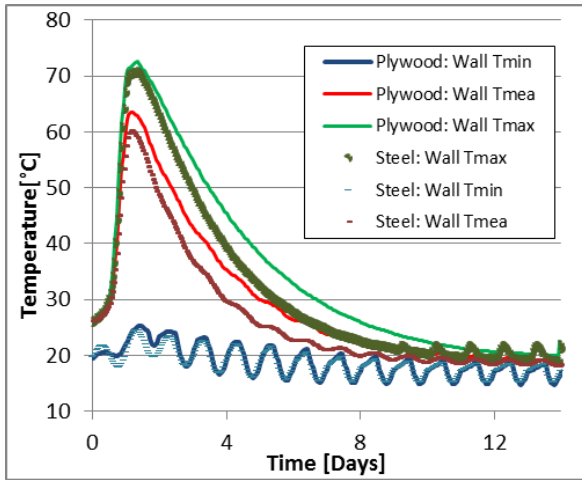


Figure 2.30 Maximum, mean and minimal temperatures

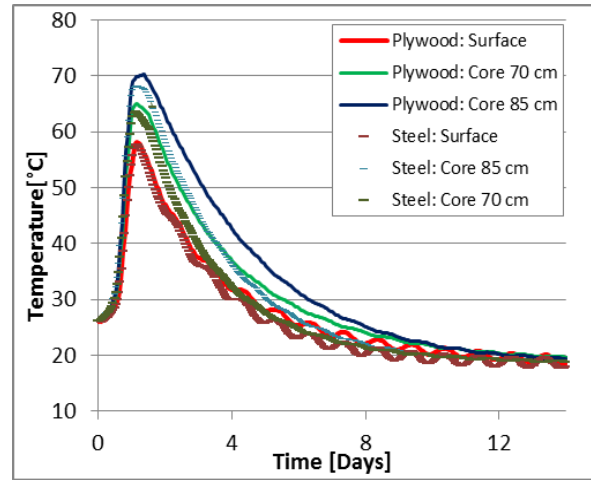


Figure 2.31 Surface and core temperatures

2.5.7 Placing frequency

The thermal responses of scenarios with different placing dates of the base slab are studied here.

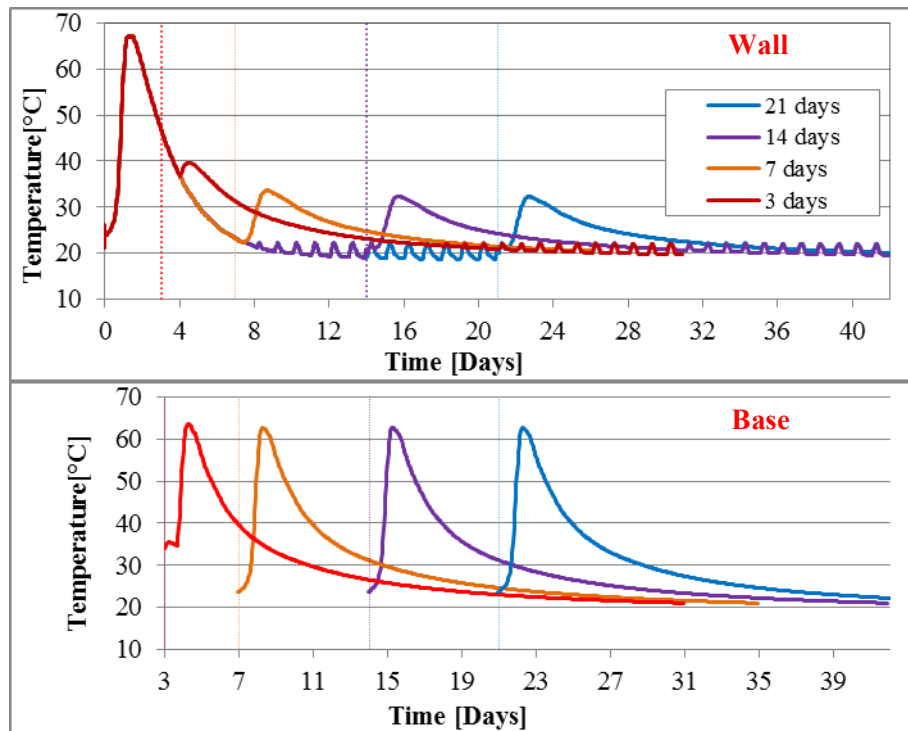


Figure 2.32 Maximum temperatures reached for different placing days

According to the Figure 2.32, for placing dates after 7 days, the peak of maximum temperature obtained in the base slab is just shifted with respect to the placing day of the base slab assembly. This is due to the fact that almost all hydration reaction has been completed after 7 days in the walls. In terms of magnitude, the placing date affects negligibly the maximum temperature in the slab. For the assembly at 3 days a very small feedback of the wall temperatures on the base slab inferior to

1° C can be observed. The same tendency was also observed regarding the overall temperature response.

An accurate mechanical analysis should be performed in order to verify the effects of the placing date on the mechanical and cracking behavior of the structure. Indeed, other temperature-dependent phenomena such as creep and autogeneous shrinkage affects the mechanical response and are key issues in the determination of the cracking risks. Such analysis is presented in the next chapter.

2.6 CONCLUSIONS AND PERSPECTIVES

In this chapter, the role of the boundary and initial conditions on the thermal response of massive concrete structures was investigated. A simplified 1D solution for the thermal problem in a semi-infinite domain was proposed in order to help in the definition of simulation scenarios for a more complex and computationally costly 3D FE analysis. We focused on the contribution of the phenomena affecting the thermal response of massive concrete structures at early-ages, namely, the solar flux, natural and forced convection, reradiation and conduction through older structural members. The case of a real structure, for which experimental data concerning the chemo-thermal properties and the evolution of the temperature are available, was investigated for the 3D FEM analysis. This study allows concluding that:

- The simplified solution of the 1D problem proposed here is a good first estimation of the influence of the different phenomena affecting the thermal response. Although not directly applicable to more complex geometries or in zones where the 1D hypothesis does not hold, this solution can be useful in defining scenarios of numerical simulation in the context of complex 3D geometries and boundary conditions such as non-constant solar flux and ambient temperature. Simplified estimations of the maximum temperature reached within the structure have also been proposed (LCPC, 2009).
- After the validation against *in situ* data, a cosinusoidal variation of the ambient temperature during the day is a suitable choice to represent the temperature oscillation for modelling purposes. The effect of this oscillation on the mechanical response remains to be evaluated. Otherwise, the solar radiation flux does not impact significantly the oscillation of temperature observed within the structure near the exposed surface; the oscillation of ambient temperature appears to be the main responsible of this effect.
- The influence of solar radiation and the impact of wind in convection conditions must be taken into account for a reliable thermal analysis. The solar radiation induces temperature rises on the structure surfaces, but also affects the core temperatures for structures with dimensions similar to the structure studied here (wall and slabs with 0.7 to 0.85 m thickness). Regarding the impact of wind on convection conditions, compared to a scenario

with no wind (but in which natural convection is present) using the mean wind velocity, the temperatures on the surface and the core are reduced by less than 2°C.

- The absence of solar flux can lead to more pronounced gradients of temperature near the surface. This effect is more remarkable in cold months and for higher values of convection and reradiation coefficients.
- The concreting temperatures, namely the ambient temperature and the placing temperature, affect directly the maximum temperature reached in the structure. A linear relation between these temperatures and the maximum temperature can be defined for the domain of temperatures used in the present analysis. For the placing temperature, compared to a scenario with no increment of the placing temperature with respect to the ambient one, the difference in the maximum temperature reached has approximately the same value of the increment. This conclusion is only valid for placing temperatures close to each other. The thermo-activation of hydration induces higher differences for placing temperatures differing from more than 5°C. The influence of ambient temperature, in the domain of the analysis, remains also almost linear with respect to the maximum temperature reached. This behaviour is in agreement with the results of the 1D solution proposed.
- The thermal conductivity of the formwork material affects the temperature response of the structure. Formwork whose material has a lower thermal conductivity (as plywood for example) may lead to an elevation of temperature closer to the adiabatic case, which can be unfavourable regarding the maximum admissible temperature.
- Regarding the preliminary results of placing frequency, the results show that the temperature profiles for assembly day superior to a time in which the hydration is close to completion and the heat released has enough time to transfer in the atmosphere (in the case studied here, $t > 3$ days) just shift from each other. Next chapter presents a study about the mechanical impact of the assembly date.

A mechanical analysis accounting for autogenous shrinkage and ageing creep in the behaviour of concrete massive structures at early age and focusing on the prediction of cracking risks is presented in the next chapter. Moreover, the effects of mass transfer phenomena, namely drying, coupled with the chemo-thermal and mechanical model would also deserve further developments.

3. MECHANICAL MODELLING

This chapter is based on the papers (Honorio et al., 2015a; T. Honorio et al., 2014).

A relevant analysis of the overall behaviour of the structure in which the cracking risks are assessed needs an adequate description of the evolution of key physical properties but also a description of the thermal and mechanical boundary conditions.

From the modelling point of view, the thermo-chemo-mechanical behaviour of concrete structures has been extensively studied (see e.g. (Azenha, 2009; Briffaut et al., 2012, 2011; de Borst and van den Boogaard, 1994; Gawin et al., 2006; Hattel and Thorborg, 2003; Ishida et al., 2011; Potgieter and Gamble, 1983; Toutlemonde and Torrenti, 2012)), which reflects the industrial interest in this kind of analysis, in spite of their intrinsic complexity. This is, in particular, the case of the nuclear park structures whose behaviour must be predicted and often monitored during the construction phase. Among the different approaches proposed in the literature, we highlight the contributions of Ulm and Coussy (Ulm and Coussy, 2001, 1998), which developed a model in a thermodynamic framework pointing out the couplings between the different physical mechanisms. The authors considered plasticity behaviour and no creep strains were accounted for. Furthermore, De Schutter (2002a, 2002b) accounts for creep but not for the influence of the temperature on creep. Interestingly, (Fairbairn et al., 2004) used genetic algorithms in order to determine the optimized set of conditions related to the construction site of a dam including the different lifts. Faria et al. (2006) proposed also a coupled approach in which basic creep but no damage is taken into account, while Buffo-Lacarrière et al (2014, 2007) proposed a coupled analysis accounting also for an anisotropic visco-damage model. Also, Gaspar et al. (2014) performed a sensibility analysis using probabilistic tools in order to study the influence of different parameters concerning the chemo-thermal problem. Except in Fairbairn et al. (2004), a study in which different scenarios of concreting temperatures as well as other factors of interest related to the construction site conditions is not effectively performed in a more exhaustive way.

In general, different factors related to construction site conditions must be accounted for on the design phase of concrete massive structures in order to provide a reliable prediction of cracking at early-age. We identify the following key factors from the literature and from previous analysis:

- **Concreting temperatures and thermal boundary conditions**, as shown in Chapter 2, affect directly the chemo-thermal behaviour of concrete (Honorio et al., 2014a; Potgieter and Gamble, 1983).
- **Restraint conditions**. When restrained, the early-age strains may induce an increase in the stresses within the material, which may reach the strength of the material (Cope et al., 2002). Internal restraint, due to the volume of concrete itself or the reinforcement, and external

restraint, due to the fixing conditions or linked structural members, are present in reinforced concrete structures.

- **Assembly date or placing frequency.** In the case of structures with many lifts or assembled structural members, the chemo-thermal behaviour of both new and old material is affected since the heat released by the new structural member can be evacuated through the older members (Fairbairn et al., 2004). Also, the old members function as a restraint condition to the new placed members.

In this chapter, we propose to study the influence of some relevant aspects of these factors, combined in different scenarios, on the mechanical response at early age of a massive nuclear waste disposal structure. Some scenarios studied in the previous chapter are analysed through the mechanical aspect here.

We apply the model proposed by Benboudjema and Torrenti (2008), based on a chemo-thermo-elastic-damage approach (smeared crack) in which a coupling between creep and damage is introduced (Mazzotti and Savoia, 2003). This model is briefly described in the following section.

The main objectives of this chapter are to critically investigate simplified and more realistic modelling strategies of coupled early-age analysis of massive concrete structures. Often different scenarios regarding the factors presented above may be of interest due to performance or economic criteria. As observed in the previous chapter, a more exhaustive analysis, accounting for several scenarios which may potentially interest the contractor (scenarios for example, with different initial and ambient temperatures, assembly frequencies, restraints conditions, etc.), leads to massive simulations campaigns. For the mechanical analysis the scenarios were chosen accounting for two aspects:

- **Thermo-mechanical boundary conditions description:** Two ambient temperatures are considered (Set 3 and Set 5 in Figure 2.14). The simplified strategy of considering the ambient temperature within a day as a constant is compared to a more realistic modelling strategy of accounting for the oscillation of the ambient temperature within a day (Set 3 and Set 2 in Figure 2.14). Scenarios with presence of asymmetrical solar flux radiation on different surfaces of the structure are compared to scenarios without solar flux. Simplified mechanical boundary conditions in which the ground is not meshed are compared to the cases with meshed ground.
- **Cracking risk evaluation:** CI based analysis is compared to damage based analysis. This allows to better defining some of the limits of applicability of CI based strategies, which are more commonly used in engineering practice and much less computationally expensive than damage based strategies. A sensibility study regarding the coupling between creep and damage is conducted, and the resulting differences in the damage patterns and its potential influence on crack opening are highlighted. A preliminary attempt to evaluate crack opening

shows that damage will potentially not affect significantly the sealing capacity or durability of the studied structure.

We treat these aspects with significant examples illustrating some important features of the structure performance. The present analysis may be extended for similar structures and serve as referential of strategy to treat the problem of massive concrete structure behaviour at early age. The proposed strategy may help in the decision making process of construction of such structures of current use in, for example, nuclear applications.

3.1 THERMO-CHEMO-MECHANICAL PROBLEM

From the analysis of the coupling existing at early-age it can be shown that, after neglecting a possible chemical dilation due to hydration reaction, we can write the following state equation (Ulm and Coussy, 1998):

$$\boldsymbol{\sigma} = \mathbf{C}(\xi): (\boldsymbol{\varepsilon} - \boldsymbol{\varepsilon}_{in}) \quad (3.1)$$

where $\boldsymbol{\sigma}$ is the stress tensor, $\mathbf{C}(\xi)$ is the stiffness tensor function of the degree of hydration ξ , $\boldsymbol{\varepsilon}$ is the total strain tensor, $\boldsymbol{\varepsilon}_{in} = \boldsymbol{\varepsilon}_{bc} + \boldsymbol{\varepsilon}_{au} + \boldsymbol{\varepsilon}_{th}$ is the inelastic strains occasionally undergone by the material, including basic creep $\boldsymbol{\varepsilon}_{bc}$, autogenous strains $\boldsymbol{\varepsilon}_{au}$ and thermal strains $\boldsymbol{\varepsilon}_{th}$. The determination of these strains is detailed in the following.

As pointed out in the introduction, no humidity transfer is considered. This simplifying hypothesis seems adequate for structures in which measures preventing hydric exchanges with the exterior are adopted and considering a limited analysis period.

3.1.1 Autogenous strains

In cement based materials, the autogenous shrinkage is the external (or apparent) volume variation of the material at a free stresses state. Different mechanisms are involved. Before the setting, the autogenous shrinkage is equal to the chemical shrinkage (Lura et al., 2003). The chemical shrinkage is the consequence of the volume of reactants (cement and water) being superior to the volume of products (hydrates), as studied by Le Chatelier (1904). After setting, the solid skeleton formed will oppose to the strains and the chemical shrinkage will be responsible for the formation of pores within the material. This volume does not appear in the external volume change but will induce the self-desiccation shrinkage. So, after the setting the autogenous shrinkage refers to the self-desiccation shrinkage.

A linear relationship between the autogenous strains and the degree of hydration has been reported (see e.g. (Briffaut, 2010; Ulm and Coussy, 1998)), which allows accounting for this effect by

$$\boldsymbol{\varepsilon}_{au} = -\kappa \xi \mathbf{1} \quad (3.2)$$

where κ is a constant material parameter.

Moreover, often an initial swelling is reported. Different phenomena have been invoked to explain this initial swelling (Benboudjema and Torrenti, 2008; Briffaut, 2010; Le Chatelier, 1904). Here, the experimental autogenous strain is fitted as a function of the degree of hydration and with the identification of swelling and shrinking zones.

3.1.2 Thermal strains

The thermal strains are given by:

$$\boldsymbol{\varepsilon}_{th} = \alpha (T - T_0) \mathbf{1} \quad (3.3)$$

where α is the coefficient of thermal expansion (CTE) [$^{\circ}\text{C}^{-1}$], T is the temperature at a given time and $\mathbf{1}$ is the identity matrix. This coefficient varies at the very first days and then remains almost constant for a given temperature and humidity conditions (Sellevold and Bjontegaard, 2006). The cement paste is reported to shrink with the increase of temperature, whilst both mortar and concrete dilate driven mostly by the aggregates behaviour (Cruz and Gillen, 1980). These variations will be neglected in this part.

3.1.3 Ageing elasticity

The ageing behaviour of concrete is modelled using the phenomenological proposition of De Schutter et al. (De Schutter, 1999; De Schutter and Taerwe, 1997). The Young modulus E and the tensile strength f_t are given by:

$$E(\xi) = E_{\infty} \xi^n ; f_t(\xi) = f_{t\infty} \xi^m \quad (3.4)$$

where m and n are fitting parameters depending on the material behaviour, and E_{∞} and $f_{t\infty}$ are the Young modulus and tensile strength at late ages, respectively. The normalized degree of hydration (or Degree of Reaction) is given by:

$$\check{\xi} = \left\langle \frac{\xi - \xi_0}{\xi_{\infty} - \xi_0} \right\rangle_+ \quad (3.5)$$

where ξ_0 is the hydration degree corresponding to the mechanical percolation threshold and ξ_{∞} is the final degree of hydration.

The Poisson ratio can be estimated as a function of the degree of hydration by (De Schutter and Taerwe, 1997):

$$\nu(\xi) = (v_{\infty} - v_0 e^{-10}) \sin \frac{\pi \check{\xi}}{2 \xi_{\infty}} + v_0 e^{-\frac{10 \check{\xi}}{\xi_{\infty}}} \quad (3.6)$$

where the initial (v_0) and final (v_{∞}) values are to be identified as a function of the degree of hydration. Note that accounting for the Poisson ratio evolution is reported not to affect very significantly the mechanical response at early-age (Briffaut, 2010).

3.1.4 Basic creep

The creep behavior of concrete is described using the model of Benboudjema (2002), in which a Kelvin-Voigt chain is associated with an ageing dashpot (Figure 3.1). This rheological model allows accounting for the partially reversible part of basic creep. The problem is described by the following differential equation (Benboudjema and Torrenti, 2008):

$$\tau_{bc}^{kv} \dot{\boldsymbol{\varepsilon}}_{bc}^{kv} + \left(\tau_{bc}^{kv} \frac{k_{bc}^{kv}(\xi)}{k_{bc}^{kv}(\xi)} + 1 \right) \dot{\boldsymbol{\varepsilon}}_{bc}^{kv} = \frac{\tilde{\boldsymbol{\sigma}}}{k_{bc}^{kv}(\xi)} \quad (3.7)$$

$$\tilde{\boldsymbol{\sigma}} = \eta_{bc}^{dp}(\xi, t, T) \dot{\boldsymbol{\varepsilon}}_{bc}^{dp} \quad (3.8)$$

where the superscript kv refers to the Kelvin-Voigt chain with a constant characteristic time τ_{bc}^{kv} ; to which a strain tensor of basic creep $\boldsymbol{\varepsilon}_{bc}^{kv}$, a spring stiffness k_{bc}^{kv} and a viscosity η_{bc}^{kv} are associated. Similarly, the superscript dp refers to the ageing dashpot. Finally, $\tilde{\boldsymbol{\sigma}}$ is the effective stress as defined in Eq. (2.14).

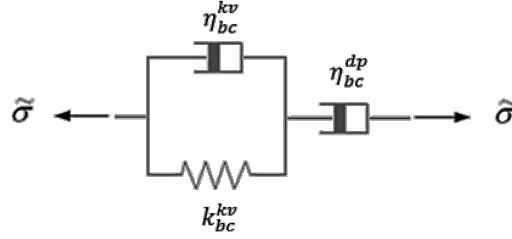


Figure 3.1 Rheological model for ageing creep

The total basic creep strain reads then:

$$\boldsymbol{\varepsilon}_{bc} = \boldsymbol{\varepsilon}_{bc}^{kv} + \boldsymbol{\varepsilon}_{bc}^{dp} \quad (3.9)$$

Following the De Schutter's (De Schutter, 1999; De Schutter and Taerwe, 1997) approach, the spring stiffness and viscosity are ageing, so we have:

$$k_{bc}^{kv}(\xi) = k_{bc}^{kv}(\xi_{\infty}) \frac{0.473}{2.081 - 1.608} \xi^p \quad (3.10)$$

$$\eta_{bc}^{kv}(\xi) = \eta_{bc}^{kv}(\xi_{\infty}) \frac{0.473}{2.081 - 1.608} \xi^p \quad (3.11)$$

where $k_{bc}^{kv}(\xi_{\infty})$ and $\eta_{bc}^{kv}(\xi_{\infty})$ are the final stiffness and viscosity, respectively, which can be determined by fitting experimental data; and p is a fitting parameter.

The creep dependency on temperature is modelled by an Arrhenius-like term, with which an energy of activation for creep E_{ac} is associated. This model is similar to the one proposed by (Bazant et al., 2004). The main hypothesis is that the increase in creep due to temperature rises is due to the decrease in the viscosity of water. Therefore, the value of E_{ac} corresponds to the energy of activation related to the change of water viscosity ($E_{ac} = 17.5$ kJ/mol). Thereby, we have for Eqs. (2.10 – 2.11):

$$k_{bc}^{kv}(\xi, T) = k_{bc}^{kv}(\xi_{\infty}) \frac{0.473}{2.081 - 1.608} \xi^p e^{\frac{E_{ac}}{R} \left(\frac{1}{T} - \frac{1}{T_0} \right)} \quad (3.12)$$

$$\eta_{bc}^{kv}(\xi, T) = \eta_{bc}^{kv}(\xi_\infty) \frac{0.473}{2.081 - 1.608} \xi^p e^{\frac{E_{ac}}{R} \left(\frac{1}{T} - \frac{1}{T_0} \right)} \quad (3.13)$$

3.1.5 Damage

As a quasi-brittle material, the Young modulus of concrete decreases due to the formation of microcracks, after exceeding a certain threshold, with the increase of loading. A simple and widely used model to describe this effect is the Mazars damage model (Mazars, 1984), which is based on a single scalar internal variable D describing isotropically the damage. The stresses are given by:

$$\boldsymbol{\sigma} = (1 - D)\tilde{\boldsymbol{\sigma}} \quad (3.14)$$

with, for tensile state of stresses:

$$D = 1 - \frac{\kappa_0}{\hat{\varepsilon}} \left((1 + A_t) \exp(-B_t(\hat{\varepsilon} - \kappa_0)) - A_t \exp(-2B_t(\hat{\varepsilon} - \kappa_0)) \right) \text{ for } \hat{\varepsilon} \geq \kappa_0(\xi) \quad (3.15)$$

where, A_t and B_t are material parameters to be determined; κ_0 is the damage threshold; and $\hat{\varepsilon}$ is the equivalent strain defined from the positive eigenvalues of elastic and creep strains. To define $\hat{\varepsilon}$, we use an extension of the original formulation with :

$$\hat{\varepsilon} = \sqrt{\langle \varepsilon_e + \beta \varepsilon_{bc} \rangle_+ \cdot \langle \varepsilon_e + \beta \varepsilon_{bc} \rangle_+} \quad (3.16)$$

where β is a weight parameter which allows accounting for the effects of creep strains on the damage evolution, as proposed by (Mazzotti and Savoia, 2003). This coupling is introduced in order to reproduce the experimental observations (Reviron et al., 2007). Different values of β can be found in the literature (for example, $\beta = 0.24$ (Reviron et al., 2007; Thai et al., 2014), $\beta = 0.1$ (Mazzotti and Savoia, 2003; Thai et al., 2014), $\beta = 0.05$ (Reviron et al., 2007), $\beta = 0.4$ (Briffaut et al., 2011)). However, the characterization of this parameter remains not very well understood and it may vary as a function of the level and type of loading as well as the age of the material (De Larrard, 2010). As highlighted by Pijaudier-Cabot and Dufour (2013), we assumed with the proposed formulation that creep and damage are coupled phenomena that lead to tertiary creep and then failure. Note that some works (see e.g. (Ladaoui et al., 2012; Rossi et al., 2012)) raise that damage may appear moderately during creep (due in particular to the mismatch of strain at the micro/meso levels) or even be the source of creep, and not only in the tertiary phase.

The damage variable changes as soon as the damage threshold κ_0 is reached. κ_0 is computed by:

$$\kappa_0(\xi) = \frac{f_t(\xi)}{E(\xi)} \quad (3.17)$$

Since the strength and the Young modulus evolve differently, the kinetics of κ_0 is different from the kinetics of the tensile strength and Young modulus.

The application of softening laws like (Mazars, 1984) original model generally leads to problems in finite elements solution. Unrealistic solution with fracture obtained at zero energy dissipation and mesh dependency may occur (Pijaudier-Cabot and Bažant, 1987). A strategy to deal with this problem is to adopt a nonlocal approach. The idea is to replace the usual local damage

energy release rate with its spatial average over the representative volume of the material, whose size is a characteristic of the material (Pijaudier-Cabot and Bažant, 1987).

To limit the mesh-dependency of the FE simulation results, we adopt a regularization method based on the fracture energy conservation (Hillerborg et al., 1976) in tension. At the scale of the Gauss point, the cracking energy $g_{ft}(\xi)$ is calculated from the integral of the stress-strain response in a uniaxial tension test; $g_{ft}(\xi)$ is a continuous variable corresponding to a density of the energy dissipated during cracking. The total surface cracking energy $G_{ft}[\text{J. m}^{-2}]$ is then given by (Hillerborg et al., 1976):

$$G_{ft}(\xi) = g_{ft}(\xi) l_c = \left\{ \frac{f_t(\xi)(1 + A_t/2)}{B_t(\xi)} + \frac{\kappa_0(\xi)f_t(\xi)}{2} \right\} l_c \quad (3.18)$$

where the characteristic length $l_c = \sqrt[3]{V_{ef}}$ is in 3D a function of the volume of the finite element V_{ef} . To ensure an adequate consumption of $G_{ft}(\xi)$ one has to work at the finite element level with the $g_{ft}(\xi)$. This is an intrinsic material property which is assumed to evolve with respect to the degree of hydration (De Schutter and Taerwe, 1997):

$$G_{ft}(\xi) = G_{ft_\infty} \xi^q \quad (3.19)$$

where G_{ft_∞} is the final value of the total surface cracking energy and q is a fitting parameter. The empirically determined exponent 0.46 is adopted in the following (De Schutter and Taerwe, 1997).

3.1.6 Cracking index

To estimate the susceptibility to cracking, we define a cracking index CI:

$$CI = \max_{\Omega} \left\langle \frac{\sigma_{ii}(t)}{f_t(t)} \right\rangle_+ \quad (3.20)$$

where σ_{ii} is the i^{th} principal stress in the volume Ω and f_t is the tensile strength at the same location. Note that this index is the inverse of the cracking index proposed by the JCI (JCI, 2008). We propose this definition so that the index is defined as a fraction of the tensile strength. A CI close to 1 means that the state of stress in a region of the domain Ω might potentially leads to cracking in this region. As proposed by the JCI (JCI, 2008), the probability of cracking, assuming that the cracking probability has a Weibull distribution, may be estimated by:

$$P(CI) = 100 \times [1 - \exp[-(1.087/CI)^{-4.29}]] \quad (3.21)$$

In order to avoid cracking, $P(CI)$ must be inferior or equal to 5%. Then, the CI obtained from the simulation must be inferior to 54% so that $P(CI) \leq 5\%$. However, for some particular cases higher risk of thermal cracking may be accepted (JCI, 2008). Other less conservative cracking criteria has been used. Craeye (Craeye, 2010) follows Rostàsy et al. (2002) approach in which cracking is deemed to occur if the tensile stresses in a given direction exceed 70% of the strength of the material at that age.

Note that the simulations without damage for evaluating the CI provide potentially ‘cracked’ zones (i.e. where the CI exceeds the limit 1), but these zones may be different from the ones obtained with damage since the corresponding calculations induce inevitably significant redistribution of stresses and strains. Consequently the damage would probably tend to propagate in certain cases in adjacent regions. Such effects cannot be accurately captured without accounting for the strain-softening characteristics of concrete material in tension.

3.1.7 Crack opening

The estimation of crack opening is important for the evaluation of risks related to durability problem in concrete structure. A post-treatment technique developed by Matallah et al. (2010) is used to assess the crack opening from the stress and damage states. The method is based on the fracture energy regularization, as presented in Section 2.1.5. Thereby, the material behaviour in the fracture process zone is characterized in a smeared manner through a strain-softening constitutive law (Matallah et al., 2010). It is assumed that only one crack crosses the finite element.

The total strains within the element are decomposed in an elastic part and a cracking part $\boldsymbol{\varepsilon}_{co}$. The crack opening tensor $\boldsymbol{\delta}_n$ is taken as the fracture strain accumulated over the characteristic length l_c of the finite element:

$$\boldsymbol{\delta}_n = l_c \boldsymbol{\varepsilon}_{co} \quad (3.22)$$

where $\boldsymbol{\varepsilon}_{co} = \mathbb{C}^{-1} : \boldsymbol{\sigma}_{in}$. The inelastic stress tensor $\boldsymbol{\sigma}_{in}$ is computed from the difference between the total stress $\boldsymbol{\sigma}$ and the equivalent stress $\tilde{\boldsymbol{\sigma}}$, as defined above.

Here, we assess the cracking opening by the maximum value of $\boldsymbol{\delta}_n$ in the principal basis. Even if this approach was initially developed to estimate crack opening for a non-ageing material, the extension to the case with ageing is straightforward since the ageing aspects are accounted for in the computation of the inelastic stresses.

3.2 DESCRIPTION OF FEM SIMULATIONS

In addition to the description of the structure presented in the section 1.4, the reinforcement is explicitly considered for the mechanical simulations. The resulting mesh owns about 100 thousand 2D bar finite elements, for which the local behaviour is given by the displacements of the nodes in both extremities (Figure 3.2). The colours in Figure 3.2 correspond to the different reinforcement densities. Steel bars with 25 and 32 mm diameter are distributed according to different spacing varying from 12 to 16 cm in vertical and horizontal directions. A covering thickness of 4.5 cm is considered. Couplers between the walls and the slab are accounted for. A perfect bond between steel and concrete is adopted in the following.

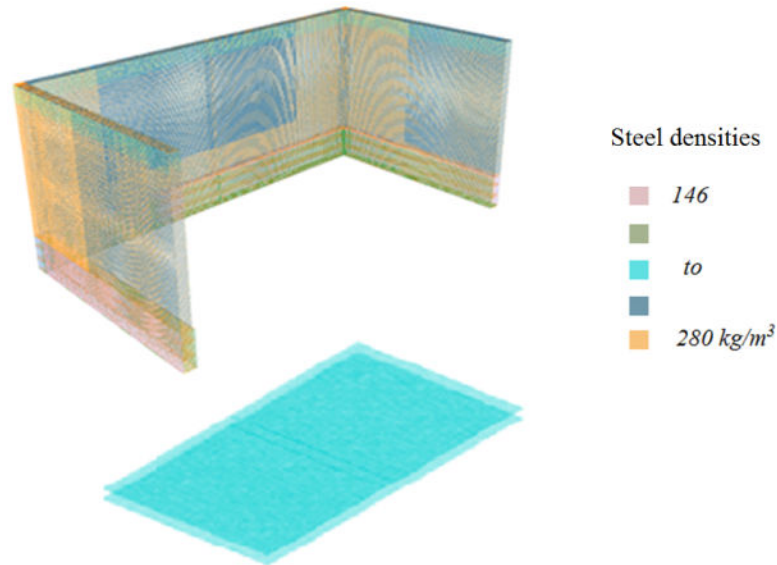


Figure 3.2 Meshed reinforcement of walls and base slab.

As in the last chapter, the symmetry with respect to the East-West axis allows reducing by half the analysed structure; a further mesh reduction with respect to the North-South axis would not be possible since solar radiation induces a non-symmetrical load with respect to this axis.

3.2.1 Restraint conditions

The external restraint conditions studied are listed below; no ground is explicitly considered in the first three conditions:

- RC1 all displacements are blocked at the interfaces ground-wall and ground-slab.
- RC2 at the interface ground-wall, the vertical displacements are blocked; all the displacements at the interface ground-slab are blocked.
- RC3 all horizontal displacements are free at the interface ground-slab.
- RC4 the ground is considered. All the displacements are blocked at the bottom of the ground

These restraint conditions have been defined to evaluate whether simplified boundary conditions applied directly on the wall and slab bottom surfaces may be sufficient to accurately describe the structure behaviour, when compared to the simulations considering also the ground. As such, the displacements at the interface between wall-slab and ground are blocked or kept free according to the different scenarios RC1-RC3. For the meshed ground, as recommended by (JCI, 2008), the ground lateral dimensions were twice the lateral dimensions of the structure and a depth of 10 m was considered (Figure 2.11).

3.2.2 Mechanical input data

The mechanical parameters identified for the concrete used in the simulations are listed in Table 3.1. The corresponding behaviour and experimental data used (provided by ONDRAF/NIRAS) in the determination of the parameters are plotted in Figure 3.3 and Figure 3.4 showing strength evolution and autogenous (with swelling) and basic creep strains. For the reinforcement, $E = 210$ GPa, $\nu = 0.3$ and $\alpha = 11 \times 10^{-6} \text{ K}^{-1}$ were taken as data provided by ONDRAF/NIRAS.

Table 3.1 Mechanical properties and parameters for concrete

E_∞	34.2 GPa	τ_{bc}^{kv}	4.5 day
ν	0.16	k_{bc}^{kv}	81 GPa
f_{t_∞}	4.2 MPa	η_{bc}^{kv}	160 GPa.s/s
n	0.45	τ_{bc}^{dp}	28 days
m	0.50	ξ_0	0.1
p	0.62	ξ_∞	1
		G_{ft_∞}	100 N/m

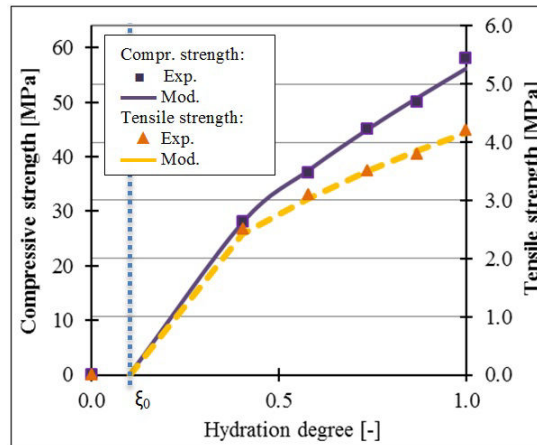


Figure 3.3 Determination of strength evolution: comparison against experimental data

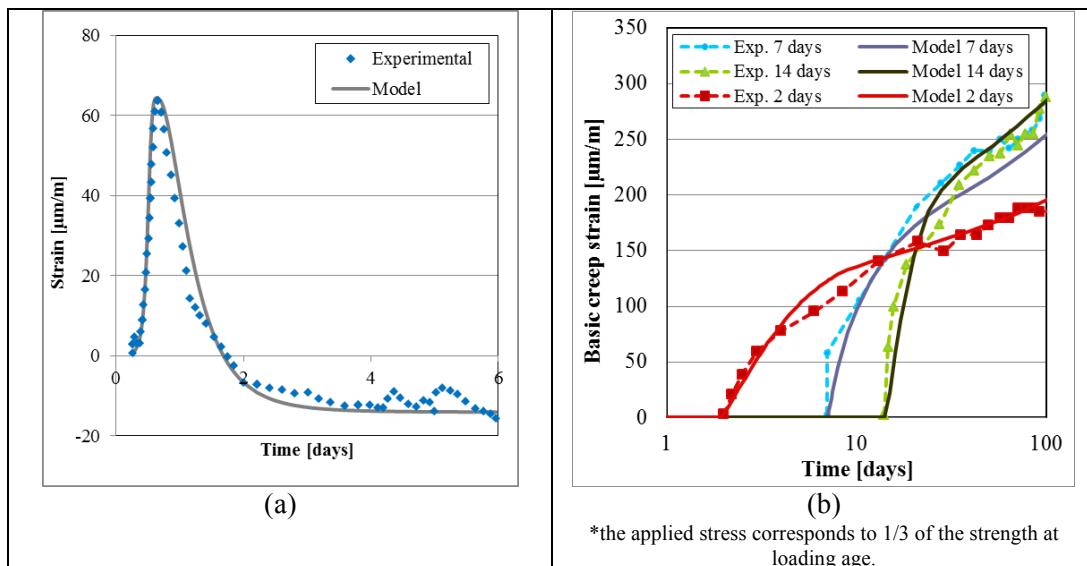


Figure 3.4 Autogenous (a) and basic creep (b) strains: fitted curves and experimental results

3.2.3 Structural assembly

The assembly of the new structural member is reproduced by first defining a material with low mechanical properties ($E = 10 \text{ Pa}$) in the place of the members to be placed. Then, after the phasing day, the properties of this ‘ghost’ member are updated to the actual values in the materials definitions. This procedure was verified, and the effect of the ‘ghost’ member is negligible on the older structural members.

3.2.4 Mechanical properties of the ground

An elastic constitutive behaviour is attributed for the different layers of the embankment (Figure 2.11, from sand-cement at the top to natural soil at the bottom). The Young modulus of the sand-cement, gravel base and compacted sand are provided by ONDRAF/NIRAS (Table 3.2). The other properties necessary for the modelling are estimated from literature data (they are marked with an asterisk in the Table 3.2).

Table 3.2 Elastic and thermal properties of the ground layers

	E [MPa]	ν [-]	α [K^{-1}]
Sand-cement	135	0.2*	7.10^{-6} *
Gravel base	140	0.2*	7.10^{-6} *
Compacted sand	20	0.2*	7.10^{-6} *
Natural soil	20*	0.2*	7.10^{-6} *

*(Farouki, 1981; Kersten, 1952; McIntosh and Sharratt, 2001)

3.3 RESULTS AND DISCUSSION

At first, the effects of mechanical and thermal boundary conditions are studied. Different scenarios are analysed in order to define a reference scenario to be studied accounting for damage and its coupling with creep.

Computations without damage take less than 3 days with a 12-cores, 2.8 GHz/96Go machine, for all the assembly frequencies. The time of computations with damage increases with β exceeding for instance 1 week for $\beta = 0.4$ with the same machine.

3.3.1 Influence of restraint and thermal boundary conditions: evaluation by the cracking index

3.3.1.1 External restraint conditions

The external restraint conditions presented in section 2.2.1 are studied here. No damage is accounted for in these simulations. The dead weight of the structure is considered in all cases.

An example of the highest eigenstress obtained for a given time is shown in Figure 3.5.

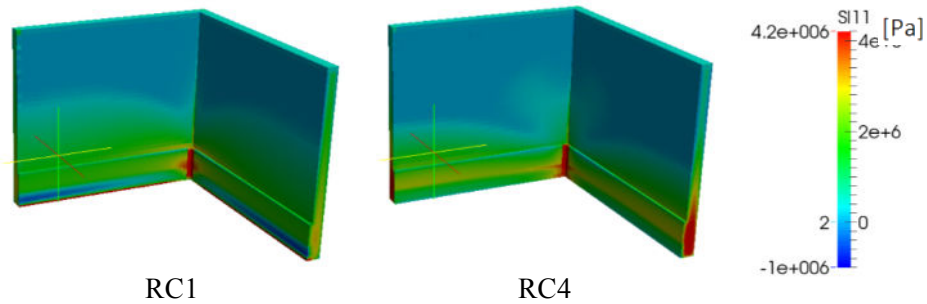


Figure 3.5 Highest eigenstress for RC1 and RC4 (other cases not shown for conciseness), $t = 15.31$ days, SET 3

Before the assembly, the maximum principal stresses reached are higher in the scenarios RC1 and RC2 compared to RC3 and RC4, but more zones exceeding the strength of the material are observed for RC3 and RC4. For RC1 and RC2, the higher stresses are reached mainly near the outer corner. From the analysis of the support reaction it is possible to identify the tendency of the points near the corners to move laterally due to the early-age solicitations. In RC1 and RC2 these displacements are restraint, which leads to the level of stresses observed (exceeding 6 MPa). In RC3 and RC4 these displacements are just partially restraint; so, a lower level of tensile stresses is observed. Regarding the CI (Figure 3.6 and Figure 3.7), before the assembly, cracking is observed ($CI > 0.54$) at the rising temperature period for all RC. With RC1 and RC2 CI exceeds 1 during most part of the simulations.

Regarding the walls, after the assembly of the slab, besides the external corners, the interface wall-slab rises as another region with higher stress level for RC1 and RC2 (Figure 3.6 and Figure 3.7). For RC3 the external corners and the internal corners are the most solicited regions (in tension). Finally, in the scenario with RC4, the bottom parts of the wall are the region with higher tensile stresses. The CI exceeds 0.54 for all the scenarios, after the assembly. The zones exceeding these values cross the bottom of the structure (Figure 3.6). If the cracking criterion adopted is $CI < 0.7$, no traversing zones exceeding the criterion are found. At later ages ($35 \text{ days} > t > 19 \text{ days}$), again the RC1 and RC2 present potential cracking; for RC3 and RC4, the CI remains below 0.54.

Regarding the slab, potential cracking is observed in the period of rising temperature and at later ages. The zones more likely to crack are located near the interface with the wall, especially near the internal corners. In these zones, the exposed surfaces and the interface with the ground are more solicited than the core of the slab. For all scenarios these zones where the greater tensile eigenstress exceeds 54% of the strength of the material do not cross the thickness of the slab. The tensile eigenstress at the interface regions between slab and walls are lower than in the upper part of the slab for RC1 and RC2 scenarios, while it is the reverse for RC3 and RC4 scenarios. This may be a consequence of the boundary conditions at the interface slab-ground: the displacements are totally blocked for the first two scenarios, while horizontal displacements are allowed for the last two ones.

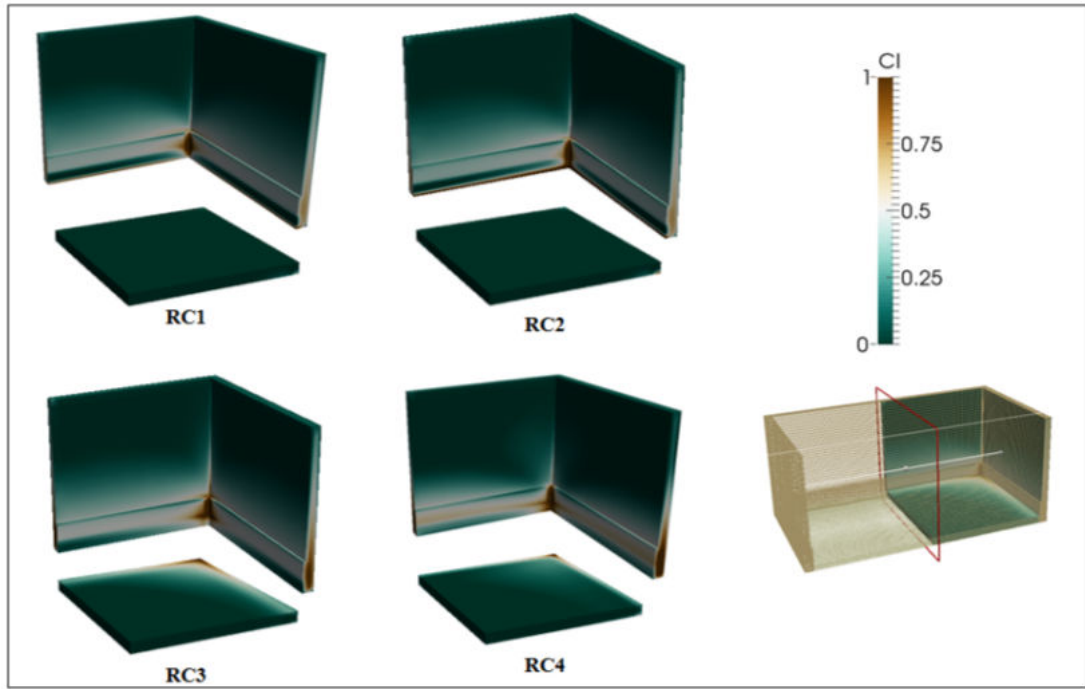


Figure 3.6 CI at $t = 15.31$ days

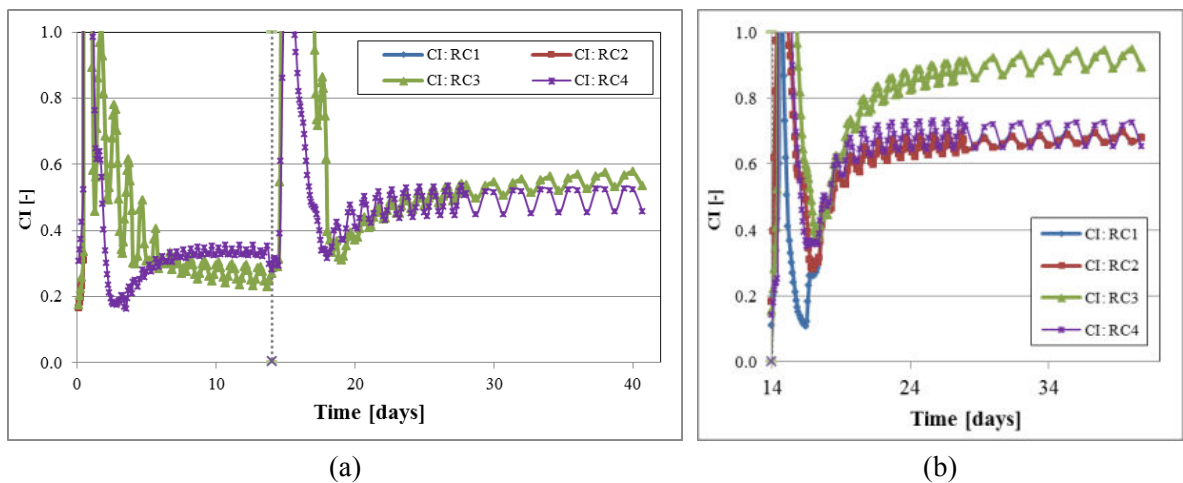


Figure 3.7 CI for the walls (a) and slab (b) according to the thermal boundary conditions

Tensile effort is observed in the interface ground-wall in the vertical direction for RC4, especially near the wall corners. For a real concrete structure, this kind of solicitation would hardly occur (the part of the structure inducing the tensile effort would “lift” instead, in a way there would be no contact anymore with the ground). Since the vertical displacements are blocked in RC1, RC2 and RC3, the same artefact is observed in the corresponding scenarios. The values of these tensile efforts remain low compared to the stresses developed in the structure.

The evolution of the CI (Figure 3.7) follows a similar tendency, which can be divided in four periods:

- 1) The rising of temperature within the wall ($t < 4$ days);

-
- 2) The first “delayed effect” period within the wall ($14 \text{ days} > t > 4 \text{ days}$);
 - 3) The rising of temperature within the slab ($19 \text{ days} > t > 14 \text{ days}$);
 - 4) The delayed effect period within the wall and slab ($t > 19 \text{ days}$)

Note that both periods of rising temperature (within the wall or the slab) are the most favourable to cracking development. The rising of temperature in the slab induces potential cracking in all scenarios. The interface wall-slab is particularly susceptible to cracking. Finally, the delayed behaviour, observed from 3 days after the assembly, also presents stresses exceeding the strength of the material.

Regarding the external restraint conditions studied, the scenarios in which the ground was not considered showed a mechanical behaviour significantly different from the scenario with the ground. Even if measures have been considered in order to establish a sliding support for the walls, a completely sliding condition does not seem realistic since the normal effort due, for instance, to the dead weight of the structure induces friction. The tensile stresses reached as well as the zones more likely to crack, as assessed by the CI, are quite different in the scenarios without the ground with respect to the scenario with the ground. This highlights the need of accounting for the ground in the thermo-mechanical analysis of the considered structure at early-age for more precisely assessing the cracking risks.

3.3.1.2 Internal restraint conditions: influence of the reinforcement

Although the reinforcement grants an increase in both rigidity and tensile strength of the composite concrete material, it also creates internal restraints to concrete (Cope et al., 2002; Sule and van Breugel, 2004). Taking RC4 as a reference, as can be seen in Figure 3.8, before the assembly of the base slab, the first eigenstress (defined here as the maximum value of the eigenstresses) is inferior in the scenario with no reinforcement compared to the scenario with the reinforcement. The additional restraint induced by the reinforcement leads to an increase of 2 orders of magnitude in the maximum value of principal stresses reached. After the assembly, the restraint provided by the base slab contributes to the increasing of the level of tensile stresses in both cases. It should be noted that the influence of the mesh size on these results has not been evaluated, though it may probably have some consequences as it is known that refining the mesh leads generally to a more accurate description of the strain and stress fields.

The reinforcement obviously plays an important role in increasing the overall tensile strength and stiffness of the structure, but at early age the reinforcement bars also induce local restraints that lead to an increase in the level of stresses reached. This conclusion is valid if the assumption of perfect bond between concrete and steel bars is adopted. The zones near the steel bars arise then as potential zones in which cracking may occur. As will be observed in the simulations accounting for damage in the next section, the damaged zones tend to follow the orientation of the reinforcement. More comprehensive studies (e.g. Kolani, 2012) are necessary to investigate these effects.

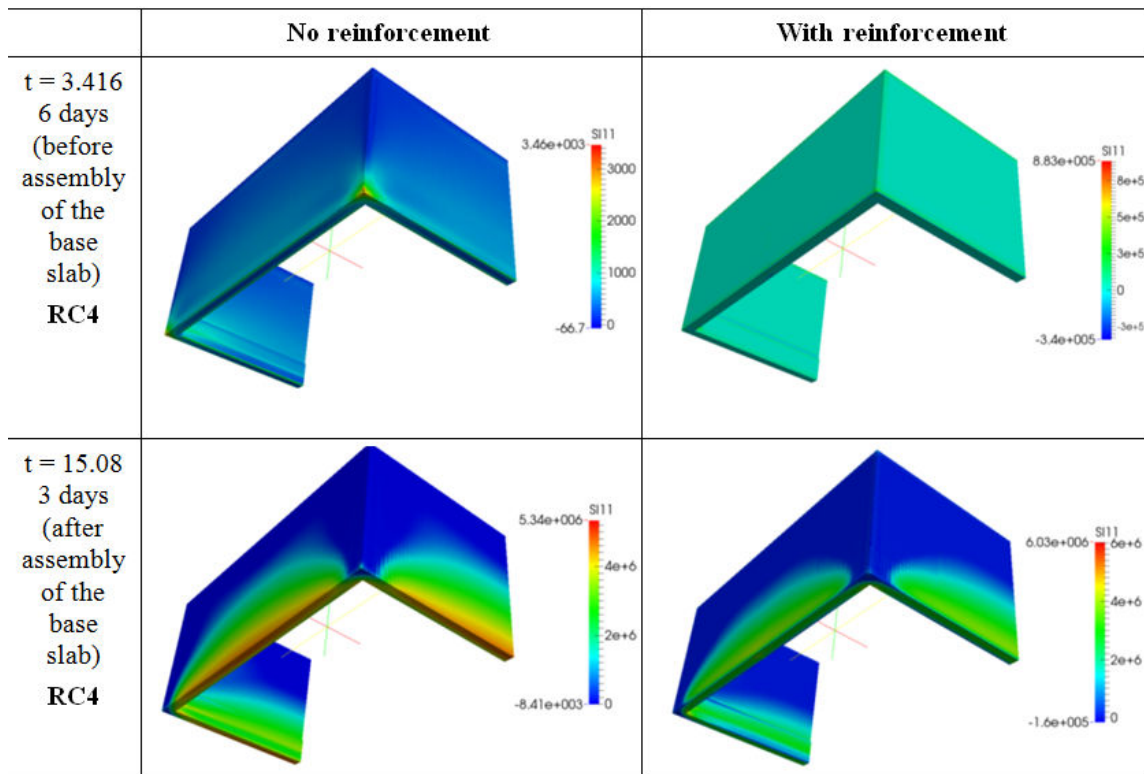


Figure 3.8 First eigenstress within the walls: scenario with (right) and without (left) reinforcement (no damage considered).

3.3.2 Influence of the thermal conditions

In this section we investigate the influence of the ambient temperature and its variations within a day as well as of the solar flux on the mechanical response. Three of the scenarios presented in Figure 2.14 are chosen, namely Set 2, Set 3 and Set 5. The first two sets correspond to August temperatures and the latter set corresponds to November temperatures. For all cases, no damage is considered and RC4 is adopted as it represents more realistic conditions.

- Influence of the ambient temperature:** The scenario with August temperatures Set 3 is compared to the scenario with November temperatures Set 5. The maximum eigenstress within the wall is shown in Figure 3.9 after the assembly of the slab. As expected, the tensile eigenstress developed in the November scenario is inferior to the ones in August scenario. Similar results are obtained for the first eigenstress within the slab (Figure 3.9). Lower compressive stresses are also found for these ages when the third eigenstress is analysed (not shown for conciseness). The CIs are shown in the Figure 3.10. The same critical periods defined in Section 2.3.1 are found for the November scenario. But the effects are delayed (for Set 5 the peaks of CI concerning the risings of temperature appear some hours after the Set 3 peaks) mainly because of the thermal activation of the phenomena involved. The CI obtained for T3 in the rising temperature periods are inferior to the ones obtained with Set 3. The same is observed at later ages. From this CI analysis, we

conclude that not surprisingly concreting at a month with November's temperature (and solar radiation flux) is more favourable to avoid cracking. Note, however, that because of the slow hydration kinetics in the November scenario, the evolution of the strength in this scenario is affected.

- **Influence of the solar flux:** Set 3 with varying solar flux is compared to Set 3 without solar flux. The tensile eigenstress developed in both scenarios in the periods of rising temperatures, within the wall and slab, are similar. Likewise, the corresponding CIs are similar (the corresponding curves are mostly superposed in Figure 3.10). For the conditions analysed here, the solar flux, even if it can induce higher temperatures gradients near the exposed surface and also influence the maximum temperature reached within the structure studied (Honorio et al., 2014a), does not affect significantly the mechanical response of the structure. As a consequence, although the solar flux induces an asymmetrical thermal load due to the daily varying exposition of the sun, the mechanical response remains quite symmetrical.

- **Influence of the variation of the temperature within a day:** The scenario with oscillating temperature within a day (Set 3) is compared to the scenario with constant ambient temperature (Set 2). The highest eigenstress within the wall and the slab is shown in Figure 3.9. The tensile eigenstress developed in both scenarios is similar for the wall and slab, with the average of the values in the oscillating scenario being slightly superior to the results of the scenario with constant temperature. The CI analysis (Figure 3.10) shows that the variation of temperature within a day may increase the CI in 0.05 for some cases. For these conditions, accounting for the oscillation of temperature is a more conservative measure since it can lead to higher CI and consequently probabilities of cracking.

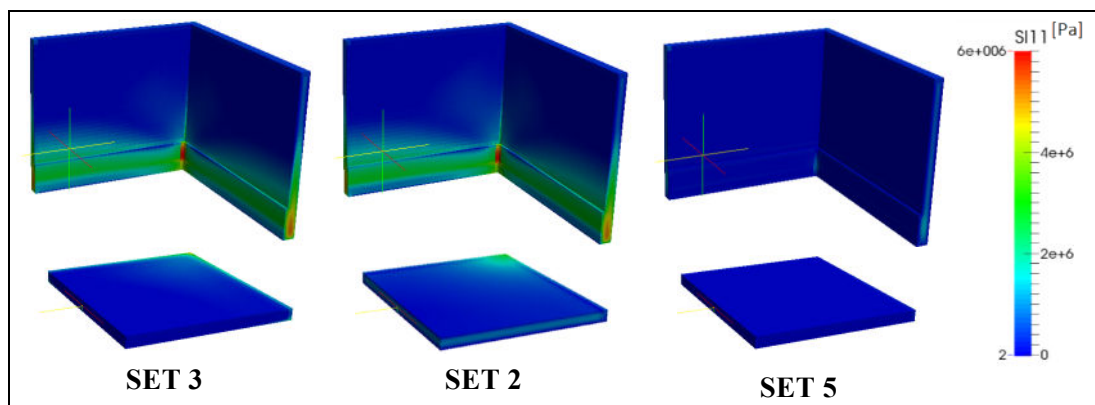


Figure 3.9 Highest eigenstress at $t = 15.08$ days according to the thermal boundary conditions, RC4

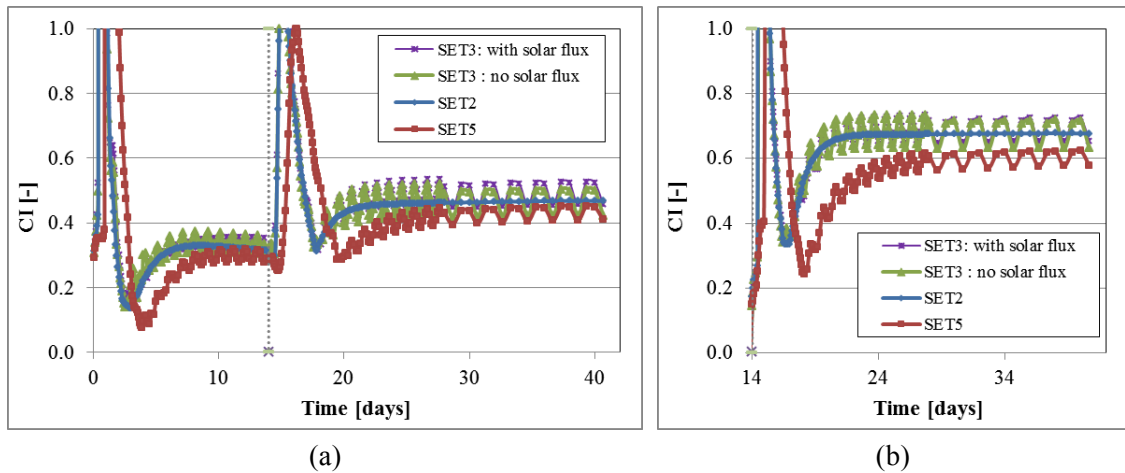


Figure 3.10 Cracking index for the walls (a) and slab (b) according to the thermal boundary conditions

According to the scenarios studied in this section, the influence of the ambient temperature (Set 3 vs. Set 5) is the factor affecting more strongly the mechanical response. The influence of the oscillation of the ambient temperatures within a day (Set 2) showed a less significant influence, which might be, though, non-negligible in some analysis.

3.3.3 Placing frequency

In the previous chapter (section 1.5.7), it was shown that for placing dates after 7 days (i.e. when almost all hydration reaction has been completed), the maximum temperature just shifted with respect to the placing day of the base slab assembly. Before 7 days, a small feedback of the wall temperatures on the base slab can be observed.

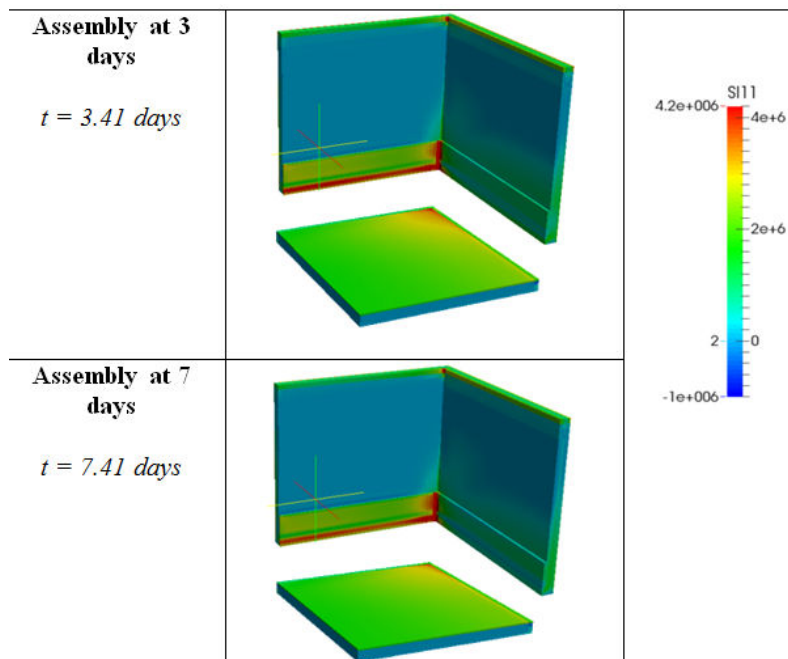


Figure 3.11 Highest eigenstress after the assembly (to be compared with the assembly at 14 days as shown in Figure 2.14 -Set 3), RC4

Although the temperature profiles were similar for the different placing dates, differences in the mechanical response may arise from the ageing aspect of the material which will act as a restraint condition to the new casted concrete. In the following the mechanical simulations presented are done with RC4 conditions, and at first no damage is considered.

The Figure 3.11 shows the highest eigenstress after the assembly according to the casting time. In spite of the different ages, the mechanical response in terms of this eigenstress and CI (not shown for conciseness) are similar for both cases. The response for the assembly at 3 days, compared to the scenario with assembly at 7 days, shows a slightly bigger region in which the stresses exceed the strength of the material. As expected, for the walls, the maximum value of the higher eigenstress decreases with the increase of the assembly time. High values of eigenstress are observed also at later ages. The CI and probability of cracking exceeds 1 for all scenarios in the periods of temperature rising and delayed effects. From these results, the assembly before 7 days is not recommended.

3.3.4 Simulations accounting for damage

The results concerning the simulations in which the damage model is used are presented here. As mentioned above, the simulations for evaluating the CI take into account only in a certain manner the loading history in the zones which have exceeded the strength of the material (mainly through the viscous effects), but do not describe any crack opening nor consecutive propagation. However, this index has the advantage of being easily computed and without adding supplementary non-linearities to the problem. On the other hand, with a damage model, the loading history in the zones which have exceeded the strength of the material is accounted for much more accurately, and in particular the resulting redistributions of stresses and strains are reproduced. These aspects add supplementary non-linearities to the problem making the analysis computationally more expensive. Moreover, a study about the coupling between damage and creep is performed. The focus of the present analysis is to identify the zones more likely subjected to cracking within the structure, and to evaluate the importance of the damage and its evolution with time.

As presented in Eq. (2.9), a strong coupling between damage and creep through the parameter β is proposed in the literature in order to more accurately reproduce the experimental results. Figure 3.12 shows the stress-strain response in uniaxial tension for some values of β and loading times; the rate of linear strain loading is $7.50 \times 10^{-9} \text{ s}^{-1}$. Note that stress and strain threshold so that damage initiates decreases with β for a given age of loading, and the stress threshold increases with the age of loading for a given β . This is due to the fact that β quantifies the proportion of (positive) viscoelastic strains entering in the calculation of the damage evolution through the equivalent strain (see Eq. 2.9): the greater β is, the greater this equivalent strain is, which leads to a higher damage value. Correspondingly, the post-peak part of the stress-strain response is significantly affected by β . The rate of loading also affects the response with respect to β . The stress-strain response for slow rates of

loading shows a stronger dependence of β than of the age of loading. This is expected for hydration kinetics much faster than the rate of loading. For faster rates of loadings, the response depends more strongly on the age of loading. For ages corresponding to low degrees of hydration (Figure 3.12, $\tau = 0.1$), damage occurs very early. Note, however, that in this case, part of the stiffness is restored due to the pursuit of hydration reactions.

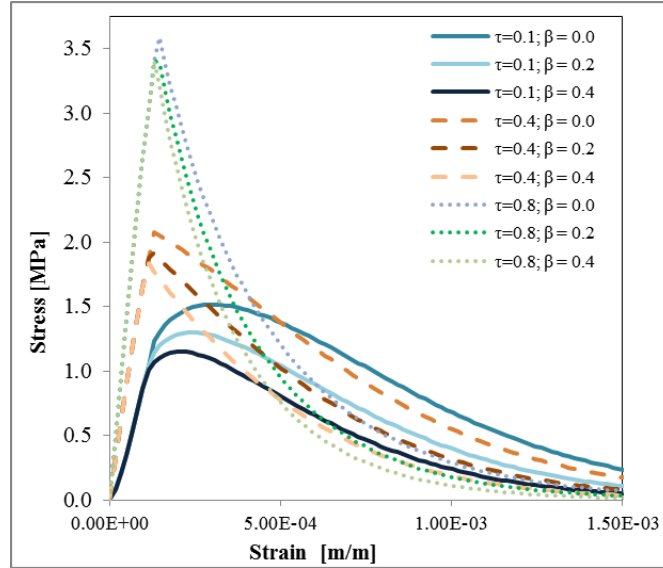


Figure 3.12 Uniaxial stress-strain response in tension as a function of β and ξ (τ indicates the ξ of the time at which the loading is applied), rate of strain loading = $7.50 \times 10^{-9} \text{ s}^{-1}$

We compare now simulations with $\beta = 0, 0.05, 0.1$ and 0.2 with simulations with no damage considered. Regarding the simulations of the structure, before the casting of the slab, similar stress states are observed in all cases.

After the casting, the additional restraint provided by the slab as well as the thermal strains and initial autogenous swelling lead to an increase of the highest eigenstress. The damage threshold is exceeded within the periods of rising of temperature (Figure 3.13). Similar damage patterns were also obtained by other authors (e.g. (Klemczak and Knoppik-Wrobel, 2015)). Although damage is observed in all scenarios, different behaviours take place as a function of β . As expected, the higher the value of β the higher the values of D and the larger the damaged regions. Most of the damaged zones in the $\beta = 0$ scenario are not percolating and are localized near the corners meaning that the confinement capacity of the structure still operates. For the $\beta = 0.05$ and 0.1 scenarios, a small volume of the structure is damaged, with part of these regions crossing the thickness of the structure (mostly in the interface with the ground). For the $\beta = 0.2$ scenario, the percolating zone is observed again in the interface with the ground, The most part of the damage volume occurs, though by the surface of the structure and in this case it is not percolating.

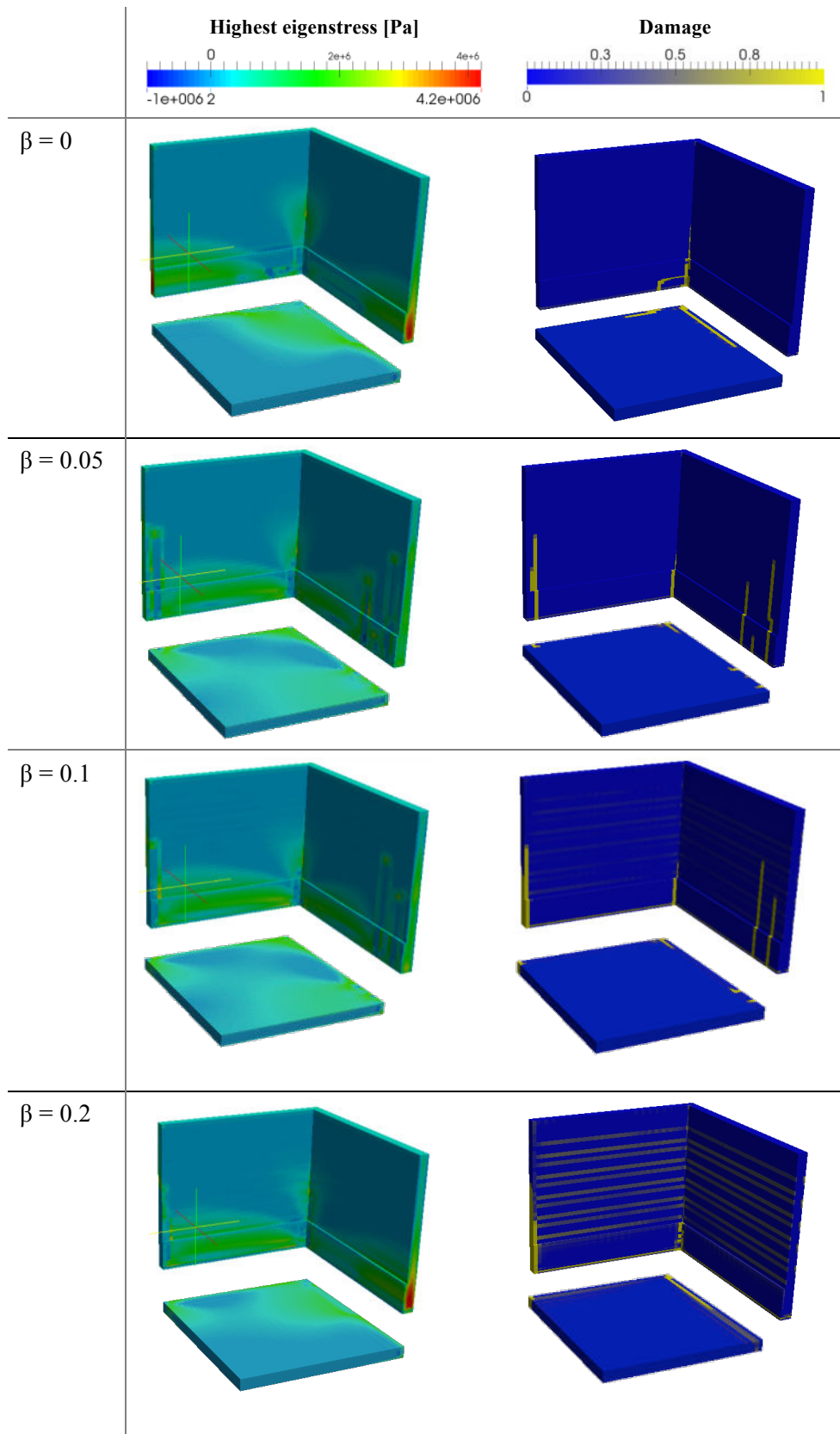


Figure 3.13 Highest eigenstress (left) and damage (right) at $t = 15.08$ days, RC4, SET 3

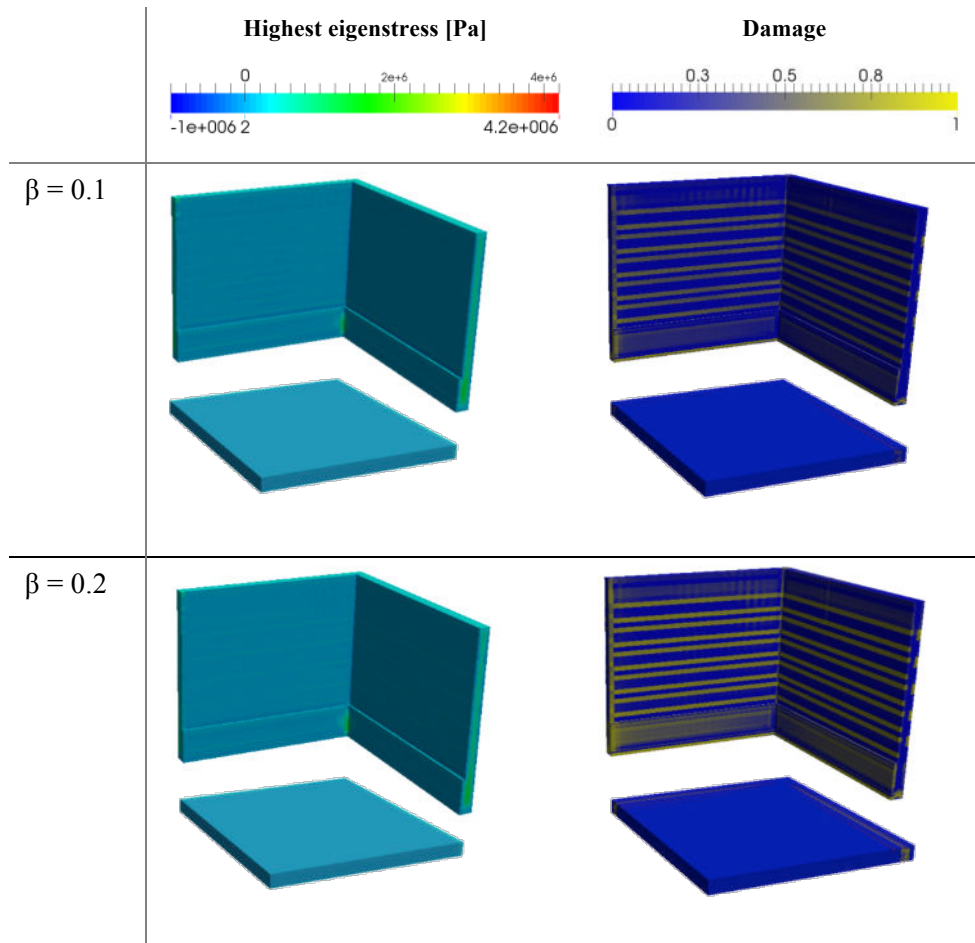


Figure 3.14 Highest eigenstress (left) and damage (right) at $t=15.08$ days for November temperatures (Set 5), RC4

We observe that the redistribution of stresses, induced by the presence of damaged regions, occurs locally in the neighbourhood and following the orientation of the reinforcements. As can be seen in Figure 3.13, for the $\beta = 0.1$ and 0.2 scenarios the damage patterns near the wall surfaces are strongly impacted by the presence of the reinforcement bars.

At later ages, only a slight evolution of the damaged zones is observed for $\beta = 0$ to 0.2 . For these cases, as already mentioned, the rising temperature periods are the most critical for damage and cracking formation. For a scenario with $\beta = 0.4$ (not shown for conciseness) a strong evolution of the damaged zones is observed; the same is expected for higher values of β .

From these results, it is clear that the parameter β plays an important role in the determination of the damaged regions. Its accurate identification would require tests such as the ring-test (Briffaut et al., 2011). Small variations of β can lead to different damage patterns. For $\beta = 0$, the damaged zones are localized near some corners; for $\beta = 0.05$ and 0.1 the damaged zones appear in the middle parts of the walls rising from the ground; for $\beta = 0.2$, the damaged zones are mostly limited to the exposed surfaces of the structure; in all cases the interface with the ground is damaged.

It is noteworthy that the obtained damage levels do not affect the overall integrity of the structure. However from the durability viewpoint, some scenarios may be questionable and specific measures should probably be done to guarantee the confinement function of the structure for very long periods, i.e. considering corrosion related issues, for example.

Figure 3.14 shows the highest eigenstress and the damage for November temperatures (Set 5). The response in terms of maximum principal stresses is similar in both cases. But compared to the scenario with August temperatures (Set 3), slightly more zones get damaged with Set 5. Also, the damaged zones are less localized with November temperatures. For $\beta = 0.1$, contrary to the Set 3 case, just a small part of the damaged zones reaches $D = 1$. For, $\beta = 0.2$, more zones reach $D = 1$. The damage occurs essentially on the exposed surfaces, which, because of the low ambient temperatures of November, have its strength evolving slower than in the Set 3 scenario. From these results, we infer that the most favourable scenario regarding the concreting temperatures, as assessed by the visco-damage model used here, can just be defined for a specific β .

3.3.5 Crack opening

The scenarios with more damaged volume ($\beta = 0.2$) obtained in the previous section for the August and November temperatures are analysed in terms of cracking opening evaluated as defined in section 2.1.6. The cracking opening is assessed by the maximum value of the crack opening tensor in the principal basis (denoted as EPXX). The cracks exceeding $1 \mu\text{m}$ are shown in Figure 3.15. Note that, for some classes of exposition $300 \mu\text{m}$ is defined as the maximum cracking opening allowed (EN 1992-1-1, 2004: table 7.1N). The slab does not present crack opening exceeding $100 \mu\text{m}$ for the analysed cases.

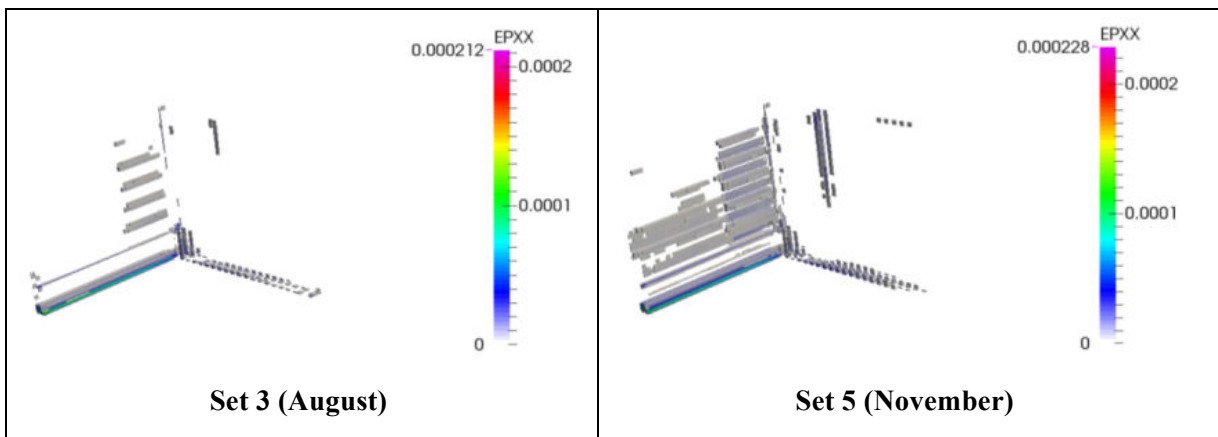


Figure 3.15 Cracking opening at 31.33 days (RC4, $\beta = 0.2$). EPXX [m] is the maximum value of the crack opening tensor in its principal basis

The zones with cracking opening exceeding $100 \mu\text{m}$ are the same for August and November scenarios. The maximum opening values are 229 and $212 \mu\text{m}$ for November and August scenarios, respectively. In both cases these zones are localized at the interface with the ground and are not

percolating. Note however that the patterns of cracking opening not exceeding 100 μm (not shown for conciseness) are different for each scenario. The maximum value of the cracking opening and the volume of finite elements presenting cracking opening exceeding 100 μm for November is slightly superior to the ones observed in August scenario. So, adopting $\beta = 0.2$ we may conclude that the possible cracking taking place within the structure studied does not affect substantially its containment performance.

3.4 CONCLUSIONS AND PERSPECTIVES

In this chapter, we have presented numerical simulations for evaluating the mechanical response at early age of a massive reinforced concrete structure. The model proposed by (Benboudjema and Torrenti, 2008) was employed, based on a chemo-thermo-elastic-damage approach (smeared crack) in which a coupling between creep and damage is introduced. At first, simplified simulations considering different restraint conditions and thermal scenarios are carried out in a less computationally costly approach without accounting for damage. These first analyses allowed identifying the most unfavourable scenarios through the calculation of a CI. These scenarios are subsequently analysed in simulations accounting for damage, in which the coupling between creep and damage is highlighted. The main following conclusions can be drawn from the simulations results and their analyses:

- Regarding the external restraint conditions studied, the scenarios in which the ground was not considered showed a mechanical behaviour significantly different from the scenario with the ground. The vertical displacements which are not totally restricted in the scenario with the soil play an important role. Correspondingly, the tensile stresses reached as well as the zones more susceptible of cracking, as assessed by the CI, are quite different in the scenarios without the ground with respect to the scenario with the ground. These points out the need of accounting for the ground in the thermo-mechanical analysis at early-age.
- Accounting for the solar flux radiation, in the conditions described here for Dessel region, does not affect significantly the mechanical response. Accordingly, the asymmetrical thermal loading induced by the solar radiation seems negligible. Note however that accounting for the solar flux is important in the determination of the maximum temperature reached within the structure especially for the structure studied here where no isothermal or adiabatic regions of temperature rising can be very well defined (Honorio et al., 2014a). As a consequence, the analysis presented here could have been performed accounting only for a quarter of the structure instead of the half part, for a much lesser computational cost and very close results.
- Regarding the influence of the concreting temperature, as expected, the simulation with November temperatures is more favourable for avoiding cracking as assessed by the CI. By contrast, in the simulation accounting for damage, compared to the scenarios with August

temperatures (Set 3), more zones get damaged and the damaged zones are less localized. It is also shown that the most favourable scenario regarding the concreting temperatures, as assessed by the visco-damage model used here, can just be defined for a specific β .

- The comparison of the scenario with varying ambient temperature within a day (Set 3) and constant temperature (Set 2) shows that a variation of 0.05 in the CI may arise from the oscillation of the temperature. Accounting for this oscillation is then a relevant issue to a reliable analysis at early age. The simplified assumptions regarding this aspect do not seem appropriate.
- The coupling between damage and creep affects directly the mechanical response. A strong dependency of the parameter β is observed. Small variations of β can lead to different damage patterns. As expected, for values of β near to 0 the damage evolves less than that for higher values of β . Note that β must be determined experimentally for the material studied so that a more accurate analysis could be effectively performed.
- With the damage analysis, most part of damaged zones is inscribed within the zones with $CI > 0.54$. The exception is the damage occurring on the surface of the upper part of the walls. But, as shown in Section 3.3.5, this surface damage leads to a negligible crack opening. Note also that, in general, these damaged zones occur in the vicinity of the reinforcement. A more precise identification of these zones as well as an estimation of the crack opening are possible with the damage model. This allows concluding that the CI analysis provides a reasonable first indication of the global zones more likely to crack, especially if β is not known.

As perspectives, we suggest the consideration of measures to prevent or reduce cracking, in particular at the wall-slab junction. In this case increasing the reinforcement in this zone could be an interesting measure, but which would deserve more investigations since the same reinforcement may also induce supplementary restraint. Further, in order to avoid the artefact identified in Section 2.3.1, the interface ground-structure could be modelled with sliding (Coulomb) elements. The influence of the internal restraint would also deserve an analysis accounting for the influence of the mesh size, so that the local effects may be more precisely identified. The effects of the formwork on the mechanical behaviour would merit also a comprehensive study. Additionally, the effects of early age damage on the durability at long-term as well as the coupling with long-term simulations are suggested as future developments.

PART II. ESTIMATION OF AGEING PROPERTIES FROM THE PASTE COMPOSITION

An investigation combining numerical and analytical tools is proposed in order to estimate the ageing linear viscoelastic properties of cement-based materials at early age within a multiscale framework. The goal is to contribute to the prediction of the mechanical behaviour at early age of different cementitious materials at the macroscale from the knowledge and understanding of some mechanisms occurring at the microscale. At first, a simplified mechanism-based hydration kinetics model is presented. Secondly, analytical homogenization schemes are rederived in an ageing linear viscoelastic framework to allow estimating early-age properties. Then, a combined numerical and analytical approach is used to estimate the mechanical properties of cement-based materials. Finally, the properties estimated with the multiscale approach are confronted with the phenomenological description used in the Part I.

4. MODELLING HYDRATION

This chapter is based on the papers Honorio et al. (submitted; 2014b).

As already mentioned before, a relevant description of hydration kinetics is necessary in the study of cement-based materials at early-age. Heat release as well as transfer and mechanical properties evolve as a function of the degree of hydration. Also, the viscoelastic behaviour is dependent of the ageing processes imposed by the evolution of the material due to hydration reactions.

Microstructure-based models have been developed to study cement hydration (Biernacki and Xie, 2011; Bishnoi and Scrivener, 2009a; Bullard et al., 2011; Masoero et al., 2013; Thomas, 2007) and have the advantage of providing a more precise representation of the microstructure at the level of the cement grain as well as a more precise assessment of the influence of the particle size distribution on the kinetics. However, these models may be computationally expensive to be coupled with multiscale and multiphysics approaches necessary to determine the behaviour of a concrete structure at early-age.

Empirical or simplified analytical laws have often been used instead (Bezjak and Jelenić, 1980; Krstulović and Dabić, 2000; Pignat, 2005), but generally these laws do not completely and

accurately capture some important mechanisms driving cement hydration, such as the influence of the PSD and additional materials on kinetics. Moreover, since the main mechanisms are not explicitly taken into account, such kind of models cannot in general be directly extrapolated to other scenarios of interest with, for example, different compositions, w/c or PSD. This motivates the development of an analytical model that would be able to capture the main driving mechanisms underlying the kinetics of cement hydration but remaining sufficiently simple to be easily coupled with more complex analyses.

The identification of the relevant mechanisms to be taken into account may be a complex task because some key phenomena concerning the mechanisms of cement hydration remain not completely understood. Regarding the hydration of alite, which is the main constituent of Portland cement (Taylor, 1997), five periods are generally identified (Bullard et al., 2011): 1) initial dissolution controlled, 2) latent, 3) acceleration, 4) deceleration and 5) slow reaction periods. Nucleation and growth are deemed to be the driving mechanisms of latent, acceleration and at least the initial part of the deceleration period (Bullard et al., 2011). Diffusion controlled reaction is deemed to drive the slow reaction phase (Bullard et al., 2011). The transition from deceleration to slow reaction is still a controversial subject (Biernacki and Xie, 2011; Bishnoi and Scrivener, 2009a). The decrease of available surface for reaction, local variations of concentration on the grain surface and the space filling has been pointed out as factors affecting the deceleration (Scrivener and Nonat, 2011).

The behaviour at late ages, especially within the first 28 days is of practical interest for constructions in concrete, since the most part of important properties for the structural design such as the Young modulus and the strength develops in this stage. These properties have been often described as a function of the degree of hydration (De Schutter, 1999). However, most of the studies on cement hydration kinetics focus on the early hydration (up to the deceleration period); the description of hydration at long term has been much less studied (Scrivener and Nonat, 2011). For common Portland cements with no additions, the deceleration period starts within the first day and after 28 days only about 20% remains non-hydrated (mostly belite phase) (Scrivener and Nonat, 2011). This highlights the importance of a kinetic description accounting for the potential progress in hydration reactions within the slow reaction period.

The PSD of cement grains, as generally occurs in heterogeneous solid-state kinetics, is reported to affect the description of cement hydration (Bishnoi and Scrivener, 2009a; Masoero et al., 2013; Scrivener and Nonat, 2011; Taylor, 1997; Termkhajornkit and Barbarulo, 2012). Since the range of grain sizes is very large in cements (Scrivener and Nonat, 2011), the influence of the PSD on the kinetics of hydration should be explicitly taken into account in a relevant model (Scrivener and Nonat, 2011). Some works intend to reproduce this influence by accounting for the surface area of the reactive powder in question (Lin and Meyer, 2009), but according to the mechanisms considered this property seems not to be sufficient to describe accurately the actual influence of the

PSD on the kinetics. Among the different approaches proposed so far in the literature, we highlight the reference (Termkhajornkit and Barbarulo, 2012) in which the PSD of cement and supplementary cementitious materials (SCM) are taken into account explicitly by means of a discrete approach; no mechanistic approach is used to determine the rate at which the particles are consumed, though. Nonat and coworkers propose a model in which the PSD is considered in order to determine the surface of the growth; the model parameters, namely, the number of initial nuclei, the parallel growth rate, the perpendicular growth rate and a coefficient describing the permeability of the C-S-H layer formed around the grain, are fixed by the physical chemistry aspects (Scrivener and Nonat, 2011). This approach requires, however, a more fundamental understanding of the thermodynamic aspects related to the different species present in the reacting system, which is beyond the scope of an early-age concrete structure analysis.

Hydration occurs often in a confined zone (Scherer, 2012), so the space availability for products to grow potentially affects the kinetics. A microstructure-based model developed by Bishnoi and Scrivener (Bishnoi, 2008; Bishnoi and Scrivener, 2009a) describes, from the geometry of cement particles, the hydration following different kinetics mechanisms. These authors propose space-filling process coupled with boundary nucleation and growth to explain the deceleration period rather than a transition of a diffusion-controlled reaction. Since the geometry is explicitly represented, the space available to products growth and the impingements can be accounted for directly. To account for the space availability in an analytical way, an exponential box can be used as proposed by Biernaki and Xie (2011). These authors employ the boundary nucleation and space-filling growth and propose the exponential box in order to account for the interaction with the neighbouring particles in a one-particle-based model. The size of this zone is a function of the w/c ratio and the particle size. Additionally, the idea of a reaction zone has been investigated by Masoero et al. (2013) within a microstructure-based model. These authors define the confined zone based on a fixed distance from the dissolving surface. In this case, differently from Biernaki and Xie (2011), the confined zone is not a function of the w/c, but is rather used as a fitting parameter. The confined zone as defined by Biernaki and Xie (2011) represents the overall space available for products to grow according to space left by water in the system. On the other hand, the confined zone as defined by Masoero et al. (2013) restricts the available space to a zone near the particle reacting, independently, *a priori*, of the particle size and w/c. In this latter sense, a characteristic length defining this confined zone would be related to hydration. Mechanisms related to diffusion of the species resulting from the dissolution of clinker minerals could explain the existence of such a zone, which is coherent with the idea of boundary nucleation and growth.

Diffusion-controlled growth is deemed to drive slow reaction period. Different diffusion-controlled kinetics were used to describe cement and clinker minerals hydration (Bezjak and Jelenić, 1980; Fujii and Kondo, 1974; Gartner et al., 2002; Knudsen, 1980; Krstulović and Dabić, 2000; Pignat, 2005; Taplin, 1968, 1960). Fujii and Kondo (1974) equation, which is derived for a specific

particle size and accounts for a transition time from which diffusion becomes the rate limiting process, is extensively used to describe late hydration (Gartner et al., 2002).

4.1 OBJECTIVES

We propose to model (semi)-analytically the kinetics of hydration by means of a mechanistic approach. Because of the inherent complexity of some upscaling methods used in the next chapters, a simple analytical description of hydration is desired. Additionally, as highlighted in the introduction, a ‘mechanistic’ approach, compared to a phenomenological one, allows generalizing the response for different cement formulations. In this chapter, a simple analytical approach comprising early and late hydration is proposed, in which key mechanisms are explicitly accounted for. These mechanisms are boundary nucleation and space-filling growth in a fixed confined zone for early hydration and diffusion-controlled kinetics for late hydration combined in a formulation in which the PSD is explicitly considered. Differently of previous works, to account for the confined zone effect, we combine two different but complementary approaches: the exponential box and the fixed length defining the reaction zone as proposed by Biernacki and Xie (Biernacki and Xie, 2011) and Masoero et al. (Masoero et al., 2013), respectively. Also, the developed formulation allows keeping the same set of parameters for different w/c and PSD configurations, which seems more physically founded.

We focus on the acceleration and deceleration periods of alite hydration, at first. The influence of the PSD of cement grains is highlighted. The model is fitted to experimental data from calorimetry tests (Costoya, 2008). Then, we propose an extension of the model to a multiphasic system in order to study cement hydration. Early and late hydration are considered. The late hydration is driven by diffusion-controlled kinetics. Finally, the model is validated against calorimetric data for the cement hydration (data for the same cement as obtained by Craeye (2010) and in specific tests done in the parallel experimental campaign for cAt project). Because many aspects are involved in cement hydration, some simplifying hypotheses are adopted and will be detailed along the chapter. Other aspects which may affect the kinetics, such as flocculation (Chamrova, 2010) and shear effects (Berodier and Scrivener, 2014), are not considered.

4.2 MECHANISMS DRIVING THE KINETICS

In this section, the mathematical formulations of the different mechanisms are presented. The strategy to model the interaction with the neighbouring particles, the influence of the PSD and of the temperature is described. The model is developed for C_3S hydration based on the formation of C-S-H, the main reaction product. The extension is straightforward for C_2S hydration, for which some rate constants may take into account the more limited reactivity of belite compared to alite.

4.2.1 Boundary nucleation and growth (BNG)

In boundary nucleation and growth models, the nucleation and growth is favoured on a specific site near the boundary of the untransformed phase rather than homogeneously in the reacting domain (Balluffi et al., 2005). Heterogeneous nucleation occurs in competition with homogeneous nucleation; the mechanism with the faster kinetics dominates (Balluffi et al., 2005). The presence of special sites in the material that are capable of lowering the critical energy needed to form a nuclei favours the heterogeneous nucleation rather than the homogenous one (Balluffi et al., 2005). A hypothesis generally adopted in heterogeneous kinetics models, in which concurrent nucleation and growth occur, is the stochastic independence of the nucleation events, i.e. any particular nucleation event in the untransformed material is not influenced by any other nucleation event (Balluffi et al., 2005). This means that the likely impingement between hydrates growing in neighbouring particles is generally not taken into account (Scherer et al., 2012).

4.2.1.1 Cahn's BNG formulation

Different authors applied Cahn (1956) BNG model to cement hydration (Bishnoi and Scrivener, 2009a; Bullard et al., 2011; Honorio et al., 2014b; Kumar et al., 2012; Masoero et al., 2013; Scherer et al., 2012; Thomas, 2007). Good agreement with experimental data has been observed for the acceleration and early deceleration periods. The formulation accounts for the superposition of hydrates growing near to each other but does not account for impingements with growing products of neighbouring particles (Scherer et al., 2012). The model remains explicit and may account for anisotropic and symmetrical growth (see (Scherer et al., 2012) for more details).

Assuming that the anisotropy in the growth is small, in a BNG model with a constant number of nuclei, the degree of transformation is (Scherer et al., 2012):

$$\xi_{\text{NG}}(t) = A \left[1 - \exp \left[-2 k_g (t - t_N) \left(1 - \frac{F_D[k_s(t - t_N)]}{k_s(t - t_N)} \right) \right] \right] \quad (4.1)$$

where t_N is the nucleation time and F_D is the Dawson function defined by $F_D(x) = \exp(-x^2) \int_0^x \exp(y^2) dy$. The parameter A is the ratio between the chemical shrinkage and the fraction of the initial volume that is occupied by the hydrates (Scherer et al., 2012). The constants k_g and k_s are function of the rate of nucleation N_s , the isotropic growth rate G (see (Scherer et al., 2012) for the anisotropic case) and the parameter r_g standing for symmetrical ($r_g = 1$) or non-symmetrical ($r_g = 1/2$) growth:

$$k_g = r_g O_V^B G; \quad k_s = G \sqrt{\pi N_s} \quad (4.2)$$

The area of substrate per unit volume of paste O_V^B , as defined by (Scherer et al., 2012), is function of the surface area of the grain S , water to cement ratio w/c , and the densities of water and of the grain, ρ_w and ρ_c , respectively:

$$O_v^B = S/V \text{ with } V = \left(\frac{w/c}{\rho_w} + 1/\rho_c \right) \quad (4.3)$$

Note that $\xi_{NG}(t)$ is a function of the surface area of the reactive powder, but does not depend directly on the PSD of this powder (i.e. grains with different PSD but with the same surface area might have the same evolution of ξ_{NG}).

Biernacki and Xie (2011) highlight, though, that results with this formulation may be inconsistent with the stoichiometry and microstructural transformations related to alite hydration. Actually, for bulky products with constant density growing in- and outwards, the resulting particle size (anhydrous core + product layer) would be twice the size of the original unreacted particle. According to these authors, the formulation would not also be in agreement with the theoretical radius of a single hydration particle proposed by (Pommersheim and Clifton, 1979). Additionally, space-filling, which is deemed to play an important role in hydration kinetics (Bishnoi and Scrivener, 2009a; Hoover and Ulm, 2015), are not accounted for in this formulation. A BNG formulation accounting for these aspects is developed in the next section.

4.2.1.2 Boundary nucleation and space-filling growth

Bishnoi and Scrivener (2009) proposed a formulation in which the nuclei can form due to homogeneous nucleation in a specific volume between the initial radius R_0 of the reacting particle and $R_0 + g_2 t$, where g_2 is the rate of growth in the normal direction with respect to the surface of the particle. In this case, the mass of product formed $M(t)$ is a function of the age of the product:

$$M(t) = \int_{R_0}^{R_0 + g_2 t} 4\pi r^2 \left(1 - \exp \left[-k_{NG} \left(t - \frac{r - R_0}{g_2} \right)^n \right] \right) f_{free} \rho(t, r) dr \quad (4.4)$$

where k_{NG} is the rate constant and f_{free} is the fraction of outer surface of the product that is available for growth due to impingement of the neighboring particles. The term $\frac{\rho(t, r)}{\rho_{max}}$ accounts for the space-filling process of the product situated at the radius r . As detailed further (Section 4.2.6), the degree and rate of hydration can be estimated from M and the stoichiometric relations. *A priori*, the Eq. (4.4) applies for products forming around the reacting grain. The space-filling aspect can be switched off for bulky products. Other strategy is to consider a homogenized layer of products forming around the particle in which a main phase presents space-filling. This strategy is adopted in the following.

The rate constant k_{NG} is a function of the rate of growth in the directions parallel to the surface, the dimensionality of the reaction n , the rate of nucleation and initial number of nuclei (Bishnoi and Scrivener, 2009a; Scherer et al., 2012). This rate constant can be estimated as a function of the time at which half the surface of the particles is covered $t_{1/2}$ (Bishnoi and Scrivener, 2009a):

$$k_{NG} = \frac{-\text{Ln}(0.5)}{t_{1/2}^n} \quad (4.5)$$

$t_{1/2}$ gives an indication of the time corresponding to the peak in the rate curves.

4.2.2 Space-filling

A process of ‘densification’ of C-S-H has been proposed to explain the deceleration period of alite hydration (Bishnoi and Scrivener, 2009a). This mechanism was suggested to justify the evolution of C-S-H surface areas (Bentz, 2006; Daimon et al., 1977; Jennings, 2004; Powers, 1960; Tennis and Jennings, 2000). Experimental results have further been used to support this mechanism (Muller et al., 2012). Following Bishnoi and Scrivener (Bishnoi and Scrivener, 2009a) approach, we assume in this paper that the C-S-H surface area varies linearly with the rate of change of density, which takes the simplified form:

$$\rho(t, r) = \rho_{max} - (\rho_{max} - \rho_{min}) \exp \left[\frac{-k_{DEN}}{\rho_{max} - \rho_{min}} \left(t - \frac{r - R_0}{g_2} \right) \right] \quad (4.6)$$

where k_{DEN} is a rate constant; ρ_{max} and ρ_{min} are the maximum and minimum density of the C-S-H, respectively.

4.2.3 Interaction with neighbouring particles and reacting zone hypothesis

In non-dilute systems the growth of neighbouring particles disturbs the growth at the local level. Bishnoi and Scrivener (2009) account for this effect with the parameter f_{free} in Eq. (4.4). Biernacki and Xie (2011) interpreted this parameter as corresponding to a definition of a representative volume of the system. These authors propose an exponential box, in which they apply Avrami correction to the ensemble of particles. The equivalent system radius R_{lim} can be obtained from the w/c ratio by:

$$R_{lim}^3 = R_0^3 \left(1 + \frac{w}{c} \frac{\rho_c}{\rho_w} \right) \quad (4.7)$$

The extended volume fraction is given by:

$$f_v^* = \frac{r^3 - R_0^3}{R_{lim}^3 - R_0^3} \quad r \geq R_0 \quad (4.8)$$

Applying Avrami correction, Biernacki and Xie (Biernacki and Xie, 2011) propose then to use:

$$f_{free} = e^{-f_v^*} \quad (4.9)$$

According to the last equations R_{lim} determines a reacting zone that would increase indefinitely with the w/c ratio. Masoero et al. (2013) propose that, for alite, C-S-H forms only in a fixed reaction zone close to the surface of the reacting particles. This zone, *a priori*, does not depend

on the space available as defined by the w/c ratio. In their simulations, they found a reaction zone limited to $e_{lim} = 0.4$ to $1 \mu\text{m}$ from the surface of the reacting grain. This reaction zone hypothesis leads to a kinetics that is poorly affected by the w/c during the early hydration stages (Masoero et al., 2013). Then, as already mentioned the confined zone defined by Biernaki and Xie (2011) results from the space available for products to grow, while the one defined by Masoero et al. (2013) constrains this available space in a zone near the reacting particle. The existence of such a zone may be justified by diffusive phenomena due to the dissolution of clinker minerals.

Here, we propose to combine both definitions of confined zone. The idea is to limit the reacting zone by defining a superior bound $R_0 + e_{lim}$ to the confined zone. Differently from Masoero et al. (2013) who characterized the confined zone from the reacting surface, here this zone is defined with respect to the initial surface of the grain. So, we introduce then a constraint to the denominator in Eq. (4.8):

$$R_{lim} \leq R_0 + e_{lim} \quad (4.10)$$

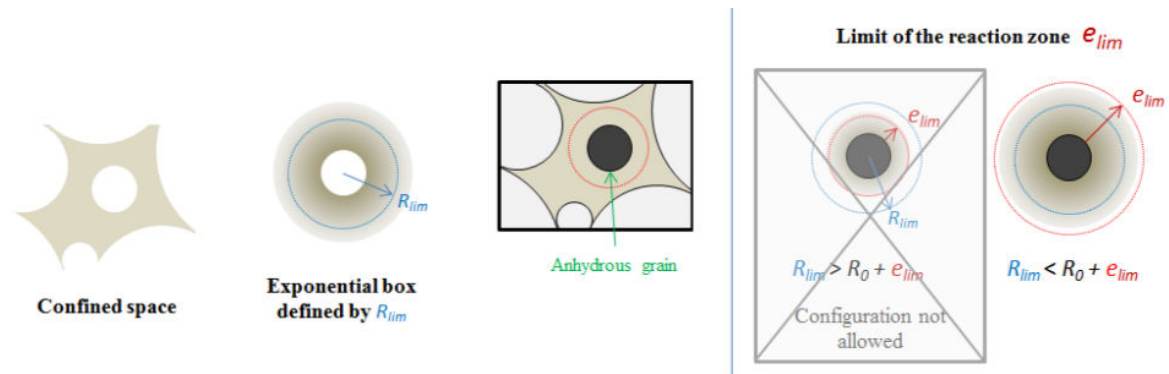


Figure 4.1 Confined reaction zone

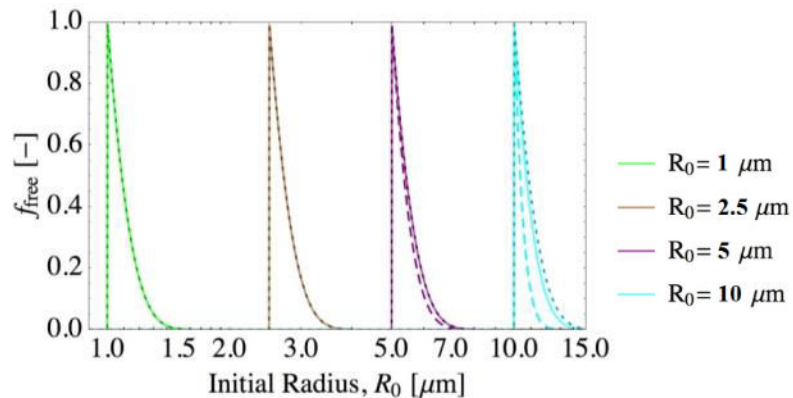


Figure 4.2 f_{free} for different particles sizes and reaction zones thickness: $e_{lim} = 0.5 \mu\text{m}$ (dashed lines), $e_{lim} = 1 \mu\text{m}$ (full lines) and $e_{lim} = 10 \mu\text{m}$ (dotted lines).

Figure 4.1 shows a schematic representation of the concepts of the exponential box and fixed reaction zone. Note that, due to the constraint in Eq. (4.10), no effect of the fixed e_{lim} is observed if $R_{lim} < R_0 + e_{lim}$: in this case R_{lim} , as defined by Eq. (4.7), determines alone the confined zone. In the opposite case $R_0 + e_{lim}$ defines the limit of the confined zone. Figure 4.2 shows the evolutions of f_{free} resulting from different initial particle radii and thickness of the reaction zone. As expected, we observe that the effects of e_{lim} on f_{free} increase with the size of the particle.

The degree of hydration ξ_{BN} due to boundary nucleation and space-filling growth (BN) can be computed by means of the stoichiometric relations of the involved reactions and the molar volumes of products and reactants. As it will be further detailed, for alite hydration, this computation involves some hypothesis regarding the composition and porosity of C-S-H as well as the presence of trapped water. The mass of product formed outwards expressed by Eq. (4.4) is used to compute the volume of product formed ($M(t)/\rho_{hp}$), for which a homogenised mass volume ρ_{hp} is attributed. Since we adopt the simplifying hypothesis in which the space between the original surface of the reacting particle and its actual surface at a given time is filled by a high density product layer, the resulting volume V_{in} of inner products must to be taken into account. By means of the stoichiometric equations, we define the constant ς as the ratio between the molar volume of products and the molar volume of reactants.. The degree of hydration can be then computed with respect to the initial volume of the reacting particle V_0^{Rp} :

$$\xi_{BN}(t) = \varsigma \left(\frac{M(t)}{\rho_{hp}} + V_{in} \right) / V_0^{Rp} \quad (4.11)$$

4.2.4 Diffusion-controlled growth (DF) and slow reaction period

The formulation developed here so far is applicable to the early-hydration periods of acceleration and deceleration. To explain the behaviour in the slow reaction periods, a diffusion-controlled kinetics is usually used (Scrivener and Nonat, 2011). Previous works proposed a combination of boundary nucleation and growth with diffusion-controlled kinetics (Allen et al., 2004; Honorio et al., 2014b; Peterson and Whitten, 2009).

With a diffusion-controlled kinetics the rate of product formation decreases proportionally with the thickness of the product barrier layer; this involves a moving boundary (of the reacting particle). Different diffusion controlled kinetics have been proposed in the literature for solid-state kinetics (Khawam and Flanagan, 2006). Here, some modelling approaches are presented in order to justify the choice of Fujii and Kondo (Fujii and Kondo, 1974) formulation.

4.2.4.1 Jander model and other propositions

In the derivation of analytical equation for diffusion-controlled kinetics normally we assume that (1) the reaction takes place at constant temperature; (2) the contact between the interfaces of the

products and reactants is perfect; (3) the different products grow simultaneously constituting compact layers (i.e. with no pores or crack formation); (4) local thermodynamic equilibrium occurs inside the reaction layers and on the interfaces; and (5) the quasi steady-state assumption can be adopted (Buscaglia and Milanese, 2005).

Jander (Jander, 1927) model has been applied for different materials (Khawam and Flanagan, 2006) including cement materials (Gartner et al., 2002; Honorio et al., 2014b) and is the simplest way of representing a diffusion-controlled kinetics. Figure 4.3 (a) shows a schematic representation of Jander model in which the diffusing reactant B has to cross the interface product AB in order to reach the solid reactant A. From the hypothesis of a linear concentration gradient of the diffusing reactant B in the interface product layer AB, the parabola law $l^2 = k_{DF} t$ for the evolution of the interface thickness is obtained (Khawam and Flanagan, 2006). The constant of the diffusion controlled kinetics k_{JA} in Jander model is (Khawam and Flanagan, 2006):

$$k_{JA} = 2 D_f \frac{M_{AB}}{\rho_{AB} M_B} (C_2 - C_1) \quad (4.12)$$

where D_f is the diffusion coefficient; M_{AB} is the molecular mass of the product; ρ_{AB} is the specific mass of the product; M_B is the molecular weight of the diffusing reactant; C_2 and C_1 are the concentration of B on the interfaces A-AB and B-AB, respectively. The resulting kinetics is given by (Jander, 1927):

$$(1 - (1 - \xi)^{1/3})^2 = 2 \frac{k_{JA}}{R_0^2} t \quad (4.13)$$

Since Jander's formulation is derived for a plane surface, it may not hold for high conversion rates in particles in which the product layer is not negligible with respect to the size of the particle (Khawam and Flanagan, 2006).

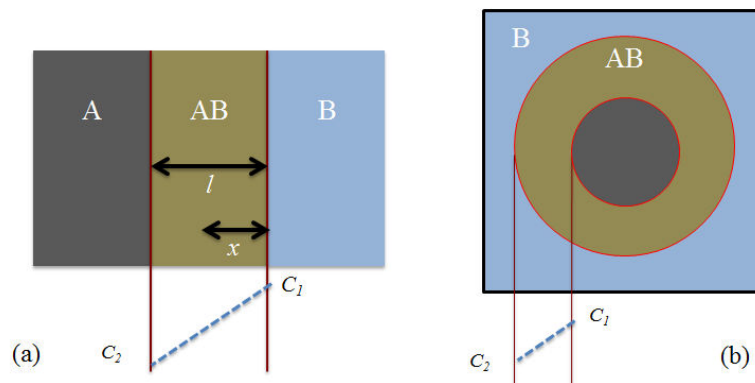


Figure 4.3 Schematic representation of (a) Jander and (b) Ginstling-Brounstein diffusion-controlled kinetics

Ginstling and Broushstein (1950) used the solution of the first Fick law for spherical particles in their derivation of a diffusion-controlled kinetics (Figure 4.3 b). In this case, the formulation is

valid also for high conversion rates but no volume changes are considered. Both cited models only consider a single layer of product formed around the reacting particle. Other propositions with multilayers were proposed in the literature (Buscaglia and Anselmi-Tamburini, 2002; Buscaglia and Milanese, 2005; Taplin, 1968, 1960) and may be useful in the investigation of the influence of inner and outer product on the diffusion-controlled kinetics. This aspect is not considered in the following.

4.2.4.2 Fujii-Kondo model

For sake of simplicity, a formulation based on Jander model is adopted. Accounting for the time t_d at which diffusion-controlled growth becomes the limiting mechanism, Fujii and Kondo (Fujii and Kondo, 1974) propose the following equation:

$$\xi_{DF}(t) = 1 - \left\{ [1 - \xi(t_d)]^{\frac{1}{3}} - R_0^{-1} [2D_i (t - t_d)]^{\frac{1}{2}} \right\}^3 \quad \text{for } t \geq t_d \quad (4.14)$$

where ξ_{DF} is the degree of hydration in the diffusion-controlled kinetics period and D_i is an effective diffusion coefficient concerning global ion mobility within the system. This diffusion-controlled kinetics is often applied to alite and cement hydration kinetics (Allen et al., 2004; Peterson and Whitten, 2009). With Cahn (Cahn, 1956) model it is possible to estimate the fraction of coverage of the surface of the reacting particle (Scherer et al., 2012). From this coverage degree a transition time t_d may be defined but for a coverage fraction inferior to 100% (Honorio et al., 2014b). Here, we use t_d as an additional fitting parameter.

Instead of using the average size of particle as proposed initially by Fujii and Kondo (Fujii and Kondo, 1974), we perform the integration over the PSD as proposed in the next section.

Note that with the proposed formulation, the identification of the diffusing species is not necessary. For alite hydration different diffusing species are present: H_2SiO_4 is reported to be the limiting rate species to be accounted for (Kirby and Biernacki, 2012) but water diffusivity should also be considered. In the following, D_i is treated as a fitting parameter; no interpretation of this coefficient regarding the diffusion of any species present in the reactive system is carried out.

4.2.5 Influence of the Particle Size Distribution

The development made so far accounts only for a system with particles of same size. In order to take into account the polydispersivity the volume of product V^* formed for a specific size of particle is integrated over the particle size distribution $w(R_0)$ of the system:

$$V^*_{PSD} = \int_0^{\infty} w(R_0) V^*(r, R_0) dR_0 = \langle V^* \rangle \quad (4.15)$$

The probability distribution we choose to describe a multimodal particle size distribution is (Knudsen, 1980):

$$w(R_0) = \sum_i c_i (e^{-a_i R_0^{m_i}} - e^{-b_i R_0^{m_i}}) \quad (4.16)$$

where a_i , b_i , c_i and m_i are fitting parameters for a given mode i .

With this formulation, the small particles may grow even if their anhydrous core has been completely consumed. A term turning off the contribution of these consumed particles may be added to Eq. (4.15), but this would significantly complexify the numerical integration. On the other hand, for a PSD in which the volume fraction of particles with radii smaller than e_{lim} (whose typical values range between 0.5 and 1 μm) is small, as in the cases studied here, we consider that this term can be neglected.

4.2.6 Degree and rate of hydration

With the equations presented in the previous sections combined with the stoichiometric relations, the overall degree of hydration $\xi(t)$ can be determined following the algorithm in Figure 4.4. The kinetics attributed to BN and DF mechanisms are used to obtain the volume $V^*(t)$, which is integrated over the PSD. With the resulting V^*_{PSD} the degree of hydration $\xi(t)$ can be then computed regarding each mechanism by means of similar considerations made in Eq. (4.11). The rate of hydration is computed by applying the Leibniz rule of derivation under integral. In this study, we assume that the different products form homogeneously within both inner and outer regions, with only C-S-H presenting a space-filling character.

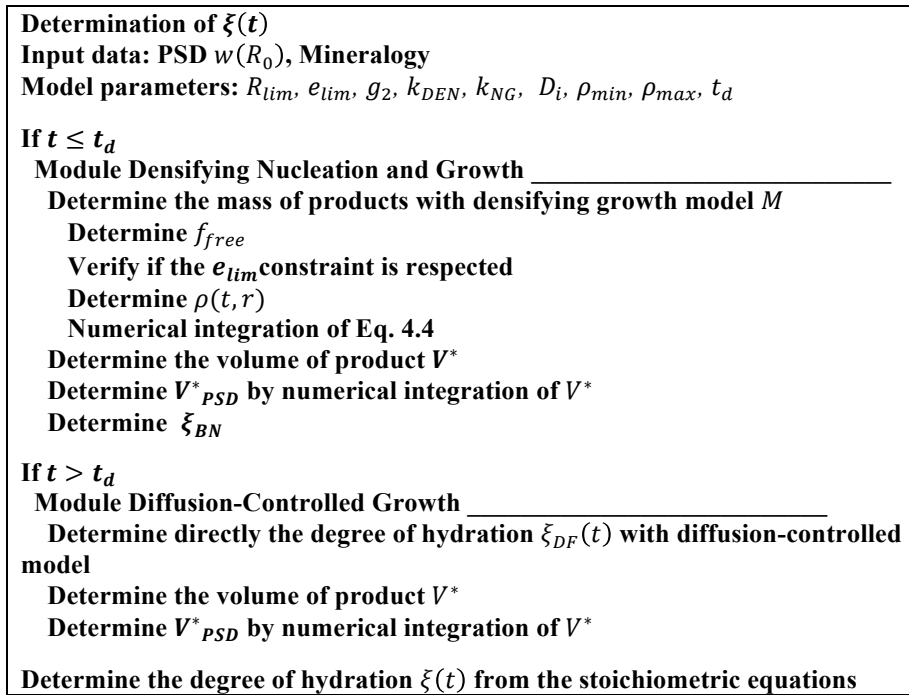


Figure 4.4 Algorithm for the determination of the degree of hydration

4.2.7 Effects of the temperature

As is well known, the temperature affects directly the kinetics (Taylor, 1997). To model this effect, an Arrhenius law is currently combined with the rate equation, so we obtain for a given temperature T (in K):

$$\dot{\xi}_T(t, T) = \dot{\xi}(t, T_0) \exp[-E_a/R (1/T - 1/T_0)] \quad (4.17)$$

where E_a is the energy of activation which depends on the mechanism considered, R is the gas constant and T_0 is the reference temperature.

Other factors such as pressure (Lin and Meyer, 2009; Taylor, 1997) and internal relative humidity (RH) or saturation degree (Flatt et al., 2011) affect the kinetics, but are not considered here for simplicity purposes.

4.3 APPLICATION TO ALITE EARLY HYDRATION

In this section, the approach developed above is applied to alite early hydration (no diffusion-controlled kinetics is considered). In the balance reaction equation of alite hydration, we take into account the additional water that is trapped in the C-S-H nanopores, as proposed by Jennings (Jennings, 2004; Masoero et al., 2013):



Note that because of that water which is not available for further hydration, we write $C_{1.7}SH_{3.9}$ instead of the usual formula $C_{1.7}SH_{1.8}$. As pointed out by Masoero et al.(2013), accounting for this aspect is necessary in the consideration of the space-filling phenomena. The volume of the C-S-H nanopores is 34.5% (Masoero et al., 2013), which corresponds to the volume of nanopores in Jennings colloid model of C-S-H LD (Jennings, 2004). In order to compare with calorimetric data, the heat of C_3S hydration is taken as $Q_{C_3S} = 546$ J/g (Jennings, 2004).

4.3.1 Influence of the PSD

At first, we test the sensibility of the model to the particle size of one single particle.

Figure 4.5 shows the time evolutions of rate and degree of hydration for different particle sizes whose diameter ranges from 2 to 20 μm . For this sensibility study, the parameters were adapted or chosen among some proposed values in the literature (see Table 4.1).

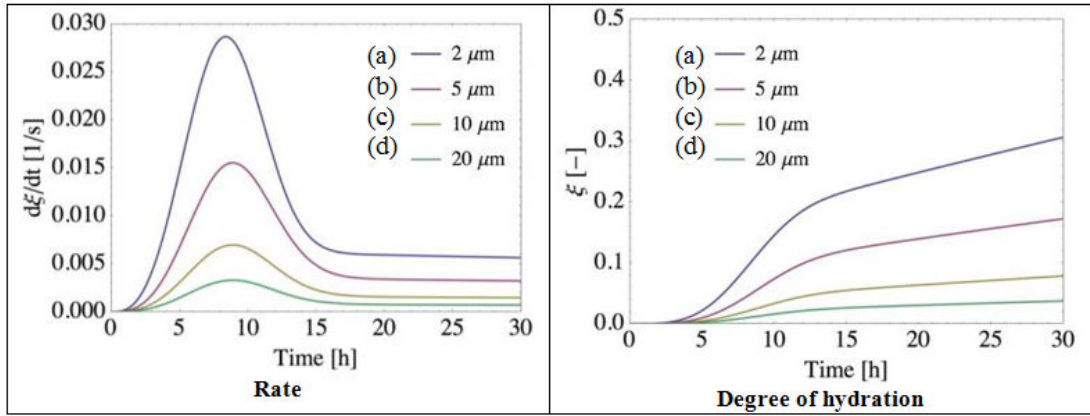


Figure 4.5 Rate and degree of hydration for monodisperse cases. Particle sizes: (a) 2 μm , (b) 5 μm , (c) 10 μm and (d) 20 μm . $w/c = 0.4$; $e_{lim} = 0.5 \mu\text{m}$; $g_2 = 0.3 \mu\text{m/h}$; $t_{1/2} = 7 \text{ h}$, $k_{DEN} = 0.01 \text{ g/cm}^3/\text{h}$; $\rho_{max} = 2.2 \text{ g/cm}^3$; $\rho_{min} = 0.2 \text{ g/cm}^3$.

Table 4.1 Parameters used in the simulations based on values in the literature, for $w/c = 0.4$

Ref.	PSD	g_2 [$\mu\text{m/h}$]	$t_{1/2}$ [h]	k_{DEN} [$\text{g/cm}^3/\text{h}$]	ρ_{max} [g/cm^3]	ρ_{min} [g/cm^3]	e_{lim} [μm]
Our values	All	0.42	12	0.018	2.2	0.2	0.5
(Bishnoi and Scrivener, 2009a)	18 μm	0.35	7.4	0.012	2.2	0.185	-
(Bishnoi and Scrivener, 2009a) (alter.)	18 μm	0.70	8.8	0.0115	2.2	0.145	-
(Masoero et al., 2013)	18 μm	0.036	-	-	2.05	-	0.7 – 1.1
(Biernacki and Xie, 2011) (exp. box)	18 μm	0.2	9.3	0.02	2.2	0.2	-

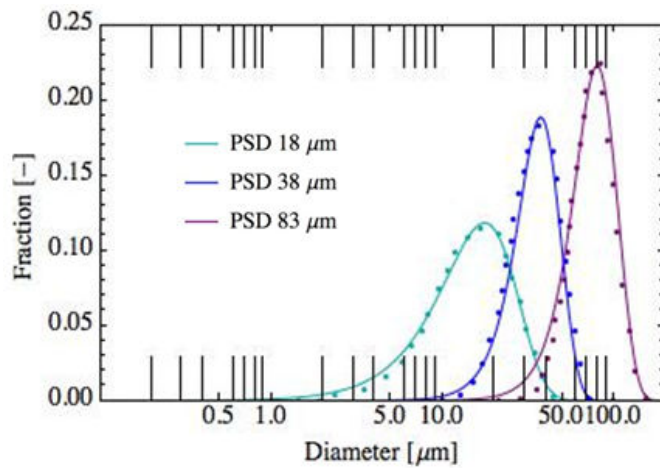


Figure 4.6 Particle size distribution of alite from Costoya (2008) experimental data (dots) and fitted curves (full lines)

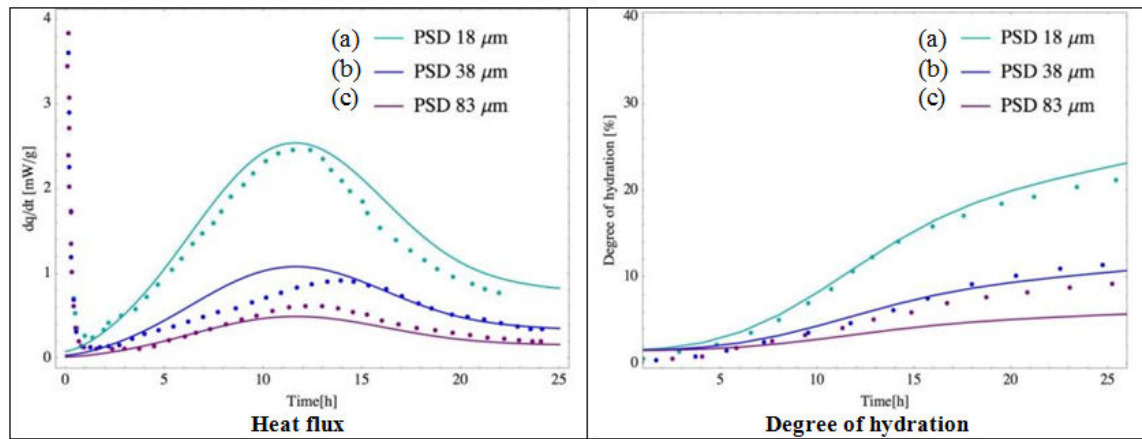


Figure 4.7 Fitted calorimetric data (dots are experiments (Costoya, 2008), lines are the model results) for C_3S hydration according to different PSD: (a) 18 μm , (b) 38 μm and (c) 83 μm . $w/c = 0.4$; The parameters used here are presented in 0.

The peak in the rate curve occurs for almost the same time for the particle sizes studied. Similar results are found in the literature in experiments and simulations (Biernacki and Xie, 2011; Bishnoi, 2008). Note that this feature is not obtained when no fixed reaction zone is imposed: in this case, the time at which the peak occurs increases with the size of the particle.

Regarding complete PSD, we employ Costoya (2008) experimental results concerning the influence of the PSD on alite hydration to validate the model. Different PSD of alite were studied by this author with some cases close to monodisperse distributions. Figure 4.6 shows the three PSDs studied here.

Figure 4.7 shows the curves obtained by the model concerning the heat flux (left) and degree of hydration (right) for the three PSDs. Some of the same results were also studied by (Biernacki and Xie, 2011; Bishnoi, 2008; Masoero et al., 2013; Scherer et al., 2012). Note that, differently from these authors, here the same set of parameters is used in all cases, which seems physically more satisfactory; only the PSD is varying. We observe that the model captures reasonably well the effect of the PSD on the heat flux and degree of hydration.

4.3.2 Influence of the w/c ratio

Figure 4.8 illustrates the response of the model in terms of rate of hydration with respect to the particle size and w/c ratio. The time at which the peak of the rate curves occurs is approximately the same for the different particles sizes and w/c ratios. On the other hand, the value of the rate depends on the particle size. With $e_{lim} = 0.5 \mu\text{m}$, a significant difference among the rate values is observed for a diameter $d = 1 \mu\text{m}$. For bigger particles the rate values do not depend on the particle size due to the imposition of a reaction zone. Therefore, if $e_{lim} = 0.5 \mu\text{m}$ is adopted, only a slight influence of the w/c ratio on the rate (at early hydration) is expected for PSDs currently observed in cement. This effect is evident in Figure 4.9, in which just a slight difference is observed at early hydration in the rate and degree of hydration curves for different w/c ratios.

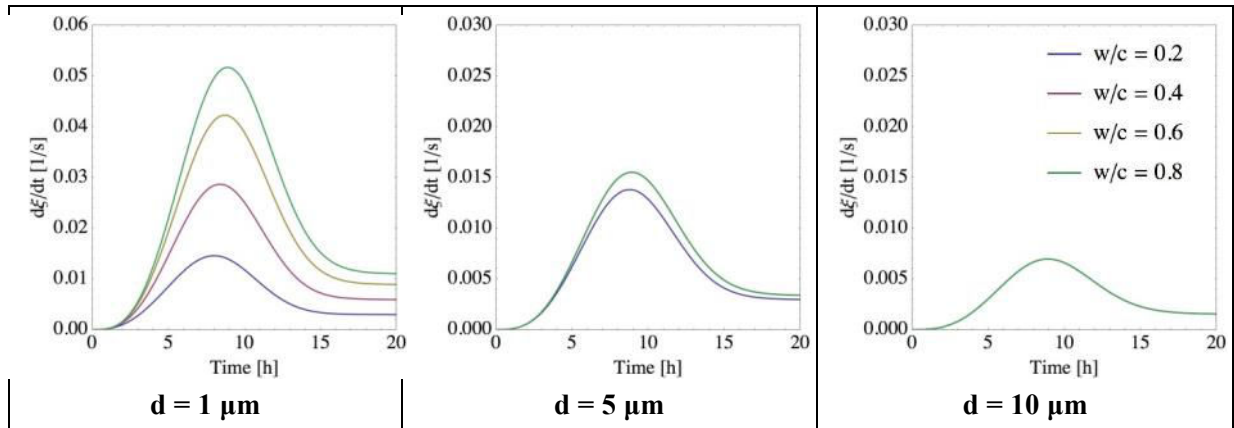


Figure 4.8 Rates of hydration according to the particle size and w/c ratio. Same parameters as in the sensibility study in

Figure 4.5 ($e_{lim} = 0.5 \mu\text{m}$; $g_2 = 0.3 \mu\text{m/h}$; $t_{1/2} = 7 \text{ h}$, $k_{DEN} = 0.01 \text{ g/cm}^3/\text{h}$; $\rho_{max} = 2.2 \text{ g/cm}^3$; $\rho_{min} = 0.2 \text{ g/cm}^3$). The non-visible curves are indistinguishable with the green curve for $d = 5 \mu\text{m}$ and $d = 10 \mu\text{m}$.

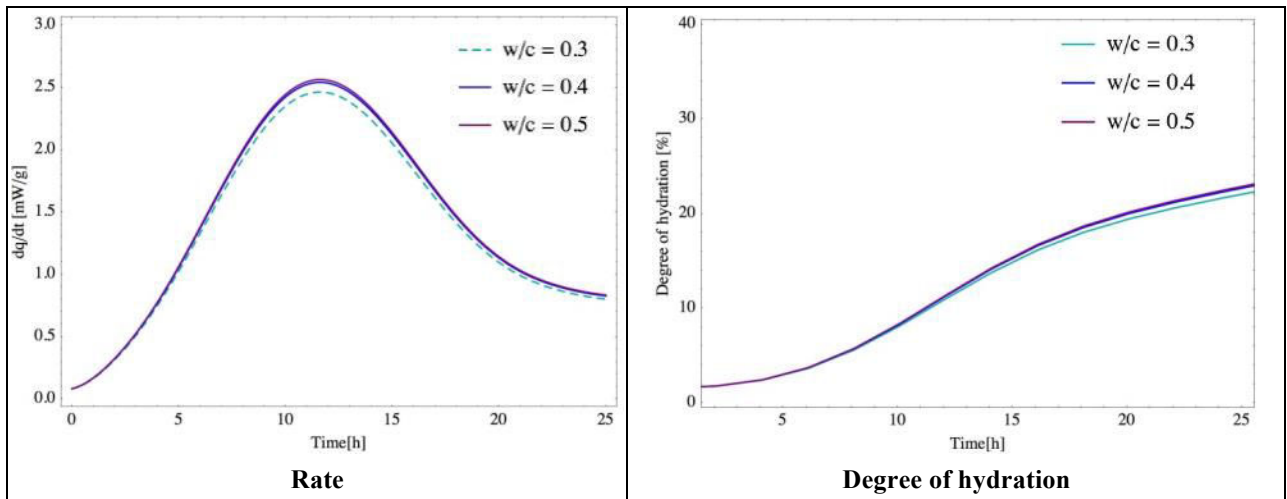


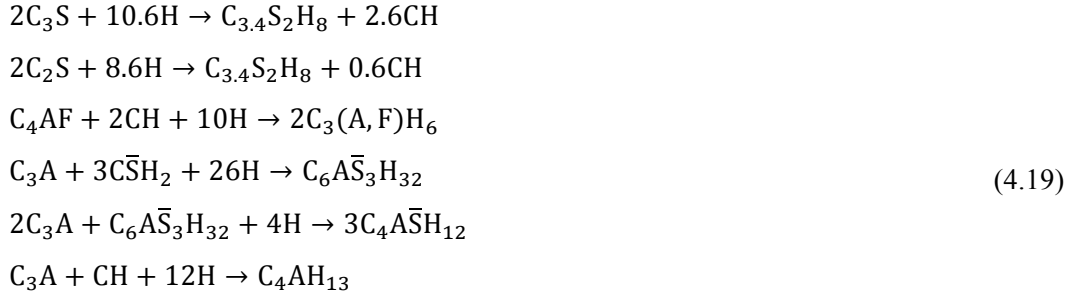
Figure 4.9 Heat flux and degree of hydration according to different w/c ratios for the PSD 18 μm . Parameters from Table 4.1. Note that the curves for w/c = 0.4 and 0.5 are superposed.

4.4 APPLICATION TO CEMENT EARLY AND LATE HYDRATION

Besides C_3S , other mineral phases, namely C_2S , C_4AF , C_3A are present in ordinary Portland cement. Describing the whole process of cement hydration in details cannot evidently be done with a single formulation as the one proposed here. The effects of the hydration of the other minerals cannot be simply added together since impingements with growing products of other phases take place (Scherer et al., 2012), which is not accounted for here. Assuming that these coupled effects of the hydration of clinker minerals can be neglected, the overall response of the system is the weighted average of the evolution of the volume fraction of each mineral. In order to estimate the volume fraction of the products, Tennis and Jennings (2000) reactions balance may be used, for instance. With these hypotheses, we propose in this section to apply the previous model to the early and late hydration of a CEM I cement.

4.4.1 Hydration reactions balance

In order to estimate the volume fraction of the products, we use the (Tennis and Jennings, 2000) reactions balance and assumptions regarding the hydration of different phases (in cement notation):



The first two equations concerning the formation of C-S-H and CH are the most important. For the aluminate hydration it is assumed that ettringite ($C_6\bar{A}\bar{S}_3H_{32}$ or AFt) is formed until the depletion of gypsum ($\bar{C}\bar{S}H_2$). Then, monosulfoaluminates ($C_4\bar{A}\bar{S}H_{12}$ or AFm) are formed with the additional C_3A . Finally, when all ettringite is depleted, calcium aluminates hydrates are formed. A hydrogarnet ($C_3(A, F)H_6$) is formed from ferrite hydration. Other aluminium containing compounds may form according to different conditions, but the ones used remain representative of the main products of long-term hydration. (Tennis and Jennings, 2000) model distinguishes two types of C-S-H: low density C-S-H LD and high density C-S-H HD. Also, the porosity of the C-S-H is accounted for. The properties of the phases are shown in the Table 4.2.

Table 4.2 Properties of phases (Tennis and Jennings, 2000)

Compound	Cement notation	Specific mass [kg/m ³]	Molar mass [kg/mol]	Molar volume [10 ⁻⁵ m ³ /mol]
Alite	C_3S	3150	0.228	7.24
Belite	C_2S	3280	0.172	5.24
Aluminate	C_3A	3030	0.270	8.92
Ferrite	C_4AF	3730	0.486	13.03
Water	H	998	0.018	1.80
Gypsum	$\bar{C}\bar{S}H_2$	2320	0.172	7.41
Portlandite	CH	2240	0.074	3.31
Hydrogarnet	$C_3(A, F)H_6$	2670	0.407	15.27
AFm (saturated)	$C_4\bar{A}\bar{S}H_{12}$	1990	0.623	34.6
AFt (saturated)	$C_6\bar{A}\bar{S}_3H_{32}$	1750	1.255	71.7
Calcium aluminate hydrate	C_4AH_{13}	2050	0.560	27.4
C-S-H LD	$C_{3,4}S_2H_8$	1440	0.365	25.2
C-S-H HD	$C_{3,4}S_2H_8$	1750	0.365	21.1

4.4.2 Experimental data

The composition of the cement is given in Table 4.3. The cement is of type CEM I 42.4 N-SR3, i.e. with a low C_3A content, which was chosen for the concrete modules in cAt project. Figure 4.10 shows the passing PSD of the cement; the experimental data obtained from laser granulometry (provided by Holcim Belgium), are fitted with Eq.(4.16). Note that the fraction of particles with radius inferior to $0.5 \mu\text{m}$ is very small and justifies the simplification regarding the integration of Eq. (4.15). The calorimetry results were obtained by isothermal methods as already communicated by (Craeye, 2010; Craeye et al., 2010). The results concerning the influence of the w/c were obtained by chemically bond water measurements in which drying between 105 and $550 \text{ }^\circ\text{C}$ were effectuated at given ages following (LCPC, 2002) method. With this method, the degree of hydration is defined as the ratio between the bond water at a given time and the final bond water. The final bond water was computed here following the procedure explained in (LCPC, 2002). Note that different final values of degree of hydration can be obtained if different drying temperatures are employed.

Table 4.3 Normative cement composition computed from the oxide composition as provided by Holcim

Mineral	Initial mass fraction [%]
C_3S	64.0
C_2S	23.1
C_3A	1.5
C_4AF	2.0
$C\bar{S}H_2$	2.0
Others	7.35

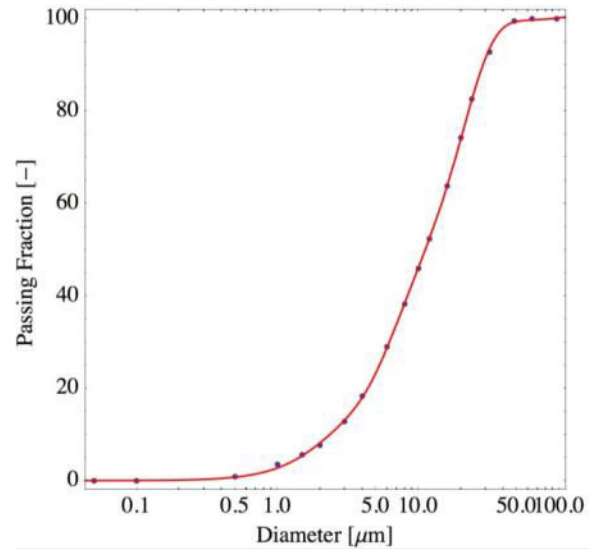


Figure 4.10 Passing particle size distribution of cement. The dots are experimental measures (provided by Holcim) and the full line the fitted distribution

In order to compare with calorimetry data, the heat of hydration of the other clinker minerals are taken as $Q_{C_2S} = 250 \text{ J/g}$; $Q_{C_3A} = 1340 \text{ J/g}$ and $Q_{C_4AF} = 420 \text{ J/g}$ (Meinhard and Lackner, 2008). Instead of accounting individually for the different possible reactions concerning the aluminate phases (Tennis and Jennings, 2000), we adopt the simplifying hypothesis that the reactions regarding C_3A (the last three equation in Eq. (4.19)) release in average Q_{C_3A} . The energy of activation experimentally determined for the cement is 39.1 kJ/mol . A more precise way of dealing with the thermal activation is to account for different energies of activations for the possible reactions involving the clinker minerals and intermediate products. As in the case of the enthalpies of reaction, in this paper we are not adopting this more detailed description.

Table 4.4 Fitting parameters for each clinker phase

Model parameters	C ₃ S	C ₂ S	C ₃ A	C ₄ AF
$G_2 [\mu\text{m} \cdot \text{h}^{-1}]$	0.42	0.42	0.42	0.42
$t_{1/2} [\text{h}]$	11	20	20	20
$k_{DEN} [\text{g} \cdot \text{cm}^{-3} \cdot \text{h}^{-1}]$	0.02	0.02	-	-
$\rho_{min} [\text{g} \cdot \text{cm}^{-3}]$	0.2	0.2	-	-
$\rho_{max} [\text{g} \cdot \text{cm}^{-3}]$	2.2	2.2	-	-

4.4.3 Early hydration and influence of the temperature

The heat flux of cement for $w/c = 0.5$ is shown in Figure 4.11, with the fitting parameters listed in Table 4.4. The dashed curves represent the contributions of each clinker phase hydration, according to their initial mass fraction. Note that for the set of parameters used, the boundary nucleation and space-filling growth do not capture accurately the late stage of hydration (after about 50 h), as can be seen in Figure 4.11. Further investigations accounting for a more precise description of belite hydration and possible interactions between the reactions involving the different clinker minerals are needed to better understand this aspect. In our proposition we assume that a diffusion-controlled process becomes the rate limiting mechanism at the late periods.

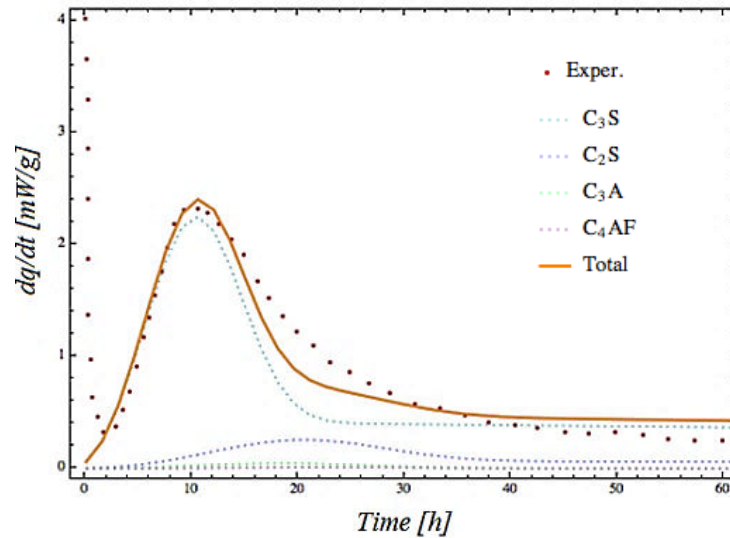


Figure 4.11 Experimental and modelled heat flux of cement. $w/c=0.5$; $e_{lim} = 0.475 \mu\text{m}$.

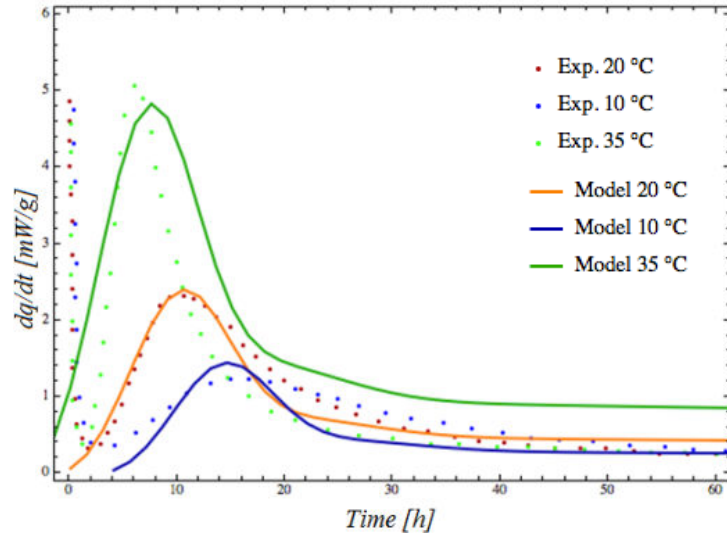


Figure 4.12 Cement heat flux for different temperatures; comparison with isothermal calorimetric data from (Craeye et al., 2010). $w/c=0.5$; $e_{lim}=0.475 \mu\text{m}$.

The effect of temperature on the rate of hydration is illustrated in Figure 4.12. Again, isothermal calorimetry results are compared to the model results. Different $t_{1/2}$ were adopted for each temperature (the values of $t_{1/2}$ at 20 °C in Table 4.4 are modified according to the temperature: $t_{1/2} - 2$, for all minerals at 10 °C and $t_{1/2} + 2$, for all minerals at 35 °C); the other parameters remain the same. For the results at 35 °C the resulting heat flow is not very well captured at the deceleration and late stages. Besides the $t_{1/2}$, which is related to the rate constant of the nucleation and growth processes, the other parameters could also be affected by the temperature.

4.4.4 Late hydration

The experimental results (Poyet, 2014) for the degree of hydration up to 700 hours are compared to the model results in Figure 4.13. In order to capture the tendency after 50-70 hours the diffusion-controlled kinetics presented in Section 4.2.4.2 is used. Note that for computations without this diffusion-controlled kinetics, the densification progresses quite fast, reaching in the case of $w/c = 0.47$ the total hydration ($\xi = 1$) by 600 h. Different t_d for each w/c were employed (55, 65, 70 and 75 h for $w/c = 0.25, 0.3, 0.40$ and 0.47 , respectively), to fit at best the experimental data. Globally, the model provides satisfying results for all considered cases. The effect of the w/c in the late hydration appears well described for w/c superior to 0.30.

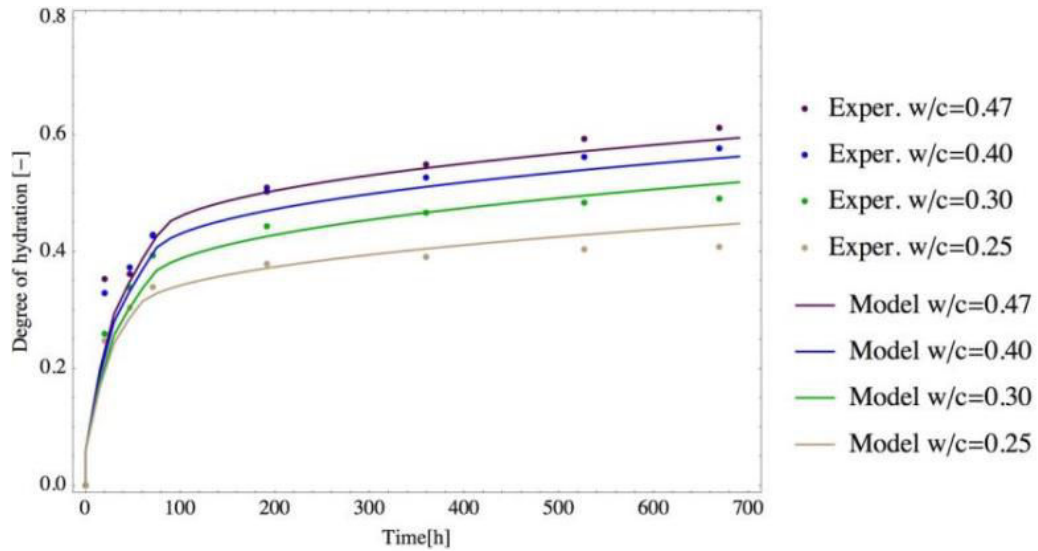


Figure 4.13 Degree of hydration according to different w/c ratios for cement. $e_{lim} = 0.475 \mu\text{m}$; $g_2 = 0.42 \mu\text{m/h}$; $t_{1/2} = 11 \text{ h}$, $k_{DEN} = 0.005 \text{ g/cm}^3/\text{h}$; $\rho_{max} = 2.2 \text{ g/cm}^3$; $\rho_{min} = 0.2 \text{ g/cm}^3$; $D_i = 15 \times 10^{-15} \text{ cm}^2/\text{h}$.

For lower w/c ratios, we observe a slight overestimation of the degree of hydration. This is probably because the model does not take into account the influence of the internal RH on the hydration. Indeed, below about 80% of internal RH alite hydration stops or slows down significantly (Flatt et al., 2011; Jensen et al., 1999). The same is reported for other clinker minerals at different RH (Jensen et al., 1999). This effect could be introduced into the model by means e.g. of a phenomenological law as a function of the degree of saturation of the material. On the other hand, a mechanistic approach should take into account the thermodynamic effects induced by the decrease of the internal RH (Flatt et al., 2011), which is beyond the scope of this work and is left to a further investigation.

4.4.5 Evolution of the volume fractions

With the balance equations (Eq. (4.19)) of hydration process and the kinetics model developed in this chapter, the evolution of the volume fraction of clinker minerals and hydration products can be directly estimated. Figure 4.14 shows this evolution according to the w/c.

In Chapter 6, these results are used in the definition of the microstructure at the cement paste level and mortar level (regarding the composition of the ITZ).

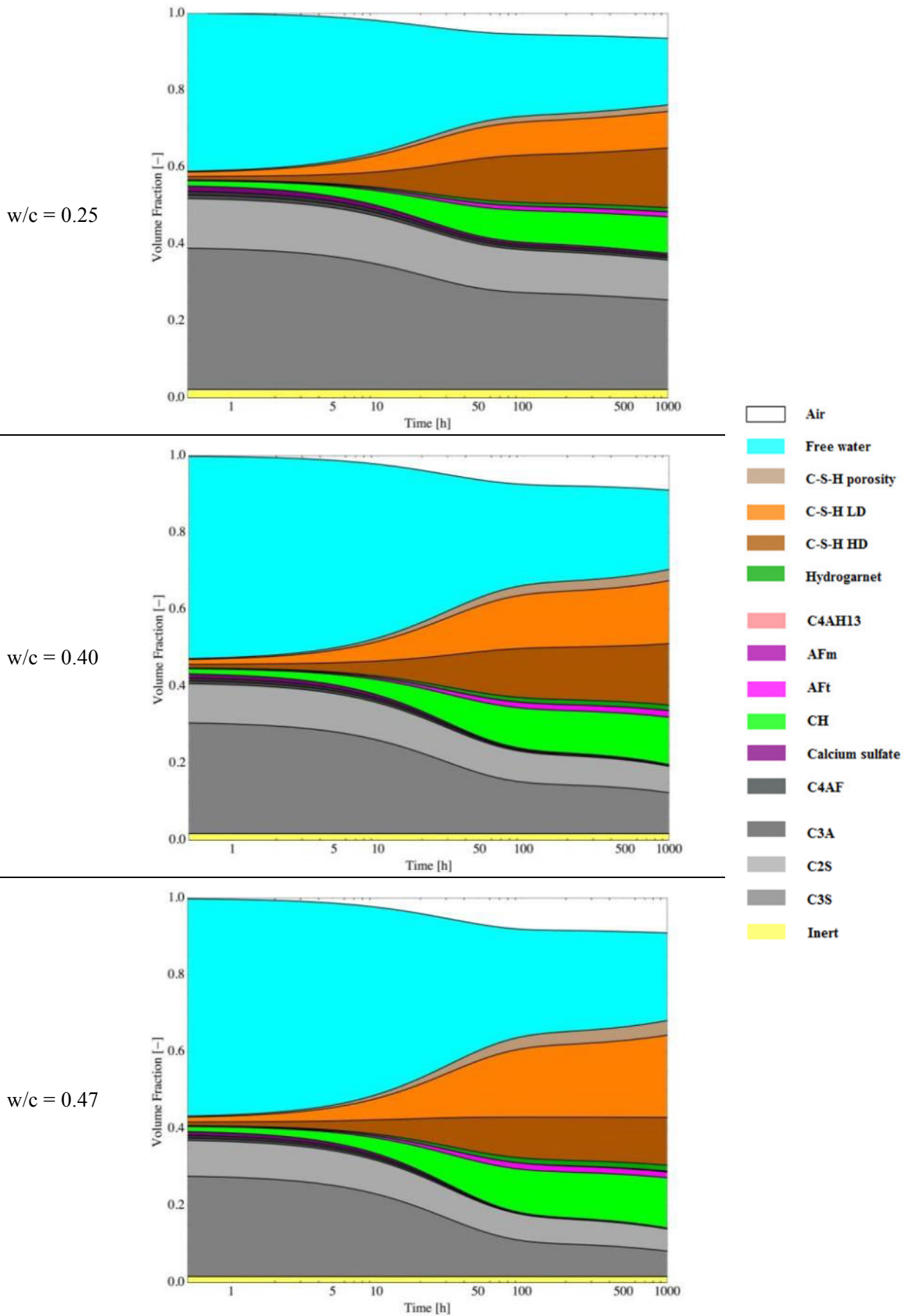


Figure 4.14 Evolution of the volume fractions according to the w/c ratio

4.5 CONCLUSION AND PERSPECTIVES

A simplified (semi)-analytical kinetics model of hydration is developed in this chapter. It is based on boundary nucleation and space-filling growth with a fixed confined zone imposed for early hydration and a diffusion-controlled kinetics for late hydration. An original approach to define the reaction zone, combining an exponential box and a fixed limiting parameter, is proposed. The PSD is explicitly accounted for. The model remains quite simple so that it can be integrated in more complex analyses, as for instance, to determine the mechanical parameters at early-age. An application to alite hydration is followed by an extension to CEM I cement hydration.

The model was compared against different experimental data and adequate fittings were obtained. Even if good fitting does not mean necessarily that the actual mechanisms are correctly considered, the results here present an acceptable physical sense since the model parameters were kept the same with respect to the PSD or w/c when the other conditions are fixed. Keeping in mind these reserves, we conclude that:

- The model captures the effects of the PSD and w/c on hydration. With the formulation used here for the space-filling process, the effects of the w/c depend on the particle size. Small particles present different peaks in the rate curves compared to bigger particles.
- Regarding alite hydration, good fittings are obtained for acceleration and early deceleration periods with a same set of parameters. The parameters used here are similar to the values obtained in other research works in which a more precise representation of the microstructure is adopted (Biernacki and Xie, 2011; Bishnoi and Scrivener, 2009a).
- Regarding cement hydration, in spite of the simplifications assumed, consistent results are found. The boundary nucleation and space-filling growth capture quite well the acceleration and deceleration periods for the cement with low C_3A content studied. The diffusion-controlled kinetics was necessary to explain the late stages of hydration (from about 50 h up to 700 h). With both mechanisms the model can describe the influence of w/c for values superior to 0.30. Effects related to the decrease in the internal RH should be added in order to more precisely consider lower w/c formulations.
- Further investigations are to be performed concerning this extension to cement hydration, in which, for example, systems with supplementary cementitious materials and cements with higher contents of aluminate phases may be studied.

In chapter 6 the results of the evolution of the volume fraction of products and reactants will be used as an input data in the determination of the mechanical properties of concrete. Before doing that, upscaling tools derived in an ageing viscoelastic framework are presented in chapter 5.

5. HOMOGENIZATION IN AN AGEING LINEAR VISCOELASTIC FRAMEWORK

For conciseness purposes we briefly introduce some basic aspects related to homogenization methods. For a complete introduction to the subject see e.g. (Dormieux and Ulm, 2005; Milton, 2002; Torquato, 2002; Zaoui, 1998).

Homogenization methods are concerned with determining the appropriate averaged (or macroscopic) governing partial differential equations which describe physical phenomena occurring in heterogeneous materials when the length scale of the heterogeneities tends to zero (Torquato, 2002). The methods apply when the following condition is respected:

$$L_M \geq \Lambda \gg l_\mu \quad (5.1)$$

where L_M is the macroscopic scale associated with the extent of the system, l_μ is a microscopic scale associated with the heterogeneities and Λ is a characteristic length associated with the mesoscale at which the composite appears as statistically homogeneous and at which macroscopic fields have a slow variation (Milton, 2002; Torquato, 2002).

A Representative Elementary Volume (REV), with dimensions $O(\Lambda)$, must be defined to apply the methods. The REV is generally defined as a volume of heterogeneous material that is sufficiently large to be statistically representative of the composite, i.e., to effectively include a sampling of all microstructural heterogeneities that occur in the composite (Kanit et al., 2003). Thus, in the REV a large number of the composite microheterogeneities needs to be represented, but at the same time it must remain small enough to be considered as a volume element of continuum mechanics.

As shown in Figure 1.2, cement-based materials own a strong multiscale character. Application of homogenization techniques demands the determination of a REV for each scale of interest. Such methods in elasticity have often been applied in the study of cement-based materials as will be discussed in more details in chapter 7. Solutions in non-ageing viscoelasticity are straightforward in e.g. Laplace-Carson space due to Mandel (1966) correspondence principle.

After the pioneering works of Boltzmann (1874) on the linear viscoelastic behaviour of materials, followed by the important further developments brought by Volterra (1959), the *ageing* linear viscoelastic behaviour seems to be first studied by Maslov (1940) to describe concrete behaviour (Lubliner and Sackman, 1966). Different mechanisms related to the degradation or evolution of the microstructure may lead to an ageing behaviour. For example, an ageing may be caused by solidification of non-aging constituent (Bazant, 1977; Carol and Bazant, 1993). The kinetics of solidification, and the way in which the solidifying phase precipitates affect the viscoelastic response (Sanahuja, 2013b). These aspects are treated in the next chapter.

Here, analytical and numerical techniques to determine the effective properties of heterogeneous materials are developed in an ageing linear viscoelastic framework.

5.1 AGEING LINEAR VISCOELASTICITY

In the context of linear viscoelasticity, Boltzmann principle holds, i.e. the superposition of the efforts implies the superposition of the homologue responses (Salençon, 2009). Accordingly, causality principle applies, i.e. the history of stresses until time t is associated to a linear combination of the history of strains, and the inverse correspondence is also true. The history of stresses is given by the Riemann-Stieltjes integral:

$$\boldsymbol{\sigma}(t) = \int_{-\infty}^t \frac{d\boldsymbol{\sigma}(t')}{dt'} dt' \equiv \int_{t'_0}^t H_{t'}(t) d\boldsymbol{\sigma}(t') + \sum_{t'_i \leq t} \llbracket \boldsymbol{\sigma} \rrbracket_i H_{t'_i}(t) \quad (5.2)$$

where $\boldsymbol{\sigma}$ is equal to $\mathbf{0}$ for $t < t'$ and differentiable and piecewise continuous for $t > t'$; $H_{t'}$ is the Heaviside function $H_{t'}(t) = \begin{cases} 0 & t < t' \\ 1 & t \geq t' \end{cases}$; t'_i accounts for the times in which $\boldsymbol{\sigma}$ is discontinuous and $\llbracket \boldsymbol{\sigma} \rrbracket_i$ is the corresponding jumps where the functions are evaluated by the right side (t'_0).

The strain response can be obtained by applying the Boltzmann principle (Salençon, 2009):

$$\boldsymbol{\varepsilon}(t) = \int_{t'=-\infty}^t \mathbb{S}(t, t') : d\boldsymbol{\sigma}(t') \quad (5.3)$$

where $\mathbb{S}(t, t')$ is the compliance tensor.

Similarly, the stress response can be defined by means of a relaxation tensor $\mathbb{R}(t, t')$:

$$\boldsymbol{\sigma}(t) = \int_{t'=-\infty}^t \mathbb{R}(t, t') : d\boldsymbol{\varepsilon}(t') \quad (5.4)$$

The component $\mathbb{R}_{ijkl}(t, t_0)$ gives the stress along ij at time t resulting from a unit strain step along kl occurring at t_0 . The tensors $\mathbb{R}(t, t_0)$ and $\mathbb{S}(t, t')$ are related by a Volterra integral equation of the second kind with parameter t_0 (Bazant and Huet, 1999). This kind of integral equation always have a unique solution for a fixed t_0 (Bazant and Huet, 1999).

Compared to the non-ageing cases the compliance and relaxation tensors depend independently on t and t' ; i.e., the evolution of the properties does not depend on the age in which the loading is applied. In this case, the Eqs. (5.3) and (5.4) reduce to convolution products and Mandel (1966) correspondence principle holds. Also, unlike the non-ageing case, the lower limit of the time integral in Eqs. (5.3) and (5.4) need not be written as 0_- because a jump of stress or strain at $t = 0$ is physically impossible since at $t = 0$ the material begins to harden and thus cannot sustain a finite shear stress yet (Bazant and Huet, 1999).

5.1.1 Creep and relaxation tests

Creep tests consist of measuring the time-dependent strain resulting from the application of a steady uniaxial stress (Figure 5.1). On the other hand, stress relaxation tests consist of monitoring the time-dependent stress resulting from a steady strain (Figure 5.2). From these tests, some *a priori*

defined properties can be determined either in “real” tests or in simulations. Dynamic loading is another way of experimentally assess the viscoelastic behaviour of material, but it is not considered in this work.

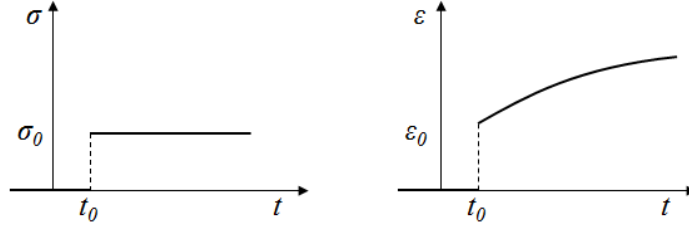


Figure 5.1 Creep test (uniaxial)

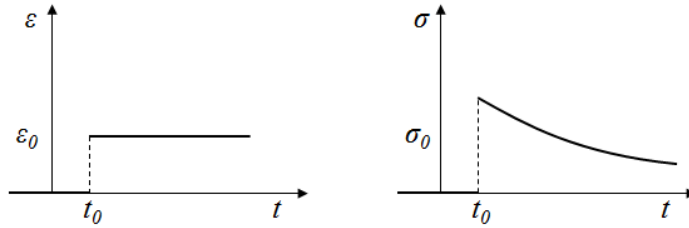


Figure 5.2 Relaxation test

Considering tridimensional viscoelasticity, in a creep test we have (Salençon, 2009):

$$\begin{cases} \boldsymbol{\sigma}(t) = \boldsymbol{\sigma}_0 H_{t_0}(t) \\ \boldsymbol{\boldsymbol{\epsilon}}(t) = \mathbb{S}(t, t_0): \boldsymbol{\sigma}_0, \quad \forall \boldsymbol{\sigma}_0 \end{cases} \quad (5.5)$$

where we have $\boldsymbol{\sigma}_0 = \begin{bmatrix} \sigma_0 & 0 & 0 \\ 0 & 0 & 0 \\ 0 & 0 & 0 \end{bmatrix}$. In this case, it is possible to derive the material scalar creep function $J(t, t_0)$, corresponding to uniaxial creep, by (Salençon, 2009):

$$J(t, t_0) = \frac{\varepsilon_{xx}(t)}{\sigma_0} H_{t_0}(t) \quad (5.6)$$

Analogously, in a relaxation test we have (Salençon, 2009):

$$\begin{cases} \boldsymbol{\boldsymbol{\epsilon}}(t) = \boldsymbol{\boldsymbol{\epsilon}}_0 H_{t_0}(t) \\ \boldsymbol{\sigma}(t) = \mathbb{R}(t, t_0): \boldsymbol{\boldsymbol{\epsilon}}_0, \quad \forall \boldsymbol{\boldsymbol{\epsilon}}_0 \end{cases} \quad (5.7)$$

where $\boldsymbol{\boldsymbol{\epsilon}}_0 = \begin{bmatrix} \varepsilon_0 & 0 & 0 \\ 0 & 0 & 0 \\ 0 & 0 & 0 \end{bmatrix}$. From what, we can derive the material scalar functions (Salençon, 2009):

$$\left\{ \begin{array}{l} \mu(t, t_0) = \frac{\sigma_{xy}(t)}{\varepsilon_0} H_{t_0}(t) \\ \lambda(t, t_0) + 2\mu(t, t_0) = \frac{\sigma_{xx}(t)}{\varepsilon_0} H_{t_0}(t) \\ 3\lambda(t, t_0) + 2\mu(t, t_0) = -\frac{p(t)}{\varepsilon_0} H_{t_0}(t), \quad \text{for } \boldsymbol{\sigma}(t) = -p(t)\mathbf{I} \end{array} \right. \quad (5.8)$$

where $\mu(t, t_0)$ is the shear relaxation function (in a simple shear relaxation test), $\lambda(t, t_0) + 2\mu(t, t_0)$ is the relaxation function in simple extension and $3\lambda(t, t_0) + 2\mu(t, t_0)$ is the relaxation function in isotropic compressions. A bulk relaxation function k can be defined than as by $\lambda(t, t_0) = k(t, t_0) - \frac{2}{3}\mu(t, t_0)$.

5.1.2 Definition of a division ring

The Eqs. (5.3) - (5.4), and consequently the phenomena previously described, can be rewritten within a division ring (or skew field) in which the multiplication operator " \circ " is defined as:

$$(f \circ g)(t, \tau) \equiv \int_{t'=-\infty}^t f(t, t') d_{t'} g(t', \tau) \quad (5.9)$$

This operator is named Volterra integral operator (Sanahuja, 2013a) as a tribute to Volterra pioneer works on this kind of integral equations.

In a set F of functions f , we define a ring $(F; +, \circ)$ in which the binary operator satisfies:

1. *Additive associativity*: For all $a, b, c \in F$: $(a + b) + c = a + (b + c)$,
2. *Additive commutativity*: For all $a, b \in F$: $a + b = b + a$,
3. *Additive identity*: there exists an element $0 \in F$ such that for all $a \in F$: $0 + a = a + 0 = a$,
4. *Additive inverse*: for every $a \in F$ there exists an element $-a \in F$ such that $a + (-a) = 0$,
5. *Multiplicative associativity*: for all $a, b, c \in F$: $(a \circ b) \circ c = a \circ (b \circ c)$,
6. *Multiplicative identity*: there exists an element $H \in F$ such that for all $a \in F$: $H \circ a = a \circ H = a$,
7. *Multiplicative inverse*: for every $a \in \mathcal{U}$ not equal to 0, there exists an element $a^{-1} \in F$ such that $a^{-1} \circ a = a \circ a^{-1} = H$
8. *Left and right distributivity*: for all $a, b, c \in F$: $a \circ (b + c) = (a \circ b) + (a \circ c)$, and $(b + c) \circ a = (b \circ a) + (c \circ a)$.

The identity for the product " \circ " is the Heaviside function $H_{t'}$.

Similarly, we can define a ring for a set of matrix \mathbf{F} and the Volterra matrix inner product $(\mathbf{F}; +, \overset{\circ}{*})$ and for a set of tensors \mathbb{F} and the Volterra tensor product $(\mathbb{F}; +, \overset{\circ}{\cdot})$. For these division rings, the identity elements are $H_{t'}(t) \mathbf{I}$ and $H_{t'}(t) \mathbb{I}$, where \mathbf{I} and \mathbb{I} are the matrix and fourth order

tensor identities, respectively. In the matrix case, we assume in the following that the left and right inverses are identical.

Note that for all $a \in F$ and c or $d = kH_{t'}(t)$: $(a + c) \circ (a + d) = a \circ a + a \circ d + c \circ a + c \circ d = (a + d) \circ (a + c)$, since a , c and d commutates. Functions which can be written as linear combination of the same basis also commute with respect to the " \circ ".

5.1.3 Correspondence with elasticity

Using the formalism defined here, a correspondence between elasticity and the ageing linear viscoelastic behaviour is found. The stress-strain relationships in Eqs. (5.3) and (5.4), in a volume Ω , can be written as:

$$\boldsymbol{\varepsilon}(\mathbf{x}, t) = \mathbb{S}(\mathbf{x}, t, \cdot) \overset{\circ}{\hat{}} \boldsymbol{\sigma}(\mathbf{x}, \cdot), \quad \forall \mathbf{x} \in \Omega \quad (5.10)$$

$$\boldsymbol{\sigma}(\mathbf{x}, t) = \mathbb{R}(\mathbf{x}, t, \cdot) \overset{\circ}{\hat{}} \boldsymbol{\varepsilon}(\mathbf{x}, \cdot), \quad \forall \mathbf{x} \in \Omega \quad (5.11)$$

where the " \cdot " stands for integration variable. The relaxation and compliance tensors can be obtained from each other by the inversion with respect to the operator " \circ ":

$$\mathbb{S} \overset{\circ}{\hat{}} \mathbb{R} = \mathbb{R} \overset{\circ}{\hat{}} \mathbb{S} = H_{t'} \mathbb{I} \quad (5.12)$$

5.2 ANALYTICAL HOMOGENIZATION

This section is based on the paper (Honorio et al., submitted). Some previous results were equally presented in Honorio and Bary (2015).

5.2.1 Estimation of the effective behaviour

Together with Eq. (5.11), the localization problem on the REV Ω , composed of a heterogeneous ageing linear viscoelastic material, in terms of the microscopic stress and strains field is:

$$\mathbf{u}(\mathbf{x}, t) = \mathbf{E}(t) \cdot \mathbf{x}, \quad \mathbf{x} \in \partial\Omega \quad (5.13)$$

$$\boldsymbol{\varepsilon}(\mathbf{x}, t) = \frac{1}{2} (\nabla \mathbf{u}(\mathbf{x}, t) + \nabla^t \mathbf{u}(\mathbf{x}, t)) \quad (5.14)$$

$$\nabla \cdot \boldsymbol{\sigma}(\mathbf{x}, t) = \mathbf{0} \quad (5.15)$$

where $\mathbf{E}(t)$ is the prescribed displacement history and the infinitesimal strain hypothesis is adopted. The solution of the linear viscoelastic problem defined by the previous equations in terms of the microscopic stresses and strains field can be written as depending linearly, regarding the Volterra operator, of the macroscopic fields (Maghous and Creus, 2003):

$$\boldsymbol{\varepsilon}(\mathbf{x}, t) = \mathbb{A}(\mathbf{x}, t, \cdot) \overset{\circ}{:} \mathbf{E}(\cdot) \quad (5.16)$$

where $\mathbb{A}(\mathbf{x}, t, \cdot)$ is the strain localization tensor. The average condition applied on the REV leads to the identity $\langle \mathbb{A}(\mathbf{x}, t, \cdot) \rangle = H_{t'}(t) \mathbb{I}$.

The classical schemes based on Eshelby solutions can be derived within the formalism defined in the previous section. In this sense, Sanahuja (2013) provides the diluted, Mori-Tanaka and Self-consistent estimations.

In the following, the (t, \cdot) dependencies will be omitted for conciseness.

5.2.2 Mori-Tanaka estimations

Mori and Tanaka (1973) derived estimations for a matrix-inclusions composite in which the matrix is taken as the reference medium. The estimations are based on Eshelby solution in elasticity for an inclusion in an infinite medium. The phase interaction is taken into account in a collective way (Mori and Tanaka, 1973).

In the ageing linear viscoelastic framework, for spherical inclusions, Mori-Tanaka estimations of the bulk and shear modulus for a N -phases composite are given, respectively, by (Sanahuja, 2013):

$$k_{MT} = \left(\sum_{i=0}^N f_i^v k_i \circ {}^k A_i^0 \right) \circ \left(\sum_{i=0}^N f_i^v {}^k A_i^0 \right)^{-1} \quad (5.17)$$

$$\mu_{MT} = \left(\sum_{i=0}^N f_i^v k_i \circ {}^\mu A_i^0 \right) \circ \left(\sum_{i=0}^N f_i^v {}^\mu A_i^0 \right)^{-1} \quad (5.18)$$

where f_i^v is the volume fraction of the phase (i) (with $i = 0$ corresponding to the matrix and $i > 0$ corresponding to the inclusions). The localization tensor within the spherical inclusions was decomposed in a hydrostatic and deviatoric parts given, respectively, by (Sanahuja, 2013):

$${}^k A_i^0 = (3k_i + 4\mu_0)^{-1} \circ (3k_0 + 4\mu_0) \quad (5.19)$$

$${}^\mu A_i^0 = H_{t'} + 2(2H_{t'} + 3\Xi) \circ [2\mu_i \circ (2H_{t'} + 3\Xi) + 2\mu_0 \circ (6H_{t'} - \Xi)]^{-1} \circ (\mu_0 - \mu_i) \quad (5.20)$$

with ${}^j A_1^1 = {}^k A_1^1 = H_{t'} \mathbf{I}$ and $\Xi = \frac{2}{3}(k_0 + \mu_0)^{-1} \circ \mu_1$. As expected, these estimations of k_i and μ_i are a generalization of the results in elasticity and non-ageing viscoelasticity.

5.2.3 Generalized self-consistent (GSC) scheme: n-coated spherical inclusion estimations

In this section, the estimations of the effective shear and bulk modulus of a n-coated spherical inclusion morphology are derived using the formalism defined in section 5.1.3. All phases are assumed homogeneous and isotropic and no defects on the interfaces are accounted for. Phase 1 is

the spherical core with radius R_1 embedded in concentric shells of phase (i) with internal radius R_{i-1} and external radius R_i (Figure 5.3) with $i \in [1, n + 1]$. $R_{n+1} \rightarrow \infty$.

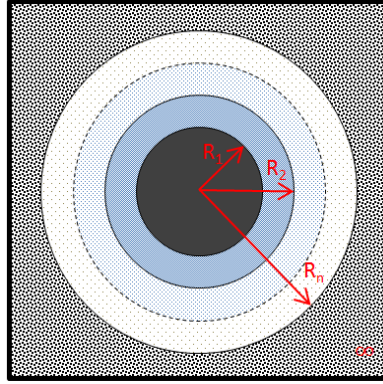


Figure 5.3 Microstructure representation

5.2.3.1 Bulk modulus

Applying an isotropic uniform strain $\mathbf{E}(\mathbf{t}) = e(t)\mathbf{1}$ at infinity on the microstructure of Figure 5.3 right, the displacement field in each phase (i) is given, in spherical coordinates, by (Love, 1944):

$$\mathbf{u}_i(\mathbf{x}, t) = \left(f_i(t) r + \frac{g_i(t)}{r^2} \right) \mathbf{e}_r \quad (5.21)$$

where f_i and g_i are functions dependent of the time. Due to spherical symmetry the problem is reduced to one dimension. The stress in the rr direction is given then by (Love, 1944; Sanahuja, 2013a):

$$\sigma_{rr} = 3k_i(t) \circ f_i(t) + \frac{1}{r^3} 4\mu_i(t) \circ g_i(t) \quad (5.22)$$

Applying the boundary conditions with $r \rightarrow 0$ and $r \rightarrow \infty$, we get $g_1(t) = 0$ so that no singularity is obtained at the origin and $f_{n+1}(t) = e(t)$. Applying the continuity of the stress and displacement fields σ_{rr}^i and u_r^i at the interface $r = R_i$ between the phases i and $(i + 1)$, we obtain:

$$\mathbf{J}_i(R_i) \overset{\circ}{\ast} [f_i, g_i]^t = \mathbf{J}_{i+1}(R_i) \overset{\circ}{\ast} [f_{i+1}, g_{i+1}]^t \quad (5.23)$$

with " $\overset{\circ}{\ast}$ " being, as defined in section 5.1.3, the matrix product in the sense of Volterra operator and

$$\mathbf{J}_i(r) = \begin{bmatrix} r & 1/r^2 \\ 3k_i & \frac{-4}{r^3} \mu_i \end{bmatrix} \quad (5.24)$$

Then, the vector $[f_{i+1}, g_{i+1}]^t$ can be written as:

$$[f_{i+1}, g_{i+1}]^t = \mathbf{J}_{i+1}^{-1}(R_i) \overset{\circ}{*} \mathbf{J}_i(R_i) \overset{\circ}{*} [f_i, g_i]^t = \mathbf{N}^{(i)} \overset{\circ}{*} [f_i, g_i]^t \quad (5.25)$$

where

$$\mathbf{N}^{(i)} = \mathbf{J}_{i+1}^{-1}(R_i) \overset{\circ}{*} \mathbf{J}_i(R_i) = [4\mu_{i+1} + 3k_{i+1}]^{-1} \circ \begin{bmatrix} 4\mu_{i+1} + 3k_i & \frac{4}{R_i^3}(\mu_{i+1} - \mu_i) \\ 3R_i^3(k_{i+1} - k_i) & 3k_{i+1} - 4\mu_i \end{bmatrix} \quad (5.26)$$

Note that because of the non-commutativity of the operator " \circ ", the inversion of \mathbf{J}_{i+1} must take into account the non-commutativity of the elements of the matrix \mathbf{J} . Matrices in non-commutative rings may own a right and a left inverse. For a 2x2 matrix the inversion is easy to compute, and the right inverse corresponds to the left inverse for \mathbf{J} as defined here.

Following Herve and Zaoui (1993) derivation, we can similarly define the matrix $\mathbf{Q}^{(i)}$ from:

$$[f_{i+1}, g_{i+1}]^t = \overbrace{\prod_{j=1}^i}^{\circ} \mathbf{N}^{(j)} \overset{\circ}{*} [f_1, g_1]^t = \mathbf{Q}^{(i)} \overset{\circ}{*} [f_1, g_1]^t \quad (5.27)$$

where the product $\overbrace{\prod_j^i}^{\circ} \mathcal{F}^{(j)}$ is defined in terms of the operator " $\overset{\circ}{*}$ ".

From the previous equation and taking into account that $g_1 = 0$, we obtain:

$$\begin{aligned} f_k &= Q_{11}^{(k-1)} \circ [Q_{11}^{(n)}]^{-1} \circ f_{n+1} \\ g_k &= Q_{21}^{(k-1)} \circ [Q_{11}^{(n)}]^{-1} \circ f_{n+1} \end{aligned} \quad (5.28)$$

with $k \in [1, n]$.

The energy conditions defined by (Christensen and Lo, 1979) for a 3-phase model, as cited by Herve and Zaoui (1993), demands that the average strain in the composite inclusion $\bar{\boldsymbol{\epsilon}}(t)$ is the same as the macroscopic strain imposed at the infinity $\boldsymbol{\epsilon}_0(t)$, i.e. $\bar{\boldsymbol{\epsilon}}(t) = \boldsymbol{\epsilon}_0(t)$. Similar reasoning can be made for uniform stress conditions. Accordingly, for an n-phase sphere composite we have $g_{n+1} = 0$.

From Eqs. (5.25) and (5.27), we can write:

$$[f_{i+1}, g_{i+1}]^t = \mathbf{N}^{(n)} \overset{\circ}{*} \mathbf{Q}^{(n-1)} \overset{\circ}{*} [f_1, g_1]^t \quad (5.29)$$

From this equation, g_{i+1} may be written as:

$$\begin{aligned} g_{i+1} &= [4\mu_{n+1} + 3k_{n+1}]^{-1} \circ \left([3R_n^3(k_{n+1} - k_n)] \circ Q_{11}^{(n-1)} + [3k_{n+1} - 4\mu_n] \circ Q_{21}^{(n-1)} \right) \\ &\quad \circ f_1 \end{aligned} \quad (5.30)$$

which allows determining, the effective bulk modulus $k_{(n)}^{eff}$ for a n-layered composite sphere:

$$k_{(n)}^{eff} = k_{n+1} = \left[3R_n^3 k_n \circ Q_{11}^{(n-1)} - 4\mu_n \circ Q_{21}^{(n-1)} \right] \circ \left[3R_n^3 Q_{11}^{(n-1)} + 3Q_{21}^{(n-1)} \right]^{-1} \quad (5.31)$$

For $n = 2$, i.e. a 3 phase scheme, we have :

$$k_{(2)}^{eff} = \left[k_2 \circ [4\mu_2 + 3k_2]^{-1} \circ [4\mu_2 + 3k_1] - 4\mu_2 \circ [4\mu_2 + 3k_2]^{-1} \circ [f_{12}^v(k_2 - k_1)] \right] \circ \left[[4\mu_2 + 3k_2]^{-1} \circ [4\mu_2 + 3k_1] + 3[4\mu_2 + 3k_2]^{-1} \circ [f_{12}^v(k_2 - k_1)] \right]^{-1} \quad (5.32)$$

where f_{12}^v is the volume fraction of phase 1 with respect to phase 2: $f_{12}^v = R_1^3/R_2^3$. In the elastic case, this equation reduces, as expected, to Herve and Zaoui (1993) equation or Hashin and Shtrikman (1963) lower bound:

$$k_{(2)}^{eff} = k_2 + \frac{f_{12}^v}{\frac{1}{(k_2 - k_1)} + \frac{3(1 - f_{12}^v)}{(3k_2 + 4\mu_2)}} \quad (5.33)$$

Similarly, for $n = 3$, we have

$$k_{(3)}^{eff} = \left[3R_3^3 k_3 \circ Q_{11}^{(2)} - 4\mu_3 \circ Q_{21}^{(2)} \right] \circ \left[3R_3^3 Q_{11}^{(2)} + 3Q_{21}^{(2)} \right]^{-1} \quad (5.34)$$

with

$$Q_{11}^{(2)} = [4\mu_2 + 3k_2]^{-1} \circ [4\mu_2 + 3k_1] \circ [4\mu_3 + 3k_3]^{-1} \circ [4\mu_3 + 3k_2] + [4\mu_2 + 3k_2]^{-1} \circ \left[\frac{4}{R_1^3} (\mu_3 - \mu_2) \right] \circ [4\mu_3 + 3k_3]^{-1} \circ [3R_2^3 (k_3 - k_2)] \quad (5.35)$$

$$Q_{21}^{(2)} = [4\mu_2 + 3k_2]^{-1} \circ [3R_1^3 (k_2 - k_1)] \circ [4\mu_3 + 3k_3]^{-1} \circ [4\mu_3 + 3k_2] + [4\mu_2 + 3k_2]^{-1} \circ [3k_2 - 4\mu_1] \circ [4\mu_3 + 3k_3]^{-1} \circ [3R_2^3 (k_3 - k_2)]$$

5.2.3.2 Shear modulus

Applying a deviatoric uniform strain $\mathbf{E}(t) = e(t)(\mathbf{e}_1 \otimes \mathbf{e}_1 - \mathbf{e}_2 \otimes \mathbf{e}_2)$, \mathbf{e}_1 and \mathbf{e}_2 orthogonal unitary vectors, at the boundary of the microstructure shown in Figure 5.3 right, the displacement in the phase (i) is given by (Love, 1944):

$$\mathbf{u}^{(i)}(\mathbf{x}, t) = u_r^{(i)}(r, t) \sin^2 \theta \cos 2\phi \mathbf{e}_r + u_\theta^{(i)}(r, t) \sin \theta \cos \theta \cos 2\phi \mathbf{e}_\theta + u_\phi^{(i)}(r, t) \sin \theta \sin 2\phi \mathbf{e}_\phi \quad (5.36)$$

where \mathbf{e}_r , \mathbf{e}_θ and \mathbf{e}_ϕ are the unitary vectors corresponding to the spherical coordinates (r, θ, ϕ) .

The solution of the equilibrium of the stresses field within each phase allows writing in an ageing viscoelastic framework (Sanahuja, 2013a):

$$\begin{aligned}
u_r^{(i)} &= a_i(t)r - 3(k_i - 2\mu_i) \circ b_i(t)r^3 + 3\frac{c_i(t)}{r^4} + 3[\mu_i]^{-1} \circ (k_i + \mu_i) \circ \frac{d_i(t)}{r^2} \\
u_\theta^{(i)} &= a_i(t)r - (15k_i - 11\mu_i) \circ b_i(t)r^3 - 2\frac{c_i(t)}{r^4} + 2\frac{d_i(t)}{r^2} \\
u_\phi^{(i)} &= -u_\theta^{(i)}
\end{aligned} \tag{5.37}$$

where a_i, b_i, c_i and d_i are function of the time. Applying the continuity of the stresses and displacement fields at $r = R_k$ for $\sigma_{rr}, \sigma_{r\theta}, \sigma_{r\phi}, u_r, u_\theta$ and u_ϕ (note that only four of these conditions are independent), we obtain

$$\mathbf{L}_i(R_i) \overset{\circ}{*} [a_i, b_i, c_i, d_i]^t = \mathbf{L}_{i+1}(R_i) \overset{\circ}{*} [a_{i+1}, b_{i+1}, c_{i+1}, d_{i+1}]^t \tag{5.38}$$

with

$$\mathbf{L}_i(r) = \begin{bmatrix} r & -3r^3(k_i - 2\mu_i) & \frac{3}{r^4} & \frac{3}{r^2}[\mu_i]^{-1} \circ (k_i + \mu_i) \\ r & -r^3(15k_i - 11\mu_i) & -\frac{2}{r^4} & \frac{2}{r^2} \\ \mu_i & \frac{r^2}{2}[\mu_i]^{-1} \circ (3k_i - 2\mu_i) & -\frac{12}{r^5}\mu_i & -\mu_i \circ (9k_i + 4\mu_i) \frac{1}{r^3} \\ \mu_i & -\mu_i \circ (5\mu_i + 8k_i) \circ [\mu_i]^{-1}r^2 & \frac{8}{r^5}\mu_i & \frac{3}{r^3}k_i \end{bmatrix} \tag{5.39}$$

where, again, " $\overset{\circ}{*}$ " is the matrix product in the sense of Volterra operator.

Defining the bulk modulus as $k_i = \frac{2}{3}\mu_i \circ (H + \check{\nu}_i) \circ (H - 2\check{\nu}_i)^{-1}$, where H is the Heaviside function in which the age of loading t' is omitted, we obtain a form corresponding to $\mathbf{L}_i(r)$ derived by (Herve and Zaoui, 1993), where $\check{\nu}$, in the elastic case, would correspond to the Poisson ratio. In the ageing viscoelastic case, this definition of Poisson ratio seems to us natural as it is obtained straightforwardly from moduli, but may not be unique if defined from strains ratio due to complex time and loading dependencies (see e.g. (Hilton and Yi, 1998) for a related discussion in the linear viscoelastic context).

For the phase $i + 1$ we can write then:

$$[a_{i+1}, b_{i+1}, c_{i+1}, d_{i+1}]^t = \mathbf{L}_{i+1}^{-1}(R_i) \overset{\circ}{*} \mathbf{L}_i(R_i) \circ [a_i, b_i, c_i, d_i]^t = \mathbf{M}^{(i)} \overset{\circ}{*} [a_i, b_i, c_i, d_i]^t \tag{5.40}$$

where

$$\mathbf{M}^{(i)} = \mathbf{L}_{i+1}^{-1}(R_i) \overset{\circ}{*} \mathbf{L}_i(R_i) \tag{5.41}$$

Note that because of the boundary conditions at $r = 0$ and $r \rightarrow \infty$, c_1, d_1 and b_{n+1} vanish and $a_{n+1} = e(t)$.

Similar to the inversion of \mathbf{J} in the last section, the inversion of \mathbf{L} must take into account that some elements of the matrix are non-commutative. Here we use a method based on the Schur complement to compute \mathbf{L}^{-1} (Horn, 1990) via NCAAlgebra (<http://math.ucsd.edu/~ncalg/>), a package for non-commutative algebra for Mathematica. We obtain:

$$\mathbf{M}^{(k)} = \frac{1}{5}(\mathbf{H} - \check{\nu}_{k+1}) \circ \begin{bmatrix} \frac{C_k}{3} & \frac{R_k^2}{5}(3B_k - 7C_k) \circ (\mathbf{H} - 2\check{\nu}_k)^{-1} & & & \\ 0 & \frac{1}{7}(\mathbf{H} - 2\check{\nu}_{k+1}) \circ B_k \circ (\mathbf{H} - 2\check{\nu}_k)^{-1} & & & \\ \frac{R_k^5 \alpha_k}{2} & \frac{-R_k^7}{70}(2A_k + 147\alpha_k) \circ (\mathbf{H} - 2\check{\nu}_k)^{-1} & \dots & & \\ \frac{-5R_k^3}{6}(\mathbf{H} - 2\check{\nu}_{k+1}) \circ \alpha_k & \frac{7R_k^5}{2}(\mathbf{H} - 2\check{\nu}_{k+1}) \circ \alpha_k \circ (\mathbf{H} - 2\check{\nu}_k)^{-1} & & & \\ & -\frac{12\alpha_k}{R_k^5} & \frac{4}{15R_k^3}(F_k - 27\alpha_k) \circ (\mathbf{H} - 2\check{\nu}_k)^{-1} & & \\ \dots & \frac{-20}{7R_k^7}(\mathbf{H} - 2\check{\nu}_{k+1}) \circ \alpha_k & \frac{12}{7R_k^5}(\mathbf{H} - 2\check{\nu}_{k+1}) \circ \alpha_k \circ (\mathbf{H} - 2\check{\nu}_k)^{-1} & & \\ & \frac{D_k}{7} & \frac{R_k^2}{35}(G_k - 7E_k) \circ (\mathbf{H} - 2\check{\nu}_k)^{-1} & & \\ & 0 & \frac{1}{3}(\mathbf{H} - 2\check{\nu}_{k+1}) \circ E_k \circ (\mathbf{H} - 2\check{\nu}_k)^{-1} & & \end{bmatrix} \quad (5.42)$$

where

$$\begin{aligned} A_k &= (7\mathbf{H} - 10\check{\nu}_k) \circ (\mu_{k+1}^{-1} \circ \mu_k) \circ (7\mathbf{H} + 5\check{\nu}_{k+1}) - (7\mathbf{H} - 10\check{\nu}_k) \circ (7\mathbf{H} + 5\check{\nu}_{k+1}) \\ B_k &= 4(7\mathbf{H} - 10\check{\nu}_k) + (\mu_{k+1}^{-1} \circ \mu_k) \circ (7\mathbf{H} + 5\check{\nu}_k) \\ C_k &= (7\mathbf{H} - 5\check{\nu}_{k+1}) + 2(4\mathbf{H} - 5\check{\nu}_{k+1}) \circ (\mu_{k+1}^{-1} \circ \mu_k) \\ D_k &= (7\mathbf{H} + 5\check{\nu}_{k+1}) + 4(7\mathbf{H} - 10\check{\nu}_{k+1}) \circ (\mu_{k+1}^{-1} \circ \mu_k) \\ E_k &= 2(4\mathbf{H} - 5\check{\nu}_k) + (\mu_{k+1}^{-1} \circ \mu_k) \circ (7\mathbf{H} - 5\check{\nu}_k) \\ F_k &= (4\mathbf{H} - 5\check{\nu}_k) \circ (7\mathbf{H} - 5\check{\nu}_{k+1}) - (4\mathbf{H} - 5\check{\nu}_{k+1}) \circ (\mu_{k+1}^{-1} \circ \mu_k) \circ (7\mathbf{H} - 5\check{\nu}_k) \\ G_k &= 105(\mathbf{H} - \check{\nu}_{k+1}) + 12(7\mathbf{H} - 10\check{\nu}_k) \circ \alpha_k \\ \alpha_k &= (\mu_{k+1}^{-1} \circ \mu_k) - \mathbf{H} \end{aligned} \quad (5.43)$$

The parameters in Eq. (5.40) of phase $(i + 1)$ can be written then as a function of the parameters related to the core (phase 1) by:

$$[a_{i+1}, b_{i+1}, c_{i+1}, d_{i+1}]^t = \overbrace{\prod_{j=1}^i \mathbf{M}^{(j)}}^{\circ} \overset{\circ}{\ast} [a_1, b_1, c_1, d_1]^t = \mathbf{P}^{(i)} \overset{\circ}{\ast} [a_1, b_1, c_1, d_1]^t \quad (5.44)$$

where $\mathbf{P}^{(k)}$ is obtained, as $\mathbf{Q}^{(k)}$ in Section 5.2.2, by means of matrix product regarding the operator " \circ " .

Because $b_{n+1} = 0$, we obtain, for a n -layered inclusion:

$$\begin{aligned} a_1 &= - \left(P_{12}^{(n)} \circ P_{22}^{(n)-1} \circ P_{21}^{(n)} - P_{11}^{(n)} \right)^{-1} \circ a_{i+1} \\ b_1 &= \left(P_{12}^{(n)} - P_{11}^{(n)} \circ P_{21}^{(n)-1} \circ P_{22}^{(n)} \right)^{-1} \circ a_{i+1} \end{aligned} \quad (5.45)$$

$$\begin{aligned} [a_i, b_i, c_i, d_i]^t &= \mathbf{P}^{(i-1)} \overset{\circ}{*} \left[- \left(P_{12}^{(n)} \circ P_{22}^{(n)-1} \circ P_{21}^{(n)} - P_{11}^{(n)} \right)^{-1}, \left(P_{12}^{(n)} - P_{11}^{(n)} \circ P_{21}^{(n)-1} \right. \right. \\ &\quad \left. \left. \circ P_{22}^{(n)} \right)^{-1}, 0, 0 \right]^t \circ a_{i+1} \end{aligned} \quad (5.46)$$

As in the elastic case, so that the average strain of the n -layered composite sphere is the same as the macroscopic strain imposed at the infinity, the condition $d_{n+1} = 0$ is necessary. With this conditions, we can write:

$$-P_{41}^{(n)} \circ \left(P_{12}^{(n)} \circ P_{22}^{(n)-1} \circ P_{21}^{(n)} - P_{11}^{(n)} \right)^{-1} + P_{42}^{(n)} \circ \left(P_{12}^{(n)} - P_{11}^{(n)} \circ P_{21}^{(n)-1} \circ P_{22}^{(n)} \right)^{-1} = 0 \quad (5.47)$$

Finally, from Eq. (5.44), we obtain the general form:

$$\begin{aligned} & - \left(M_{41}^{(n)} \circ P_{11}^{(n-1)} + M_{42}^{(n)} \circ P_{12}^{(n-1)} + M_{43}^{(n)} \circ P_{13}^{(n-1)} + M_{44}^{(n)} \circ P_{14}^{(n-1)} \right) \\ & \circ \left(-M_{11}^{(n)} \circ P_{11}^{(n-1)} - M_{12}^{(n)} \circ P_{21}^{(n-1)} - M_{13}^{(n)} \circ P_{31}^{(n-1)} - M_{14}^{(n)} \circ P_{41}^{(n-1)} \right. \\ & + \left(M_{11}^{(n)} \circ P_{12}^{(n-1)} - M_{12}^{(n)} \circ P_{22}^{(n-1)} - M_{13}^{(n)} \circ P_{32}^{(n-1)} - M_{14}^{(n)} \circ P_{42}^{(n-1)} \right) \\ & \circ \left(M_{21}^{(n)} \circ P_{12}^{(n-1)} - M_{22}^{(n)} \circ P_{22}^{(n-1)} - M_{23}^{(n)} \circ P_{32}^{(n-1)} - M_{24}^{(n)} \circ P_{42}^{(n-1)} \right)^{-1} \\ & \circ \left(M_{21}^{(n)} \circ P_{11}^{(n-1)} - M_{22}^{(n)} \circ P_{21}^{(n-1)} - M_{23}^{(n)} \circ P_{31}^{(n-1)} - M_{24}^{(n)} \circ P_{41}^{(n-1)} \right)^{-1} \\ & + \left(M_{41}^{(n)} \circ P_{11}^{(n-1)} + M_{42}^{(n)} \circ P_{22}^{(n-1)} + M_{43}^{(n)} \circ P_{32}^{(n-1)} + M_{44}^{(n)} \circ P_{42}^{(n-1)} \right) \\ & \circ \left(M_{11}^{(n)} \circ P_{12}^{(n-1)} + M_{12}^{(n)} \circ P_{22}^{(n-1)} + M_{13}^{(n)} \circ P_{32}^{(n-1)} + M_{14}^{(n)} \circ P_{42}^{(n-1)} \right. \\ & - \left(M_{11}^{(n)} \circ P_{11}^{(n-1)} + M_{12}^{(n)} \circ P_{21}^{(n-1)} + M_{13}^{(n)} \circ P_{31}^{(n-1)} + M_{14}^{(n)} \circ P_{41}^{(n-1)} \right) \\ & \circ \left(M_{21}^{(n)} \circ P_{11}^{(n-1)} + M_{22}^{(n)} \circ P_{21}^{(n-1)} + M_{23}^{(n)} \circ P_{31}^{(n-1)} + M_{24}^{(n)} \circ P_{41}^{(n-1)} \right)^{-1} \\ & \circ \left(M_{21}^{(n)} \circ P_{12}^{(n-1)} + M_{22}^{(n)} \circ P_{22}^{(n-1)} + M_{23}^{(n)} \circ P_{32}^{(n-1)} + M_{24}^{(n)} \circ P_{42}^{(n-1)} \right)^{-1} \\ & = 0 \end{aligned} \quad (5.48)$$

Note that, although k_{n+1} is present in $\mathbf{M}^{(n)}$ through \check{V}_{k+1} , in Eq. (5.48) this term is eliminated with the substitutions of terms of matrix $\mathbf{M}^{(n)}$.

In the elastic case, Eq. (5.48) reduces to the second degree polynomial as obtained by Herve and Zaoui (1993). Once a method to evaluate the Volterra integral is chosen, this equation can be similarly solved for $(\mu_{k+1}^{-1} \circ \mu_k)$ which appears in the equation (5.43).

5.2.3.3 Average strains

To determine the strain and stress localization tensors for the GSC scheme in an ageing viscoelastic ground, the average strain in each phase is computed by (Herve and Zaoui, 1993):

$$\boldsymbol{\varepsilon}^{(i)} = \frac{1}{V_i} \int_{V_i} \boldsymbol{\varepsilon}^{(i)} dV = \frac{1}{V_i} \left[\int_{S_i} (\mathbf{u}^{(i)} \otimes \mathbf{n})^s dS - \int_{S_{i-1}} (\mathbf{u}^{(i)} \otimes \mathbf{n})^s dS \right] \quad (5.49)$$

where V_i is the volume of the phase (i), between the surface shells S_i and S_{i-1} ; and $(\cdot)^s$ is the symmetrical part operator.

For uniform strain conditions prescribed at infinity, as in the elastic case (Herve and Zaoui, 1993), the volumetric part of the strain phase (i) is shown to be uniform and the average vanishes for the case of prescribed uniform deviatoric strain conditions \mathbf{e}_0 . We obtain then the average of the volumetric part of the strain in phase (i) is:

$$\bar{\boldsymbol{\theta}}^{(i)} = f_i \circ [f_{n+1}]^{-1} \boldsymbol{\theta}_0 \quad (5.50)$$

where in the displacement approach the boundary displacement are $\mathbf{u}^{(0)} = r \theta_0 \mathbf{e}_r$.

Similarly, for the deviatoric part we have:

$$\begin{aligned} \text{dev} \int_{S_i} (\mathbf{u}^{(i)} \otimes \mathbf{n})^s dS \\ = -\frac{4\pi}{5} [a_{n+1}]^{-1} \\ \circ \left(\frac{5}{3} R_i^3 a_i - 7 R_i^5 [H - 2\check{\nu}_i]^{-1} \circ b_i + \frac{4}{3} (4H - 5\check{\nu}_i) \circ [H - 2\check{\nu}_i]^{-1} \circ d_i \right) \mathbf{e}_0 \end{aligned} \quad (5.51)$$

The same equation is true for S_{i-1} by changing the index (i) by $(i-1)$, which leads after some manipulations to the average deviatoric strain in phase (i):

$$\bar{\boldsymbol{\varepsilon}}^{(i)} = [a_{n+1}]^{-1} \circ \left(a_i - \frac{21}{5} \frac{(R_i^5 - R_{i-1}^5)}{(R_i^3 - R_{i-1}^3)} \circ b_i \right) \mathbf{e}_0 \quad (5.52)$$

Again, the correspondence with elastic results obtained by Herve and Zaoui (1993) is effective, provided the order with respect to the operator “ \circ ” is respected. The strain and stress localization tensors can be calculated by applying the results obtained in this section.

5.2.4 Numerical evaluation of the Volterra integral

The trapezoidal rule is used to compute the Volterra product. This is a common method of numerical evaluation of Volterra integral equations (Jerri, 1999). Here, we employ Bažant (1972) algorithm. The time is discretised in $p + 1$ steps. The kernel $f(t, t')$ is converted in a matrix $[[f]]_{(p+1) \times (p+1)}$ and the product " \circ " in a matrix-vector product (Sanahuja, 2013a):

$$y = f \circ x \simeq [y] = [[f]] \cdot [x] \quad (5.53)$$

with

$$2f_{ij} = \begin{cases} f(t_0, 0) + f(t_0, t_0) & \text{for } i = j = 0 \\ f(t_i, 0) + f(t_i, t_1) & \text{for } i \geq 1, j = 0 \\ f(t_i, t_{j-1}) - f(t_i, t_{j+1}) & \text{for } i \geq 2, 1 \leq j \leq i - 1 \\ f(t_i, t_{i-1}) + f(t_i, t_i) & \text{for } i \geq 1, j = i \\ 0 & \text{for } 1 \leq i + 1 \leq j \leq p \end{cases} \quad (5.54)$$

As expected, because of the causality principle, $[[f]]$ is lower triangular (Bažant, 1972). The inversion with respect to Volterra operator is then easily computed as a matrix inversion. Note that with this form of evaluation of the Volterra integral, the entire behaviour is obtained.

To solve Eq. (5.48), a system with $(p + 2)^2/2$ equations must be solved. This task can be quite expensive computationally if direct solvers are used. Here, we rewrite the problem as a constrained optimization problem where the sum of the square of the elements of the matrix formed with the algorithm in Eq. (5.50) is minimized. Mori-Tanaka solution is used as a starting point of the optimization process. This minimization procedure is carried out in Mathematica®.

With this conversion, in the Volterra integral operator formalism, the compliance tensor can be computed by matrix inversion of the relaxation tensor.

5.3 NUMERICAL HOMOGENIZATION

Direct numerical simulations of heterogeneous materials were developed by the end of 1960s (Adams and Doner, 1967; Needleman and Tvergaard, 1993; cited by Chamrova, 2010). Since that time, with the increasing in the computational capacity, more complex microstructures have been studied with different numerical methods being employed in the determination of the effective properties of heterogeneous materials. Finite Element Method, Fast Fourier Transform (FFT) and Extended Finite Element Method (XFEM) are examples of numerical methods currently used (Dunant et al., 2013).

Compared to analytical approaches, numerical homogenization allows, in one hand, to assess more complex mesostructures. Analytical homogenization is often limited to simple geometries such as spheres and ellipsoids. With numerical homogenization mesostructures closer to the real ones (with, for instance, polyhedral inclusions or even mesostructure obtained from tomography) can be assessed. Additionally, numerical homogenization allows obtaining local information within the

mesostructure, while analytical homogenization provides in general only the averaged fields evaluated within the considered phases. With numerical homogenization, these fields can be obtained within each inclusion and subvolume of the matrix. This is an important feature in the study of the mismatch of properties in heterogeneous materials, since it allows identifying the zones where the stresses (or strains) may potentially reach the strength of the material.

Regarding the applications, different mesoscopic models were applied to determine concrete or cement-based material effective behaviour (see e.g. (Briffaut et al., 2013; Sadouki and Wittmann, 1988; Schorn and Rode, 1991; Wang et al., 1999; Wriggers and Moftah, 2006)). Again, as for analytical homogenization, ageing viscoelastic behaviour was less studied with numerical homogenization.

The details about the behaviour, microstructure and mesh generation as well as the determination of effective properties are discussed in the following.

Part of the numerical campaign presented in the following was performed in the framework of the Master project of R. Fares on the numerical estimation of ageing linear viscoelastic properties of composites with random microstructures (Fares, 2015).

The ageing linear viscoelastic behaviour can be implemented following an algorithm similar to the one of Bažant (1972) introduced in Section 5.4.2. This behaviour was implemented in Cast3m by means of MFront code generator (<http://tfel.sourceforge.net/>).

5.3.1 Mesostructure generations

The geometries studied here are obtained by randomly distributing the inclusions in a box. Only spherical inclusions are considered in this chapter. Polyhedral aggregates of various sizes and shapes obtained by a classical Voronoi space decomposition (de Larrard et al., 2013) will be considered in Chapter 6. The number and volume of inclusions are defined to match the ones of the corresponding spheres assembly according to the sieve curve described in de Larrard et al. (2013).

The procedure for constructing the mesostructures is detailed in Bourcier et al. (2014) and Bary et al., (2009). The open-source python library Combs based on the Computer-Aided Design code (Salome) is used to generate geometry and meshes of the mesostructures (Bourcier et al., 2014). The GJK 3D algorithm has been recently implemented in Combs for fast convex particles distance computation (see e.g. <http://www.dyn4j.org/2010/04/gjkdistance-closest-points>).

The mesostructures are tested to evaluate their isotropy: the loading is applied in the three orthogonal directions and the responses are compared. If the results are close enough, the mesostructure is considered as isotropic. Figure 5.4 shows an example of such verification.

Special attention must be paid to the errors induced by the intrinsic approximations in numerical methods. Errors may arise, for example, from the discretization (elements too large to capture the strain gradients) and geometry non-conformity (e.g. approximate representation of the

particles boundaries which may affect the volume fraction of the phases) (Dunant et al., 2013). A study concerning the mesh refinement is conducted in section 5.4.3.

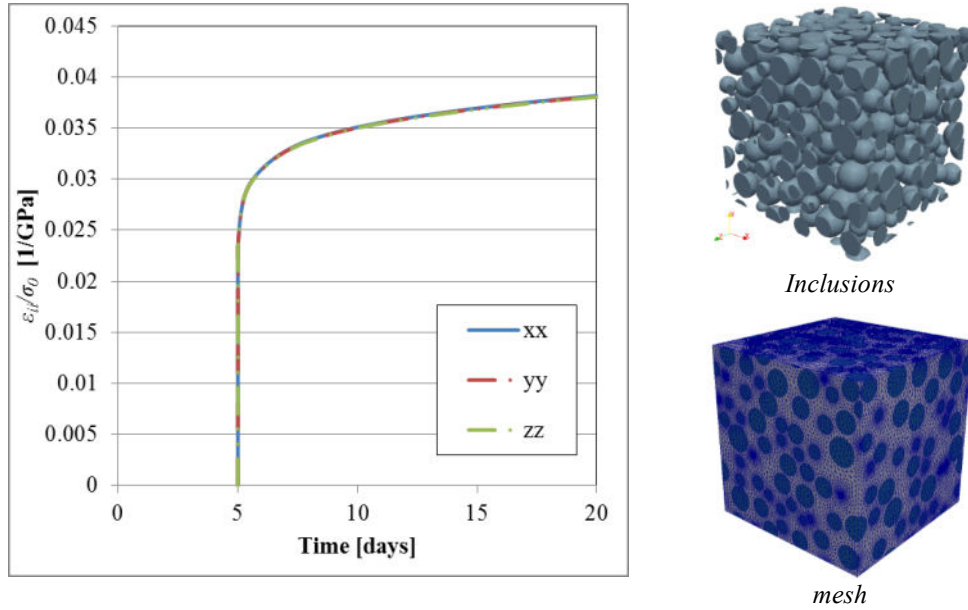


Figure 5.4 Example of verification of the isotropy (left) for a meshed mesostructure (right): Evaluation of the ratio strain/stress in the direction ii of the loading. The curves are superposed.

The size of the mesostructure with respect to the maximum size of the inclusions should be defined in order to limit the estimation errors. Drugan and Willis (1996) reported that estimations using a mesostructure size of about twice the maximum diameter of the inclusions (biphasic material) yields errors of the order of 5%, whereas using a mesostructure whose edges are 5 times the diameter of biggest inclusion yields errors of about 1% in the estimations independently of the phase contrast. In this chapter, the side of the (cubic) mesostructure is 6.6 times the maximum equivalent diameter of the inclusions.

5.3.2 Influence of the boundary conditions

The estimation of the effective properties depends on the boundary conditions imposed on the numerical samples. Kinematic uniform (KUBC) (see Eq. (5.13)), static uniform (SUBC) (Eq. (5.55)) and periodic boundary conditions (Eq. (5.56)) are currently imposed on numerical mesostructures. KUBC and SUBC provide bounds for other BC in simulations in the case of elasticity (Sab, 1992).

$$\boldsymbol{\sigma}(\mathbf{x}, t) \cdot \mathbf{n} = \boldsymbol{\Sigma}(t) \cdot \mathbf{n}, \quad \forall \mathbf{x} \in \partial\Omega \quad (5.55)$$

$$\mathbf{u}(\mathbf{x}, t) = \mathbf{E}(t) \cdot \mathbf{x} + \mathbf{v}, \quad \mathbf{x} \in \Omega, \quad \mathbf{v} \text{ periodic} \quad (5.56)$$

where \mathbf{n} is the normal to $\partial\Omega$.

Pecullan et al. (1999) showed that the apparent *elastic* moduli are overestimated under SUBC, and underestimated under KUBC. The difference between both estimations depends strongly on the phase contrast: KUBC provides a more accurate estimate if the matrix is stiffer than the inclusions;

while SUBC provides a more accurate estimate if the matrix is less stiff than the inclusions (Pecullan et al., 1999). Accordingly, these authors point out that the size of the mesostructure for high contrast composites should be larger than those for composites with low contrast (Kanit et al., 2003).

Regarding *non-ageing linear viscoelastic* behaviour, Huet (1999) highlights that the independency of the overall properties regarding the boundary conditions is to be understood as the creep function tensor in SUBC, for instance, being the convolutive reciprocal of the relaxation function tensor in KUBC, and vice versa.

To our knowledge, no formal definitions of the effects of the boundary conditions and coupled size effects were proposed to date for *ageing linear viscoelastic* behaviours.

5.3.3 Determination of effective properties

In elasticity, the effective bulk and shear moduli can be obtained from the macroscopic state of stress Σ and strain \mathbf{E} , by the formula e.g. (Wriggers and Moftah, 2006):

$$k^{app} = \frac{1 \operatorname{tr}[\Sigma]}{3 \operatorname{tr}[\mathbf{E}]} \quad (5.57)$$

$$\mu^{app} = \frac{1}{2} \sqrt{\frac{\operatorname{dev}[\Sigma]:\operatorname{dev}[\Sigma]}{\operatorname{dev}[\mathbf{E}]:\operatorname{dev}[\mathbf{E}]}} \quad (5.58)$$

In ageing viscoelasticity the estimation of these effective properties depends on the features of the simulation experiments. As shown in section 5.1.1, from a creep test it is possible to derive the creep scalar function $J(t, t_0)$ from the stresses and strains fields at a given time (with no need to account for the historic). The corresponding compliance tensor can be written for this case. Likewise, by means of the inversions relations of the complaisance and relaxation tensors the effective material properties, k^{app} and μ^{app} , can be obtained from the stress and strain fields at a given time with the hypothesis of isotropy.

5.4 APPLICATION TO AGEING MATERIALS

The results obtained with analytical homogenization are compared to results from numerical simulations. A composite with elastic cores and phases with intrinsically ageing viscoelastic behaviour is studied. In the latter, we adopt the generalized Maxwell behaviour associated with an ageing function $f_{age}(t')$. The ageing function arbitrarily chosen, illustrated in Figure 5.5, is given by:

$$f_{age}(t') = \frac{3}{4} (1 - \exp[-t']) \quad (5.59)$$

with t' being the age of loading.

The bulk and shear relaxation functions are given, respectively, by:

$$k_i(t, t') = \left(k_i^0 + \sum_{j=1}^m k_i^j e^{-\frac{t-t'}{\tau_i^j}} \right) f_{age}(t') \text{ and} \quad (5.60)$$

$$\mu_i(t, t') = \left(\mu_i^0 + \sum_{j=1}^m \mu_i^j e^{-\frac{t-t'}{\tau_i^j}} \right) f_{age}(t')$$

where k_i^j and g_i^j ($j = 0..m$) are the stiffness of the $m + 1$ springs and τ_i^j ($j = 1..m$) are the characteristics times of the m dashpots associated with the springs. The corresponding parameters for each phase considered in the computations are shown in Table 5.1. The resulting behaviours of the ageing linear viscoelastic phases concerning the bulk and shear relaxation functions are shown in Figure 5.6.

In the numerical simulations, at first, the SUBC is adopted and a uniaxial constant stress loading is applied. The mesostructure is $(120 \times 120 \times 120) \text{ mm}^3$. The diameter of the inclusions ranges from 8 to 18 mm.

Table 5.1 Elastic properties and parameters for the generalized Maxwell model

	E [GPa]	ν [-]	k^0	k^1	k^2	k^3	μ^0	μ^1	μ^2	μ^3	τ^1	τ^2	τ^3
			[GPa]				[GPa]				[days]		
Phase 1	150	0.3	-	-	-	-	-	-	-	-	-	-	-
Phase 0	30	0.2	10.0	4.0	3.0	3.0	6.0	2.4	1.8	1.8	0.1	1	10
Phase 2	40	0.2	8.88	5.55	4.44	3.33	6.66	4.16	3.33	2.5	0.1	1	10

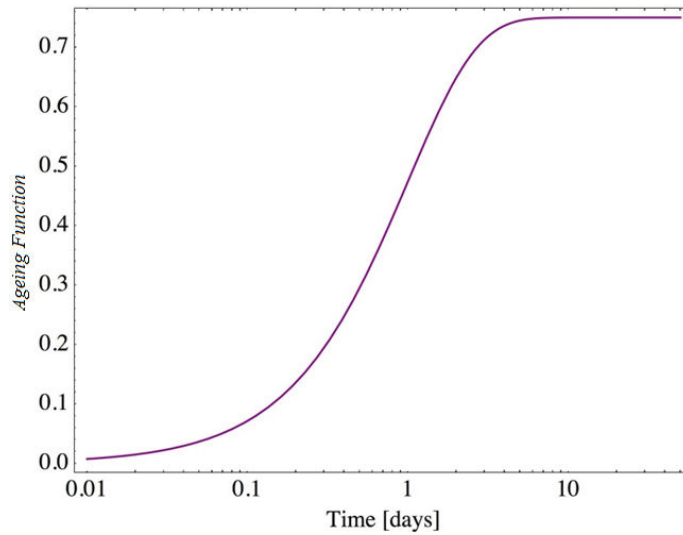
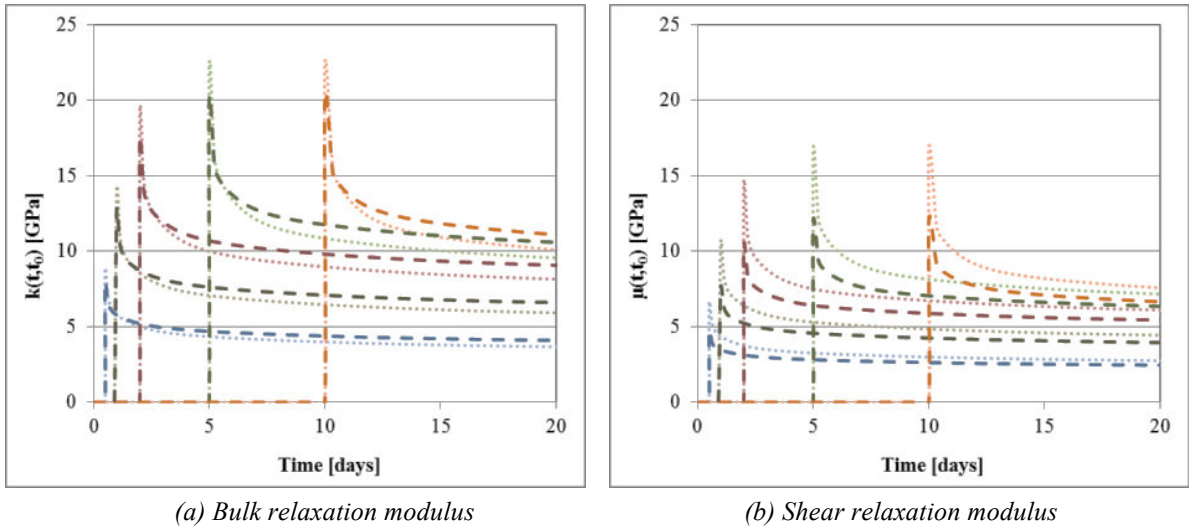


Figure 5.5 Ageing function given by Eq. (5.59)



(a) Bulk relaxation modulus (b) Shear relaxation modulus
Figure 5.6 Bulk and shear relaxation behaviour of phases: Phase 0 (Dashed) and Phase 2 (Dotted)

5.4.1 Two-phase material

The effective behaviour of a heterogeneous material with an ageing viscoelastic matrix and elastic inclusions is obtained according to different volume fractions of the phases. For the numerical simulations, the corresponding mesostructures are shown in Figure 5.7.

Note, as pointed out in Section 5.1.1, that the direct comparison between analytical and numerical estimations of the moduli can only be done because a creep test (with constant loading) is used in the numerical simulations.

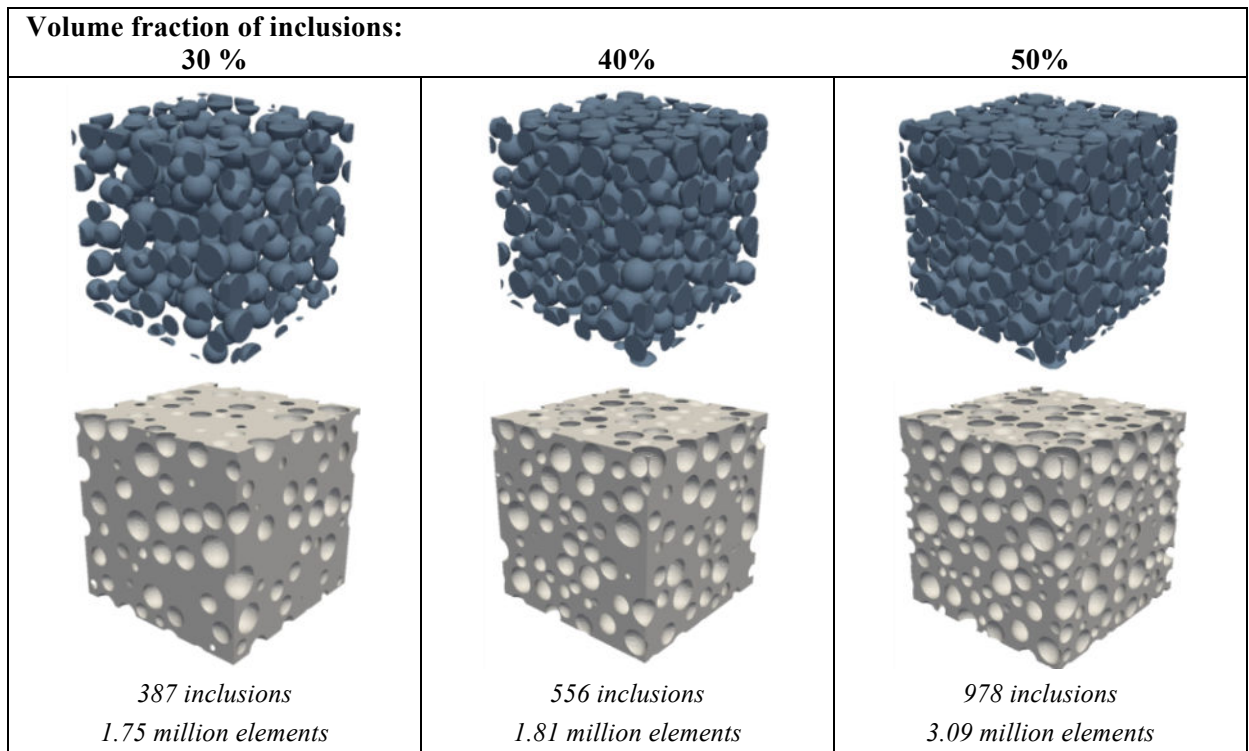


Figure 5.7 Biphasic mesostructures: matrix (bottom) and inclusions (top)

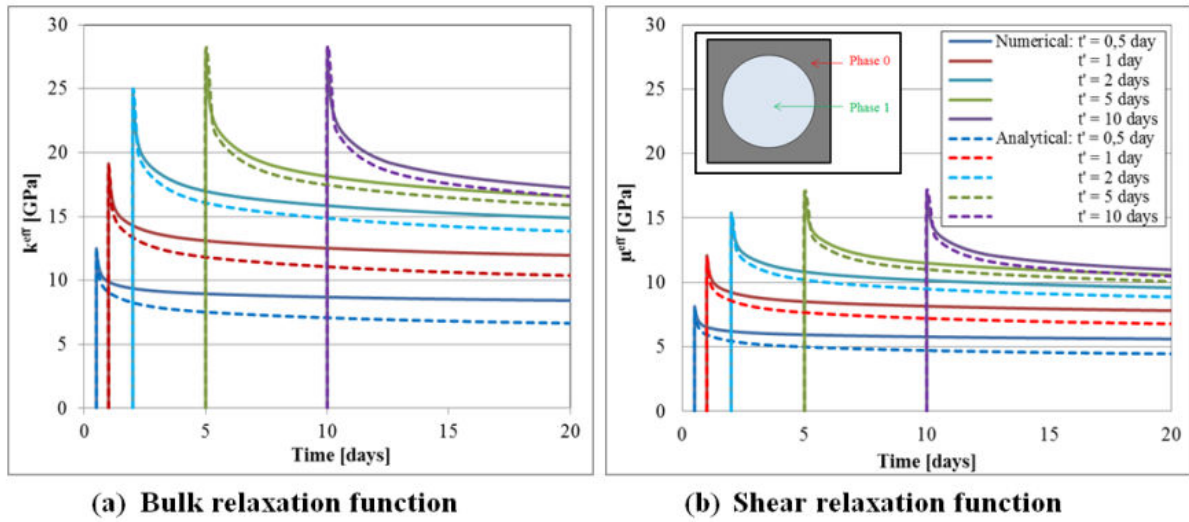


Figure 5.8 Bulk and shear relaxation function for uniaxial loading at different loading ages: comparison with numerical homogenization (SUBC)

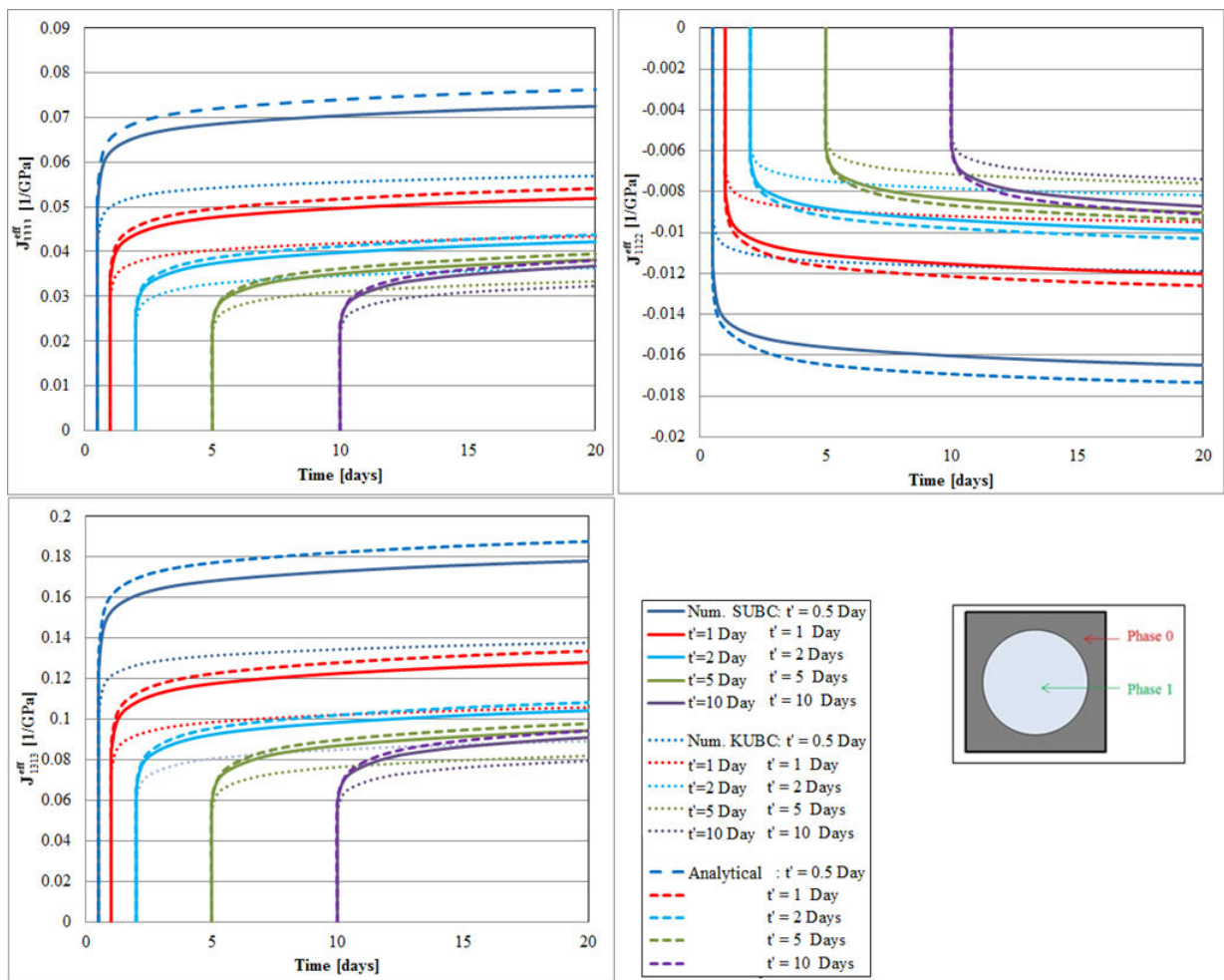


Figure 5.9 Creep functions for uniaxial loading at different loading ages: comparison with numerical homogenization (KUBC and SUBC)

For a microstructure with a volume fraction of inclusions equal to 40%, the bulk and shear relaxation functions are shown in Figure 5.8. The analytical results obtained with the formulation derived in section 5.2.3 are compared to numerical simulations, at different loading ages. The instantaneous elastic responses at the time corresponding to the loading age are the same for numerical with SUBC and analytical simulations. For early loading ages, in which the phase contrast are higher compared to late ages, the difference in the evolution of the moduli are more pronounced. Similar behaviour is observed regarding the creep functions in Figure 5.9.

As can be seen also on Figure 5.9, as expected, estimations under SUBC are closer to the analytical estimation than KUBC estimations. Moreover, the composite is stiffer for greater inclusions volume fractions, since the matrix is more compliant than the aggregates.

Regarding the influence of the volume fractions (Figure 5.10), as expected, the lower the volume fraction of the inclusions the closer the analytical and numerical results are to each other. Figure 5.10 shows also Mori-Tanaka estimations. As expected, the estimations of bulk relaxation function with the n-coated spheres schemes coincide with Mori-Tanaka estimations for $n = 2$.

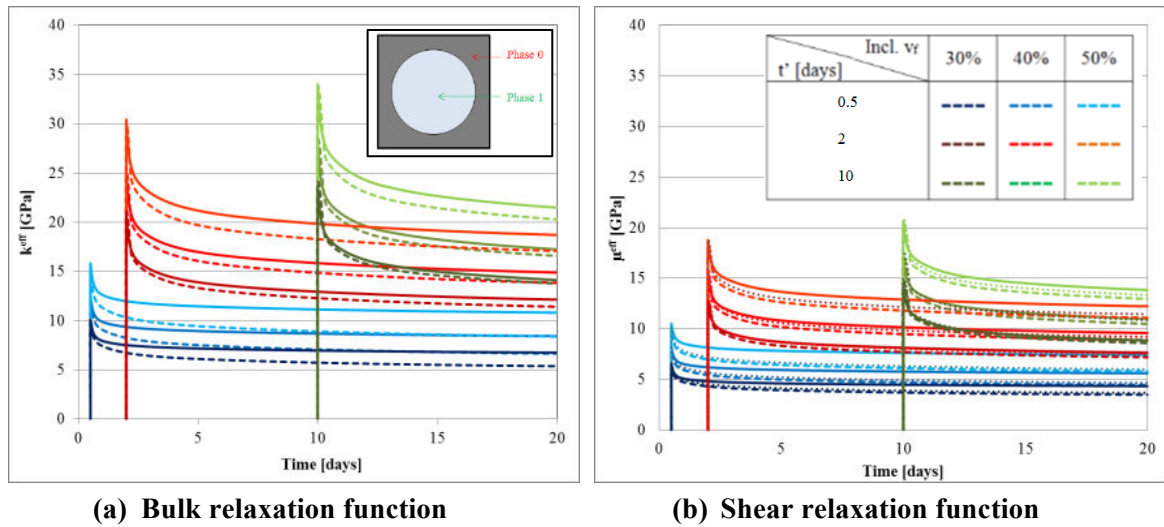


Figure 5.10 Effect of the volume fraction: GSC (dashed lines) compared to Mori-Tanaka (dotted lines) and numerical SUBC (full lines) estimations

5.4.2 Three-phase material

The effective behaviour of a heterogeneous material, with an ageing viscoelastic matrix and composite inclusions with an elastic core coated by an ageing viscoelastic phase, is obtained by numerical and analytical simulations. For the numerical simulations, the corresponding mesostructure is shown in Figure 5.11.

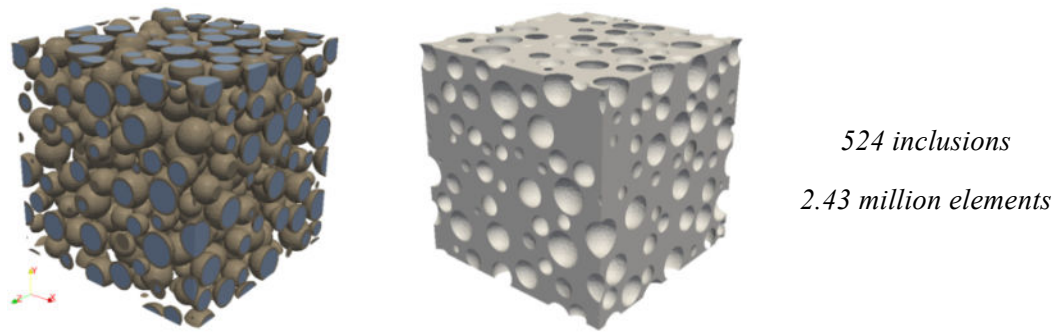


Figure 5.11 Three-phase mesostructure: matrix (right) and biphasic inclusions (left). 40% of inclusions: core (25%) and coat (15%)

The effective bulk and shear relaxation functions are shown in Figure 5.12. The analytical results obtained with the formulation derived in section 5.2.3 (for $n = 3$) are compared to numerical simulations, at different loading ages. The analytical and numerical results obtained for the shear relaxation function are closer than for the bulk relaxation. Again, for early loading ages, in which the phase contrasts are higher compared to late ages, the difference in the evolution of the moduli are more pronounced. Similar behaviour is observed regarding the creep functions in Figure 5.13.

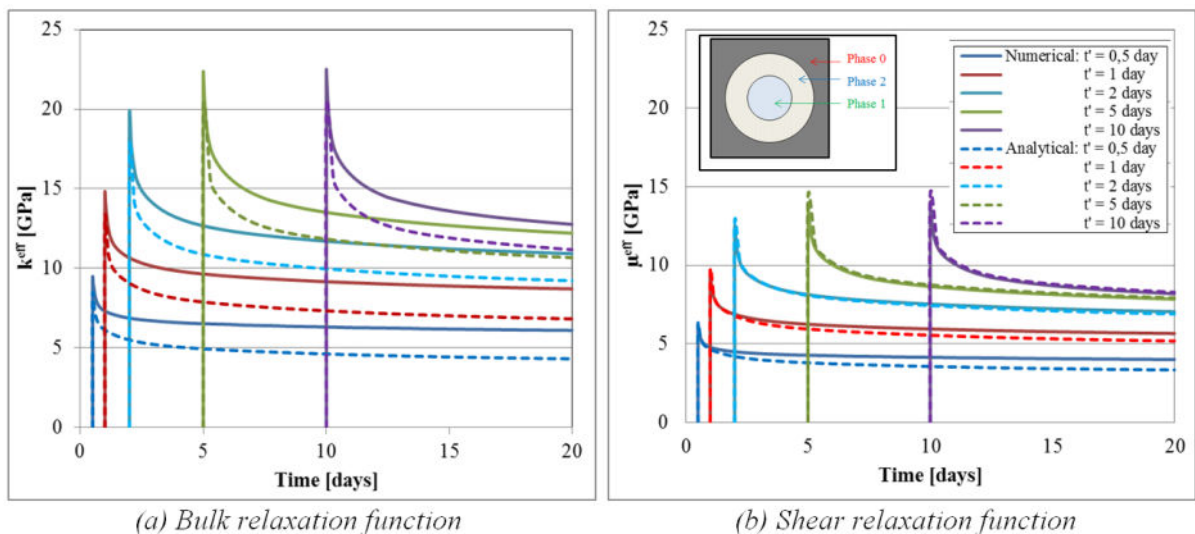


Figure 5.12 Bulk and shear relaxation functions: analytical (dashed lines) compared to numerical SUBC (full lines) estimations

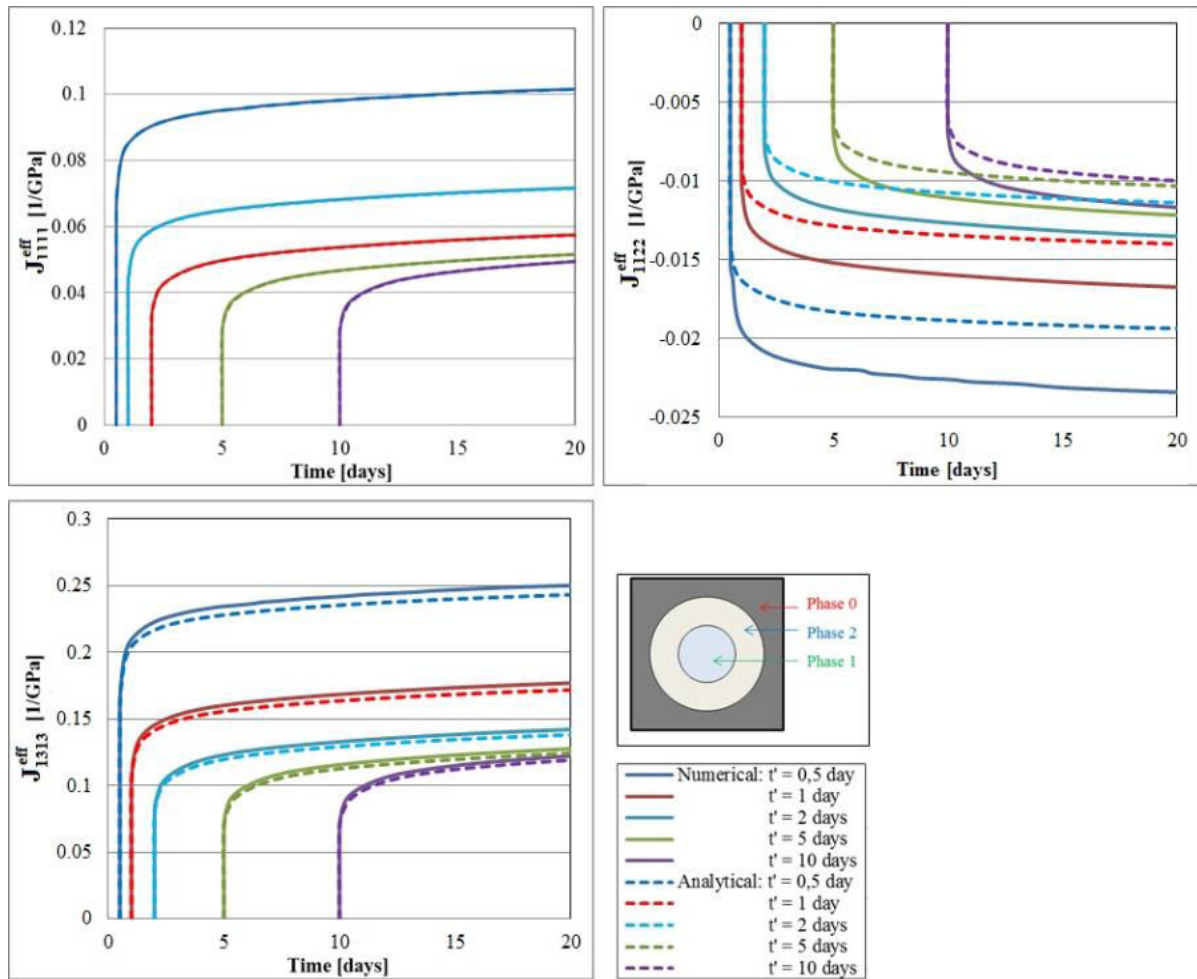


Figure 5.13 Creep functions: analytical (dashed lines) compared to numerical SUBC (full lines) estimations.

Figure 5.14 and Figure 5.15 show the average strains and stresses, respectively, per phase as computed by the localization tensor derived in section 5.2 and the numerical simulations. Again, a reasonable agreement between both estimations is obtained.

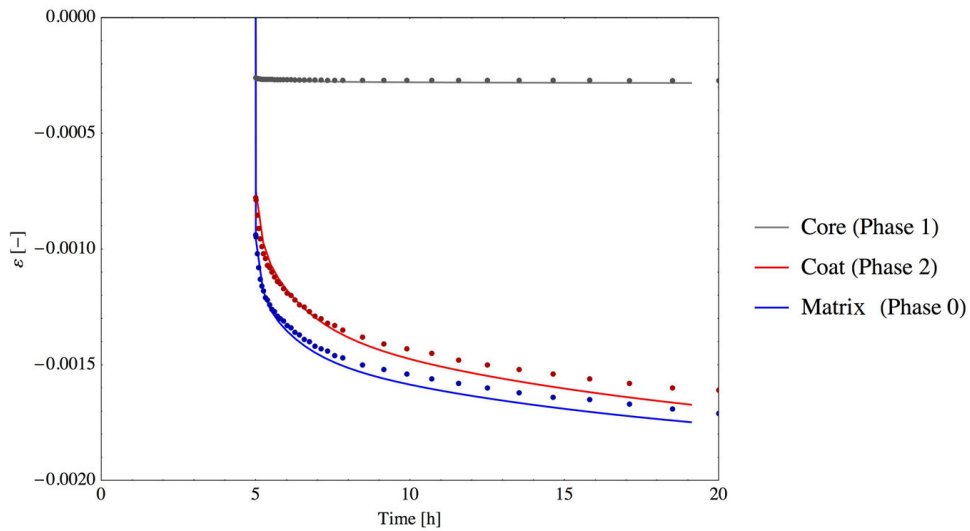


Figure 5.14 Average strains per phase: analytical estimations (lines) compared to numerical estimations (points)

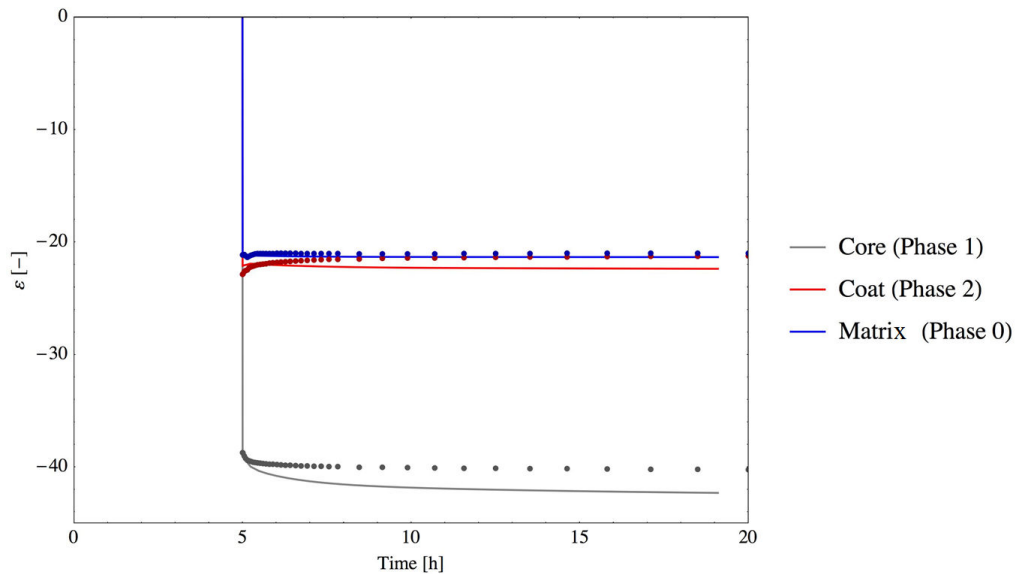


Figure 5.15 Average stresses per phase: analytical estimations (lines) compared to numerical estimations (points)

5.4.3 Influence of the discretization

The influence of the space discretization was assessed using the meshes shown in Figure 5.16. As can be seen in Figure 5.17, similar results were obtained for the tested meshed. For the same time discretization, the simulations with the coarser mesh took about 1.2 h, the intermediary mesh 2.2 h and the finner mesh 4 h in a computer with 16 cores, 2.0 GHz frequency and memory with 64Gb DDR 3 1600 MHz .

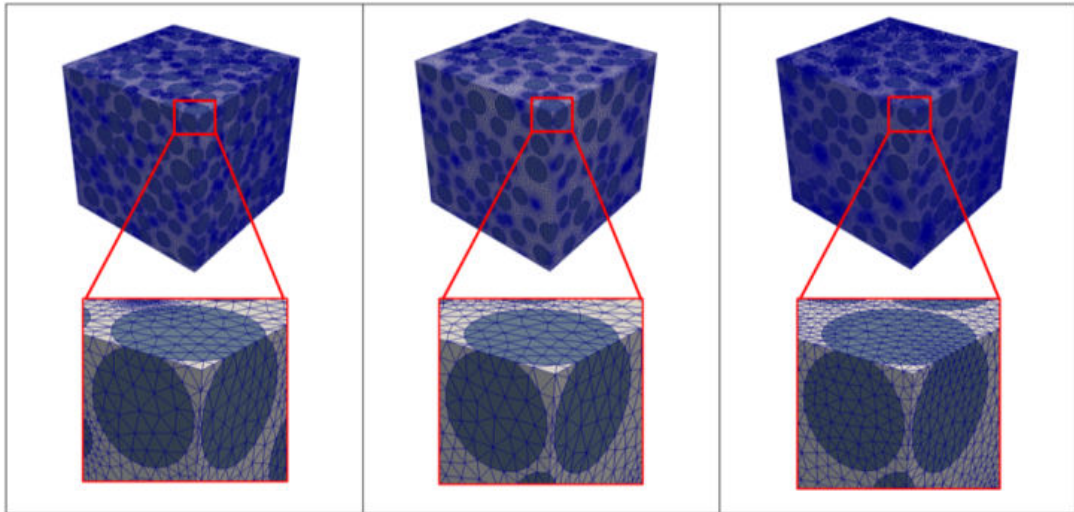


Figure 5.16 Discretization: 0.98 (left), 1.81 (centre) and 3.67 (right) millions tetrahedral finite elements

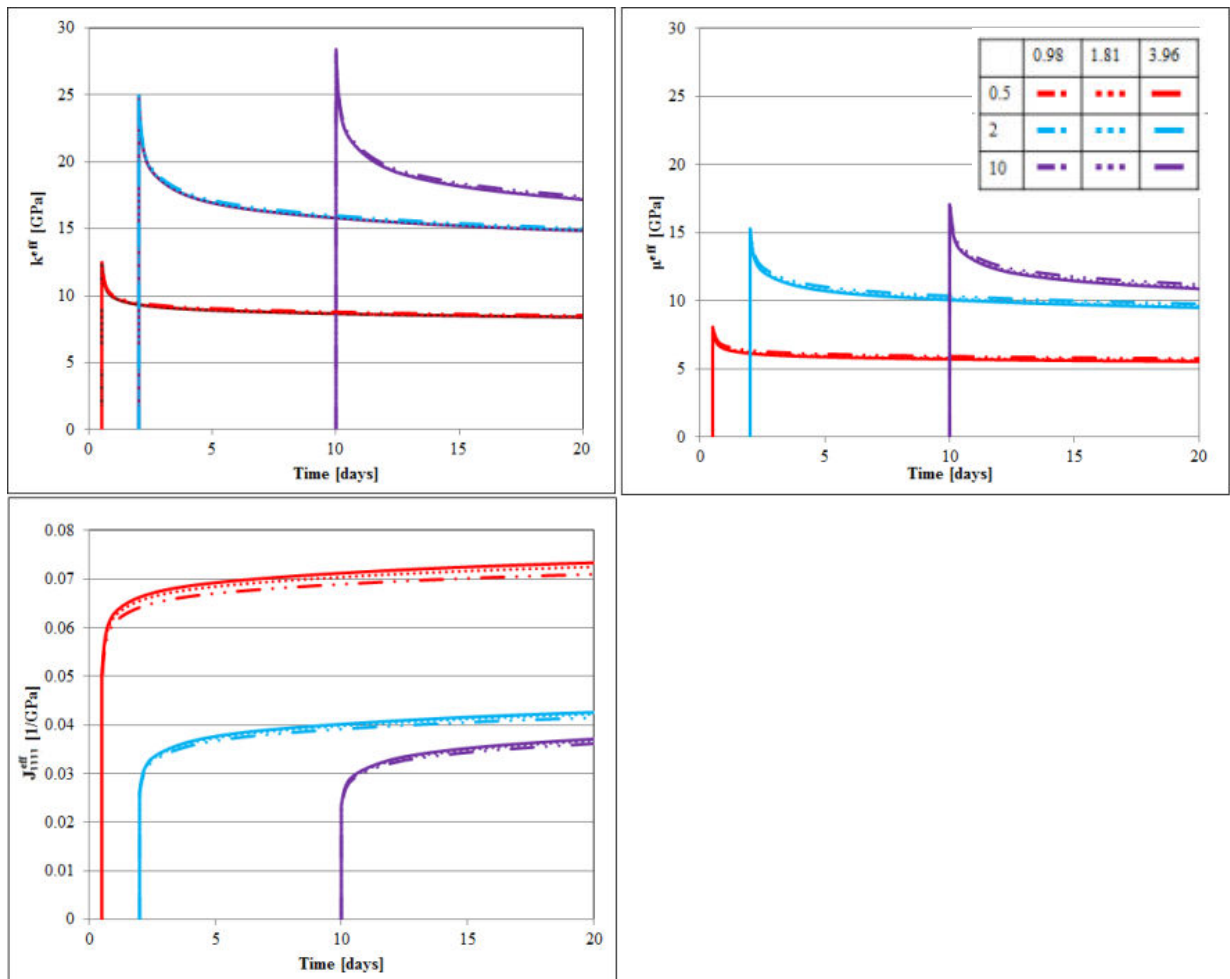


Figure 5.17 Influence of the mesh refinement: bulk and shear relaxation (up) and creep function (down)

The results with 1.81 million elements are close enough to the ones with 3.67 million elements to justify choosing the former as a good compromise between computation time and precision.

5.5 CONCLUSIONS

Analytical and numerical tools to estimate the effective behaviour of heterogeneous materials in an ageing linear viscoelastic framework were presented in this chapter.

- The classical estimation based on an n-coated spherical inclusion morphology was rederived using the formalism of a division algebra in which the Volterra integral operator is the product. Bulk and shear relaxation functions were analytically estimated for this morphology. The results were compared to Mori-Tanaka estimations using the same formalism as derived by (Sanahuja, 2013a).
- An ageing linear viscoelastic behaviour was implemented in Cast3M based on Bažant (1972) algorithm . Mesostructures with spherical inclusions and composite spherical inclusions were tested.
- To properly estimate the bulk and shear relaxation functions as well as the creep function, homogeneous boundary conditions were used in the simulations. A formal treatment to define the coupled size effects and the influence of the boundary conditions in an ageing linear viscoelastic behaviour are still to be developed.
- Numerical and analytical estimations returned comparable and coherent results even if the mesostructures and the assumption made in the definition of the morphologies are not exactly the same (except for MT scheme). Indeed, in the GSC scheme the inclusions are deemed to fill completely the space until an infinitesimally small size, which cannot obviously be done in numerical samples. For low volume fraction of inclusions and lower contrast between matrix and inclusions properties the numerical and analytical estimations returned adequately close results.
- The early the age of loading, the higher is the difference between numerical and analytical estimations because of the higher contrast between the matrix and inclusions properties. This feature was observed for both studied composites, i.e. with 1-phase or 2-phases spherical inclusions. Numerical estimations under SUBC are closer to analytical estimations than numerical estimations under KUBC. For matrices less stiff than inclusions, SUBC estimations are reported to return better results in elasticity (Pecullan et al., 1999), which is in agreement with these results.
- We consider that these results and the aspects discussed here validate the analytical and numerical upscaling techniques presented in this chapter.

With the tools presented in this chapter, the properties of cement-based materials are estimated in Chapter 6, by means of an approach combining numerical and analytical homogenization.

6. ESTIMATION OF THE AGEING LINEAR VISCOELASTIC PROPERTIES OF CEMENT-BASED MATERIALS

This chapter is an extension of the papers (Honorio et al., 2015, in preparation).

The multiscale character of cement-based materials needs to be accounted for in the estimation of some key properties such as the elastic moduli, creep and relaxation functions and some thermal properties.

Using **analytical homogenization**, different properties of cement-based materials can be estimated at early and late ages. The elastic properties of concrete are estimated in e.g. (Bernard et al., 2003; Constantinides and Ulm, 2004; Hashin and Monteiro, 2002; Sanahuja et al., 2007; Ulm et al., 2004); the non-ageing linear viscoelastic properties at late ages can be upscaled by means of analytical techniques in Laplace-Carson space (e.g. Thai et al., 2014).

The *ageing* linear viscoelastic behaviour of concrete was less studied in a multiscale framework. Note that the ageing character may be a result of changes in the microstructure of the material which can be originated from degradation phenomena or due to hydration processes at early-age. In the following the ageing aspect is due to hydration process. In this regard, Scheiner and Hellmich (2009) proposed an upscaling strategy using Mori-Tanaka and Self-Consistent schemes in Laplace-Carson space. Homogenization is applied at cement paste, mortar and concrete scales. The creep and relaxation tensors were obtained by numerical inversion of Laplace transforms. Then, the resulting ageing behaviour of the material was obtained by integration over the changes in the volume fraction of the constituents in time. The evolutions of the volume fraction are described by Avrami laws combined with a simplified description of the phases potentially present in the hydration processes. Another recent proposition in the direction of estimating the ageing linear viscoelastic behaviour of cement-based materials is made by Sanahuja (2013b). Even if the full description of the scales of interest in cement-based material (from C-S-H up to concrete) is still not made, the author proposes, using the formalism presented in Chapter 5 for the derivation of the GSC scheme, a strategy which can be useful is the estimation of effective properties at different levels. Similar approach is adopted here.

Correspondingly, using **numerical homogenization**, the elastic and non-ageing viscoelastic properties of concrete were estimated by different authors (see e.g. (Lavergne et al., 2015; Sadouki and Wittmann, 1988; Sanahuja and Toulemonde, 2011; Schorn and Rode, 1991; Wang et al., 1999; Wriggers and Moftah, 2006)) in studies of the long-term behaviour of concrete. Early-age investigations require a specific approach to deal with the evolution of the microstructure at the cement paste level. In this regard, the works involving the platforms *μic* (Bishnoi and Scrivener, 2009b; Do, 2013), *CEMHYD* (Bentz, 2005) and *Hymostruc* (Van Breugel, 1997) are potentially leading-edge by allowing coupling hydration microstructure-based models with FEM (or other

numerical methods) simulations to determine the effective properties of cement-based materials at early age. Once again, the ageing linear viscoelastic behaviour at early age was less studied. In this respect, for 2D mesostructures we highlight the works of Briffaut et al. (2013). Do (2013) estimated the ageing viscoelastic behaviour by means of FEM simulations with outputs of *mic* platform (Bishnoi and Scrivener, 2009b); a scenario in which the space-filling intervenes in the C-S-H behaviour was studied by the author.

In this chapter, we propose an investigation combining numerical and analytical tools to estimate the ageing viscoelastic properties of cementitious materials within a multiscale framework. With analytical homogenization the properties at the cement paste and mortar scale are estimated by a combination of Generalized Self-Consistent (GSC) and Mori-Tanaka (MT) schemes. With numerical homogenization the effective properties at the concrete scale are estimated. As discussed in the last chapter, numerical homogenization has the advantage of allowing to assess local information as well as to study more complex geometries. This combined strategy constitutes a promising tool to investigate how different mechanisms leading to ageing at the hydrate products scale, as well as other features of cement-based materials such as the Interfacial Transition Zone (ITZ), affect the viscoelastic behaviour at superior scales.

No effects of drying and temperature on the viscoelastic behaviour are considered in this chapter. In other words, we are only dealing with *basic* creep and relaxation phenomena. Also, the discussion is focused on the early-age behaviour, so the mechanisms acting in the long-term behaviour are not accounted for.

6.1 ORIGINS OF THE VISCOELASTIC BEHAVIOUR IN CEMENT-BASED MATERIALS

As previously mentioned, viscoelastic behaviour is experimentally observed at concrete, mortar and cement paste. Among the different phases present in the cement paste, only C-S-H is reported to show a non-negligible creep behaviour (Acker, 2004). Different mechanisms are proposed to explain the origins of such behaviour (Carol and Bažant, 1993; Rossi et al., 2012; Thomas and Jennings, 2006; Vandamme and Ulm, 2009). At early-age, solidification theory as proposed by (Carol and Bažant, 1993) shows that a viscoelastic ageing behaviour can be obtained from non-ageing phases in the presence of precipitation processes. This aspect will be considered more in details in section 6.3.1.

The viscoelastic behaviour of cement-based materials has been probed mainly at the scale of mortar and concrete (Acker and Ulm, 2001). Less experimental data is available for the cement paste, especially at ages inferior to 72 hours (Do, 2013). Direct evaluation of viscoelastic response of C-S-H is a more challenging task (Smilauer and Bazant, 2010; Vandamme and Ulm, 2009). Water is often pointed out as playing a major role in the driving mechanisms (Acker and Ulm, 2001). Dried concrete in which the evaporable water has been eliminated is reported to not present creep (Acker and Ulm, 2001). According to (Acker, 2004) the most probable mechanism to explain C-S-H creep

is: “the [C-S-H] structure progressively collapses, producing a kind of consolidation process of the gel, as happens when a loose soil is drained. This involves drainage of the water from the gel up to the capillary pores; its kinetics is dictated by the gel's degree of compactness or porosity, and the curve shape is asymptotic because the gel's compactness has a physical limit, i.e. that of the compact arrangement.”

C-S-H structure can be represented by layered structures replicating the crystalline structure of tobermorite or clays (Feldman and Sereda (1970) cited by (Jennings, 2004)) or by colloid structure (Powers (1968), Wittman (1979) cited by (Jennings, 2004); (Jennings, 2008)). Refining his colloid model (Figure 6.1), Jennings (2008) proposes, based on an analysis of different techniques, to model C-S-H as an assembly of non-spherical globules with equivalent diameter of the order of ~ 5 nm. A nematic character is attributed to the assembly of the globules with low range order and a subsequent fractal region in which globule flocs can overlap (Figure 6.1). Three different pore classes, which are accessible to water, can be identified: intraglobule pores (IGP); small gel pores (SGP: trapped between neighbouring globules) and large gel pores (LGP: at the scale of the globule flocs). In this framework, the viscoelastic behaviour may involve reorientation of the globules leading to an increased local packing and reducing the surface area (Jennings, 2008). The viscoelastic behaviour, as well as autogenous shrinkage, would involve decreasing LGP volume which is, as pointed out by Jennings (2008), similar to the microprestress theory of solidification as proposed by (Bazant et al., 1997) to explain the ageing behaviour. For the latter, a microstructural change is associated with the gradual removal of the mechanism of irreversible creep with time, not being necessarily associated with the formation of new product (Jennings, 2008).

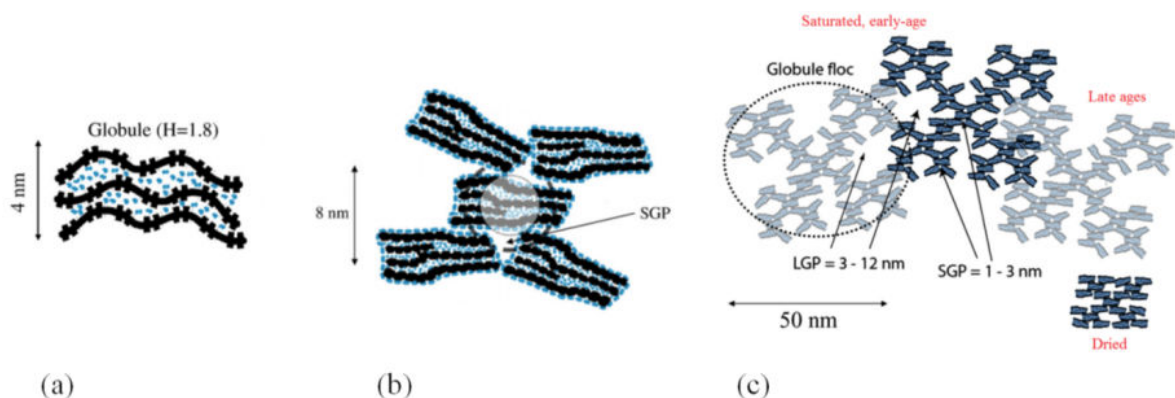


Figure 6.1 Structure of C-S-H according to Jennings Colloid model (adapted from (Jennings, 2008)) : (a) gobule scale with the IGP, (b) local arrangement of globules and (c) globule flocs overlapping

Short and long-term components of the viscoelastic behaviour are generally identified. The short-term component is reported to occur due to a change of the hygral equilibrium in the gas filled space which generates strains, stresses and microcracking ((Ruetz, 1966; Wittmann, 1982)) cited by (Acker and Ulm, 2001)). The long-term component corresponds to an irreversible viscous behaviour

which may be related to slippage between layers of C-S-H, and which would increasingly fade in time and is reported to occur at constant volume (Acker and Ulm, 2001). Further investigations are needed in order to better understand the origins of the viscoelastic behaviour in cement-based materials.

6.2 MULTISCALE STRATEGY

Analytical homogenization is used to estimate the properties at the cement paste and mortar scale (Figure 6.2). A two-coated sphere morphology is used to represent the cement paste and mortar microstructures (Honorio et al., 2014c; Honorio and Bary, 2014), as proposed previously by e.g. (Bary and Béjaoui, 2006; Stora et al., 2009). Regarding the cement paste, the hydrating particle is embedded in a high density (HD) products layer which is, in turn, embedded in a low density (LD) products layer. Regarding the mortar, the sand particle is embedded in an ITZ layer which is, in turn, embedded in a cement paste layer. The GSC scheme is used to obtain the homogenized properties of the cement paste and mortar. MT scheme is used to estimate the properties within each coat. The formulation of the schemes follows Chapter 5.

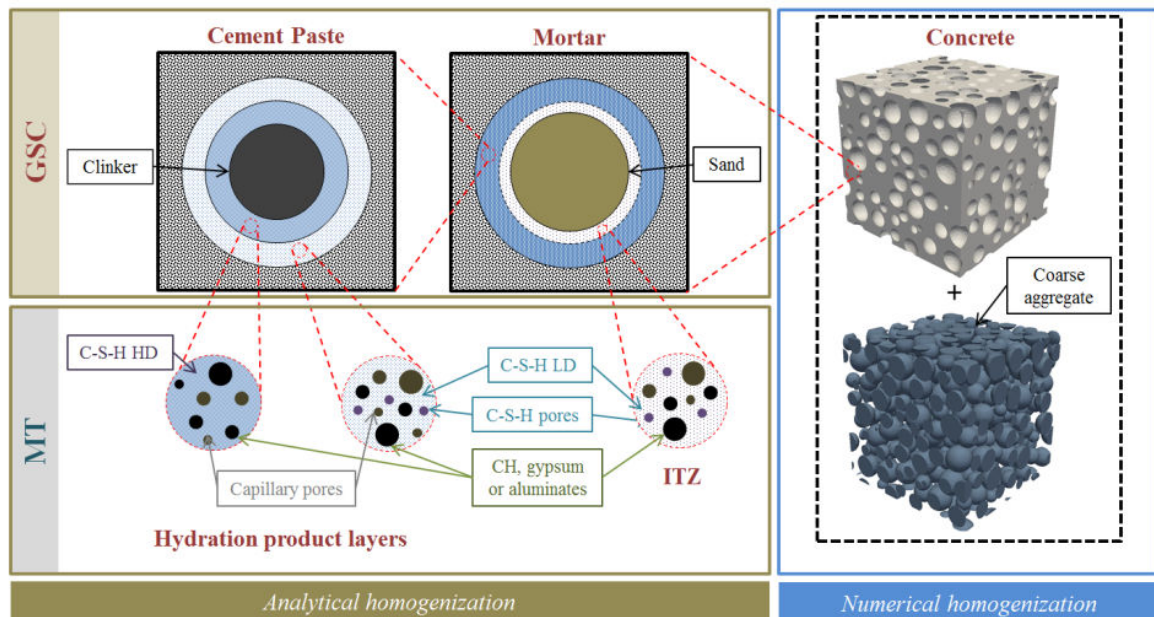


Figure 6.2 Multiscale strategy with combined analytical and numerical homogenization

Numerical homogenization is used to estimate the properties at the concrete scale. As in Chapter 5, we use a specific procedure associated with the Finite Elements code (Cast3m) to generate and compute 3D microstructures (Bourcier et al., 2014; de Larrard et al., 2013). Local information regarding the stresses and strains repartition in the heterogeneities and in definite regions of the matrix are assessed. This is an advantage compared to analytical schemes which generally

provide accurate estimations only on averaged fields. With the local information, the zones in which stresses are localized can be more precisely identified. Previous results showed that a considerable dispersion of the averaged stresses within the inclusions and matrix subvolumes is observed (Bary et al., 2014).

6.3 CEMENT PASTE SCALE

At cement paste scale, the evolution of the volume fractions of the cement minerals and hydration products, as described in Chapter 4, has to be accounted for. Following the microstructure representation in Figure 6.2, two levels are identified:

- Level 1a and 1b of the inner products and outer products, respectively, in which C-S-H HD and C-S-H LD, respectively, function as a matrix in which the other hydration products and capillary pores are embedded.
- Level 2 in which the previous layers of inner and outer products are taken into account in composite inclusions morphology.

In this representation an evolution of the volume fraction occurs at both levels. At level 1, the volume fraction of non-bonded water decreases with its consumption by hydration reaction and the volume fraction of the forming products takes the left place. At level 2, the dissolving clinker particle leaves place to the growing of inner product layer.

The analytical upscaling tools developed in Chapter 5 can be applied iteratively to represent these volume changes due to dissolution and precipitation.

6.3.1 Dissolution/Precipitation and solidification mechanisms

Bazant (1977) showed that an ageing effective behaviour can be observed in materials in which one of the constituents shows a change in its volume fraction in time, as occurs for example in a solidification process. This effect is observed even if the basic constituents are non-ageing themselves (Carol and Bažant, 1993). This so-called solidification theory can be extended to a general form in which dissolution and precipitation of multiphasic systems occur in more complex geometries (Figure 6.3). Sanahuja (2013b) proposed a tensorial extension of this theory. The relaxation tensor for a given phase solidifying at time t_i^S is identified by:

$$\mathbb{R}_i(t, t_0) = \mathbb{R}_s(t - t_0) H(t_0 - t_i^S) \quad (6.1)$$

where $\mathbb{R}_s(t - t_0)$ is the relaxation tensor of the solidified material.

The solidification can occur following different processes. Generally the assumption of dissolution followed instantaneously by precipitation is adopted. Sanahuja (2013b) studied cases in which the precipitation can occur in two different ways: inwards pores or by occupying entirely and instantaneously some class of pores. The changes in the volume fraction of phases are taken into

account with analytical homogenization by applying iteratively the upscaling schemes. This strategy involves a discretization of the ageing function in n steps, corresponding to the same volume fraction of solid f_{age}^{∞}/n precipitating:

$$f_{age}(t_i^s) = \left(i - \frac{1}{2}\right) \frac{f_{age}^{\infty}}{n} \quad (6.2)$$

with f_{age}^{∞} being the final value of the volume fraction of the phase solidifying. The estimation of the effective properties then is made by determining the properties of a fictitious n -phases composite.

Sanahuja (2013b) showed that the precipitation mechanism and the kinetics of the ageing process affect directly the effective ageing viscoelastic response.

Here, an evolution function is attributed to each phase present in the paste according to the hydration kinetics model of cement proposed in Chapter 4. The repartition of the products in High Density and Low Density layers is made proportionally to the volume of C-S-H in the layer (Figure 6.4). A part of the products is reserved to the ITZ, as will be discussed in Section 6.4. The corresponding elastic properties of the different phases are shown in Table 6.1. Non-ageing viscoelastic behaviour is attributed to C-S-H phases; the other phases are assumed to behave elastically.

Table 6.1 Elastic properties of the different phases

	Clinker	C-S-H		CH	AFt	AFm	C ₃ (A,F)H ₆	C ₄ AH ₁₃	Gypsum	Sand
		LD	HD							
E [GPa]	140	21.7	29.4	38	22.4	42.3	22.4	25	45.7	74.5
ν	0.3	0.24	0.24	0.305	0.25	0.324	0.25	0.25	0.33	0.2
Ref.	**	^^	^^	§§	%%	%%	oo	oo	oo	##

** (Velez et al., 2001); ^^ (Bernard et al., 2003); §§ (Monteiro and Chang, 1995); %% (Kamali, 2003); oo (Haecker et al., 2005); (Stora, 2007)

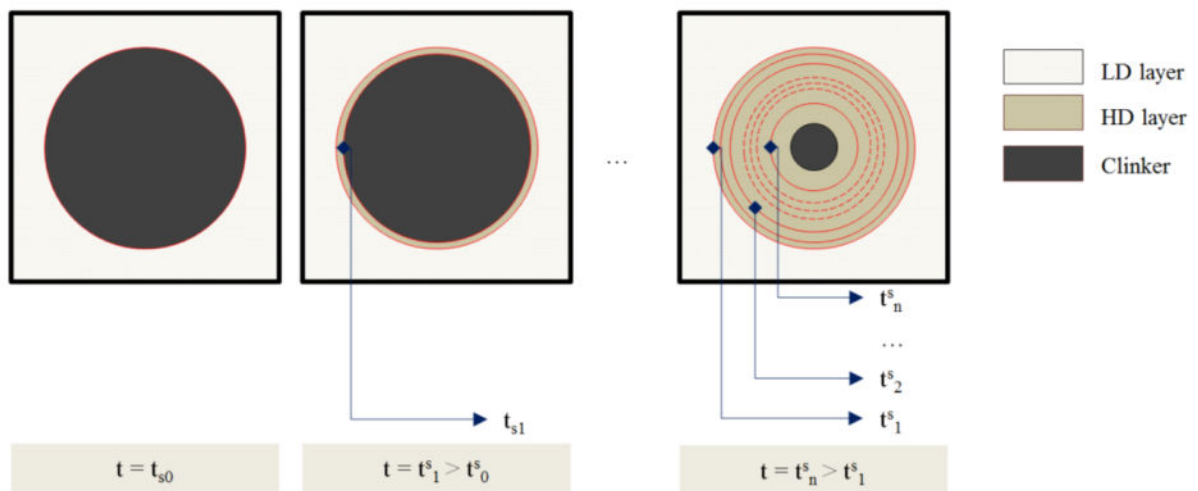


Figure 6.3 Schematic representation of the solidification process adopted at the cement paste level

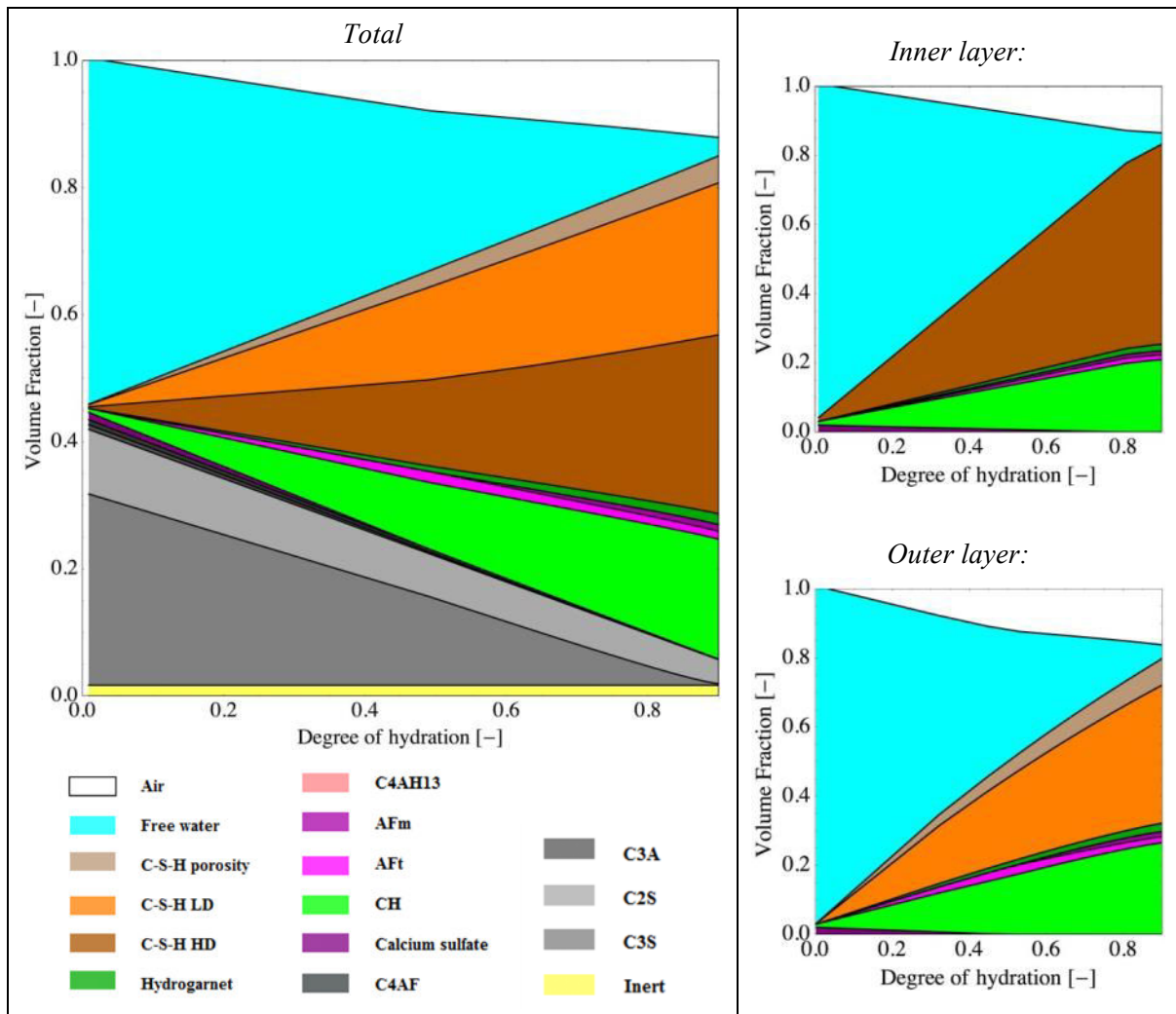


Figure 6.4 Repartition of the products: Inner and Outer products. The ITZ is shown in Figure 6.14

6.3.2 C-S-H behaviour

The identification of C-S-H viscoelastic behaviour is generally done by means of indirect approaches. Some of these methods are briefly presented in the following.

6.3.2.1 Behaviour obtained from mechanistic modelling

Sanahuja and Dormieux (2010) propose a micromechanical modelling of C-S-H based on the relative sliding of the sheets with nanogranular C-S-H grains. Spherical grains with isotropic orientation are considered. With this representation, the resulting non-ageing viscoelastic behaviour of the elementary particle is obtained by means of the correspondence principle in Laplace-Carson domain. The model accounts for one single level to represent the C-S-H structure. Their results are function of the porosity φ_{gel} found in-between the grains. For a direct application this porosity would correspond to the SGP and LGP in Jennings (Jennings, 2008) colloid model (see Section 6.1).

A two-level homogenization could be performed at the scale of the IGP, but statistical physical tools would be more adequate than continuum mechanics.

In Laplace-Carson space, the self-consistent estimations obtained for the effective bulk and shear moduli are function of the bulk modulus of the grains k , the Poisson ration ν and the $\chi = \frac{c_s}{\mu}$ (the modulus c_s which only allows simple shear activated by relative sliding of the sheets) (Sanahuja and Dormieux, 2010):

$$\overline{k^{sc}} = k f_k(\varphi_{gel}, \nu, \chi) \quad \text{and} \quad \overline{\mu^{sc}} = k f_\mu(\varphi_{gel}, \nu, \chi) \quad (6.3)$$

with

$$f_k = \frac{4(1 - \varphi_{gel}) f_\mu}{4f_\mu + 3\varphi_{gel}} \quad (6.4)$$

The function f_μ can be determined by solving a 4th order polynomial equation (not shown for conciseness). The effective behaviour can be finally obtained by inversion of the Laplace-Carson transform, which can be done, for example, by means of Gaver–Wynn–Rho method. Similar approach could be used with platelets (Sanahuja, 2014) instead of spherical grains, following Sanahuja et al. (2007).

6.3.2.2 Behaviour obtained from experimental data

Smilauer and Bazant (2010) estimated the C-S-H viscoelastic properties by means of a microstructural inverse analysis from creep data of cement paste or concrete.

Vandamme and Ulm (2013, 2009) studied the viscoelastic behaviour of C-S-H from statistical analysis of nanoindentation tests. They obtained the following formula for uniaxial creep compliance which can be written as a function of the contact creep C_v :

$$J_{un}(t, t_0) = \frac{1}{E} + \frac{1}{C_v(1 + \nu^2)} \ln \left[1 + \frac{t - t_0}{\tau} \right] \quad (6.5)$$

where τ is a characteristic time. The mean value of τ obtained by (Vandamme and Ulm, 2009) is 1.66 s, which characterizes a quite fast progress of viscous processes with a pronounced evolution within the first 3 days after what an asymptotic regime is reached. This value is retained in the following. The contact creep compliance was obtained by fitting nanoindentation data (Vandamme and Ulm, 2009):

$$C_v(\eta_p) = 1588.9(\eta_p - 0.5)_+^{1.597} \quad (6.6)$$

where η_p is the packing density of C-S-H. Note that with this equation the packing density is characterized by a percolation threshold of 50 % of solid inclusions.

The behaviour of LD and HD C-S-H can be determined by defining a given packing density for each type. The packing densities 0.66 and 0.77 were retained for LD and HD C-S-H,

respectively. The first value correspond to the one identified by Vandamme and Ulm (2009) for the LD C-S-H. The second one corresponds to an intermediary value between the HD and the UHD (Ultra-High Density) C-S-H identified by the same authors whose mean packing density values are 0.75 and 0.83, respectively.

Assuming a constant Poisson ratio we have (Salençon, 2009):

$$\boldsymbol{\varepsilon}(t) = J(t, t_0)(1 + \nu) \circ \boldsymbol{\sigma} - \nu J(t, t_0) (\text{tr } \boldsymbol{\sigma}) \mathbb{I} \quad (6.7)$$

From that it is possible to determine the volumetric and deviatoric part of the compliance tensor, J_k^{C-S-H} and J_μ^{C-S-H} , respectively, as shown in Figure 6.5 for the HD and LD C-S-H whose behaviour is non-ageing.

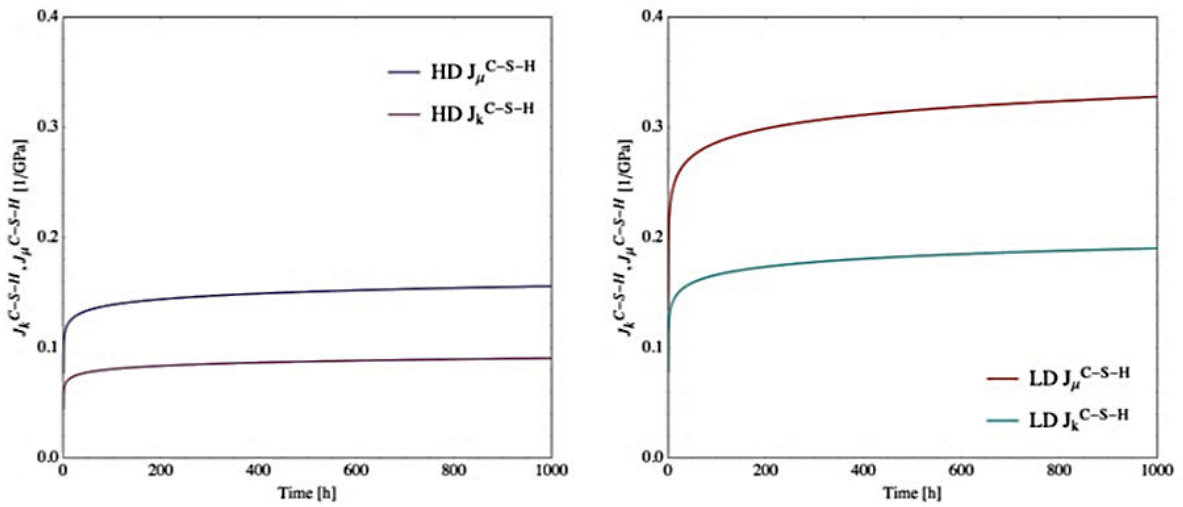


Figure 6.5 C-S-H HD and LD deviatoric and volumetric components of compliance tensor: non-ageing behaviour, no space filling accounted for.

Another strategy is to account for a space filling process (or compaction, or densification) within C-S-H, which results in an intrinsically ageing behaviour. To describe the space-filling process we propose to use a version of Eq. (4.6):

$$\eta_p = \frac{\rho(t^s)}{\rho_{max}} = 1 - \frac{(\rho_{max} - \rho_{min})}{\rho_{max}} \exp\left[\frac{-k_{DEN}}{\rho_{max} - \rho_{min}}(t^s)\right] \quad (6.8)$$

As in Chapter 4, we adopt $\rho_{max} = 2.2 \text{ g/cm}^3$ and $\rho_{min} = 0.2 \text{ g/cm}^3$; $k_{DEN} = 0.02 \text{ g/cm}^3/\text{h}$. Figure 6.6 shows the resulting evolution. This kinetics is “faster” than the one proposed by (Do, 2013) to define an intrinsically ageing behaviour to C-S-H. The resulting behaviour in terms of volumetric and deviatoric components of compliance tensor is shown in Figure 6.7 for different loading ages t_0 .

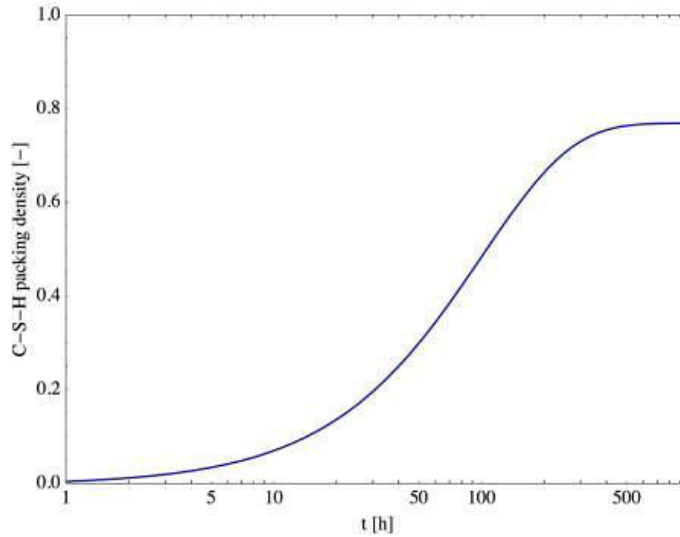


Figure 6.6 C-S-H packing density evolution according to Eq. (6.8)

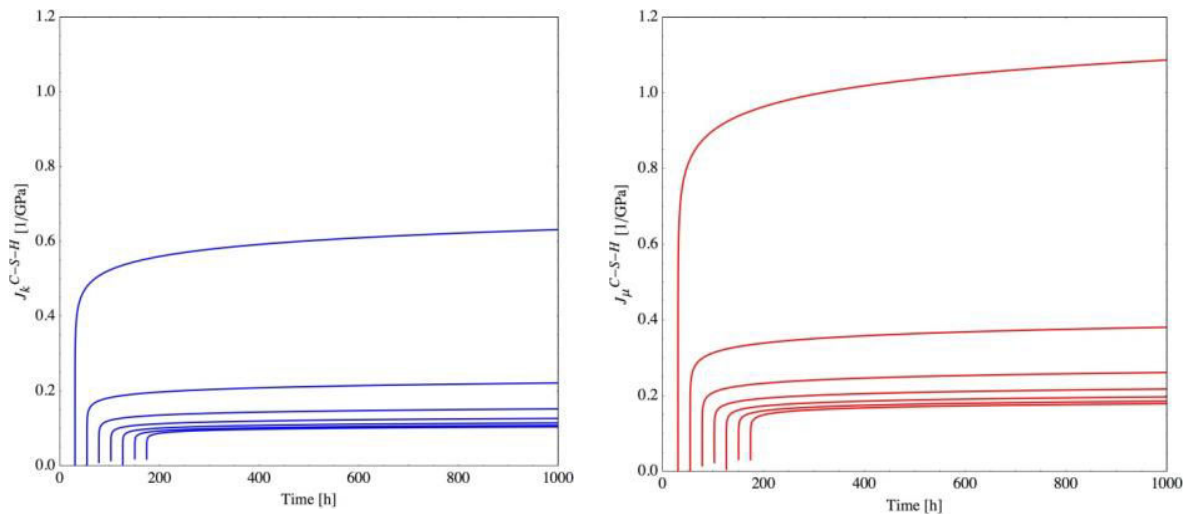


Figure 6.7 C-S-H deviatoric and volumetric components of compliance tensor for different loading ages: intrinsically ageing behaviour accounting for space filling process.

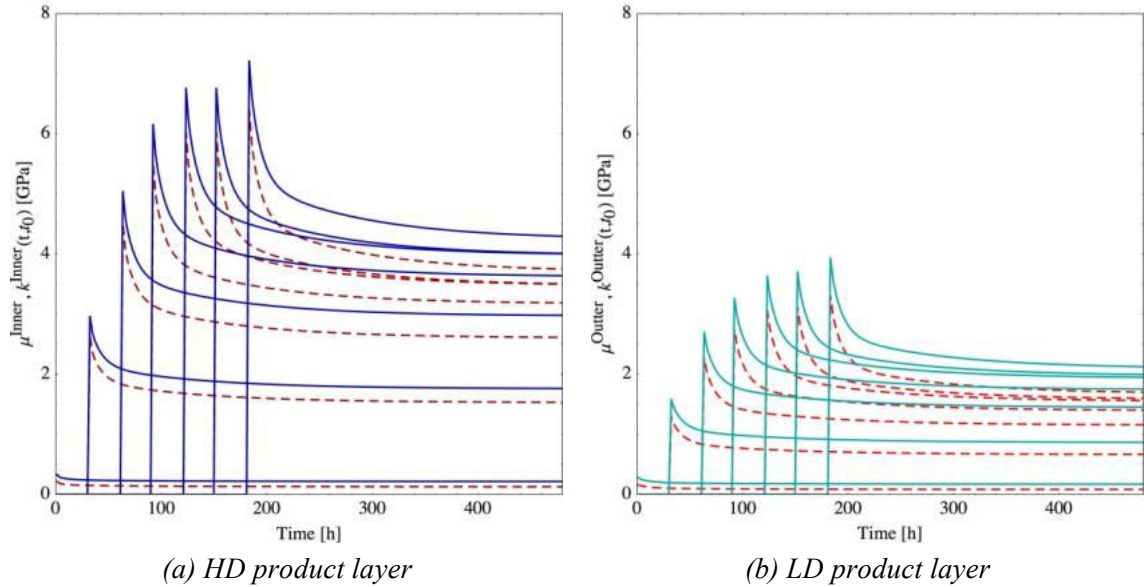
In the following, the C-S-H behaviour with no densification (Figure 6.5) is retained for the simulations. Future contributions will deal with the case with space-filling.

6.3.3 Effective properties at the cement paste scale

The effective bulk and shear relaxation function of the inner and outer layers (Level 1a and 1b) are shown in Figure 6.8. Note that, because of the solidification process, the effective behaviour is ageing. As expected, most part of the evolution in the elastic response occurs within the first 200 h, in agreement with the evolution of C-S-H volume fraction as obtained by the hydration model. In Figure 6.8, this ageing function is discretised in 50 parts ($n_{sol} = 50$), corresponding to times in which a same volume of C-S-H precipitates.

The influence of the ageing function discretization is presented in Figure 6.9. Note that the elastic response for each loading age depends on this discretization. Increasing the discretization, a

smoother evolution of this elastic response is observed. Discontinuities in the evolution are observed for coarser discretizations of the ageing function. Since the curves are enveloped by the ageing elastic response, the viscoelastic response is then underestimated with coarser discretizations of the ageing function.



(a) HD product layer (b) LD product layer
Figure 6.8 Inner and outer layers: estimated bulk (full lines) and shear (dashed lines) relaxation functions for different loading ages

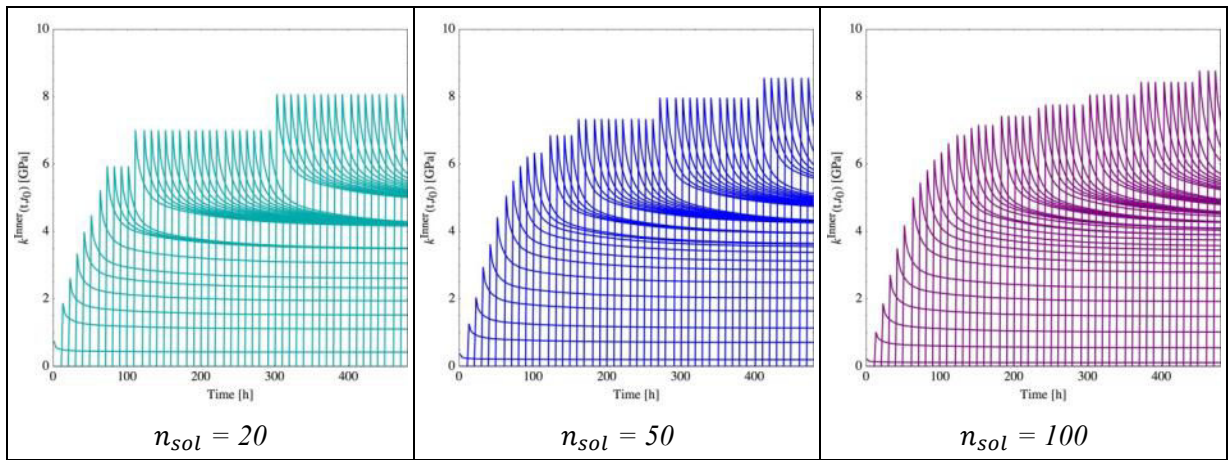


Figure 6.9 Effect of the discretization of the ageing function on the bulk relaxation function of the HD product layer

The estimated effective bulk and shear relaxation functions as well as the creep function of the cement paste are shown in Figure 6.10 and Figure 6.11, respectively. We adopted $n_{sol} = 50$. Similarly to the C-S-H behaviour, after about 300 h the ageing character of the response vanishes.

The estimations of the effective properties of the cement paste here are valid only for periods after the percolation of the microstructure. Strategies to account for the existence of a percolation threshold here are to be developed.

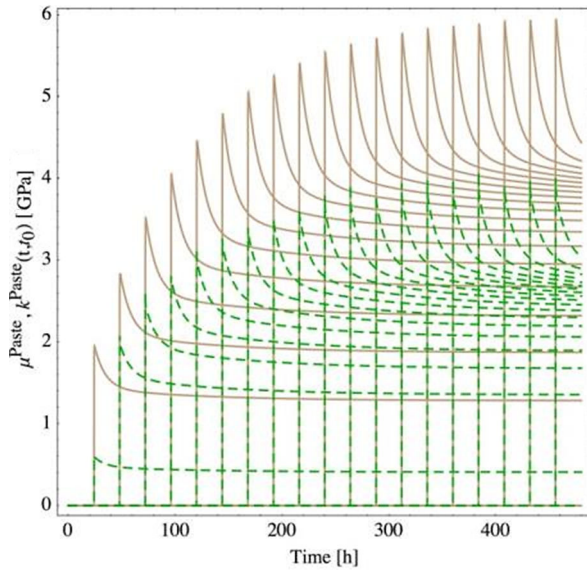


Figure 6.10 Effective behaviour of the cement paste: bulk (full brown lines) and shear (green dashed lines) relaxation function

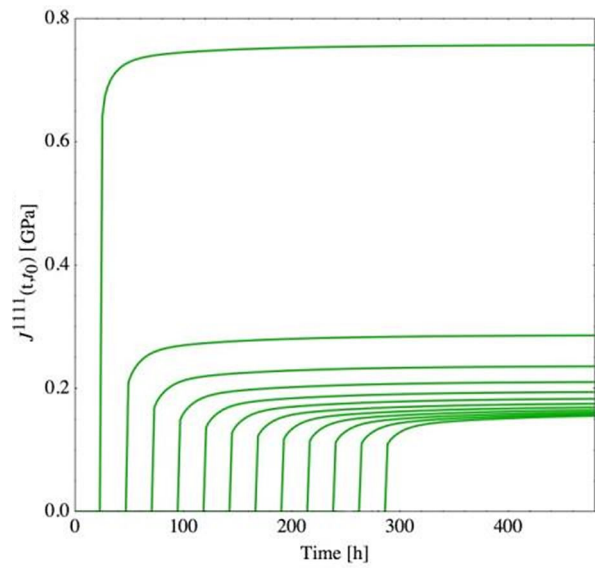


Figure 6.11 Effective behaviour of the cement paste: creep function

6.4 MORTAR SCALE

At the mortar scale (Level 3), a 3-phase composite sphere is employed to represent the microstructure (Figure 6.2). The core corresponds to the sand particle. We adopt the volume fraction of sand $f_{Sand} = 50\%$. The first coat is the ITZ and the second coat is the cement paste whose behaviour was obtained in the previous section. Note that, differently of the cement paste scale, the volumes of the three phases in the coated sphere morphology at the mortar scale remain the same; so no additional ageing from solidification processes occurs at this scale.

6.4.1 Definitions of ITZ volume and composition

An ITZ is observed near the aggregates. The properties of this zone are reported to be inferior to those of the cement paste. We assume that the ITZ is composed of C-S-H LD and a part of the other hydration products, water, gypsum and empty pores from the cement paste. The part of the products and reactants going to the ITZ is discounted from the C-S-H LD coat. In this sense, the composition of the LD layer in Figure 6.4 changes as a function of the volume and composition of the ITZ. The aspects related to the definitions of these features are discussed in this section.

Experimental evidence shows that the matrix of the mortar and the hardened cement paste present different porosities (Heukamp, 2003). We assume that this difference is due to the ITZ higher porosity compared to the cement paste. We adopted a supplementary porosity of the mortar matrix with respect to the cement paste of 10%.

Also, the ITZ is likely to contain more CH and AF-phases (Sun et al., 2007). These aspects are considered in the composition of the ITZ as shown in Figure 6.14. Compared to the LD layer, the ITZ here owns 10% more CH and AF-phases. The C-S-H content was minored by 5%.

To compute the volume of the ITZ according to the PSD $w(R_0)$ of sand, we adopt Garboczi and Bentz (1997) approach resorting to the nearest neighbour surface distribution function $e_v(r)$. In a system of polydisperse non-correlated spheres, this function allows accounting for the likely interpenetration of the ITZs. Depending on the number of particles ρ with a given size, the volume of the ITZ V_{ITZ} can be estimated in terms of $e_v(r)$. For a given thickness of the ITZ e_{ITZ} , we have (Garboczi and Bentz, 1997):

$$V_{ITZ} = 1 - V_{agg} - e_v(e_{ITZ}) \quad (6.9)$$

where V_{agg} is the volume fraction of aggregates and (Lu and Torquato, 1992; Torquato, 2002)

$$e_v(r) = (1 - V_{agg}) \exp[-\pi\rho(a r + b r^2 + c r^3)] \quad (6.10)$$

where:

$$\begin{aligned} a &= \frac{4\langle R_0^2 \rangle}{1 - V_{agg}}, & b &= \frac{4\langle R_0 \rangle}{1 - V_{agg}} + \frac{12 B \langle R_0^2 \rangle}{(1 - V_{agg})^2}, \\ c &= \frac{4}{3(1 - V_{agg})} + \frac{8 B \langle R_0 \rangle}{(1 - V_{agg})^2} + \frac{16 \mathcal{A} B^2 \langle R_0^2 \rangle}{3(1 - V_{agg})^3} \end{aligned} \quad (6.11)$$

with $\langle f \rangle = \int_0^\infty w(R_0) f(r, R_0) dR_0$ being the first momentum of a function f ; $B = 2\pi\rho\langle R_0^2 \rangle/3$ and \mathcal{A} being a parameter equal to 0, 2 or 3 depending on the approximation chosen. Garboczi and Bentz (1997) used $\mathcal{A} = 0$ in their simulations; the same value is adopted in the following.

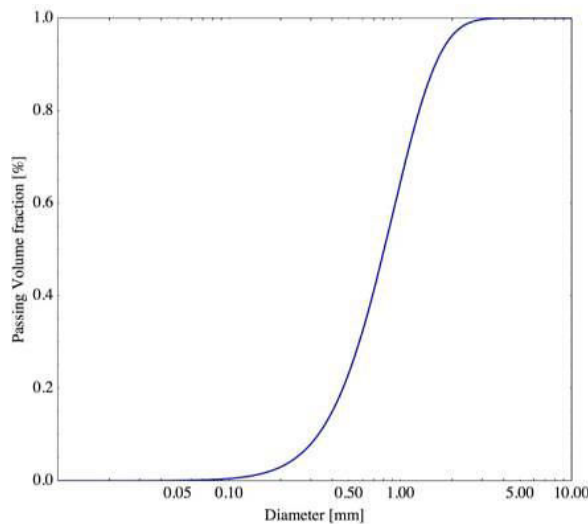


Figure 6.12 Passing volume fraction of sand used in the simulation (sand 0/4)

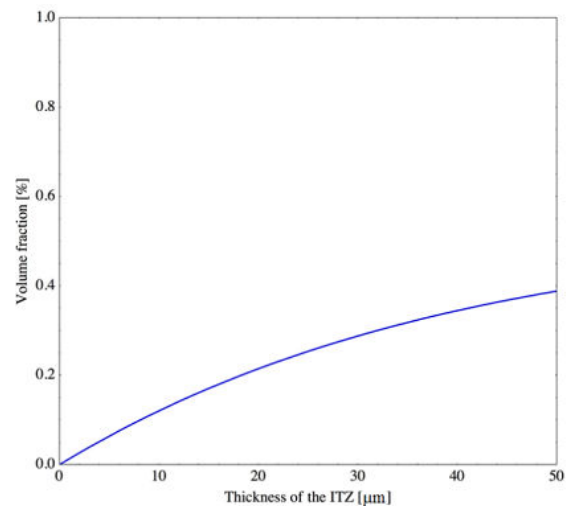


Figure 6.13 ITZ volume fraction according to the thickness of the ITZ (e_{ITZ})

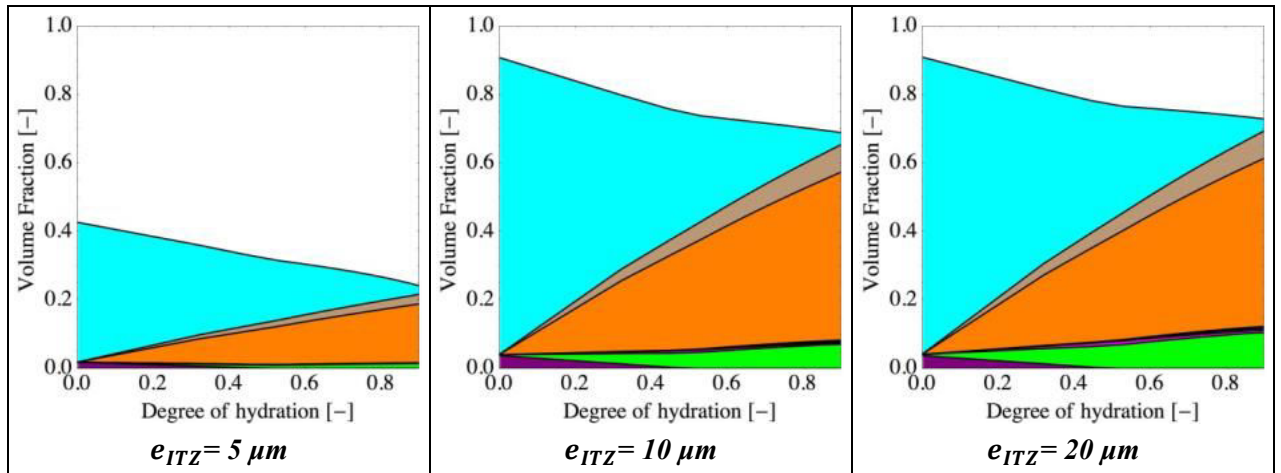


Figure 6.14 Composition of the ITZ according to the thickness of the ITZ (same legend as in Figure 6.4)

The passing volume fraction of the sand used in the simulations is shown in Figure 6.12. The volume fraction of the ITZ in the mortar using the formulation presented in Eqs. (6.8) – (6.10) is presented in Figure 6.13 for the same sand PSD. The curve is asymptotic to the value corresponding to the volume fraction of the sand ($f_{Sand} = 50\%$, here). As expected, the volume of the ITZ depends strongly on the thickness e_{ITZ} adopted. This, due to the assumptions regarding the composition of the ITZ, will specially reverberate in the estimation of ITZ porosity, as shown in Figure 6.14. The resulting compositions of the ITZ, according to three different e_{ITZ} which are commonly reported in the literature (Head and Buenfeld, 2006; Scrivener et al., 2004), are also shown in Figure 6.14.

6.4.2 Effective properties at the mortar scale

The properties of the ITZ layer are first determined. Figure 6.15 shows the estimated bulk and shear relaxation function of the ITZ with the composition corresponding to $e_{ITZ} = 20 \mu\text{m}$ in Figure 6.14. Compared to the LD layer in Figure 6.8, the behavior is less stiff but with a not very pronounced difference, as would be observed with the composition corresponding to $e_{ITZ} = 5 \mu\text{m}$.

The estimated effective bulk and shear relaxation functions as well as the creep function of the mortar are shown in Figure 6.16 and Figure 6.17, respectively, for different loading ages. Only a slight ageing character is observed after 300 h.

As expected, the creep in the cement paste (Figure 6.11) is more accentuated than in the mortar, even if the ITZ creep (not shown for conciseness) is more elevated than cement paste creep.

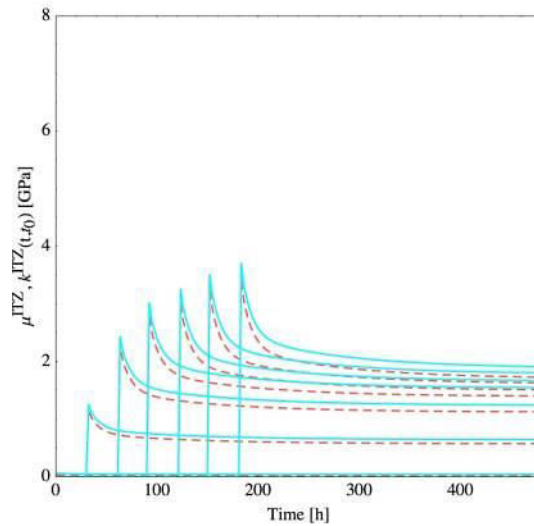


Figure 6.15 ITZ: estimated bulk (full lines) and shear (dashed lines) relaxation functions (see Figure 6.8 to be compared with LD layer)

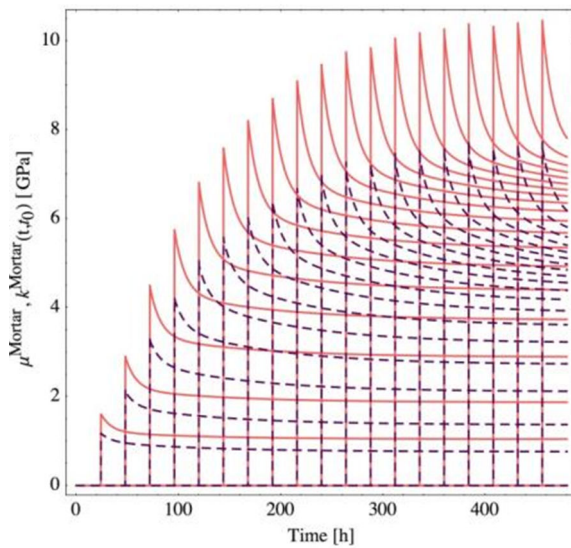


Figure 6.16 Effective behaviour of the mortar: bulk and shear relaxation function

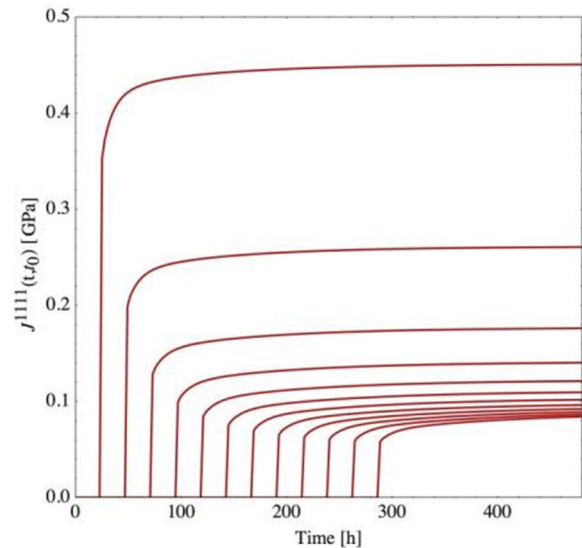


Figure 6.17 Effective behaviour of the mortar: creep function

6.5 CONCRETE SCALE

At the concrete scale (Level 4), numerical homogenization is used to estimate the properties. Two phases are considered: the coarse aggregates with elastic behaviour and the mortar matrix with ageing viscoelastic behaviour obtained from the previous sections. Note that, since the specific surface of coarse aggregates is much smaller than that of the sand, the ITZ of the coarse aggregates are neglected. Bary et al. (2015) showed, by means of numerical simulations, that the ITZ of coarse aggregate can indeed be neglected in a non-ageing viscoelastic context.

6.5.1 Mesostructures

Two mesostructures with volume fraction of coarse aggregates $f_{Gra} = 40\%$ are studied: a) with spherical particles as presented in Section 5.4.1 and (b) with convex polyhedral inclusions obtained from Voronoi decomposition (as also used in Bary et al., 2014). The mesostructures tested are shown in Figure 6.18. For the local information assessment, the matrix is divided in 512 elements. Static uniform boundary condition (SUBC) is adopted. The PSD of the inclusions in both meshes are shown in Figure 6.19. The isotropy of the mesostructure (b) was successfully verified, as done in the last chapter for the mesostructure (a).

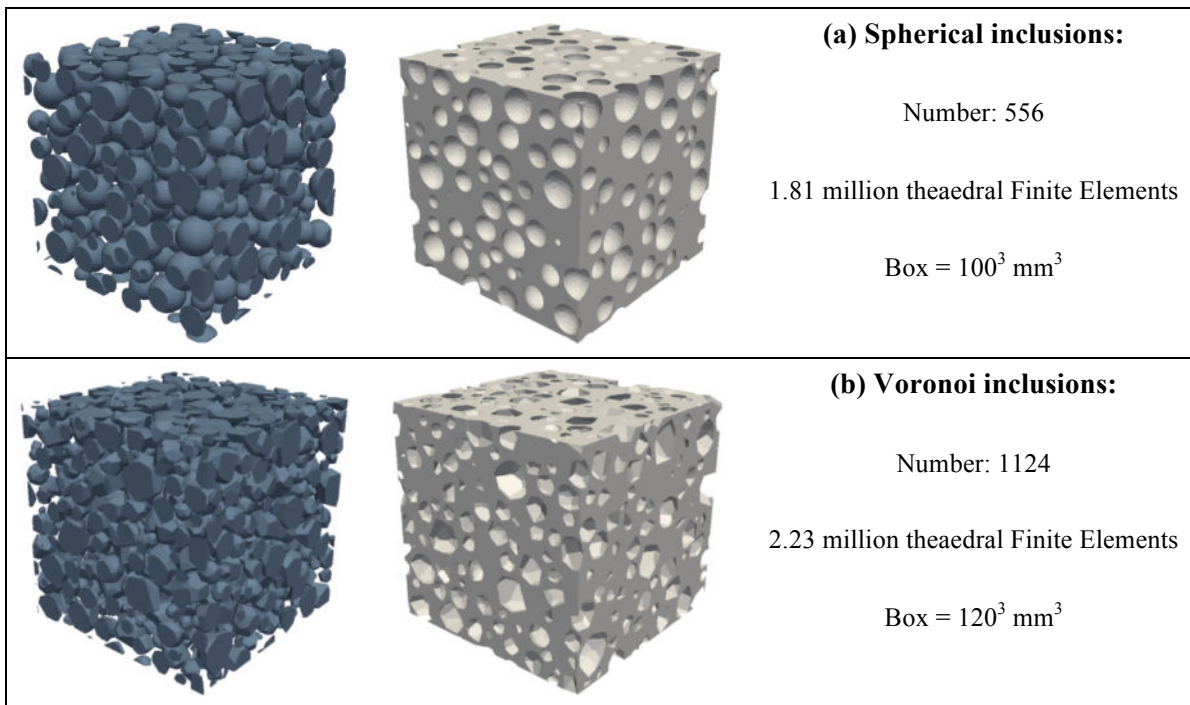


Figure 6.18 Mesostructures with matrix and spherical inclusions (up) and Voronoi inclusions (down) used in FEM simulations

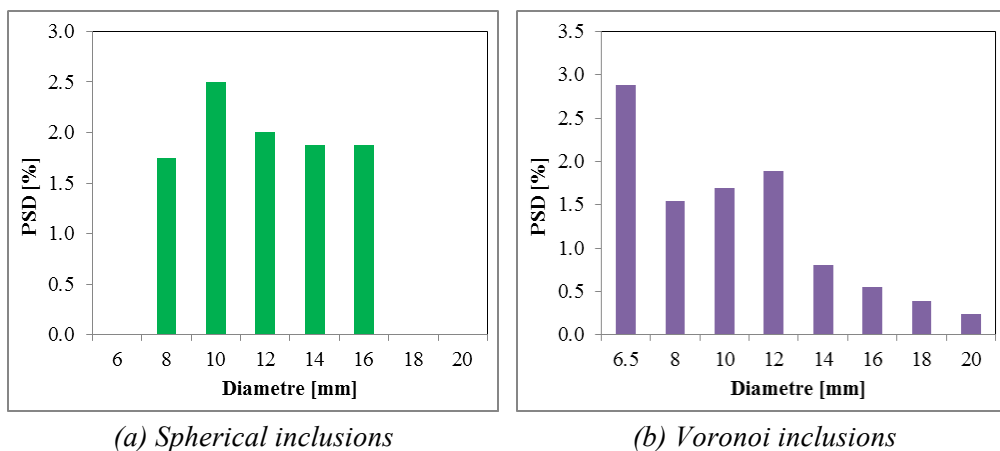


Figure 6.19 Particle size distribution of the inclusions in both meshes (a) Spherical and (b) Voronoi inclusions

The tools for numerical homogenization presented in section 5.3 are used here. Local information concerning the distribution of strains and stresses within the aggregates and subvolumes of the matrix are obtained. The algorithm presented in section 5.3 to describe the ageing linear viscoelastic behaviour is used with Cast3M for the simulations.

6.5.2 Effective properties at the concrete level

At the concrete scale, the behaviour of the mortar is fitted on the macroscopic one obtained by analytical homogenization by means of Prony series multiplied by an ageing function. Each simulation took about 3h for computing 36 time steps and effectuating the post processing.

The estimated effective bulk and shear relaxation functions as well as the creep function of the concrete are shown in Figure 6.20 and Figure 6.21, respectively. With the mortar behaviour computed in the last section, the ageing character is reproduced in the effective behaviour of concrete.

The creep values obtained are in agreement with some values found in the literature (e.g. (Laplante, 1993)). Note that the values of the relaxation properties are slightly different for the mesostructure with spherical inclusions compared to the one with Voronoi inclusions. The difference is more accentuated in the creep function estimations. The higher the contrast is (here, the earlier the loading time), the bigger the difference is between both estimations.

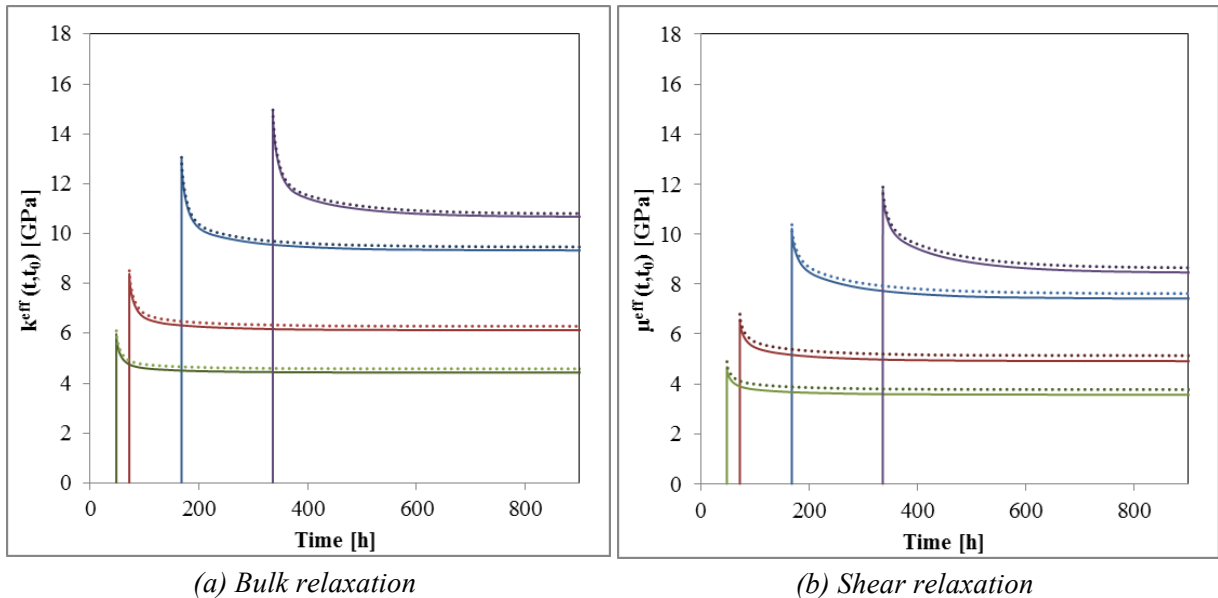


Figure 6.20 Estimated bulk and shear relaxation functions of concrete obtained by combined numerical and analytical homogenization for different loading ages: comparison between the mesostructures with spherical (full lines) and Voronoi (dotted lines) inclusions

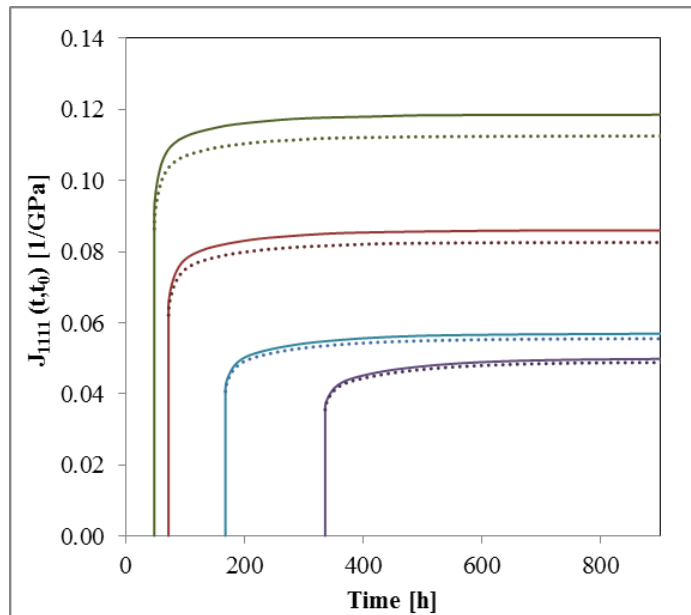


Figure 6.21 Overall uniaxial creep function of concrete obtained by combined numerical and analytical homogenization for different loading ages: comparison between the mesostructures with spherical (full lines) and Voronoi (dotted lines) inclusions

6.5.3 Local information

Figure 6.22 to Figure 6.25 show the study about the dispersion of the strains, in the direction of the loading, averaged within each matrix subvolume and each inclusion. Two loading times, $t_0 = 2$ and 14 days, are considered.

In Figure 6.22 and Figure 6.24 the evolutions of the strains are shown. The average value of the strain within the whole phase is illustrated by bold black line. Because some inclusions are in contact with the loaded surfaces, some outliers are observed among the inclusions. This aspect can be bypassed by taking as a sample a fraction of the box in which the edges are excluded in the post processing. The strains within the matrix and the inclusions evolve similarly with its absolute value increasing.

Figure 6.23 and Figure 6.25 show the evolution of the strains distributions within the matrix subvolumes and the aggregates. The distributions tend to get broader with the time. This effect is more pronounced within the matrix and for later ages of loading. The shape of the inclusions seems to affect poorly the dispersion of the strains. Figure 6.26 shows that the initial (at $t = t_0$) and final values (at $t = 40$ days) of the dispersion within the strains are quite similar for both mesostructures.

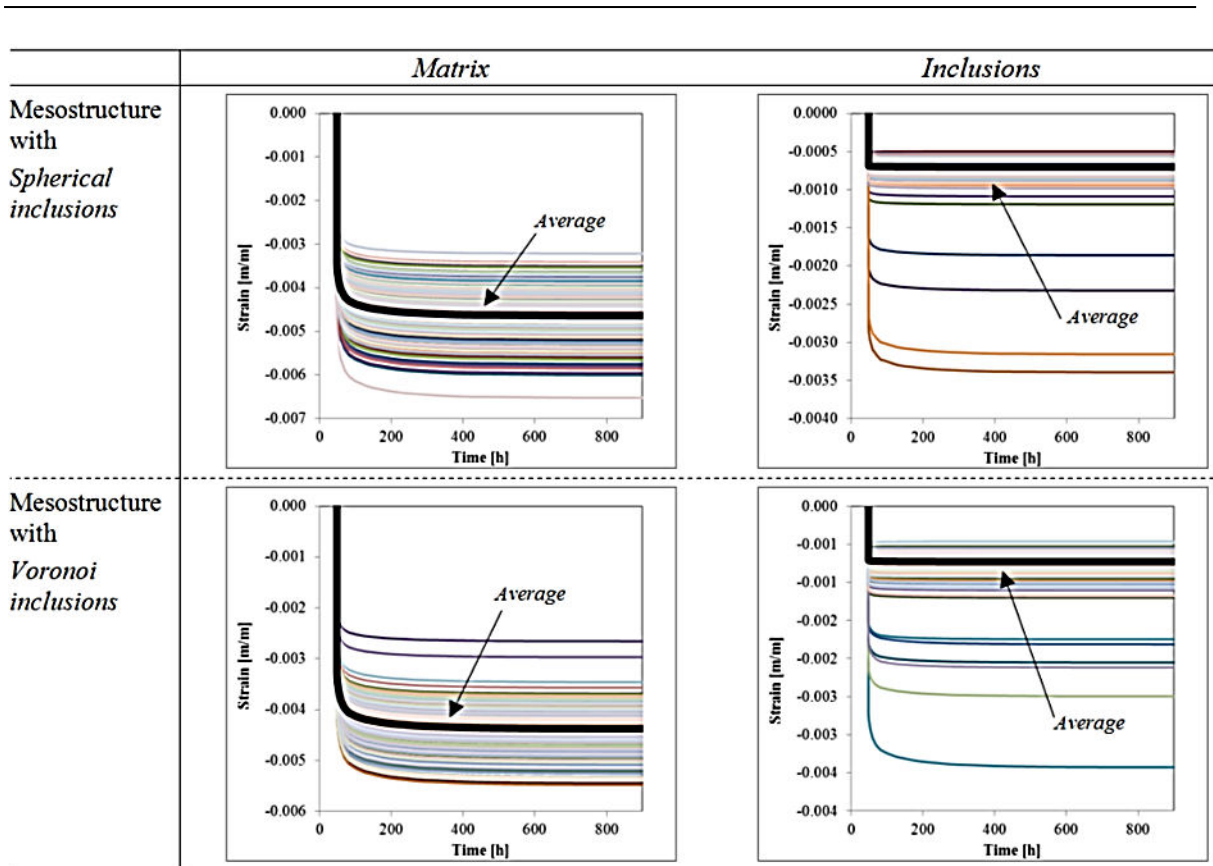


Figure 6.22 Dispersion of the uniaxial strain averaged within matrix subvolumes and aggregates, $t_0 = 2$ days

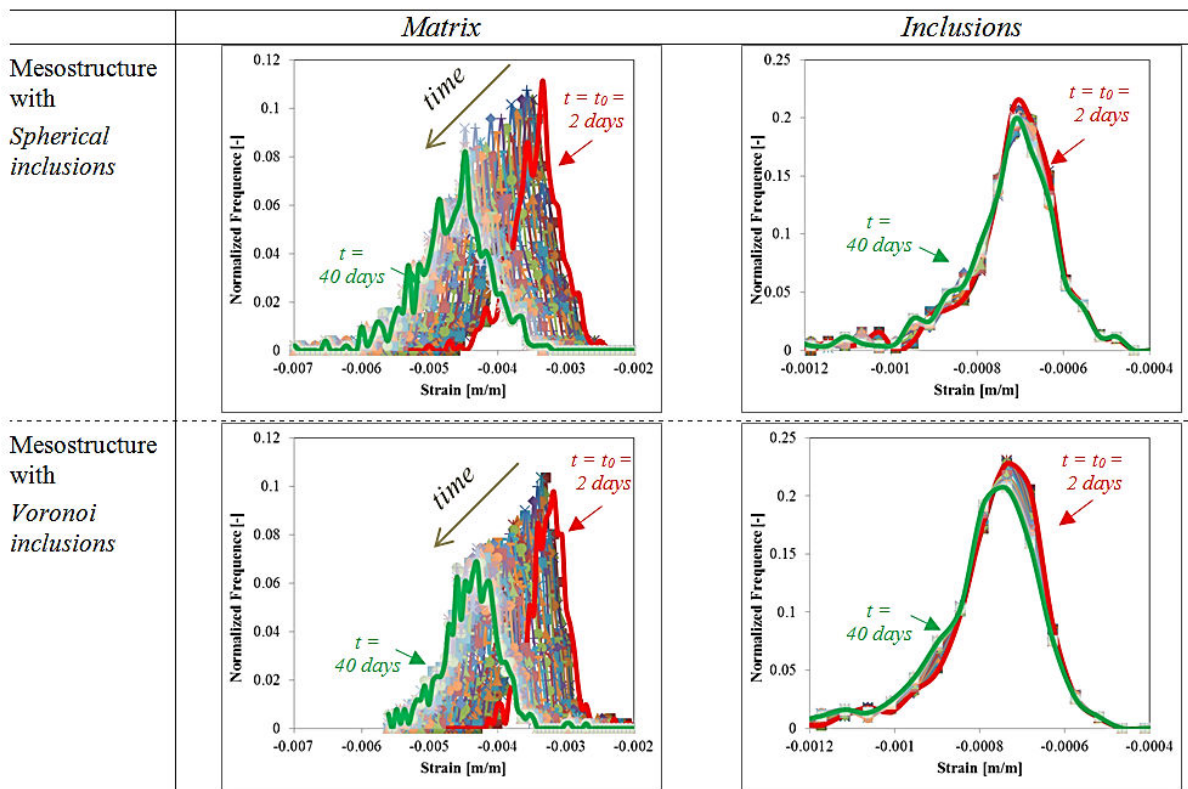


Figure 6.23 Distribution of the uniaxial strain for the matrix and the aggregates, $t_0 = 2$ days

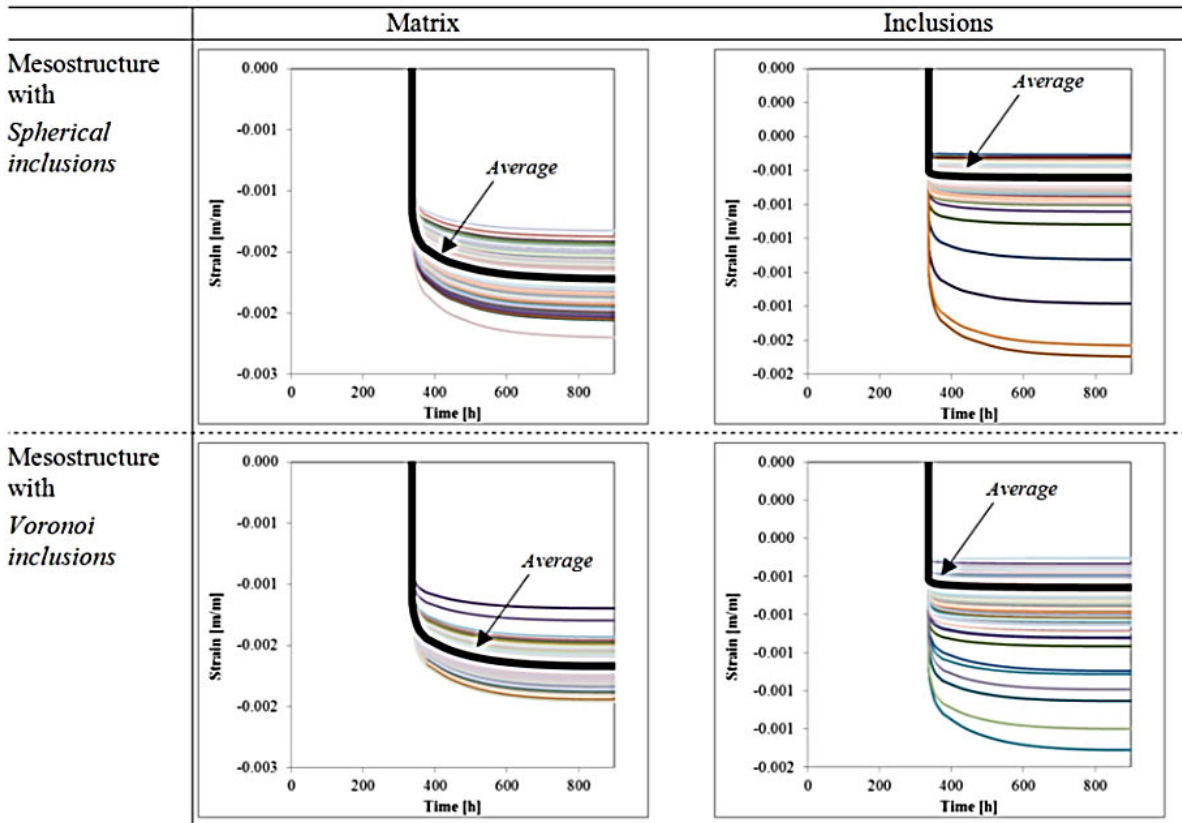


Figure 6.24 Dispersion of the uniaxial strain averaged within matrix subvolumes and the aggregates, $t_0 = 14$ days

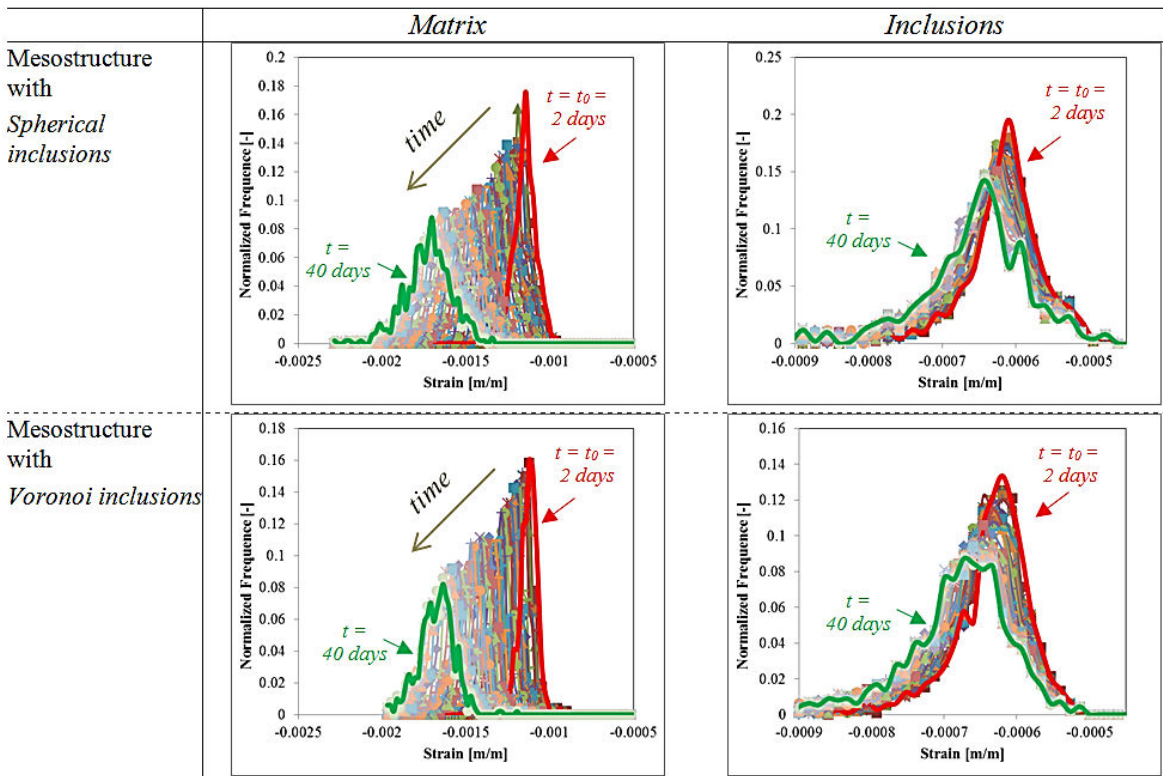


Figure 6.25 Distribution of the uniaxial strain for the matrix and aggregates, $t_0 = 14$ days

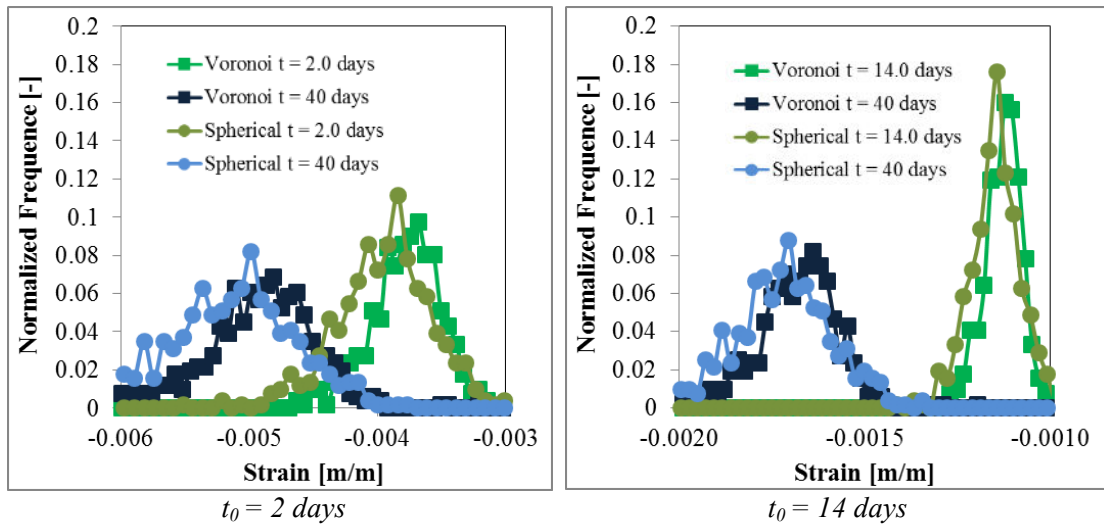


Figure 6.26 Distribution of the uniaxial strain for the matrix: comparison between microstructures with spherical and Voronoi inclusions

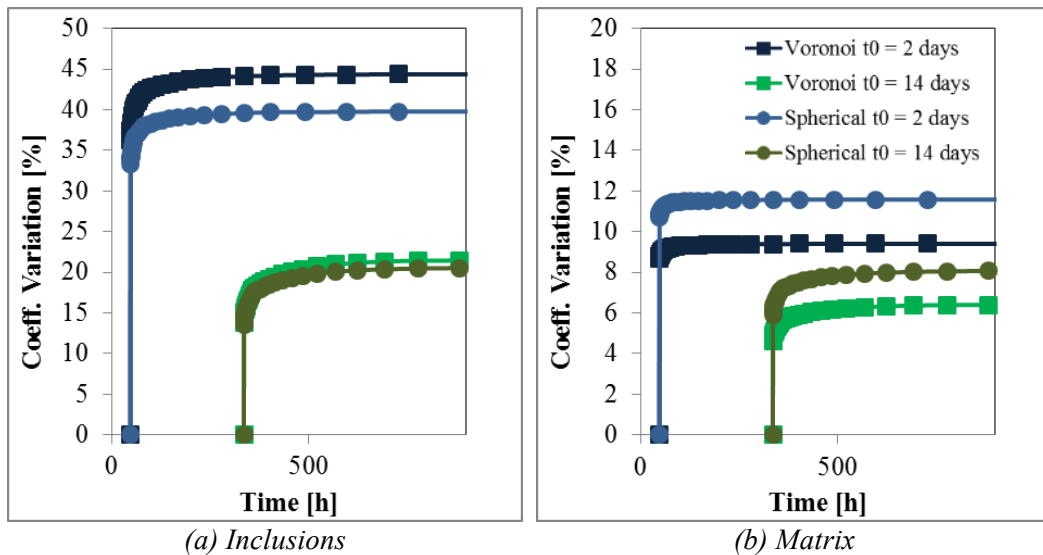


Figure 6.27 Coefficient of variation according to the shape of the inclusions and loading time

A difference is observed, though, on the coefficient of variation (CV), as shown in Figure 6.27. The CV is the ratio between the standard deviation and the mean. Regarding the strains within the inclusions, the mesostructure with spherical inclusions presents a lower CV than the one with polyhedral inclusions. The opposite is observed in the matrix subvolumes. The loading time seems to affect more strongly the CV within the inclusions. Globally, the CV is higher in the inclusions, indicating a greater dispersion in this phase, in agreement with Figure 6.22 to Figure 6.25.

Figure 6.28 shows the maps of strains, in the direction of the loading, according to the loading time and shape of the inclusions. The presence of zones with higher magnitude of strains is evident for $t_0 = 2$ days (blue zones). A more homogeneous distribution of the strains is observed for $t_0 = 14$ days. Again a similar behavior is observed for both mesostructures.

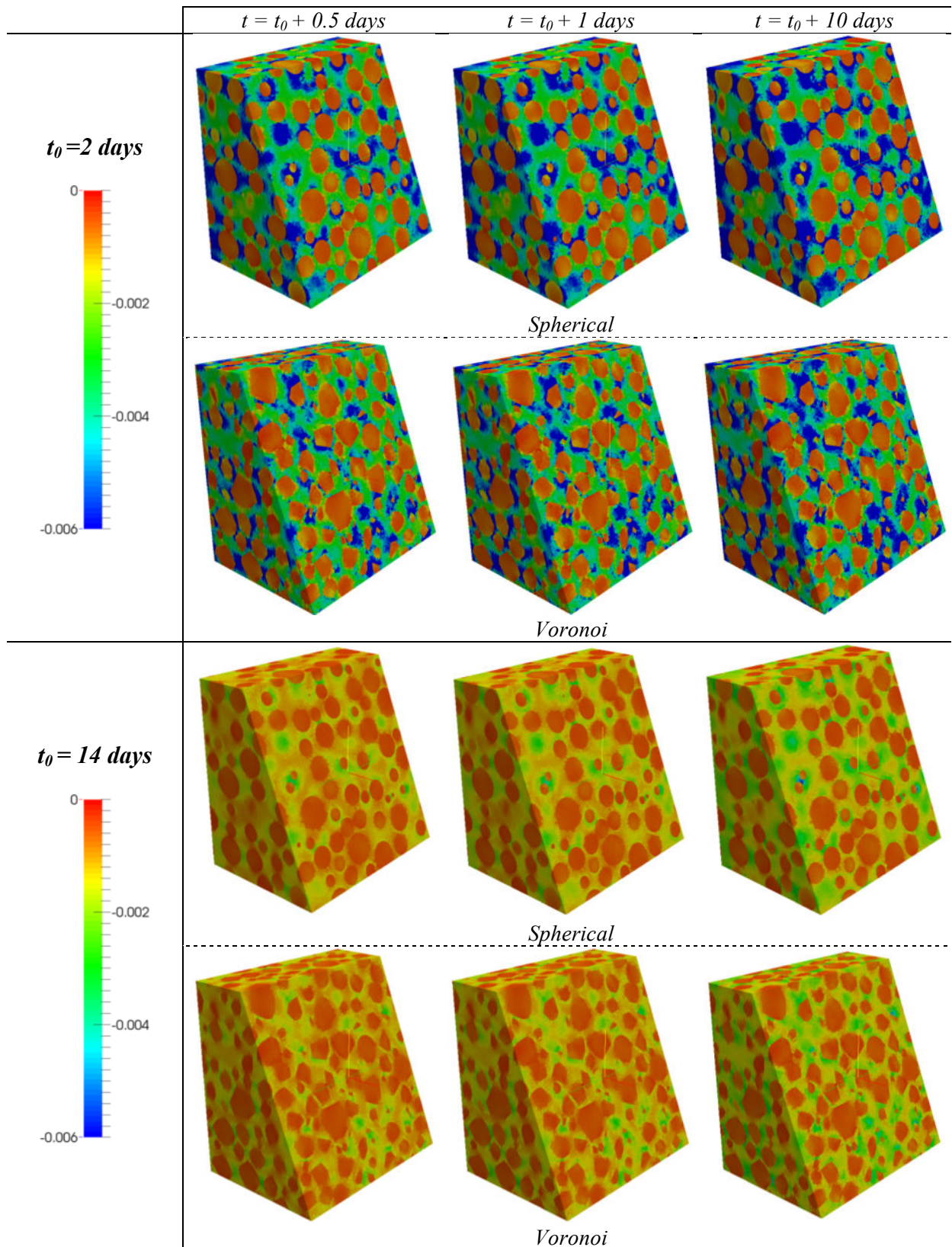


Figure 6.28 Strains (in the direction of the loading) within aggregates and mortar matrix at different ages for $t_0 = 2$ and 14 days

6.6 CONCLUSIONS AND PERSPECTIVES

A strategy combining the analytical and numerical homogenization tools presented in Chapter 5 was employed here to investigate the ageing viscoelastic behaviour of cement-based materials at early-age. Analytical schemes were used to estimate the properties at the level of hydration products, cement paste and mortar. Numerical homogenization is used to study the concrete scale.

- The combined approach proposed here allows investigating different propositions of mechanisms leading to an ageing behaviour. Simulations taking into account the space-filling process as leading to an intrinsically ageing behaviour of C-S-H can be performed.
- The estimations of the creep response are in agreement with the usual values obtained experimentally for similar concretes. In the next chapter, the results obtained here are confronted with the input data used in the simulation in the Part I regarding the ageing and viscoelastic behaviour of concrete.
- The inclusions shape affects not very strongly the overall behaviour. The earlier the loading time the higher the difference between the response of polyhedral and spherical inclusions. The local information obtained by numerical homogenization at the concrete level showed a similar dispersion in the strains for both inclusions shapes. The coefficient of variation of the strains within the inclusions is moderately higher in polyhedral inclusions.
- The upscaling approach presented here is valid only for periods after the percolation of the microstructure. Strategies to account for the existence of a percolation threshold at the cement paste level are to be developed.
- The influence of the ITZ on the ageing linear viscoelastic behaviour deserves further investigations. Mortar behaviours estimated with different ITZ thicknesses and compositions can be performed. Additionally, an adaptation of the GSC so that a fixed ITZ thickness, independent of the size of the particle, is set is another aspect to be considered.
- The mortar level can be itself studied by means of numerical homogenization too. For example, the two-coated microstructure presented in Chapter 5 could be used to represent the mesostructure of mortar. But inherent difficulties regarding the representation of the ITZ with its interpenetrations, as well as the small thickness of ITZ which demands a much finer meshing, makes this extension not trivial.
- Further studies accounting for the effect of the volume fraction of the inclusions and phase contrast on the ageing linear viscoelastic behaviour can be envisaged. The edge effect found in numerical simulation also needs further investigations.

In the next chapter, some properties used as input data in the structure simulation of Part I are estimated from the composition of the cement past by applying the developments performed so far.

7. CONTRIBUTION OF THE MULTISCALE ANALYSIS TO THE STRUCTURAL ANALYSIS

In this chapter, the thermal and mechanical properties, which were used as input data in the simulations in Part I, are estimated by means of the approach developed in the Part II. Following the strategy of chapter 6, the same microstructure representation is used with the evolution of the volume fraction of the hydrates, water and clinker minerals are taken into account following the model described in chapter 4. For the other properties, the evolutions related to the changes in the degree of hydration (the ageing aspect) are taken into account in the multiscale analysis.

With the multiscale estimation of the mechanical and thermal properties of concrete combined with the structural analysis of Part I, a full strategy for the prediction of the behaviour of massive concrete structures from the composition of the concrete may be envisaged following a sequenced approach:

- (1) the concrete behaviour is estimated using the upscaling techniques
- (2) the estimations are used as the input data to the phenomenological analysis at the structure level.

Such combined approach allows increasing the confidence in the phenomenological part, reducing in some aspects its empiricism. Additionally, this study may potentially serve as a tool to limit the amount of new experimental tests in the case of a change in the conditions in which the concrete modules are built. These conditions comprise many aspects from the concreting temperatures or other environmental aspects, passing by the composition of the concrete up to the composition of the cement itself.

Recalling the conditions adopted in chapter 6, the composition of cement is presented in Chapter 4 (section 4.4). The volume fraction of sand is set to 50% and the volume fraction of coarse aggregate is 40%. The thickness of the ITZ is taken as 20 μm .

7.1 ELASTIC PROPERTIES

With the representation of the microstructure proposed in the last chapter the estimation of the elastic properties is straightforward at the cement paste and mortar levels. Again, the concrete properties can be evaluated by numerical homogenization. Such computations were performed in the paper (Honorio et al., 2014c), on which this section is inspired. The elastic properties shown in Table 6.1 are used again.

Young modulus and elastic Poisson ratio, as shown in Figure 7.1 and Figure 7.2, respectively, are estimated as a function of time and degree of hydration. At 28 days the estimations of the Young

modulus is 30.5 GPa. For the studied concrete, the experimentally determined value of the Young modulus at 28 days was 32.4 GPa (Craeye, 2010). Considering the uncertainties and variations found within the experimental values of the properties of hydrates and aggregates used as input, the difference between experimental and calculated values seems reasonable (less than 7 %).

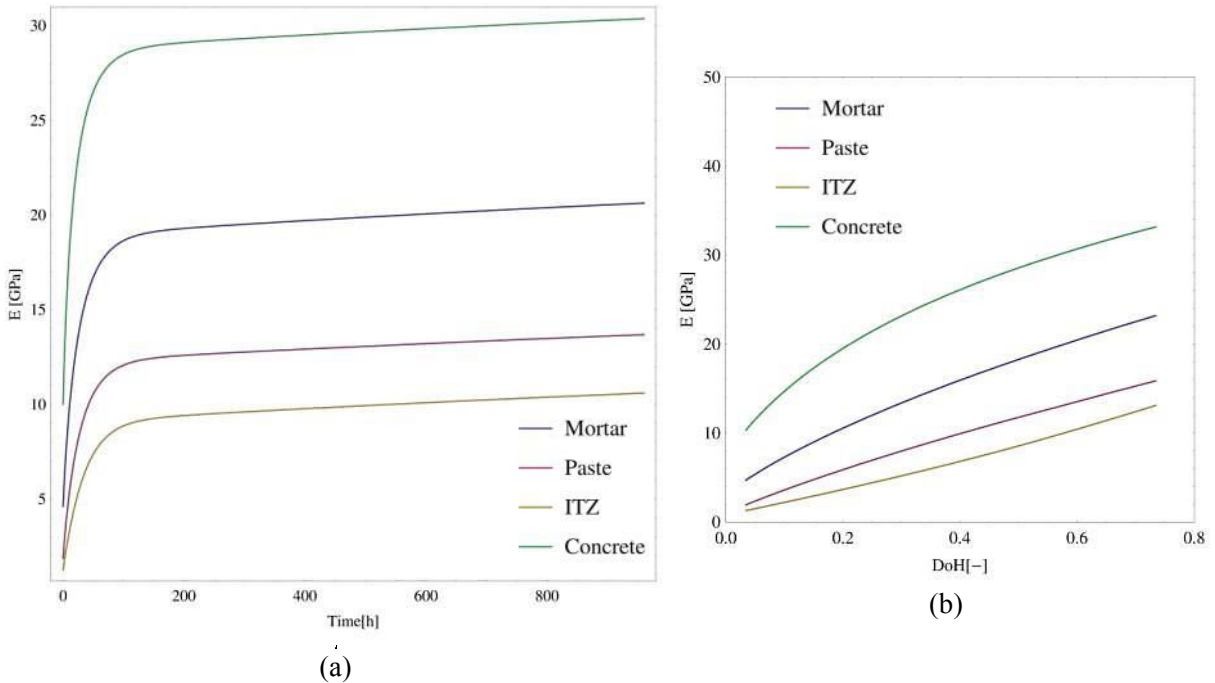


Figure 7.1 Young modulus: evolution as a function of (a) time and (b) degree of hydration

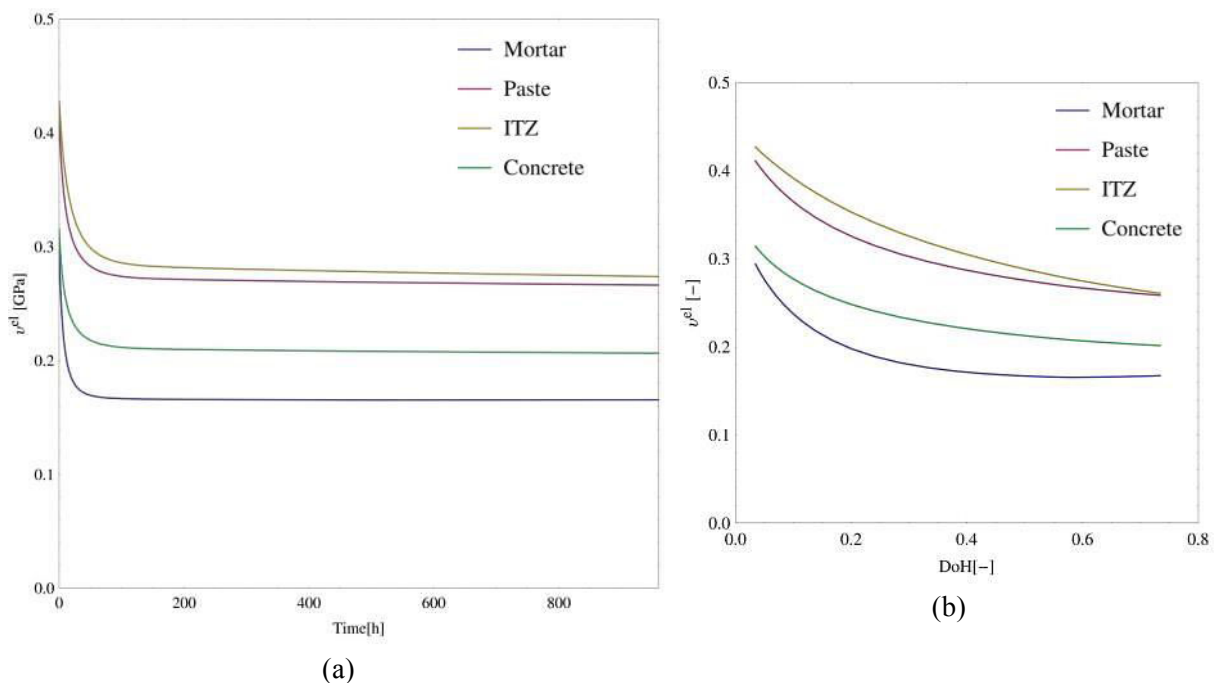


Figure 7.2 Elastic Poisson ratio (no viscous effects considered): as a function of (a) time and (b) degree of hydration

As expected, the Young moduli evolve almost linearly with respect to the degree of hydration. An exception is the behaviour of concrete at very early age. Note, however, that since no percolation

threshold is considered the evolution at low DoH must be seen with some reserves. Regarding the elastic Poisson ratio of concrete, at 28 days the experimentally measured value is 0.16, obtained from the average of three values (0.17, 0.19 and 0.14 (Craeye, 2010)). The model estimation is 0.20 at 28 days. Again, it is necessary to take into account the unavailability of some precise measurements of the properties of some phases. A non-linear evolution of the elastic Poisson ratio with respect to the degree of hydration is observed as in (Bernard et al., 2003).

Due to time-dependent effects the Poisson ratio needs to be well defined in an ageing viscoelastic framework (Hilton and Yi, 1998). Creep and relaxation functions are more useful to describe the overall behaviour in this context. The creep response is presented in next section.

7.2 AGEING VISCOELASTIC BEHAVIOUR

The results of both microstructures studied numerically in the last chapter are confronted with the experimental results of Craeye (2010) for the concrete described in section 3.2.2.

Figure 7.3 shows the basic creep strains (in which the elastic contribution was discounted for) for different loading ages and mesostructures with spherical and Voronoi inclusions. A reasonable agreement between the Voronoi inclusions mesostructure and the experimental results is observed.

However, the behaviour at the first hours is not very well described. A C-S-H behaviour with an intrinsically solidifying feature (as presented in Figure 6.7) could lead to a more gradual augmentation of the creep strains. Moreover, further investigations are necessary to extend the study to long-term behaviour associated with unloading in which the irreversible part of creep is also considered. Other perspectives include the study of the effects of drying and temperature on the viscoelastic behaviour.

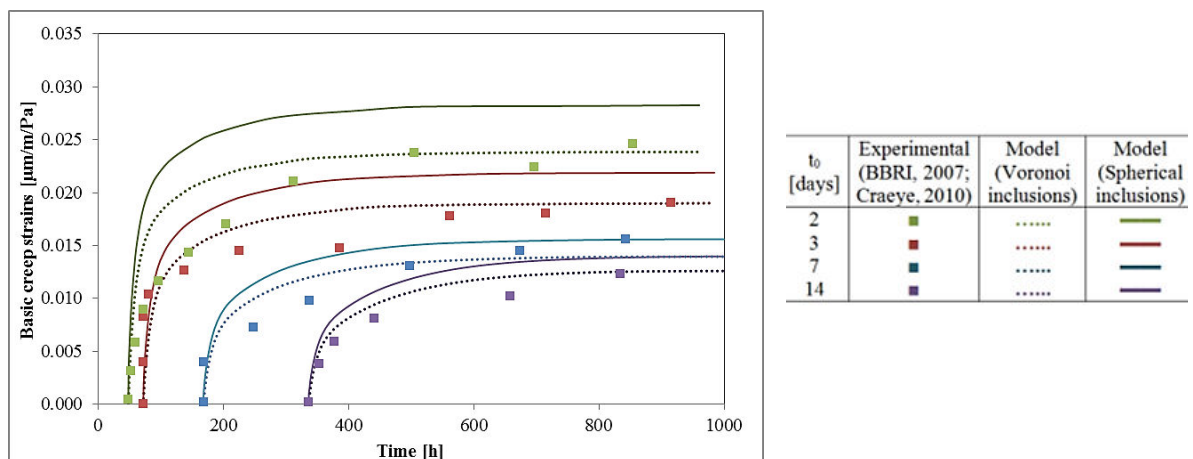


Figure 7.3 Basic creep tests at concrete level: experimental (dots) and numerical estimations (full and dashed lines for spherical and Voronoi aggregates, respectively)

7.3 THERMAL PROPERTIES

The thermal properties, namely the specific heat, thermal conductivity and coefficient of thermal expansion (CTE) are important in the determination of the early-age behaviour (Bentz, 2008). These properties evolve at early age with the changes in the microstructure of the cement-based materials. Generally this aspect is not explicitly taken into account in simulation or even experimentally. Briffaut et al. (2012) performed simulations, at the structure level, in which the heat capacity and the thermal conductivity evolved with respect to the degree of hydration. In their simulation the evolution of the heat capacity impacted the stress response more strongly than the evolution of the thermal conductivity.

Table 7.1 Thermal properties: results for different temperatures (ranging from 10 to 30 °C): the bold values are used in the simulations

Compound	Specific heat [J/(kg.K)]	Thermal conductivity (volumetric) [W/m.K]	CTE $\times 10^{-6}$ [°C ⁻¹]
Clinker	750 (1)	1.55 (1) (estimated)	
C-S-H	830- 920 (4) 970 (4)	0.98 (4)	48 (9) 45(4)
Gypsum	1080.4 (3)	0.66 (5)	
Water	4183 (free water) (18)	0.604 (1) 0.598 (17)	200-300
Air	1005	0.025 (7) 0.0242-0.0262 (17)	3430
CH	1140 (4) 1150 (4)	1.32 (4)	70 (8) 99.1 (4)
Cement Paste	736 (2) 1100-1800 (1) 1300-1740 (3) 1280 (6) 1730 (1) (fresh paste)	0.53 (2) 0.97-1.06 (3) 1.28 (6) 2.8 (7)	14.8 (10) 10-60(14)
Mortar	642 (2)	0.58 (2) 0.9-1.5 (5) 1.37-2.65 (11)	7.4-11 (10) 10-50(14)
Concrete	1109-1590 (13)	1.2-2.0 (5) 1.60-4.18 (11) 1.14-2.34 (12)	12.6-14.2 (10)
Limestone aggregates	908 845 (13)	3.15 -3.23(5) 3.15-3.49 (11) 2.65-3.22 (12) 3.22 (13)	0.4-10.2 (15) 3.1- 4.0 (16)
Siliceous aggregates and quartz	-	2.90-5.18 (5) 5.16 (12)	7.4-13.8 (15)
Basalt	766 (13)	4.03-4.30 (11) 2.86 (12) 1.70 (13)	5.3-7.4 (15)

(1)(Bentz, 2007) ; (2)(Xu and Chung, 2000); (3)(Ukrainczyk and Matusinović, 2010) (calcium aluminates cements); (4)(Abdolhosseini Qomi et al., 2015) (molecular simulations); (5)(Cerny and Rovnanikova, 2002); (6)(Yoon et al., 2014); (7)(Bouguerra (1997) cited by (Mounanga et al., 2004); (8)((Xu et al., 2007) cited by (Ghabezloo, 2011)); (9) (Ghabezloo, 2011) (inverse analysis); (10)(Cruz and Gillen, 1980) ; (11) (Khan, 2002); (12) (Kim et al., 2003); (13) (Marshall, 1972); (14) (Wyrzykowski and Lura, 2013); (15) (Johnson and Parsons, 1944); (16) (Wong and Brace, 1979); (17) (Vargaftik, 1993); (18) (Holman, 2009)

The thermal properties are also generally function of the temperature. After Morabito (2001), the thermal conductivity decreases when the temperature increases, whilst the specific heat increases with the temperature rise. Cruz and Gillen (1980) also reported a dependency of the thermal conductivity of concrete and mortar on the temperature. Similar variations with the temperature are observed for the heat capacity (Marshall, 1972) and CTE (Lura and Van Breugel, 2001). These effects of the temperature are not considered in the following.

Despite the importance of such properties in the early-age analysis, there is a lack of experimental data especially concerning the hydration products. Table 7.1 gathers some values found in the literature for some constituents of cement-based materials. These values correspond to temperature close to 20°C in almost all cases. Following the composition of the modules concrete, limestone aggregates are adopted. In Table 7.1, the values in bold are used to estimate the thermal properties in this section.

In the following the properties of C-S-H are used for estimating the ones of the hydration products which are unknown. The (free) water content seems to play a major role in the thermal properties cited (Bentz, 2007), this aspect is highlighted in the sequel. The influence of the bonded water, whose properties are different from free water, is not taken into account.

Thermal conductivity and CTE are considered as isotropic. No effects of convection and radiation are accounted for: gas and liquids are assumed transparent to radiation and the emitted radiation is considered as totally absorbed by the solid part. No temperature jumps effects are considered either (Vargaftik, 1993).

7.3.1 Heat capacity

The heat capacity is reported to significantly affect the thermo-chemo-mechanical of concrete structures (Lura and Van Breugel, 2001). A given variation of the heat capacity may lead to a variation of the same order in the computed temperatures and stresses (Lura and Van Breugel, 2001). Similar to the other thermal properties an influence of the temperature, a variation with age within the first days as well as a dependency of the w/c are reported on the heat capacity (Marshall, 1972). In the literature, a large range of heat capacity values can be found for cement-based materials (Bentur, 2003).

Because of its extensive nature, a rule of mixture can be used to estimate the heat capacity from the basic phases of the system (Bentz, 2007):

$$C^{hom} = \sum_{i=1}^N (C_p^i f_i^v) \quad (7.1)$$

where the overall heat capacity is given as a sum of the weighted contribution of the heat capacities C_p^i (at constant pressure) of phase i .

With this equation, and following the evolution of the volume fractions described in Chapter 4, we obtain the evolution of the specific heat capacity, as shown in Figure 7.4, for cement paste, ITZ, mortar and concrete.

Within the first 3 days the most part of the evolution of the specific heat capacity occurs for mortar and cement paste. In the paste and ITZ a slight evolution still takes place after that time. As can be seen in Figure 7.4b, the evolution is almost linear in all cases with respect to the degree of hydration.

The specific heat capacity used in the simulation in Part I is 1000 kJ/kg.K. This value is close to the long-term specific heat obtained analytically. However, the variation within the first days may play a non-negligible role on the thermo-chemo-mechanical response. This aspect would deserve further investigations.

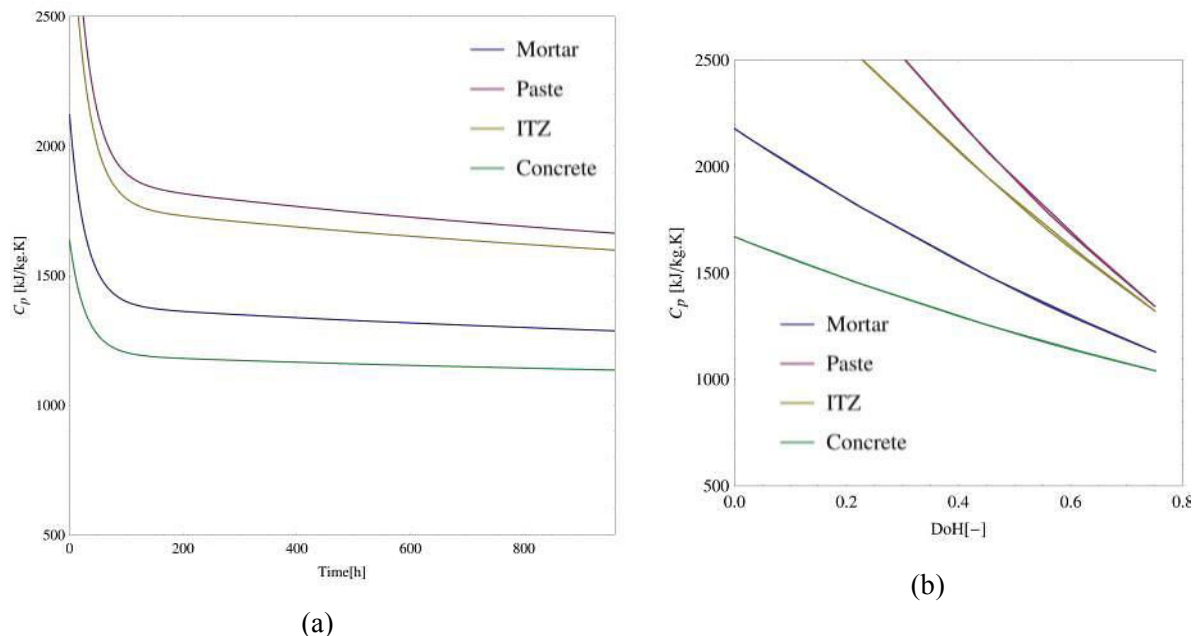


Figure 7.4 Evolution of the heat capacity of the cement paste, ITZ, mortar and concrete, w/c = 0.5: as a function of time (a) and of the degree of hydration (b)

7.3.2 Thermal conductivity

Thermal conductivity is reported to affect less strongly the thermo-chemo-mechanical behaviour and cracking risks at early-age. Lura and Van Breugel (2001) have shown that up to 5% of variation in the thermal conductivity, an almost negligible effect is observed on the temperature and stress responses.

Similar to the heat capacity, the thermal conductivity increases with the moisture content and is affected by the type of aggregate and w/c (Kim et al., 2003). However, the conductivity of solids depends on the form on the inclusions, especially the form and topology of pores (Khan, 2002).

Accordingly, cracks can reduce the thermal conductivities (Cerny and Rovnanikova, 2002), but this effect is not considered in the following.

Thermal conductivity also depends on the age, especially within the first days. Faria et al. (2006) reported that the concrete thermal conductivity in the first hours after mixing is about 20–30% greater than in hardened concrete.

Multiscale approaches have been used to determine the thermal conductivity. For example, Bentz (2007) estimated the thermal conductivity based on Hashin-Strikmann (1963) bounds. Here, we followed the same microstructure representation as in Chapter 6. To do so, MT and GSC estimations of the thermal conductivity are needed.

Mori-Tanaka estimations for the coefficient of thermal conductivity is given by (Benveniste, 1987):

$$\lambda^{MT} = \lambda_0 \left(1 + 2 \sum_{p=1}^N \left(\frac{\frac{\lambda_p}{\lambda_0} - 1}{2 + \frac{\lambda_p}{\lambda_0}} f_p^v \right) \right) / \left(1 - \sum_{p=1}^N \left(\frac{\frac{\lambda_p}{\lambda_0} - 1}{2 + \frac{\lambda_p}{\lambda_0}} f_p^v \right) \right) \quad (7.2)$$

where λ_p is the thermal conductivity of the phase (p); with $p = 0$ referring to the phase considered as the reference medium (matrix).

The 3-phases GSC estimation can be obtained by applying iteratively the 2-phases GSC estimation which is, for the thermal conductivity, the same solution as MT one (Benveniste, 1986).

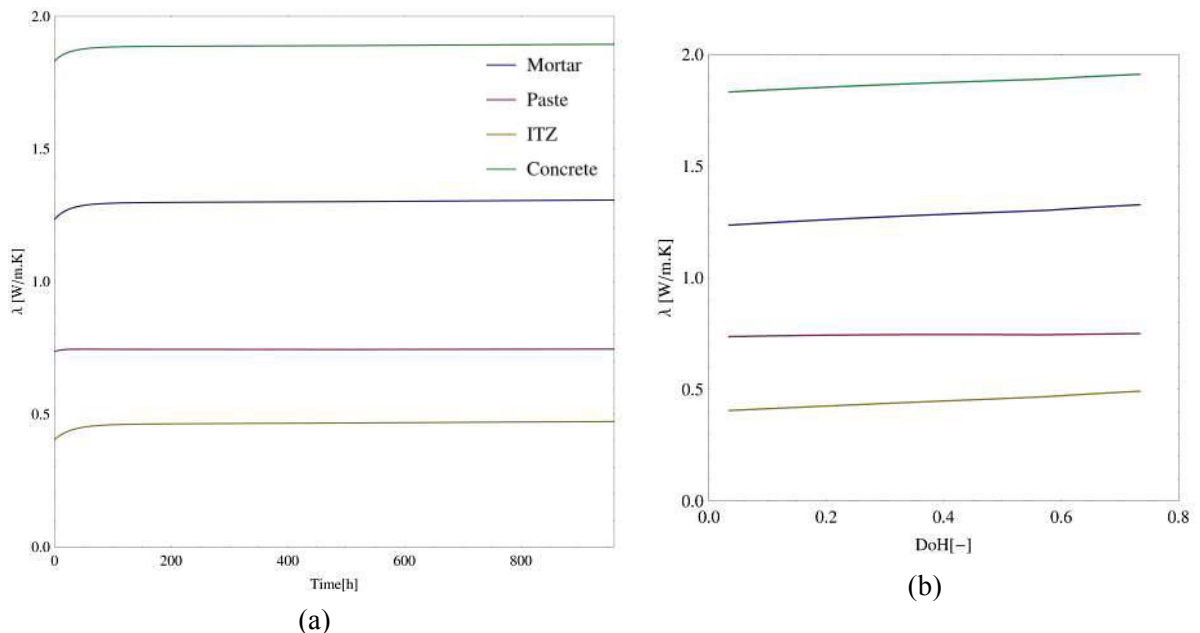


Figure 7.5 Evolution of the thermal conductivity of the cement paste, ITZ, mortar and concrete, w/c = 0.5: as a function of time (a) and of the degree of hydration (b)

Following the evolution of volume fractions described in the Chapter 4, we obtain the evolution of the thermal conductivity, as shown in Figure 7.5, for cement paste, ITZ, mortar and

concrete. Within the first 2 days the most part of the evolution of the thermal conductivity occurs for all materials. But even in the very early ages the evolution is slight. As can be seen in Figure 7.5b the evolution is almost linear in all cases with respect to the degree of hydration. Thermal conductivities ranging from 0.7 to 1.0 W/m.K were experimentally determined for cement pastes with different w/c and temperatures by Mounanga (2003). A similar evolution with a slight increase in the thermal conductivity with time was also observed.

The thermal conductivity used in the simulation in Part I of 1.8 W/m.K is in agreement with the value obtained in the multiscale estimation.

7.3.3 Coefficient of thermal expansion

The CTE affects actively the thermo-chemo-mechanical response: a variation of 16% in the CTE is reported to increase the cracking risk by about 15% (Lura and Van Breugel, 2001). On the other hand, Hilaire (2014) reported a not very pronounced impact of the CTE evolution on the mechanical response at early-age.

Again, an influence of the temperature and water content is observed with respect to the CTE.

Multiscale approaches based on Rosen–Hashin bounds (Wyrzykowski and Lura, 2013) have been used to estimate the CTE of cement-based materials. Viscous aspects are generally not taken into account. The viscoelastic behaviour is itself generally sensitive to thermal aspects. But with the adoption of a thermorheologically simple behaviour of each one of the involved phases, the temperature dependence can be incorporated into the time-scale for viscoelastic response (e.g. Schapery, 1968).

Assuming perfect bonded phases p , the CTE can be estimated by means of Levin equation (Levin, 1967):

$$\mathbf{a}^{hom} = \sum_{p=1}^N (f_p^v \mathbb{A}_p^T \cdot \mathbf{a}_p) \quad (7.3)$$

where \mathbf{a}^{hom} is the homogenized tensor of thermal expansion which is directly connected to the stress localization tensor \mathbb{A}_p^T and the tensor of thermal expansion of phases \mathbf{a}_p . This formula can be applied for both Mori-Tanaka and self-consistent schemes by adopting the corresponding localization tensor (Siboni and Benveniste, 1991). The tensor \mathbb{A}_p^T can be obtained from the averaged strains in section 5.2.3.3 together with the application of the constitutive law.

A preliminary estimation of the CTE of the mortar and concrete is performed here. Instead of accounting directly for the evolution of the volume fraction of hydrates in the solidification process as well as their individual CTE, we considered the homogenised mechanical behaviours of the cement paste and mortar (as obtained in chapter 6) to compute the mortar CTE. And in the

sequence, the concrete CTE is computed analytically using mortar CTE and the homogenised properties of concrete; no ITZ was considered at this level.

The evolution of the CTE of the cement paste, mortar and concrete for $w/c = 0.5$, from 36 hours after casting, is shown in Figure 7.6. Mortar and concrete CTE monotonously decreases with time, while cement paste CTE increases after a minimum by 2 days. A slight increase of the CTE was observed for example by Wyrzykowski and Lura (2013) for cement paste and mortar.

The obtained values of the concrete CTE are close to the experimental value found for the concrete modules of $\alpha = 11 \times 10^{-6} \text{ } ^\circ\text{C}^{-1}$. Note that a not substantial evolution of the CTE is observed after the first days.

Further investigation is necessary in order to account for the solidification process at the hydrate products levels (HD and LD layers as well as the ITZ). Again, improvements are necessary to better describe the evolution of the CTE at the very early age.

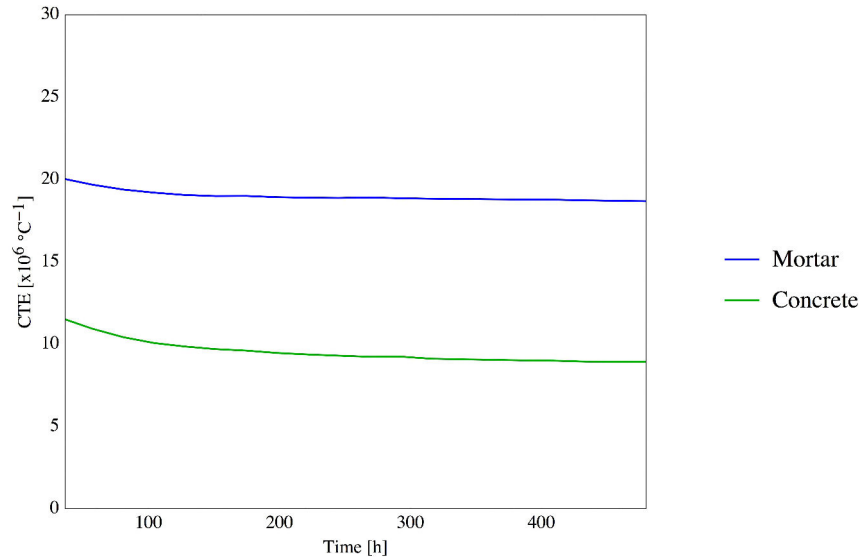


Figure 7.6 Evolution of the CTE of the cement paste, mortar and concrete, $w/c = 0.5$, as a function of time

7.4 CONCLUSIONS AND PERSPECTIVES

In this chapter, the thermal (heat capacity, thermal conductivity and CTE) and mechanical (Young modulus, elastic Poisson ratio, and viscoelastic properties) properties are estimated by means of the tools developed in Chapters 4 to 6. Note that for all cases, some assumptions were made about the behaviour of the phases at the cement paste scale due to lack of data, especially concerning thermal properties.

-
- Regarding the elastic properties, a reasonable agreement was obtained between experimental and estimated values regarding the Young modulus evolution and the final value of the Poisson ratio.
 - Similarly, the estimations of the viscoelastic behaviour at early-age seemed satisfactory with respect to the experimental data obtained by Craeye (2010). The mesostructure with the Voronoi inclusions provided results closer to the experimentally determined ones.
 - Regarding the thermal properties, adequate estimations of the final values of the heat capacity and thermal conductivity of concrete were obtained. The thermal conductivity showed only a small variation within the very first days which corroborates the choice of a constant value of thermal conductivity in part I. On the other hand, the heat capacity varied in a more pronounced way within the first 3 days. Simulation accounting for this variation could be an interesting further development of this study.
 - The CTE evolution obtained by analytical homogenization is in agreement with the experimental result obtained by Craeye (2010). This evolution after 36 hours is not very pronounced. Therefore, the hypothesis of a constant CTE adopted in the Part I seems reasonable. Further work is, though, necessary to apply the entire multiscale strategy developed in this thesis to the estimation of the CTE.
 - The confrontation of the modelling approach with a more exhaustive experimental campaign may validate in a more comprehensive way the approach developed here.
 - Again, the non-consideration of a percolation threshold limits the range of applicability of the estimations. Further researches in this direction could be interesting.
 - An approach accounting for the dependency of the temperature on the mechanical (including viscous) and thermal properties in a multiscale framework is to be developed. Also, the influence of cracking on the mechanical properties, thermal conductivity and CTE are also interesting routes of further developments.

8. GENERAL CONCLUSIONS AND PERSPECTIVES

The goal of this study was to (1) perform numerical simulations in order to describe and predict the thermo-chemo-mechanical behaviour of a concrete massive structure at early-age and (2) develop and apply upscaling tools to determine the key properties of concrete needed in an early-age analysis from the composition of the material. The first aspect, constituting the Part I of this thesis, was a modelling and simulation study answering ONDRAF/NIRAS practical needs regarding the prediction of the early-behaviour of concrete modules, as described in the introduction. The second aspect, the Part II of this manuscript, follows a more fundamental approach towards a better understanding of some key phenomena affecting the early age behaviour of cement-based materials.

In Part I a comprehensive study of the chemo-thermal problem has been performed. This study allows determining the influence of the different phenomena affecting the thermal response of the analysed structure. This structure is submitted to a complex thermal loading which makes difficult the estimation of the evolution of temperature field. The effects of the convection, solar radiation, reradiation and hydration heat are fundamental in the analysis. Practical recommendations regarding the concreting temperatures were provided in order to limit the maximum temperature reached within the structure. A mechanical analysis was performed using the results from the simulation with different sets of concreting temperatures. Simplified and more complex strategies were used to assess different scenarios in the mechanical aspect. The effect of restraint conditions and of the coupling between creep and damage were investigated.

In this first part, concrete is treated as a homogeneous material. However, different mechanisms taking place at different time and space scales affect its behaviour. These mechanisms must be studied at the scale of interest so that the macroscopic behaviour of the material may be properly determined. This multiscale investigation is done in Part II. A simplified model of cement hydration kinetics is proposed. The evolution of the volume fraction of cement, water and hydrates can be then estimated. Next, the tools to upscale the ageing properties are presented and applied to estimate the mechanical and thermal properties of cement-based materials.

The input data used in Part I are then compared with the estimations obtained in Part II. With the entire strategy proposed in this thesis, the prediction of the behaviour of massive concrete structures from the composition of the concrete is possible by means of a sequenced approach: the concrete behaviour is determined using the mechanistic strategy providing the input data to the phenomenological analysis at the structure level. Hence, the combined approach allows increasing the confidence of the phenomenological part reducing in some aspects its empiricism. Additionally, this study may potentially serve as a tool to limit the amount of new experimental tests in the case of a change in the conditions in which the concrete modules are built. These conditions comprise many aspects from the concreting temperatures or other meteorological aspects, passing by the

composition of the concrete up to the composition of the cement itself. Additionally, the multiscale approach allows extrapolating the results to the long term behaviour if the mechanisms at bottom scales are accordingly well defined.

8.1 STRUCTURE AND ITS ENVIRONMENT: PHENOMENOLOGICAL MODELLING AT THE STRUCTURE SCALE

Regarding the Part I, we conclude:

- Besides the heat of hydration, a relevant early-age analysis needs to take into account the different thermal transfer phenomena taking place at the boundary of the structure, namely convection, solar radiation, reradiation and conduction through the ground and older structural members. This aspect is highlighted by both 1D simplified solution and 3D numerical simulations, as shown in Chapter 2. A non-negligible contribution of each cited phenomena was observed in the determination of the maximum temperature reached within the structure. In this way, concreting temperatures (ambient temperature and temperature of concrete at the placement) prove to be a key contribution in the temperature response.
- The mechanical (restraint) and thermal boundary conditions affect directly the risk of cracking at early age. Simplified modelling strategies such as not accounting for the ground or not considering the oscillations within the daily temperatures may not capture accurately the mechanical response of the structure. On the other hand, the cracking index method, which is a simplified way to determine the risks of cracking, provides a reasonable first indication of the global zones more likely to crack.
- Simulations in which damage is accounted for showed that the coupling between damage and creep affects directly the mechanical response. For the cases studied here, however, the resulting cracking opening remains inferior to the preconized maximum admissible values.

As perspectives we point out:

- A study accounting for the hygral effects on the thermo-chemo-mechanical problem could provide more precise information about the behaviour of the structure at early-age.
- An improved description of the link between reinforcement and concrete could be interesting, in an investigation where the restraint induced by the reinforcement is evaluated in more details. This may be achieved in particular through analyses of specific refined zones of the structure where damage has been detected.

-
- An improved description of the link between the ground and the structure using, for example, contact or joint elements would improve the determination of the mechanical response. Note, however, that this task is not trivial given the additional non-linearities imposed by such kind of elements.
 - The calculated crack opening observed in some scenarios may affect the transfer properties of the studied structure, even if the impacts on the containment capacity of the structure are likely limited (due to the limited crack opening ($< 100 \mu\text{m}$) and their non-through-going nature). An investigation of the consequences of early-age cracking on the structure durability may serve to increase the confidence regarding this aspect.

8.2 ESTIMATION OF AGEING PROPERTIES FROM THE CONCRETE COMPOSITION

Regarding Part II, we conclude:

- The simplified kinetics model, based on boundary nucleation and growth with space filling coupled with a diffusion-controlled kinetics, captures the main effects of the paste composition and cement PSD on hydration. In spite of the simplifications assumed, results are consistent with experimental data.
- The analytical and numerical tools, presented in Chapter 5, to estimate the effective behaviour of heterogeneous materials in an ageing linear viscoelastic framework returned comparable coherent results even if the mesostructures and the assumption made in the definition of the microstructures are not exactly the same. For low volume fraction of inclusions and lower contrast between matrix and inclusions properties the numerical and analytical estimations give close results. As in the elastic case for matrices less stiff than inclusions, numerical estimations under SUBC are closer to analytical estimation than under KUBC. These aspects allow validating the analytical and numerical upscaling techniques presented in this chapter.
- Regarding the elastic properties, a reasonable agreement was obtained between experimental and estimated values for the Young modulus evolution and the final value of the Poisson ratio. Regarding the thermal properties, adequate estimations of the final values of the heat capacity and thermal conductivity of concrete were obtained. The thermal conductivity shows only a small variation within the very first days which corroborates the choice of a constant value of thermal conductivity in Part I. On the other hand, heat capacity varies in a more pronounced way within the first three days. Simulation accounting for this variation could be an interesting further development of this study.

-
- The estimations of the viscoelastic response are in agreement with the usual values obtained experimentally for similar concretes. Creep experimental data obtained by Craeye (2010) are reasonably reproduced by the combined numerical and analytical upscaling strategy developed in Chapter 6. As shown in Chapter 7, the mesostructure with the convex polyhedral inclusions returned results closer to the experimental data. This combined approach allows investigating different propositions of mechanisms leading to an ageing behaviour.

As perspectives, we highlight:

- Further investigations are to be performed concerning the extension of the hydration model to cement hydration. Systems with supplementary cementitious materials and cements with higher contents of aluminate phases may be studied. Also, more precise diffusion controlled kinetics can be employed. Effects related to the decrease in the internal RH should be added in order to more precisely consider lower w/c formulations.
- Regarding the analytical upscaling tools, a strategy to deal with improved time discretization in the determination of the shear relaxation modulus in the GSC scheme is desired. Regarding the numerical upscaling tools, a formal treatment to define the coupled size and the boundary conditions effects in an ageing linear viscoelastic behaviour are still to be developed. A specific study concerning the edge effects occurring in numerical simulations also needs further investigations. Other numerical methods as FFT-based ones could also be applied as they are particularly well adapted to such simulations, and are moreover able to directly analyse experimental microstructures obtained by e.g. tomography.
- The upscaling approach presented here is valid only for periods after the percolation of the microstructure. Further investigations to determine the percolation threshold are to be developed.
- Other C-S-H behaviours can be studied within the multiscale strategy developed in this thesis. For example, the C-S-H behaviour can be defined as intrinsically ageing due for example to a space-filling process, as presented in Chapter 6. Simulations accounting for this feature could be interesting to better understand the early-age behaviour.
- Mortar and cement paste can be also studied numerically. The coated sphere microstructure presented in Chapter 5 could be used to represent the mesostructure of mortar. More complex developments would be necessary to represent the cement paste with the evolution of the volume fraction of its different phases.

-
- A study about the dependency of the temperature on the mechanical (including viscous) and thermal properties in a multiscale framework is to be developed. Additionally, the influence of cracking on these properties is also an interesting route of further investigations.

REFERENCES

- Abdolhosseini Qomi, M.J., Ulm, F.-J., Pellenq, R.J.-M., 2015. Physical Origins of Thermal Properties of Cement Paste. *Phys. Rev. Appl.* 3, 064010. doi:10.1103/PhysRevApplied.3.064010
- ACI, 1996. (American Concrete Institute), Mass concrete, ACI 207.1R-96, Reported by ACI Committee 207.
- Acker, P., 2004. Swelling, shrinkage and creep: a mechanical approach to cement hydration. *Mater. Struct.* 37, 237–243. doi:10.1007/BF02480632
- Acker, P., 2001. Nouveaux bétons, couplages de performance. Presented at the 2ème Rencontres du Réseau Doctoral Génie Civil, Aussois, France.
- Acker, P., Ulm, F.-J., 2001. Creep and shrinkage of concrete: physical origins and practical measurements. *Nucl. Eng. Des.* 203, 143–158. doi:10.1016/S0029-5493(00)00304-6
- Adams, D.F., Doner, D.R., 1967. Transverse Normal Loading of a Unidirectional Composite. *J. Compos. Mater.* 1, 152–164. doi:10.1177/002199836700100205
- Allen, A. j., McLaughlin, J. c., Neumann, D. a., Livingston, R. a., 2004. In situ quasi-elastic scattering characterization of particle size effects on the hydration of tricalcium silicate. *J. Mater. Res.* 19, 3242–3254. doi:10.1557/JMR.2004.0415
- Azenha, M., 2009. Numerical simulation of the structural behaviour of concrete since its early ages (PhD Thesis). Universidade do Porto.
- Balluffi, R.W., Allen, S.M., Carter, W.C., Kemper, R.A., 2005. *Kinetics of materials*. J. Wiley & Sons, Hoboken, N.J.
- Bary, B., Béjaoui, S., 2006. Assessment of diffusive and mechanical properties of hardened cement pastes using a multi-coated sphere assemblage model. *Cem. Concr. Res.* 36, 245–258. doi:10.1016/j.cemconres.2005.07.007
- Bary, B., Bourcier, C., Helfer, T., 2015. Numerical analysis of concrete creep on mesoscopic 3D specimens. Presented at the Mechanics and Physics of Shrinkage, Creep and Durability of concrete: CONCREEP 10, Wien.
- Bary, B., Gélébart, L., Adam, E., Bourcier, C., 2014. Numerical analysis of linear viscoelastic 3D concrete specimens, in: *Computational Modelling of Concrete Structures*. CRC Press, pp. 373–381.
- Bary, B., Haha, M.B., Adam, E., Montarnal, P., 2009. Numerical and analytical effective elastic properties of degraded cement pastes. *Cem. Concr. Res.* 39, 902–912. doi:10.1016/j.cemconres.2009.06.012
- Bary, B., Ranc, G., Durand, S., Carpentier, O., 2008. A coupled thermo-hydro-mechanical-damage model for concrete subjected to moderate temperatures. *Int. J. Heat Mass Transf.* 51, 2847–2862.
- Bazant, Z.P., 1977. Viscoelasticity of Solidifying Porous Material°Concrete. *J. Eng. Mech. Div.* 103, 1049–1067.
- Bazant, Z.P., 1972. Numerical determination of long-range stress history from strain history in concrete. *Matér. Constr.* 5, 135–141. doi:10.1007/BF02539255
- Bazant, Z.P., Cusatis, G., Cedolin, L., 2004. Temperature effect on concrete creep modeled by microprestress-solidification theory. *J. Eng. Mech.* 130, 691–699.

-
- Bazant, Z.P., Hauggaard, A.B., Baweja, S., Ulm, F.-J., 1997. Microprestress-solidification theory for concrete creep. I: Aging and drying effects. *J. Eng. Mech.* 123, 1188–1194.
- Bazant, Z.P., Huet, C., 1999. Thermodynamic functions for ageing viscoelasticity - integral form without internal variables.pdf. *Int. J. Solids Struct.*
- BBRI, (Belgium Building Research Institute, 2007. Rapport d'essais, BBRI Report DE 611XB050.
- Benboudjema, F., 2002. Modélisation des déformations différées du béton sous sollicitations biaxiales, application aux enceintes de confinement de bâtiments réacteurs des centrales nucléaires. Université de Marne la Vallée.
- Benboudjema, F., Torrenti, J.M., 2008. Early-age behaviour of concrete nuclear containments. *Nucl. Eng. Des.* 238, 2495–2506. doi:10.1016/j.nucengdes.2008.04.009
- Bentur, A., 2003. Report 25: Early Age Cracking in Cementitious Systems - Report of RILEM Technical committee TC 181-EAS: Early age cracking shrinkage induced stresses and cracking in cementitious systems. RILEM Publications.
- Bentz, D.P., 2008. A review of early-age properties of cement-based materials. *Cem. Concr. Res.* 38, 196–204.
- Bentz, D.P., 2007. Transient plane source measurements of the thermal properties of hydrating cement pastes. *Mater. Struct.* 40, 1073–1080. doi:10.1617/s11527-006-9206-9
- Bentz, D.P., 2006. Influence of water-to-cement ratio on hydration kinetics: simple models based on spatial considerations. *Cem. Concr. Res.* 36, 238–244.
- Bentz, D.P., 2005. CEMHYD3D: A Three-Dimensional Cement Hydration and Microstructure Development Modeling Package. Version 3.0. NISTIR 7232. National Institute of Standards and Technology Interagency Report, Technology Administration, U.S. Department of Commerce, NISTIR 7232.
- Benveniste, Y., 1987. Effective thermal conductivity of composites with a thermal contact resistance between the constituents: Nondilute case. *J. Appl. Phys.* 61, 2840–2843. doi:10.1063/1.337877
- Benveniste, Y., 1986. On the effective thermal conductivity of multiphase composites. *Z. Für Angew. Math. Phys. ZAMP* 37, 696–713. doi:10.1007/BF00947917
- Bernard, O., Ulm, F.-J., Lemarchand, E., 2003. A multiscale micromechanics-hydration model for the early-age elastic properties of cement-based materials. *Cem. Concr. Res.* 33, 1293–1309.
- Berodier, E., Scrivener, K., 2014. Understanding the Filler Effect on the Nucleation and Growth of C-S-H. *J. Am. Ceram. Soc.* n/a–n/a. doi:10.1111/jace.13177
- Bezjak, A., Jelenić, I., 1980. On the determination of rate constants for hydration processes in cement pastes. *Cem. Concr. Res.* 10, 553–563.
- Biernacki, J.J., Xie, T., 2011. An Advanced Single Particle Model for C3S and Alite Hydration: Single Particle Model for C3S Hydration. *J. Am. Ceram. Soc.* 94, 2037–2047. doi:10.1111/j.1551-2916.2010.04352.x
- Bishnoi, S., 2008. Vector modelling of hydrating cement microstructure and kinetics. These.
- Bishnoi, S., Scrivener, K., 2009a. Studying nucleation and growth kinetics of alite hydration using μ c. *Cem. Concr. Res.* 39, 849–860.
- Bishnoi, S., Scrivener, K.L., 2009b. μ c: A new platform for modelling the hydration of cements. *Cem. Concr. Res.* 39, 266–274. doi:10.1016/j.cemconres.2008.12.002
- Boltzmann, L., 1874. Zur Theorie der elastischen Nachwirkung. *Wien Ber* 70.
- Bourcier, C., Dridi, W., Chomat, L., Laucoin, E., Bary, B., Adam, E., 2014. Combs: open source python library for RVE generation. Application to microscale diffusion simulations in cementitious materials, in: Caruge, D., Calvin, C., Diop, C.M., Malvagi, F., Trama, J.-C. (Eds.), . EDP Sciences, p. 02107. doi:10.1051/snmc/201402107
- Briffaut, M., 2010. Etude de la fissuration au jeune âge des structures massives en béton: influence de la vitesse de refroidissement, des reprises de bétonnage et des armatures. École normale supérieure de Cachan-ENS Cachan.
-

-
- Briffaut, M., Benboudjema, F., La Borderie, Christian, Torrenti, J.-M., 2013. Creep Consideration Effect on Meso-Scale Modeling of Concrete Hydration Process and Consequences on the Mechanical Behavior. *J. Eng. Mech.* 139, 1808–1817. doi:10.1061/(ASCE)EM.1943-7889.0000607
- Briffaut, M., Benboudjema, F., Torrenti, J.-M., Nahas, G., 2012. Effects of early-age thermal behaviour on damage risks in massive concrete structures. *Eur. J. Environ. Civ. Eng.* 16, 589–605. doi:10.1080/19648189.2012.668016
- Briffaut, M., Benboudjema, F., Torrenti, J.M., Nahas, G., 2011. Numerical analysis of the thermal active restrained shrinkage ring test to study the early age behavior of massive concrete structures. *Eng. Struct.* 33, 1390–1401.
- Buffo-Lacarrière, L., Sellier, A., Escadeillas, G., Turatsinze, A., 2007. Multiphase finite element modeling of concrete hydration. *Cem. Concr. Res.* 37, 131–138.
- Buffo-Lacarrière, L., Sellier, A., Kolani, B., 2014. Application of thermo-hydro-chemo-mechanical model for early age behaviour of concrete to experimental massive reinforced structures with strain-restraining system. *Eur. J. Environ. Civ. Eng.* 18, 814–827. doi:10.1080/19648189.2014.896754
- Bullard, J.W., Jennings, H.M., Livingston, R.A., Nonat, A., Scherer, G.W., Schweitzer, J.S., Scrivener, K.L., Thomas, J.J., 2011. Mechanisms of cement hydration. *Cem. Concr. Res.* 41, 1208–1223.
- Buscaglia, V., Anselmi-Tamburini, U., 2002. On the diffusional growth of compounds with narrow homogeneity range in multiphase binary systems. *Acta Mater.* 50, 525–535. doi:10.1016/S1359-6454(01)00367-6
- Buscaglia, V., Milanese, C., 2005. Diffusion-Controlled Solid-State Reactions of Spherical Particles, A General Model for Multiphase Binary Systems. *J. Phys. Chem. B* 109, 18475–18482. doi:10.1021/jp044500g
- Cahn, J.W., 1956. The kinetics of grain boundary nucleated reactions. *Acta Metall.* 4, 449–459.
- Carol, I., Bažant, Z., 1993. Viscoelasticity with Aging Caused by Solidification of Nonaging Constituent. *J. Eng. Mech.* 119, 2252–2269. doi:10.1061/(ASCE)0733-9399(1993)119:11(2252)
- Cerny, R., Rovnanikova, P., 2002. *Transport Processes in Concrete*. CRC Press.
- Chae, S.R., Moon, J., Yoon, S., Bae, S., Levitz, P., Winarski, R., Monteiro, P.J.M., 2013. Advanced Nanoscale Characterization of Cement Based Materials Using X-Ray Synchrotron Radiation: A Review. *Int. J. Concr. Struct. Mater.* 7, 95–110. doi:10.1007/s40069-013-0036-1
- Chamrova, R., 2010. *Modelling and measurement of elastic properties of hydrating cement paste* (PhD Thesis). EPFL.
- Christensen, R.M., Lo, K.H., 1979. Solutions for effective shear properties in three phase sphere and cylinder models. *J. Mech. Phys. Solids* 27, 315–330. doi:10.1016/0022-5096(79)90032-2
- Constantinides, G., Ulm, F.-J., 2004. The effect of two types of C-S-H on the elasticity of cement-based materials: Results from nanoindentation and micromechanical modeling. *Cem. Concr. Res.* 34, 67–80. doi:10.1016/S0008-8846(03)00230-8
- Cope, J.L., Cannon, R.W., Abdun-Nur, E.A., Diaz, L.H., Oury, R.F., Anderson, F.A., Dolen, T.P., Raphael, J.M., Boggs, H.L., Hansen, K.D., 2002. Effect of Restraint, Volume Change, and Reinforcement on Cracking of Mass Concrete. *ACI Man. Concr. Pract.*
- Costoya, M.M., 2008. Effect of particle size on the hydration kinetics and microstructural development of tricalcium silicate.
- Craeye, B., 2010. *Early-age thermo-mechanical behavior of concrete supercontainers for radwaste disposal*. Gent University.
- Craeye, B., De Schutter, G., Desmet, B., Vantomme, J., Heirman, G., Vandewalle, L., Cizer, Ö., Aggoun, S., Kadri, E.H., 2010. Effect of mineral filler type on autogenous shrinkage of self-compacting concrete. *Cem. Concr. Res.* 40, 908–913. doi:10.1016/j.cemconres.2010.01.014
-

-
- Craeye, B., De Schutter, G., Van Humbeeck, H., Van Cotthem, A., 2009. Early age behaviour of concrete supercontainers for radioactive waste disposal. *Nucl. Eng. Des.* 239, 23–35. doi:10.1016/j.nucengdes.2008.10.006
- Craeye, B., Geirnaert, M., Schutter, G.D., 2011. Super absorbing polymers as an internal curing agent for mitigation of early-age cracking of high-performance concrete bridge decks. *Constr. Build. Mater.* 25, 1–13. doi:10.1016/j.conbuildmat.2010.06.063
- Cruz, C.R., Gillen, M., 1980. Thermal expansion of Portland cement paste, mortar and concrete at high temperatures. *Fire Mater.* 4, 66–70. doi:10.1002/fam.810040203
- Daimon, M., Abo-El-Enein, S.A., Rosara, G., Goto, S., Kondo, R., 1977. Pore Structure of Calcium Silicate Hydrate in Hydrated Tricalcium Silicate. *J. Am. Ceram. Soc.* 60, 110–114. doi:10.1111/j.1151-2916.1977.tb15483.x
- de Borst, R., van den Boogaard, A., 1994. Finite-Element Modeling of Deformation and Cracking in Early-Age Concrete. *J. Eng. Mech.* 120, 2519–2534. doi:10.1061/(ASCE)0733-9399(1994)120:12(2519)
- DeGroot, S.R., Mazur, P., 1984. *Non-Equilibrium Thermodynamics*.
- De Larrard, T., 2010. Variabilité des propriétés du béton: caractérisation expérimentale et modélisation probabiliste de la lixiviation.
- de Larrard, T., Bary, B., Adam, E., Kloss, F., 2013. Influence of aggregate shapes on drying and carbonation phenomena in 3D concrete numerical samples. *Comput. Mater. Sci.* 72, 1–14. doi:10.1016/j.commatsci.2013.01.039
- De Schutter, G., 2002a. Finite element simulation of thermal cracking in massive hardening concrete elements using degree of hydration based material laws. *Comput. Struct.* 80, 2035–2042. doi:10.1016/S0045-7949(02)00270-5
- De Schutter, G., 2002b. Fundamental study of early age concrete behaviour as a basis for durable concrete structures. *Mater. Struct.* 35, 15–21. doi:10.1007/BF02482085
- De Schutter, G., 1999. Degree of hydration based Kelvin model for the basic creep of early age concrete. *Mater. Struct.* 32, 260–265.
- De Schutter, G., Taerwe, L., 1997. Fracture energy of concrete at early ages. *Mater. Struct.* 30, 67–71.
- Diamond, S., 1996. Delayed ettringite formation — Processes and problems. *Cem. Concr. Compos.* 18, 205 – 215. doi:http://dx.doi.org/10.1016/0958-9465(96)00017-0
- Do, Q.H., 2013. *Modelling Properties of Cement Paste from Microstructure: Porosity, Mechanical Properties, Creep and Shrinkage*. EPFL.
- Drugan, W.J., Willis, J.R., 1996. A micromechanics-based nonlocal constitutive equation and estimates of representative volume element size for elastic composites. *J. Mech. Phys. Solids* 44, 497–524. doi:10.1016/0022-5096(96)00007-5
- Dunant, C.F., Bary, B., Giorla, A.B., Péniguel, C., Sanahuja, J., Toulemonde, C., Tran, A.-B., Willot, F., Yvonnet, J., 2013. A critical comparison of several numerical methods for computing effective properties of highly heterogeneous materials. *Adv. Eng. Softw.* 58, 1–12. doi:10.1016/j.advengsoft.2012.12.002
- EN 1992-1-1, 2004. *Eurocode 2: Design of concrete structures*.
- Fairbairn, E.M.R., Silvano, M.M., Toledo Filho, R.D., Alves, J.L.D., Ebecken, N.F.F., 2004. Optimization of mass concrete construction using genetic algorithms. *Comput. Struct.* 82, 281–299. doi:10.1016/j.compstruc.2003.08.008
- Fares, R., 2015. *Estimation numérique multi-échelle des propriétés viscoélastiques du béton au jeune-age*. Master thesis. UPMC.
- Faria, R., Azenha, M., Figueiras, J.A., 2006. Modelling of concrete at early ages: Application to an externally restrained slab. *Cem. Concr. Compos.* 28, 572–585. doi:10.1016/j.cemconcomp.2006.02.012
- Farouki, O.T., 1981. *Thermal Properties of Soils*.
-

-
- Flatt, R., Scherer, G.W., Bullard, J.W., 2011. Why alite stops hydrating below 80% relative humidity. *Cem. Concr. Res.* 41, 987–992.
- Fujii, K., Kondo, W., 1974. Kinetics of the Hydration of Tricalcium Silicate. *J. Am. Ceram. Soc.* 57, 492–497. doi:10.1111/j.1151-2916.1974.tb11400.x
- Garboczi, E.J., Bentz, D.P., 1997. Analytical formulas for interfacial transition zone properties. *Adv. Cem. Based Mater.* 6, 99–108. doi:10.1016/S1065-7355(97)90016-X
- Gartner, E., Young, J., Damidot, D., Jawed, I., 2002. Hydration of Portland cement. *Struct. Perform. Cem.* 13, 978–0.
- Gaspar, A., Lopez-Caballero, F., Modaressi-Farahmand-Razavi, A., Gomes-Correia, A., 2014. Methodology for a probabilistic analysis of an RCC gravity dam construction. Modelling of temperature, hydration degree and ageing degree fields. *Eng. Struct.* 65, 99–110. doi:10.1016/j.engstruct.2014.02.002
- Gawin, D., Pesavento, F., Schrefler, B.A., 2006. Hygro-thermo-chemo-mechanical modelling of concrete at early ages and beyond. Part I: hydration and hygro-thermal phenomena. *Int. J. Numer. Methods Eng.* 67, 299–331.
- Ghabezloo, S., 2011. Micromechanics analysis of thermal expansion and thermal pressurization of a hardened cement paste. *Cem. Concr. Res.* 41, 520–532. doi:10.1016/j.cemconres.2011.01.023
- Ginstling, A., Brounshtein, B., 1950. Concerning the diffusion kinetics of reactions in spherical particles. *J Appl Chem USSR* 23, 1327–1338.
- Haecker, C.-J., Garboczi, E.J., Bullard, J.W., Bohn, R.B., Sun, Z., Shah, S.P., Voigt, T., 2005. Modeling the linear elastic properties of Portland cement paste. *Cem. Concr. Res.* 35, 1948–1960. doi:10.1016/j.cemconres.2005.05.001
- Hasanain, G.S., Khallaf, T.A., Mahmood, K., 1989. Water evaporation from freshly placed concrete surfaces in hot weather. *Cem. Concr. Res.* 19, 465–475. doi:10.1016/0008-8846(89)90035-5
- Hashin, Z., Monteiro, P.J.M., 2002. An inverse method to determine the elastic properties of the interphase between the aggregate and the cement paste. *Cem. Concr. Res.* 32, 1291–1300.
- Hashin, Z., Shtrikman, S., 1963. A variational approach to the theory of the elastic behaviour of multiphase materials. *J. Mech. Phys. Solids* 11, 127–140. doi:10.1016/0022-5096(63)90060-7
- Hattel, J.H., Thorborg, J., 2003. A numerical model for predicting the thermomechanical conditions during hydration of early-age concrete. *Appl. Math. Model.* 27, 1–26. doi:10.1016/S0307-904X(02)00082-3
- Head, M.K., Buenfeld, N.R., 2006. Measurement of aggregate interfacial porosity in complex, multi-phase aggregate concrete: Binary mask production using backscattered electron, and energy dispersive X-ray images. *Cem. Concr. Res.* 36, 337–345. doi:10.1016/j.cemconres.2005.09.007
- Hellmich, C., Ulm, F.-J., Mang, H.A., 1999. Consistent linearization in Finite Element analysis of coupled chemo-thermal problems with exo- or endothermal reactions. *Comput. Mech.* 24, 238–244. doi:10.1007/s004660050512
- Herve, E., Zaoui, A., 1993. n-Layered inclusion-based micromechanical modelling. *Int. J. Eng. Sci.* 31, 1–10. doi:10.1016/0020-7225(93)90059-4
- Heukamp, F.H. (Franz H., 2003. Chemomechanics of calcium leaching of cement-based materials at different scales: the role of CH-dissolution and C-S-H degradation on strength and durability performance of materials and structures (Thesis). Massachusetts Institute of Technology.
- Hilaire, A., 2014. Etude des déformations différées des bétons en compression et en traction, du jeune au long terme: application aux enceintes de confinement (phdthesis). École normale supérieure de Cachan - ENS Cachan.
- Hilaire, A., Benboudjema, F., Darquennes, A., Berthaud, Y., Nahas, G., 2014. Modeling basic creep in concrete at early-age under compressive and tensile loading. *Nucl. Eng. Des., Special*
-

-
- Issue - The International Conference on Structural Mechanics in Reactor Technology (SMiRT21), New Delhi India, Nov 06-11, 2011 269, 222–230. doi:10.1016/j.nucengdes.2013.08.034
- Hillerborg, A., Mod er, M., Petersson, P.-E., 1976. Analysis of crack formation and crack growth in concrete by means of fracture mechanics and finite elements. *Cem. Concr. Res.* 6, 773–781. doi:10.1016/0008-8846(76)90007-7
- Hilton, H.H., Yi, S., 1998. The significance of (an) isotropic viscoelastic Poisson ratio stress and time dependencies. *Int. J. Solids Struct.* 35, 3081–3095.
- Holman, J., 2009. *Heat Transfer*, 10 edition. ed. McGraw-Hill Education, Boston.
- Honorio, T., Bary, B., 2015. Upscaling Ageing Linear Viscoelastic behaviour: Effects of precipitation. Nanocem spring meeting (Poster). Nanocem consortium.
- Honorio, T., Bary, B., 2014. Multiscale estimation of the thermo-viscoelastic properties of cementitious materials at early-age: Partner Project proposal. Nanocem autumn meeting (Poster). Nanocem consortium.
- Honorio, T., Bary, B., Benboudjema, F., 2015. Factors affecting the thermo-chemo-mechanical behaviour of massive concrete structures at early-age. *Mater. Struct.* 1–19. doi:10.1617/s11527-015-0704-5
- Honorio, T., Bary, B., Benboudjema, F., 2015. Multiscale estimation of the viscoelastic properties of cementitious materials at early age: a combined analytical and numerical approach. Presented at the Mechanics and Physics of Shrinkage, Creep and Durability of concrete: CONCREEP 10, Wien.
- Honorio, T., Bary, B., Benboudjema, F., 2014a. Evaluation of the contribution of boundary and initial conditions in the chemo-thermal analysis of a massive concrete structure. *Eng. Struct.* 80, 173–188. doi:10.1016/j.engstruct.2014.08.050
- Honorio, T., Bary, B., Benboudjema, F., 2014. Analysis of the thermo-chemo-mechanical behavior of massive concrete structures at early-age, in: *Computational Modelling of Concrete Structures*. CRC Press, pp. 619–628.
- Honorio, T., Bary, B., Benboudjema, F., 2014b. Influence of the Particle Size Distribution on Hydration Kinetics: a Mechanistic Analytical Approach, in: *RILEM International Symposium on Concrete Modelling*. Presented at the CONMOD14, Beijing, China.
- Honorio, T., Bary, B., Benboudjema, F., 2014c. Estimation of Elastic Properties of Cement based Materials at Early Age based on a Combined Numerical and Analytical Multiscale Micromechanics Approach, in: *RILEM International Symposium on Concrete Modelling*. Presented at the CONMOD14, Beijing, China.
- Honorio, T., Bary, B., Benboudjema, F., in preparation. Multiscale estimation of the viscoelastic properties of cement-based materials at early age: a combined analytical and numerical approach.
- Honorio, T., Bary, B., Benboudjema, F., Poyet, S., submitted. Modelling hydration kinetics based on boundary nucleation and space-filling growth in a fixed confined zone.
- Honorio, T., Bary, B., Sanahuja, J., Benboudjema, F., submitted. Effective properties of n-coated composite spheres assemblage in an ageing viscoelastic framework.
- Hoover, C.G., Ulm, F.-J., 2015. Experimental chemo-mechanics of early-age fracture properties of cement paste. *Cem. Concr. Res.* 75, 42–52. doi:10.1016/j.cemconres.2015.04.004
- Horn, R.A., 1990. *Matrix Analysis*. Cambridge University Press.
- Huet, C., 1999. Coupled size and boundary-condition effects in viscoelastic heterogeneous and composite bodies. *Mech. Mater.* 31, 787–829. doi:10.1016/S0167-6636(99)00038-1
- Ishida, T., Luan, Y., Sagawa, T., Nawa, T., 2011. Modeling of early age behavior of blast furnace slag concrete based on micro-physical properties. *Cem. Concr. Res., Conferences Special: Cement Hydration Kinetics and Modeling*, Quebec City, 2009 & CONMOD10, Lausanne, 2010 41, 1357–1367. doi:10.1016/j.cemconres.2011.06.005
-

-
- Jander, W., 1927. Reaktionen im festen Zustande bei höheren Temperaturen. Reaktionsgeschwindigkeiten endotherm verlaufender Umsetzungen. *Z. Für Anorg. Allg. Chem.* 163, 1–30. doi:10.1002/zaac.19271630102
- JCI, 2008. Japan Concrete Institute guidelines for control of cracking of mass concrete.
- Jennings, H.M., 2008. Refinements to colloid model of CSH in cement: CM-II. *Cem. Concr. Res.* 38, 275–289.
- Jennings, H.M., 2004. Colloid model of C–S–H and implications to the problem of creep and shrinkage. *Mater. Struct.* 37, 59–70. doi:10.1007/BF02481627
- Jensen, O.M., Hansen, P.F., Lachowski, E.E., Glasser, F.P., 1999. Clinker mineral hydration at reduced relative humidities. *Cem. Concr. Res.* 29, 1505–1512.
- Jerri, A., 1999. *Introduction to Integral Equations with Applications*. John Wiley & Sons.
- Johnson, W.H., Parsons, W.H., 1944. *Thermal expansion of concrete aggregate materials*. US Government Printing Office.
- Kamali, S., 2003. Comportement et simulation des matériaux cimentaires en environnement agressifs : Lixiviation et température.
- Kanit, T., Forest, S., Galliet, I., Mounoury, V., Jeulin, D., 2003. Determination of the size of the representative volume element for random composites: statistical and numerical approach. *Int. J. Solids Struct.* 40, 3647–3679. doi:10.1016/S0020-7683(03)00143-4
- Kersten, M.S., 1952. THERMAL PROPERTIES OF SOILS, in: Highway Research Board Special Report. Presented at the 30th Annual Meeting of the Highway Research Board.
- Khan, M.I., 2002. Factors affecting the thermal properties of concrete and applicability of its prediction models. *Build. Environ., Retrofitting of Office Buildings: Papers from the Research Project Office* 37, 607–614. doi:10.1016/S0360-1323(01)00061-0
- Khawam, A., Flanagan, D.R., 2006. Solid-State Kinetic Models: Basics and Mathematical Fundamentals. *J. Phys. Chem. B* 110, 17315–17328. doi:10.1021/jp062746a
- Kim, K.-H., Jeon, S.-E., Kim, J.-K., Yang, S., 2003. An experimental study on thermal conductivity of concrete. *Cem. Concr. Res.* 33, 363–371. doi:10.1016/S0008-8846(02)00965-1
- Kirby, D.M., Biernacki, J.J., 2012. The effect of water-to-cement ratio on the hydration kinetics of tricalcium silicate cements: Testing the two-step hydration hypothesis. *Cem. Concr. Res.* 42, 1147–1156. doi:10.1016/j.cemconres.2012.05.009
- Klemczak, B., Knoppik-Wrobel, A., 2015. Reinforced concrete tank walls and bridge abutments: Early-age behaviour, analytic approaches and numerical models. *Eng. Struct.* 84, 233–251. doi:10.1016/j.engstruct.2014.11.031
- Knudsen, T., 1980. On particle size distribution in cement hydration. Presented at the 7th int. conference on the chemistry of cement, Paris.
- Kolani, B., 2012. Comportement au jeune âge des structures en béton armé à base de liants composés aux laitiers.
- Krstulović, R., Dabić, P., 2000. A conceptual model of the cement hydration process. *Cem. Concr. Res.* 30, 693–698. doi:10.1016/S0008-8846(00)00231-3
- Kumar, A., Bishnoi, S., Scrivener, K.L., 2012. Modelling early age hydration kinetics of alite. *Cem. Concr. Res.* 42, 903–918. doi:10.1016/j.cemconres.2012.03.003
- Ladaoui, W., Vidal, T., Sellier, A., Bourbon, X., 2012. Analysis of interactions between damage and basic creep of HPC and HPFRC heated between 20 and 80 °C. *Mater. Struct.* 46, 13–23. doi:10.1617/s11527-012-9879-1
- Laplante, P., 1993. *Propriétés mécaniques des bétons durcissants: analyse comparée des bétons classiques et à très hautes performances*. Ministère de l'équipement, des transports et du tourisme, Laboratoire central des ponts et chaussées, Paris, France.
- Lavergne, F., Sab, K., Sanahuja, J., Bornert, M., Toulemonde, C., 2015. Investigation of the effect of aggregates' morphology on concrete creep properties by numerical simulations. *Cem. Concr. Res.* 71, 14–28. doi:10.1016/j.cemconres.2015.01.003
-

-
- LCPC, 2009. Recommendations for preventing disorders due to Delayed Ettringite Formation, Guide Technique.
- LCPC, 2002. Caractéristiques microstructurales et propriétés relatives à la durabilité des bétons : Méthodes de mesure et d'essai de laboratoire.
- Le Chatelier, H., 1904. Recherches expérimentales sur la constitution des mortiers hydrauliques (PhD Thesis). Vve C. Dunod.
- Levin, V.M., 1967. Thermal Expansion Coefficients of Heterogeneous Materials. Lzu Akad Nauk SSSR Mekh Tuerd Tela Vol 2 88–94.
- Lin, F., Meyer, C., 2009. Hydration kinetics modeling of Portland cement considering the effects of curing temperature and applied pressure. *Cem. Concr. Res.* 39, 255–265.
- Loukili, A., Chopin, D., Khelidj, A., Le Touzo, J.-Y., 2000. A new approach to determine autogenous shrinkage of mortar at an early age considering temperature history. *Cem. Concr. Res.* 30, 915–922.
- Love, A.E.H. (Augustus E.H., 1944. A treatise on the mathematical theory of elasticity. update forthcoming.
- Lubliner, J., Sackman, J.L., 1966. On ageing viscoelastic materials. *J. Mech. Phys. Solids* 14, 25–32. doi:10.1016/0022-5096(66)90017-2
- Lu, B., Torquato, S., 1992. Nearest-surface distribution functions for polydispersed particle systems. *Phys. Rev. A* 45, 5530–5544. doi:10.1103/PhysRevA.45.5530
- Lura, P., Jensen, O.M., van Breugel, K., 2003. Autogenous shrinkage in high-performance cement paste: An evaluation of basic mechanisms. *Cem. Concr. Res.*, Papers presented at the Fall 2001 Materials Research Society Symposium on Design, Characteristics and Properties of Cementitious Materials 33, 223–232. doi:10.1016/S0008-8846(02)00890-6
- Lura, P., Van Breugel, K., 2001. Thermal properties of concrete: Sensitivity studies. Report, Improved Production of Advanced Concrete Structures (IPACS). Luleå University of Technology.
- Maghous, S., Creus, G.J., 2003. Periodic homogenization in thermoviscoelasticity: case of multilayered media with ageing. *Int. J. Solids Struct.* 40, 851–870. doi:10.1016/S0020-7683(02)00549-8
- Mandel, J., 1966. Cours de mécanique des milieux continus.
- Marshall, A.L., 1972. The thermal properties of concrete. *Build. Sci.* 7, 167–174. doi:10.1016/0007-3628(72)90022-9
- Maslov, G.N., 1940. Thermal Stress States in Concrete Masses, with Account of Concrete Creep. *Izv. NIIG Gosenergoizdat* 28, 175–188.
- Masoero, E., Thomas, J.J., Jennings, H.M., 2013. A Reaction Zone Hypothesis for the Effects of Particle Size and Water-to-Cement Ratio on the Early Hydration Kinetics of C₃S. *J. Am. Ceram. Soc.* n/a–n/a. doi:10.1111/jace.12713
- Matallah, M., La Borderie, C., Maurel, O., 2010. A practical method to estimate crack openings in concrete structures. *Int. J. Numer. Anal. Methods Geomech.* 34, 1615–1633. doi:10.1002/nag.876
- Mazars, J., 1984. Application de la mécanique de l'endommagement au comportement non linéaire et à la rupture du béton de structure. Université Paris VI.
- Mazzotti, C., Savoia, M., 2003. Nonlinear Creep Damage Model for Concrete under Uniaxial Compression. *J. Eng. Mech.* 129, 1065–1075. doi:10.1061/(ASCE)0733-9399(2003)129:9(1065)
- McCarter, W.J., Ben-Saleh, A.M., 2001. Influence of practical curing methods on evaporation of water from freshly placed concrete in hot climates. *Build. Environ.* 36, 919–924. doi:10.1016/S0360-1323(00)00048-2
- McIntosh, G., Sharratt, B.S., 2001. Thermal properties of soil. *Phys. Teach.* 39, 458–460. doi:10.1119/1.1424590
-

-
- Meinhard, K., Lackner, R., 2008. Multi-phase hydration model for prediction of hydration-heat release of blended cements. *Cem. Concr. Res.* 38, 794–802. doi:10.1016/j.cemconres.2008.01.008
- Milton, G.W., 2002. *The Theory of Composites*. Cambridge University Press, Cambridge.
- Monteiro, P.J.M., Chang, C.T., 1995. The elastic moduli of calcium hydroxide. *Cem. Concr. Res.* 25, 1605–1609. doi:10.1016/0008-8846(95)00154-9
- Morabito, P., 2001. Thermal properties of concrete. Variations with the temperature and during hydration phase, *Improved Production of Advanced Concrete Structures (IPACS)*. Luleå University of Technology.
- Mori, T., Tanaka, K., 1973. Average stress in matrix and average elastic energy of materials with misfitting inclusions. *Acta Metall.* 21, 571–574. doi:10.1016/0001-6160(73)90064-3
- Mounanga, P., 2003. Étude expérimentale du comportement de pâtes de ciment au très jeune âge : hydratation, retraits, propriétés thermophysiques. Nantes.
- Mounanga, P., Khelidj, A., Bastian, G., 2004. Experimental study and modelling approaches for the thermal conductivity evolution of hydrating cement paste. *Adv. Cem. Res.* 16, 95–103. doi:10.1680/adcr.2004.16.3.95
- Muller, A.C.A., Scrivener, K.L., Gajewicz, A.M., McDonald, P.J., 2012. Densification of C–S–H Measured by ¹H NMR Relaxometry. *J. Phys. Chem. C* 117, 403–412. doi:10.1021/jp3102964
- Needleman, A., Tvergaard, V., 1993. Comparison of Crystal Plasticity and Isotropic Hardening Predictions for Metal-Matrix Composites. *J. Appl. Mech.* 60, 70–76. doi:10.1115/1.2900781
- ONDRAF/NIRAS, 2010. The cAt project in Dessel: a long-term solution for Belgian category A waste. Master Plan.
- Pecullan, S., Gibiansky, L.V., Torquato, S., 1999. Scale effects on the elastic behavior of periodic and hierarchical two-dimensional composites. *J. Mech. Phys. Solids* 47, 1509–1542. doi:10.1016/S0022-5096(98)00111-2
- Peterson, V.K., Whitten, A.E., 2009. Hydration Processes in Tricalcium Silicate: Application of the Boundary Nucleation Model to Quasielastic Neutron Scattering Data. *J. Phys. Chem. C* 113, 2347–2351. doi:10.1021/jp807209w
- Pignat, C., 2005. Simulation of cement paste microstructure hydration, pore space characterization and permeability determination. *Mater. Struct.* 38, 459–466. doi:10.1617/14355
- Pijaudier-Cabot, G., Bažant, Z., 1987. Nonlocal Damage Theory. *J. Eng. Mech.* 113, 1512–1533. doi:10.1061/(ASCE)0733-9399(1987)113:10(1512)
- Pijaudier-Cabot, G., Dufour, F., 2013. *Damage Mechanics of Cementitious Materials and Structures*. John Wiley & Sons.
- Polianin, A.D., 2002. *Handbook of linear partial differential equations for engineers and scientists*. Chapman & Hall/CRC, Boca Raton.
- Pommersheim, J.M., Clifton, J.R., 1979. Mathematical modeling of tricalcium silicate hydration. *Cem. Concr. Res.* 9, 765–770. doi:10.1016/0008-8846(79)90072-3
- Potgieter, I.C., Gamble, W.L., 1983. Response of Highway Bridges to Nonlinear Temperature Distributions (Report). University of Illinois Engineering Experiment Station. College of Engineering. University of Illinois at Urbana-Champaign.
- Powers, T.C., 1960. Physical properties of cement paste, in: *Proceedings of the Fourth International Symposium on Chemistry of Cement*. Washington, pp. 577–613.
- Poyet, S., 2014. Suivi de l'hydratation du ciment du, Projet ONDRAF/DESSEL. Internal report. CEA Saclay, DPC/SECR/LECBA.
- Reviron, N., Benboudjema, F., Torrenti, J., Nahas, G., Millard, A., 2007. Coupling between creep and cracking in tension, in: *6th International Conference on Fracture Mechanics of Concrete and Concrete Structures, Italie*. Presented at the 6th International Conference on Fracture Mechanics of Concrete and Concrete Structures, Italie.
-

-
- RILEM, Draft. TC thermal cracking in massive structures. State of Art Report.
- Rossi, P., Tailhan, J.-L., Le Maou, F., Gaillet, L., Martin, E., 2012. Basic creep behavior of concretes investigation of the physical mechanisms by using acoustic emission. *Cem. Concr. Res.* 42, 61–73.
- Ruetz, W., 1966. Das Kriechen des Zementsteins im Beton und seine Beeinflussung durch gleichzeitiges Schwinden. *Dtsch Aussch. Stahlbetonz Heft 183 W Ernst Sohn.*
- Sab, K., 1992. On the homogenization and the simulation of random materials. *Eur. J. Mech. Solids* 11, 585–607.
- Sadouki, H., Wittmann, F.H., 1988. On the analysis of the failure process in composite materials by numerical simulation. *Mater. Sci. Eng. A* 104, 9–20. doi:10.1016/0025-5416(88)90401-6
- Salençon, J., 2009. *Viscoélasticité pour le calcul des structures.* Editions Ecole Polytechnique.
- Saling, J., 2001. *Radioactive Waste Management, Second Edition.* CRC Press.
- Sanahuja, J., 2014. Homogenization of Solidifying Random Porous Media: Application to Ageing Creep of Cementitious Materials. Presented at the CONMOD 4 - RILEM International Symposium on Concrete Modelling, Beijing, China.
- Sanahuja, J., 2013a. Effective behaviour of ageing linear viscoelastic composites: Homogenization approach. *Int. J. Solids Struct.* 50, 2846–2856. doi:10.1016/j.ijsolstr.2013.04.023
- Sanahuja, J., 2013b. Efficient Homogenization of Ageing Creep of Random Media: Application to Solidifying Cementitious Materials. *American Society of Civil Engineers*, pp. 201–210. doi:10.1061/9780784413111.023
- Sanahuja, J., Dormieux, L., 2010. Creep of a C-S-H gel: a micromechanical approach. *An. Acad. Bras. Ciênc.* 82, 25–41. doi:10.1590/S0001-37652010000100004
- Sanahuja, J., Dormieux, L., Chanvillard, G., 2007. Modelling elasticity of a hydrating cement paste. *Cem. Concr. Res.* 37, 1427–1439.
- Sanahuja, J., Toulemonde, C., 2011. Numerical homogenization of concrete microstructures without explicit meshes. *Cem. Concr. Res., Conferences Special: Cement Hydration Kinetics and Modeling, Quebec City, 2009 & CONMOD10, Lausanne, 2010* 41, 1320–1329. doi:10.1016/j.cemconres.2011.03.023
- Schapery, R.A., 1968. Thermal Expansion Coefficients of Composite Materials Based on Energy Principles. *J. Compos. Mater.* 2, 380–404. doi:10.1177/002199836800200308
- Scheiner, S., Hellmich, C., 2009. Continuum microviscoelasticity model for aging basic creep of early-age concrete. *J. Eng. Mech.* 135, 307–323.
- Scherer, G.W., 2012. Models of confined growth. *Cem. Concr. Res.*
- Scherer, G.W., Zhang, J., Thomas, J.J., 2012. Nucleation and growth models for hydration of cement.pdf. *Cem. Concr. Res.* 982–993.
- Schorn, H., Rode, U., 1991. Numerical simulation of crack propagation from microcracking to fracture. *Cem. Concr. Compos.* 13, 87–94. doi:10.1016/0958-9465(91)90003-Z
- Scrivener, K.L., Crumbie, A.K., Laugesen, P., 2004. The Interfacial Transition Zone (ITZ) Between Cement Paste and Aggregate in Concrete. *Interface Sci.* 12, 411–421. doi:10.1023/B:INTS.0000042339.92990.4c
- Scrivener, K.L., Nonat, A., 2011. Hydration of cementitious materials, present and future. *Cem. Concr. Res.* 41, 651–665. doi:10.1016/j.cemconres.2011.03.026
- Sellevoid, E.J., Bjontegaard, O., 2006. Coefficient of thermal expansion of cement paste and concrete: Mechanisms of moisture interaction.pdf. *Mater. Struct.* 39, 809–815.
- Siboni, G., Benveniste, Y., 1991. A micromechanics model for the effective thermomechanical behaviour of multiphase composite media. *Mech. Mater.* 11, 107–122. doi:10.1016/0167-6636(91)90011-N
- Smilauer, V., Bazant, Z.P., 2010. Identification of viscoelastic CSH behavior in mature cement paste by FFT-based homogenization method. *Cem. Concr. Res.* 40, 197–207.
-

- Stora, E., 2007. Multi-scale modelling and simulations of the chemo-mechanical behavior of degraded cement-based materials. Université Paris-Est.
- Stora, E., Bary, B., He, Q.-C., Deville, E., Montarnal, P., 2009. Modelling and simulations of the chemo-mechanical behaviour of leached cement-based materials: Leaching process and induced loss of stiffness. *Cem. Concr. Res.* 39, 763–772. doi:10.1016/j.cemconres.2009.05.010
- Sule, M., van Breugel, K., 2004. The effect of reinforcement on early-age cracking due to autogenous shrinkage and thermal effects. *Cem. Concr. Compos., Early Age Concrete - Properties and Performance* 26, 581–587. doi:10.1016/S0958-9465(03)00078-7
- Sun, Z., Garboczi, E.J., Shah, S.P., 2007. Modeling the elastic properties of concrete composites: Experiment, differential effective medium theory, and numerical simulation. *Cem. Concr. Compos.* 29, 22–38. doi:10.1016/j.cemconcomp.2006.07.020
- Tailhan, J.L., D'Aloia, L., 2010. Simulations numériques du comportement au jeune âge des structures en béton : Modélisation et retour d'expérience, *Bulletin des Laboratoires des Ponts et Chaussées* 278, LCPC , pp 65-77.
- Taplin, J.H., 1968. On the hydration kinetics of hydraulic cements. Presented at the Proceedings of the 5th International Symposium on chemistry of cement, Tokyo, pp. 337–348.
- Taplin, J.H., 1960. The temperature coefficient of the rate of hydration of beta-dicalcium silicate. Presented at the 4th International Symposium on Chemistry of Cement, Washington.
- Taylor, H.F.W., 1997. *Cement chemistry*. Telford, London.
- Tennis, P.D., Jennings, H.M., 2000. A model for two types of calcium silicate hydrate in the microstructure of Portland cement pastes. *Cem. Concr. Res.* 30, 855–863.
- Termkhajornkit, P., Barbarulo, R., 2012. Modeling the coupled effects of temperature and fineness of Portland cement on the hydration kinetics in cement paste. *Cem. Concr. Res.* 42, 526–538.
- Thai, M.-Q., Bary, B., He, Q.-C., 2014. A homogenization-enriched viscodamage model for cement-based material creep. *Eng. Fract. Mech.* 126, 54–72. doi:10.1016/j.engfracmech.2014.04.021
- Thomas, J.J., 2007. A New Approach to Modeling the Nucleation and Growth Kinetics of Tricalcium Silicate Hydration. *J. Am. Ceram. Soc.* 90, 3282–3288. doi:10.1111/j.1551-2916.2007.01858.x
- Thomas, J.J., Jennings, H.M., 2006. A colloidal interpretation of chemical aging of the C-S-H gel and its effects on the properties of cement paste. *Cem. Concr. Res.* 36, 30–38. doi:10.1016/j.cemconres.2004.10.022
- Torquato, S., 2002. *Random Heterogeneous Materials: Microstructure and Macroscopic Properties*. Springer Science & Business Media.
- Torrenti, J.M., Buffo-Lacarrière, L., 2009. Variabilité du champ de température dû à la chaleur d'hydratation du béton; Report GT3-1-1, Projet ANR MEFISTO. LCPC-LMDC.
- Toutlemonde, F., Torrenti, J.M., 2012. Crack control of mass concrete and related issues concerning early-age of concrete structures, in: *Proceeding of RILEM International Workshop ConCrack 3 – Control of Cracking in Concrete structures*. PRO 85. Paris.
- Ukrainczyk, N., Matusinović, T., 2010. Thermal properties of hydrating calcium aluminate cement pastes. *Cem. Concr. Res.* 40, 128–136. doi:10.1016/j.cemconres.2009.09.005
- Ulm, F.-J., Constantinides, G., Heukamp, F.H., 2004. Is concrete a poromechanics materials?—A multiscale investigation of poroelastic properties. *Mater. Struct.* 37, 43–58. doi:10.1007/BF02481626
- Ulm, F.-J., Coussy, O., 2001. What is a “massive” concrete structure at early ages? Some dimensional arguments. *J. Eng. Mech.* 127, 512–522.
- Ulm, F.-J., Coussy, O., 1998. Couplings in early-age concrete: From material modeling to structural design. *Int. J. Solids Struct.* 35, 4295–4311. doi:10.1016/S0020-7683(97)00317-X
- Ulm, F.-J., Torrenti, J.-M., Acker, P., 2004. *Comportement du béton au jeune âge: Hermès / lavoisier, Traité MIM Série Mécanique et ingénierie des matériaux*.

-
- Van Breugel, K., 1997. Simulation of Hydration and Formation of Structure in Hardening Cement-Based Materials—HYMOSTRUC.
- Van Breugel, K., Koenders, E.A.B., 2001. Solar radiation, Improved production of advanced concrete structures (IPACS). Luleå University of Technology.
- Vandamme, M., Ulm, F.-J., 2013. Nanoindentation investigation of creep properties of calcium silicate hydrates. *Cem. Concr. Res.* 52, 38–52. doi:10.1016/j.cemconres.2013.05.006
- Vandamme, M., Ulm, F.-J., 2009. Nanogranular origin of concrete creep. *PNAS*.
- Vargaftik, N.B., 1993. Handbook of Thermal Conductivity of Liquids and Gases. CRC Press.
- Velez, K., Maximilien, S., Damidot, D., Fantozzi, G., Sorrentino, F., 2001. Determination by nanoindentation of elastic modulus and hardness of pure constituents of Portland cement clinker. *Cem. Concr. Res.* 31, 555–561.
- Volterra, V., 1959. Theory of functionals and of integral and integro-differential equations [WWW Document]. CERN Doc. Serv. URL <http://cds.cern.ch/record/268343> (accessed 11.19.14).
- Wang, Z.M., Kwan, A.K.H., Chan, H.C., 1999. Mesoscopic study of concrete I: generation of random aggregate structure and finite element mesh. *Comput. Struct.* 70, 533–544. doi:10.1016/S0045-7949(98)00177-1
- Wittmann, F.H., 1982. Creep and shrinkage mechanisms, in: Z.P. Bažant, F.H. Wittmann (Eds.), *Creep and Shrinkage of Concrete Structures*. Wiley, New York, pp. 129–161.
- Wong, T., Brace, W., 1979. Thermal expansion of rocks: some measurements at high pressure. *Tectonophysics* 57, 95–117.
- Wriggers, P., Moftah, S.O., 2006. Mesoscale models for concrete: Homogenisation and damage behaviour. *Finite Elem. Anal. Des.*, The Seventeenth Annual Robert J. Melosh Competition The Seventeenth Annual Robert J. Melosh Competition 42, 623–636. doi:10.1016/j.finel.2005.11.008
- Wyrzykowski, M., Lura, P., 2013. Moisture dependence of thermal expansion in cement-based materials at early ages. *Cem. Concr. Res.* 53, 25–35. doi:10.1016/j.cemconres.2013.05.016
- Xu, H., Zhao, Y., Vogel, S.C., Daemen, L.L., Hickmott, D.D., 2007. Anisotropic thermal expansion and hydrogen bonding behavior of portlandite: A high-temperature neutron diffraction study. *J. Solid State Chem.* 180, 1519–1525. doi:10.1016/j.jssc.2007.03.004
- Xu, Y., Chung, D.D.L., 2000. Effect of sand addition on the specific heat and thermal conductivity of cement. *Cem. Concr. Res.* 30, 59–61. doi:10.1016/S0008-8846(99)00206-9
- Yip, S., Short, M.P., 2013. Multiscale materials modelling at the mesoscale. *Nat. Mater.* 12, 774–777. doi:10.1038/nmat3746
- Yoon, S., Macphee, D.E., Imbabi, M.S., 2014. Estimation of the thermal properties of hardened cement paste on the basis of guarded heat flow meter measurements. *Thermochim. Acta* 588, 1–10. doi:10.1016/j.tca.2014.04.015